Long-Term Magma Dynamics and Volcanic Deformation, with Application to the Western Galápagos

Eoin Patrick Reddin

Submitted in accordance with the requirements for the degree of
Doctor of Philosophy

The University of Leeds
School of Earth and Environment

June 2023

The candidate confirms that the work submitted is their own, except where work which has formed part of jointly authored publications has been included. The contribution of the candidate and the other authors to this work has been explicitly indicated below. The candidate confirms that appropriate credit has been given within the thesis where reference has been made to the work of others.

The work in Chapter 2 of this thesis is being prepared for submission to Volcanica, with the title:
Reddin, E., Ebmeier, S. K., Mothes, P., Aguaiza, S., Espin Bedon, P., (In Prep.). Craters of Habit: Patterns of Deformation, Unrest, and Eruption in the Western Galápagos.

E. Reddin reviewed the published literature on the Western Galápagos, and synthesised the information into a manuscript. I also performed data processing and analysis, and constructed figures to present the synthesised and new information. S. K. Ebmeier provided supervisory input as well as draft feedback and suggestions. P. Mothes, S. Aguaiza, and P. Espin Bedon provided literature suggestions, and expert opinion on results and discussion.

The work in Chapter 3 of this thesis is under revision following peer review from Nature Communications, with the title:
Reddin, E., Ebmeier, S. K., Rivalta, E., Bagnardi, M., Baker, S., Bell, A. F., Mothes, P., Aguaiza, S., Espin Bedon, P., (In Review). Shallow Reservoir Deformation at Galápagos Volcanoes Demonstrates Shared Magma Source Dynamics.

E. Reddin performed data processing, data analysis, modelling, and produced all figures. S. K. Ebmeier provided scripts to initiate Independent Component Analysis, and provided draft feedback and suggestions. E. Rivalta and M. Bagnardi provided expert opinion on the performed modelling and analysis. S. Baker provided expert opinion on the results of his PhD. A. F. Bell, P. Mothes, S. Aguaiza, and P. Espin Bedon provided expert opinion on Galápagos seismicity and volcanology.

The work in Chapter 4 of the thesis is a manuscript with the title:
Reddin, E., Ebmeier, S. K., Morgan, D. J., Rivalta, E., Nikkhoo, M., (In Prep.). The Effect of Crystallisation on Volcanic Deformation.

E. Reddin developed the crystallisation model, and ran the model simulations. S. K. Ebmeier, E. Rivalta, and D. J. Morgan provided supervisory input and provided draft feedback and suggestions. M. Nikkhoo provided expert opinion on deformation modelling, and the pCDM scripts.

Acknowledgements

First and foremost, I would like to thank Susanna Ebmeier for her constant support throughout my PhD. Her enthusiasm, constructive comments, and patience during endless hours of discussions produced this final piece of work. Susi set a standard of excellence that elevated the quality of my PhD research, but I am particularly grateful for the compassion she showed during difficult times at the end of my second year. This marked a turning point in my PhD, from which we produced research that I am genuinely proud of. Thank you, Susi.

I was fortunate to collaborate with a range of excellent people throughout the course of my PhD, from whom each contribution is valued. However I would like to particularly thank Dan Morgan, Eleonora Rivalta, and Marco Bagnardi for their opinion and support at various points of my PhD. Thanks also to the staff at the Institute of Geophysics and Tectonics for the discussions had over coffee or beers.

Thank you to my PGR colleagues in IGT for making my time in Leeds so memorable, and for the mutual support while the University was closed. Though I wound up spending more time away from Leeds than I had intended, I know that the friendships made while I was there will last a lifetime. Thanks especially to Felix and Grace for letting me stay with them, for being travel buddies, and for their constant support. I don't know how I would have done it without you.

Thanks to my family for the constant support and encouragement. Finally, thank you to Sorcha for everything. Your support, encouragement, and unwavering belief in me got me across the line, and I will always be grateful.

Go raibh maith agaibh!

Abstract

Ground deformation at volcanic centres is complex, and primarily occurs as a response to volume changes in the underlying magmatic system, providing insight into the dynamics of magma migration and storage. Syn-eruptive displacements are well studied due to their high-magnitude, and inform us about the depth and geometry of the source that fed the eruption, the location of any eruptive fissures, as well as the location and geometry of any conduits between the source and the surface, such as a dike. However, volcanic ground displacements during periods of eruptive quiescence are arguably more informative, given their use in eruption forecasting (e.g. an uptick in uplift prior to an eruption), and in evaluating changes in magma supply.

Here, I use satellite Interferometric Synthetic Aperture Radar to investigate long-term displacements at established magmatic reservoirs, with particular focus on volcanoes of the Western Galápagos. I synthesise observations of displacement from the complete geodetic record, and make new observations from 2015–2022, using Sentinel-1 data. I consider these observations in context of the eruptive and petrological record for each volcano to propose a new, unrest-based classification for Western Galápagos volcanism. I then analyse the Sentinel-1 time series in detail, and show that volcanoes here routinely undergo correlated deformation with one another. I propose that there is a regional, bottom-up, magmatic control on this behaviour. Finally, I consider long-term observations of volcanic subsidence, using examples from the Galápagos and around the world, to investigate the role of crystallisation on magmatic volume loss and deformation.

Through these three studies, I showcase the complex interactions between magmatic processes, and volcanic surface deformation. By making novel observations of volcanic ground displacement at multiple volcanoes, I provide new insight into the workings of volcanic systems, and demonstrate the utility of InSAR when considered alongside other petrological and geophysical techniques.

Contents

List of Figures

List of Tables

Nomenclature

List of acronyms

ALOS-1	Advanced Land Observing Satellite-1
ALOS-2	Advanced Land Observing Satellite-2
CDM	Compound Dislocation Model
cGPS	continuous Global Positioning System
DEM	Digital Elevation Model
DRE	Dense Rock Equivalent
ECMWF	European Centre for Medium-Range Weather Forecasts
ERS-1	European Remote-Sensing Satellite-1
ERS-2	European Remote-Sensing Satellite-2
ESA	European Space Agency
GACOS	Generic Atmospheric Correction Online Service
GBIS	Geodetic Bayesian Inversion Software
GPS	Global Positioning System
ICA	Independent Component Analysis
IGEPN	Instituto Geofísico de la Escuela Politécnica Nacional
InSAR	Interferometric synthetic aperture RaDAR
LOS	Line-of-Sight
pCDM	point Compound Dislocation Model
PDF	Probability Density Function
SAR	Synthetic aperture RaDAR
SBAS	Small Baseline Subset
SLC	Single-Look Complex
TVZ	Taupo Volcanic Zone
TCMS	Trans-Crustal Magmatic System
USGS	United States Geological Survey
VEI	Volcanic Explosivity Index

Chapter 1

Introduction

The measurement of volcanic deformation is key when monitoring volcanic unrest, providing insight into the dynamics of the magmatic system. Deformation at volcanic systems varies both in the magnitude and timescales across which it occurs. The mechanisms that cause this deformation are similarly varied: displacement may occur due to surficial processes such as slip along volcanic fault systems (e.g. Sierra Negra (Jónsson et al., 2005)) or by the cooling of volcanic deposits (e.g. Timanfaya (Purcell et al., 2022)). Volcanoes also show a deformation response to sub-volcanic processes such as hydrothermal depressurisation (e.g. Aluto (Hutchison et al., 2016)), the cooling and crystallisation of magma in shallow reservoirs (e.g. Alcedo (Hooper et al., 2007)), as well as by magma migration through the magmatic system (e.g. Cerro Azul (Guo et al., 2019)). Monitoring ground displacement signals plays an important role in eruption forecasting (Gregg et al., 2022), in analysing the conditions that caused an eruption (Galetto et al., 2020), and in understanding volcanic behaviour during periods of eruptive quiescence (Biggs et al., 2009). When considered as part of a multi-parametric approach (Goitom et al., 2015), volcanic deformation monitoring plays a critical role in understanding and reconstructing the structure of a sub-volcanic system.

Rather than being stored in large sub-volcanic bodies, magma is now believed to be distributed vertically throughout the crust, in an extensive Trans-Crustal Magmatic system (TCMS) (Cashman et al., 2017). Evidence of such vertically extensive magmatic systems can be seen in the Western Galápagos, where "stacked" reservoirs have been observed at each of Fernandina (1 km and 5 km (Bagnardi and Amelung, 2012)), Wolf (1 km and 5 km (Xu et al., 2016)), and Sierra Negra (2 km and 8 km (Bell et al., 2021b)). In the TCMS model, discrete magmatic sills (comprising a mixture of liquid melt, solid crystals, and fluid volatiles), are interspersed between magmatic mush, which develops as the volcano matures (Cashman et al., 2017; Harpp and Geist, 2018). While petrological and seismic techniques can inform about magmatic processes throughout

the TCMS, ground displacements are sensitive to volume changes within the upper 10 km of the lithosphere (Ebmeier et al., 2018; Bagnardi and Amelung, 2012; Biggs et al., 2009; Parker et al., 2016). As such, volume change of the shallowest reservoir of the entire trans-crustal magmatic system dominates the observed ground displacement signals. Deciphering these signals allows us to understand the underlying magmatic processes driving reservoir volume change.

In this thesis, I use Interferometric Synthetic Aperture Radar (InSAR) data to understand the magmatic processes that cause sub-volcanic reservoirs to produce measurable displacement, and how these processes vary with time. I first explore the magmatic causes of surface displacement in the Western Galápagos, and how they have varied with time since the beginning of InSAR studies there in 1992. I then show that shallow magmatic reservoirs there have consistently deformed due to periodic influxes of magma, causing related displacements at multiple volcanoes simultaneously. Finally, I investigate the timescales over which the cooling and crystallisation of a stalled magma may produce measurable ground surface deformation, while leveraging global datasets. In this chapter, I will introduce the key concepts that I refer to throughout the rest of this thesis. I will firstly discuss InSAR, and how it can be leveraged to monitor volcanic deformation. I then detail how specific magmatic processes within a reservoir produce measurable ground surface displacement. Finally, I will provide an overview of the structure of this thesis, as well as my primary aims and objectives.

1.1 Introduction to InSAR

InSAR is a remote sensing tool used to measure millimetre- to centimetre-scale ground surface displacements at metre scale spatial resolution, over areas of hundreds of kilometres (Bürgmann et al., 2000). Principal applications of InSAR include monitoring volcanic eruptions (Wolf, 2015 (Xu et al., 2016)), the earthquake cycle (e.g. interseismic strain accumulation (Watson et al., 2022) and coseicmic ground motion (Xu et al., 2020)), mass movement and landslides (Guangling, 2010 (Kang et al., 2017)), as well as anthropogenic processes such as geothermal extraction (Taupo Volcanic Zone, e.g. Hamling et al. (2015)). Though the manufacture, launch and maintenance costs of a satellite-based InSAR platform are undoubtedly higher than ground-based geodetic methods (e.g. seismometers, tiltmeters), it has several distinguishing advantages that have made it an essential technique in modern Earth systems monitoring. Given that it is generally a space-based technique, it facilitates the monitoring of locations that would be otherwise inaccessible, or irregularly monitored by ground-based platforms (e.g. Wolf (Stock et al., 2018)). It provides worldwide, frequent (varying with satellite repeat time (Table 1.1)) monitoring once launched, allowing for sustained Earth observation. InSAR facilitates monitoring across large areas (e.g. an entire volcanic edifice), and can capture processes that in-situ monitoring stations may miss (such as

Mission	Duration	Wavelength (cm)	Pixel Resolution (m)[a]	Repeat Time (days)
ALOS-1	2006–2011	23.5	10–100	46
ALOS-2	2014–Present	23.5	3–60	14
COSMO-SkyMed	2007–Present	3.1	1–30	16[b]
ENVISAT	2002–2012	5.6	30–150	35
ERS-1	1991–2000	5.6	26x6	35
ERS-2	1995–2011	5.6	26x6	35
JERS-1	1992–1998	23.5	18x6	44
RADARSAT-1	1995–2013	5.6	5x8–100	24
RADARSAT-2	2008–Present	5.6	5x8–100	24
Sentinel-1a	2014–Present	5.6	5–25x100	12[c]
Sentinel-1b	2016–2021	5.6	5–25x100	12[c]
TerraSAR-X	2008–Present	3.1	0.25–40	11
TanDEM-X	2010–Present	3.1	0.25–40	11
ICEYE	2018–Present	3.1	> 0.5	< 1

[a] Minimum and maximum pixel resolutions may vary with scan mode
[b] $\geq$ One day if in constellation with partner satellites
[c] Six days if in constellation with partner satellite

Table 1.1: Key parameters for satellite-based SAR platforms.

the off-caldera lateral sill propagation during the 2018 eruption of Sierra Negra (Bell et al., 2021b; Davis et al., 2021)). In the field of volcanology, these factors have made InSAR a powerful geodetic tool for monitoring eruptions and unrest. It is widely used for measuring ongoing ground deformation, as well to retrospectively study displacement during volcanic eruptions, particularly in locations where ground-based systems are absent (e.g. Nabro (Goitom et al., 2015)). It is also well suited to study low-magnitude unrest at volcanoes that are in a period of extended eruptive quiescence, as it facilitates monitoring at non-active volcanoes that are otherwise poorly studied (e.g. Darwin (Amelung et al., 2000)).

Here, I use InSAR to study surface displacements at volcanic systems. InSAR has been widely applied to volcanoes, and has captured phenomena such as long-term subsidence due to the cooling of magma (Hooper et al., 2007), and lava flows (Purcell et al., 2022), pre-eruptive inflation (Chadwick et al., 2006), syn- and post-eruptive deformation (Galetto et al., 2023), as well as non-eruptive unrest, and lateral sill propagation (Guo et al., 2019; Bagnardi and Amelung, 2012). I discuss these phenomena, and the Galápagos events in detail in Chapters 2–4. Though I primarily utilise Sentinel-1 data, I make reference to multiple satellite missions throughout this thesis. The names, dates and other key information about these satellites is provided in Table 1.1, for reference.

The signature component of InSAR studies is the interferogram, a radar image that

presents line-of-sight displacement in terms of phase change, as a series of fringes. Interferograms are constructed by combining two Synthetic Aperture Radar (SAR) images, acquired by the satellite platform, at different temporal intervals. In the following paragraphs, I will provide an overview of SAR, how it is are used to produce an interferogram, as well as the use and limitations of InSAR in a volcanic context.

1.1.1 Synthetic Aperture Radar

Synthetic Aperture Radar is a transmit-and-receive remote sensing technique, that uses the amplitude and round-trip travel times of a transmitted microwave to generate a two-dimensional image of an area, in the radar line-of-sight (Bürgmann et al., 2000). The key advantage of using wavelengths in the microwave domain (e.g. X band, C band, and L band, have wavelengths of 3 cm, 6 cm, and 24 cm respectively (Massonnet and Feigl, 1998)) is their functionality in all weather conditions, at any time of day. SAR can reliably image at night, through optically obscuring media such as clouds and fog (Massonnet and Feigl, 1998).

SAR platforms orbit the Earth in either descending (north to south), or ascending (south to north) directions. SAR satellites look to the side, at angles of between 10°–60°. This allows an area of between 50–150 km to be illuminated in the range direction (cross-track), and of 5–15 km in the azimuth (along-track) direction (Lu and Dzurisin, 2014). The side looking geometry facilitates imaging of a ground target by illuminating areas in one track direction that may be in radar shadow (an imaged area where no information is recorded (Dualeh et al., 2023)) in the other. SAR platforms image by transmitting successive pulses in a cross-track direction, as the satellite moves along its track. The location of the imaging target (e.g. that which reflected the radar wave) is determined in two steps, using the reflected echos. First, radar echos are sorted by their round trip flight time, to define a circle of equidistance, from the satellite to the ground surface (Massonnet and Feigl, 1998). The Doppler frequency shift of the echos, caused as the satellite moves along track, creates hyperbolas of equidoppler from the satellite to the ground. The target location is determined by the overlap of the equidistant circle, and the equidoppler hyperbolas (Massonnet and Feigl, 1998). This technique allows for a dramatic increase in the resolution with which a target can be imaged, by artificially creating a larger radar receiver (e.g. the "Synthetic" part of Synthetic Aperture Radar). A space-based real-aperture radar system would have a ground pixel resolution of between 5–10 km (Bürgmann et al., 2000), while InSAR platforms have metre to sub-metre scale resolution (e.g. Sentinel-1 and TerraSAR-X (Table 1.1)). The ground pixel resolution (ΔR) in the range direction is given by Equation 1.1, where c is the speed of light, τ is the radar pulse duration, and θ is the incidence angle, though this may be modified by radar compression techniques, to increase signal amplitude, and the returned signal-to-noise ratio.

$$\Delta R = \frac{c\tau}{2sin\theta} \tag{1.1}$$

Resolution in the azimuth direction (ΔA) is governed by Equation 1.2, where R_m is the slant range (distance from antenna to target), λ is the radar wavelength, and L_a is the antenna length.

$$\Delta A = R_m \frac{\lambda}{L_a} \tag{1.2}$$

1.1.2 Interferometric Synthetic Aperture Radar

A focused SAR image can be thought of as a two dimensional matrix of complex numbers, where each index refers to an imaged target on the Earth's surface (a Single-Look Complex (SLC) image). The complex numbers record the constituent components of a radar echo: amplitude and phase. Echo amplitude describes the reflectivity of the target, or its ability to return the radar wave to the receiver (Massonnet and Feigl, 1998). It varies with surface roughness, local gradient, and the dielectric properties of the target (Dualeh et al., 2023). For example, a calm lake, with flat surface will act as a perfect reflector (Massonnet and Feigl, 1998), while a choppy lake will scatter some radar energy away from the satellite, thereby decreasing the returned amplitude (Massonnet and Feigl, 1998). Echo phase is a measure of the round-trip path length between the satellite and the target (Massonnet and Feigl, 1998; Lu and Dzurisin, 2014), and is the component that is primarily used in measuring volcanic deformation. By differencing the phase information of two SAR images, we produce an interferogram. An interferogram can be considered as a two dimensional matrix, where each index refers to the phase range change between corresponding indices in individual SAR images. The interferogram line-of-sight phase change ($\Delta\phi_{LOS}$), records range changes in the ground surface (e.g. surface deformation ($\Delta\phi_{Def}$)), but also contains nuisance terms, that must be removed to accurately measure surface deformation.

$$\Delta\phi_{LOS} = \Delta\phi_{Def} + \Delta\phi_{Orb} + \Delta\phi_{Topo} + \Delta\phi_{Atm} + \Delta\phi_{Noise} \tag{1.3}$$

Here (Equation 1.3), $\Delta\phi_{Orb}$ refers to the error introduced by differences in satellite orbits. The contribution of this term between SAR orbits is minimised during interferogram processing, by assuming the satellite is viewing a smooth ellipsoid, though residual errors may persist. $\Delta\phi_{Topo}$ refers to topographic fringes, that are produced by a stereoscopic effect, due to differences in the radar view angle (Massonnet and Feigl, 1998). This term is minimised with the use of DEM, though the difference between the DEM and true topography may result in residual errors. $\Delta\phi_{Noise}$ refers to noise that is introduced and unaccounted for in the final interferogram (e.g. thermal

noise). Finally, the $\Delta\phi_{Atm}$ term refers to the phase shift that occurs as the radar wave passes through media with different refractive properties on different acquisition dates (e.g via Snells Law). While tropospheric temperature and pressure changes affect radar refractivity, variations in water vapour content during SAR acquisitions have the greatest effect (Hanssen, 2001). These variations are either from turbulent sources (causing spatially correlated refractivity heterogeneity across the entire interferogram), or from vertical stratification (causing phase refractivity changes that correlate with topography) (Hanssen, 2001). Therefore, tropospheric water vapour changes are particular issue at volcanic settings (Ebmeier et al., 2013), as they may cause apparent deformation signals (Albino et al., 2019). $\Delta\phi_{Atm}$ may be minimised using atmospheric correction techniques: phase-elevation correlation, and global weather models. Phase-elevation correction techniques use empirical models of phase with topography to correct for stratified water vapour, though are not useful for turbulent water vapour (Ebmeier et al., 2013; Purcell et al., 2022). Global weather models (e.g. Generic Atmospheric Correction Online Service (GACOS) (Yu et al., 2018b)) use high resolution data from global weather models (e.g. from the European Centre for Medium Range Weather Forecasts (ECMWF)) to produce maps of zenith phase delay that allow for phase delay correction specific to the target area and acquisition time. The appropriate use of either correction technique varies by dataset: Albino et al. (2019) find that GACOS corrections perform better than a phase-elevation correlation model at Agung, Indonesia, while Purcell et al. (2022) find a linear phase-elevation correction performed better than GACOS at Lanzarote, Spain. Once these nuisance terms have been minimised, we can study the contribution of the deformation term $\Delta\phi_{Def}$, which must exceed noise in order to be detected.

In an interferogram $\Delta\phi_{LOS}$ is wrapped, meaning that the phase value for a given pixel is cyclical, between 0–2π. This wrapping is what gives interferograms their characteristic fringes, where each fringe represents a full cycle between 0–2π, equal to half the radar wavelength (Lu and Dzurisin, 2014). The ambiguity in phase difference across an interferogram is resolved during unwrapping, when the 2π modulo is expressed as absolute phase change values. Equation 1.4 describes the relationship between LOS phase ($\Delta\phi_{LOS}$) and LOS displacement (ΔH), where λ is the satellite wavelength (e.g. 5.6 cm for Sentinel-1 (Table 1.1)).

$$\Delta\phi_{LOS} = -\frac{4\pi\Delta H}{\lambda} \tag{1.4}$$

Once this wrapped or unwrapped interferogram is produced, there are several more factors that must be considered before deformation at a volcano can be analysed. InSAR coherence represents the similarity between the constituent SAR images that compose

an interferogram, and is a measure of interferometric correlation (γ) — the change in radar backscatter characteristics between satellite acquisitions. Fully correlated pixels (those that are stable across SAR acquisitions), will have $\gamma = 1$, whereas pixels with independent backscatter properties will have $\gamma = 0$, at which point they are decorrelated. The three primary causes of interferometric decorrelation are thermal, geometric, and temporal (Bürgmann et al., 2000). Thermal decorrelation due to noise in radar instruments (Hanssen, 2001). Geometric decorrelation occurs when change across an interferometric pixel is greater than 2π. This occurs due to topographic slope, significant ground surface deformation, or from large satellite baselines (Bürgmann et al., 2000). Temporal decorrelation is due to environmental conditions causing changes in backscatter properties between acquisitions. When studying volcanoes, both geometric and temporal decorrelation commonly inhibit accurate InSAR measurements. Between satellite acquisitions, radar backscatter may be significantly altered by vegetation growth, tephra deposition, or lava flow emplacement (Dualeh et al., 2023). The deposition of eruptive products may change the backscatter properties of the target (temporal), while co-eruptive deformation may cause geometric decorrelation during an eruption, when InSAR observation is desirable. Strategies to reduce temporal decorrelation include small baseline subset analysis techniques (e.g. Berardino et al. (2002)), utilising interferograms with short temporal baselines.

1.1.3 Deformation Time Series and Modelling

Time Series Analysis

Though individual interferograms spanning volcanic unrest periods (e.g. an eruption) are often informative, to understand long-term volcanic behaviour it is necessary to produce time-series of cumulative displacement. Persistent Scatterer (PS) (Hooper et al., 2007), and Small Baseline (Berardino et al., 2002) techniques are popular methods of constructing these time series. Small Baseline InSAR uses interferograms with small baselines (e.g. little orbital separation between satellite tracks), that overlap in time in order to minimise decorrelation (Berardino et al., 2002). These temporally overlapping interferograms are "linked" through the application of singular value decomposition to estimate the mean displacement rate at individual acquisition dates. This technique has been successfully applied at numerous volcanoes (Lu and Dzurisin, 2014), and further refined by subsequent studies (e.g. temporal constraint used by NSBAS (López-Quiroz et al., 2009)). This approach reduces noise when the interferogram network may be disconnected, due to missing acquisitions or phase decorrelation. Morishita et al. (2020) present a software package (LiCSBAS) with improved time series analysis by identifying low quality interferograms (those with many unwrapping errors).

This python based package leverages interferograms that have been automatically produced by the LiCSAR interferometric processor (Lazecký et al., 2020), to construct

time series of displacement. LiCSAR automatically produces interferograms of defined frames, corresponding to areas of 250 by 250 km (Lazecký et al., 2020), using Sentinel-1 SAR data. Each acquisition is co-registered to a primary image, and then used to construct interferograms using three succeeding, and three preceding acquisitions (Lazecký et al., 2020). These interferograms are multilooked to 46 by 56 m pixel spacing before being unwrapped. Finally, the wrapped, unwrapped, and coherence images are geocoded (pixel spacing of approximately 100 m), and converted to GeoTIFF files. These final files are available to download on the COMET-LiCS Sentinel-1 InSAR portal (Lazecký et al., 2020). Once processed, the interferograms can be used in time series analysis software, such as LiCSBAS (Morishita et al., 2020). In LiCSBAS interferograms are first prepared for analysis in the following steps. First, the processed GeoTIFFs, and relevant metadata are downloaded. These files are then converted to single precision floating-point format, and can be further downsampled if full resolution is not required. Tropospheric noise can then corrected using GACOS data (Yu et al., 2018b) (Section 1.1.2), which can be optionally downloaded alongside the LiCSAR interferograms (Lazecký et al., 2020; Morishita et al., 2020). Optionally, these interferograms can be masked, either spatially, or using a coherence threshold, as well as clipped to the area of interest (e.g. a volcanic edifice). In the time series analysis steps, an initial quality check is performed to identify incomplete interferograms (e.g. missing bursts), and remove those with low coverage (Morishita et al., 2020). The dataset is then further refined using loop closure (Equation 1.5).

$$\Phi_{123} = \phi_{12} + \phi_{23} - \phi_{13} \tag{1.5}$$

Here, the loop phase (Φ_{123}), calculated by Equation 1.5, is the difference between the phase values for an interferogram (ϕ_{13}), and the sum of the phase values of two interferograms (ϕ_{12} and ϕ_{23}) spanning the same period. Bad interferograms (e.g. those with many unwrapping errors) are identified by calculating the root mean square of the loop phase. If there are no errors, this value should be close to zero. However, if this value exceeds a threshold (in radians), it probably contains errors, and is not included in the time series inversion (Morishita et al., 2020). This inversion uses a similar approach to NSBAS, and records gaps in the time series to aid interpretation. Summary dataset statistics, such as the standard deviation of velocity, are then calculated. The final time series can then be further masked, based on a given noise index, and filtered, using a spatiotemporal Gaussian filter (Morishita et al., 2020). Time series presented throughout this thesis have been produced via this methodology. I use this LiCSAR–LiCSBAS workflow here as it rapidly produces atmospherically corrected time series with a high temporal resolution, at various global settings, from the Galápagos (Chapters 2 and 3), to East Africa and New Zealand (Chapter 4). Critically, this methodology has been developed by COMET, and is well supported by numerous staff,

making tasks such as gapfilling straightforward. A disadvantage of this approach is that the final spatial resolution (approx. 100 m pixel spacing), is less informative when considering localised volcanic processes (e.g. hydrothermal unrest at Alcedo (Chapter 2)) than other potential workflows (e.g. using higher resolution interferograms). We use various methods (e.g. Independent Component Analysis) to interpret final time series of volcanic displacement. These methods are detailed in their respective chapters.

Modelling Geodetic Signals

Once deformation has been observed, it is often necessary to perform further modelling in order to determine the source parameters, particularly when studying volcanoes. This modelling informs estimates of depth, volume change and geometry, and is useful for comparing with petrological data (Stock et al., 2018), as well as reconstructing sub-volcanic structure (e.g. the stacked reservoirs at Fernandina were identified using geodetic source models (Bagnardi and Amelung, 2012)). In this thesis, there are three analytical models that I use to find expected displacement in an elastic medium, from an incompressible source. This modelling is done with the aim of characterising source parameters by inverting displacement maps, as well as through forward models, that I use to predict displacement. A key point when applying these source models is that they capture a change in parameters (e.g. volume change) of a source rather than the total geometry of the source. For example, a best fit sill opening of 0.5 m does not mean that the source sill is 0.5 m thick, but rather that it thickened by 0.5 m over the observation period.

The first, and simplest model used is the Mogi source (Mogi, 1958), which approximates a magmatic reservoir as a point source that is parameterised in terms of its X coordinate, Y coordinate, depth, and volume change. Mogi sources are isotropic, meaning that they are best suited to model processes such as sustained uplift or subsidence. Accordingly, they are ill-suited to model anisotropic processes. This, alongside the simple source geometry (a point source is not representative of any known volcanic structure) means that Mogi sources are best suited to apply first order constraints on source location and volume. Despite this, there are numerous examples where the best published estimates of source geometry is approximated as a Mogi (e.g. Darwin (Amelung et al., 2000; Manconi et al., 2007), Medicine Lake (Parker et al., 2014)).

In order to represent magmatic structures with a more realistic model geometry, rectangular dislocations (Okada, 1985) are widely used. In this thesis, I use this source as it can approximate a magmatic reservoir as a sill geometry that is parameterised in terms of its X coordinate, Y coordinate, depth, strike, length, width and opening. This allows the effective modelling of sill opening, an anisotropic process where opening along the major axis is accompanied by closing along the minor axes. These are particularly useful when modelling sources in the Western Galápagos, where the shallow reservoir

at multiple volcanoes has been frequently modelled as a sill geometry (Bagnardi and Amelung, 2012; Stock et al., 2018).

The final model used here is the Compound Displacement Model (CDM) (Nikkhoo et al., 2017). These models comprise three mutually orthogonal rectangular dislocations, the parameters of each are allowed to vary independently, allowing more complex geometries to be modelled. Each rectangular dislocation is parameterised in terms of its X coordinate, Y coordinate, depth, strike, dip, length, width and opening. In Chapter 4, I use the point Compound Dislocation Model (pCDM) to model isotropic sill contraction, which uses tensile point dislocations, rather than anisotropic rectangular dislocations (Nikkhoo et al., 2017).

When determining the best-fit parameters of a magmatic source, I use a Bayesian approach, using the Geodetic Bayesian Inversion Software (GBIS) (Bagnardi and Hooper, 2018). GBIS uses a Markov Chain Monte Carlo Algorithm, with the Metropolis-Hastings Algorithm to calculate posterior probability density functions for a source model (e.g. Mogi). The starting source parameters are either selected manually, or estimated with a direct search method, to create a prior probability distribution (Bagnardi and Hooper, 2018). A trial set of parameters is then selected by a random step in the prior distribution. The likelihood of the trial distribution is compared with that of the prior, and retained if greater. This process is repeated for a preset number of iterations, and the optimal set of source parameters is calculated from the posterior probability density function (Bagnardi and Hooper, 2018). Errors are quantified before iteration, by fitting an experimental semi-variogram to characterise the spatial variability (variance and covariance) of the data (calculated over a non-deforming area, and assumed to be constant over the deforming area) (Bagnardi and Hooper, 2018). Computational efficiency is increased by sub-sampling the data using a quadtree algorithm, where the dataset is recursively sub-divided into quadrants, until the variance in each is below a pre-determined threshold (Bagnardi and Hooper, 2018).

1.2 Mechanisms of Volcanic Ground Deformation

Volcanoes are complex natural systems, and are subject to numerous processes that can cause measurable ground deformation. This ground deformation is typically caused by volume change of either a sub-volcanic system (e.g. magma migration, hydrothermal depressurisation), or on the sub-aerial component of the volcano (e.g. lava flow/pyroclastic density current cooling and mass movement).

1.2.1 Volcanic Eruption

The most intuitive relationship between volcanic processes and ground deformation is found in the simple cycle of volcanic deformation proposed by Biggs and Pritchard

(2017). In this model, magma accumulates in a sub-volcanic reservoir (typically approximated as a single source, such as a sill) during a pre-eruptive period. This accumulation and pressurisation drives uplift that can be observed geodetically. The transition to subsidence then occurs when a critical reservoir pressure is met, and the magma reservoir rapidly empties. This results in a long-term deformation time series of steady inter-eruptive uplift, and rapid co-eruptive subsidence (Biggs and Pritchard, 2017) (Figure 1.1D). Sierra Negra, in the Galápagos is an excellent example of this deformation cycle. The volcano uplifted by 6.5 m in the 13 year inter-eruptive period from 2005–2018, from a source at approximately 2 km depth (Bell et al., 2021b). Then, in 2018, there was approximately 8.5 m of co-eruptive subsidence, as the volcano effused approximately 1.9×10^7 m^3 (Vasconez et al., 2018), from multiple fissures over a two month period. The caldera floor resumed uplift immediately following this eruption (Bell et al., 2021b), and has steadily continued as of the time of writing.

However, the complexity associated with volcanic eruptions means that while this model provides a useful foundational understanding of magma dynamics and ground deformation, it is too simple to be applied to most eruptions. Even at Sierra Negra in 2018, the magnitude of co-eruptive subsidence exceeded the pre-eruptive uplift by almost 2 m (Bell et al., 2021b), due a combination of magma loss, and slip along a trapdoor fault. Similarly, if magma supply does not immediately resume following an eruption, then the volcano may begin to subside, as magma products intruded during the pre-eruptive uplift cool and contract (e.g. Alcedo (Hooper et al., 2007; Green, 1994)). Additionally, the assumption of a single large reservoir does not align with the concept of a TCMS (Cashman et al., 2017; Bagnardi and Amelung, 2012).

Now, I will discuss other processes that may drive ground-deformation at volcanic systems. These processes often occur in tandem with one another, meaning that in InSAR geodesy, complex interferograms showing deformation from multiple sub-volcanic reservoirs, at various levels in the crust as well as from sub-aerial processes, are common and pose a challenge in deciphering the underlying volcanic process.

1.2.2 Magmatic Cooling and Crystallisation

Magma supply to shallow volcanic reservoirs is typically variable with time, even Sierra Negra has undergone periods of subsidence in the early 2000s, and 2010s (Bell et al., 2021b; Geist et al., 2006a). As magma supply wanes and ceases, so too does the corresponding uplift. Once this happens, the intruded magma will begin to cool and crystallise, and may reverse the deformation from uplift to subsidence. Here, volume loss occurs as denser-than-melt minerals crystallise from the cooling melt (Caricchi et al., 2014). If the mass remains constant, then crystallisation and density changes is the main control on volume loss (e.g. Equation 1.6, where V is volume, ρ is density, and m

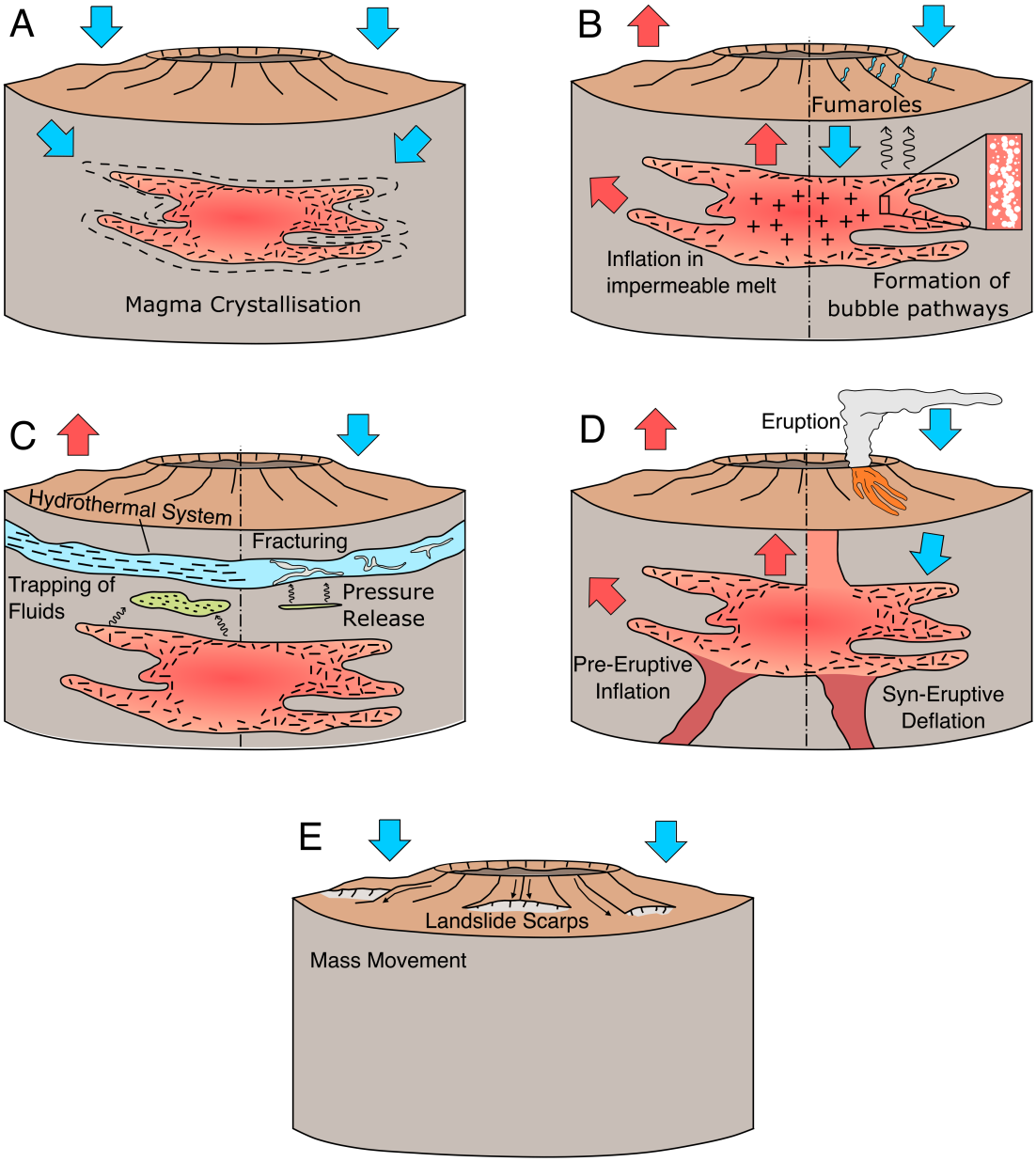

Figure 1.1: Mechanisms of deformation at volcanic centres from both magmatic processes, and sub-aerial processes. A). Subsidence due to magmatic cooling and crystallisation (e.g. Alcedo, Ecuador). B). Inflation and deflation due to volatile exsolution during second boiling (e.g. Long Valley, USA). C). Inflation and deflation due to hydrothermal activity (e.g. Fisher, USA). D). Inflation and deflation due to pre- and syn-eruptive processes (e.g. Sierra Negra, Ecuador, 2018). E). Subsidence due to mass wasting on the flanks of the volcanic edifice (e.g. Arenal, Costa Rica).

is mass, for each mineral phase).

$$V_{total} = \frac{m_{Phase1}}{\rho_{Phase1}} + \frac{m_{Phase2}}{\rho_{Phase2}} + ... \frac{m_{Phasen}}{\rho_{Phasen}} \tag{1.6}$$

Crystal phase assemblages have varying densities, the development of which is con-

trolled by the phases that form from the initial magma composition as it crystallises (Hall, 1996). Initial magmatic densities may vary between 2.17 (rhyolitic) and 2.6 (basaltic) g $cm^{3\,-1}$, depending on their composition, which may then increase to 2.28 and 2.76 g $cm^{3\,-1}$ at room temperature, for rhyolites and basalts, respectively (Hall, 1996). Therefore, the melt composition at liquidus temperature is a control on subsequent densities and volume changes in a crystallising magma (Figure 1.1A illustrates this mechanism). Medicine Lake volcano, in the USA is perhaps the archetype for this style of deformation, the volcano has been steadily subsiding, since 1954, as underlying magma crystallises (Parker et al., 2014), while at Lassen, USA, long term subsidence is due to magma cooling and crystallisation, coupled with volatile release during second boiling (Parker et al., 2016).

1.2.3 Second Boiling

In cases where the initial composition is volatile-bearing (e.g. H_2O), then the observed deformation style may be dramatically different. As the magma cools, it will precipitate solid, anhydrous crystal phases. In volatile-bearing melts, this will cause the residual melt phase to become relatively enriched in volatiles. Eventually, this volatile concentration and vapour pressure increase will cause the melt to become saturated, and exsolve its volatiles in a process known as second-boiling (Caricchi et al., 2014) (First boiling occurs as decompression driven exsolution, as pressure decreases on an ascending magma (Hildreth, 2017)).

Once exsolved, the influence of these volatiles on ground displacement patterns is controlled by the degree of degassing that they undergo. If the magma reservoir is a closed system (no mass in or out; exsolved volatiles and melts remain through the crystallisation process, Figure 1.1B), then second boiling will cause the reservoir to inflate, and may result in surface uplift despite the absence of magma intrusion (e.g. Long Valley (Hildreth, 2017)). However, in an open system volatiles and melts are separated upon exsolution (Cashman, 2004) (Figure 1.1B). Here, magma permeability (due to brittle failure, porous bubble networks, and the degree of magma crystallisation (Cashman, 2004)) promotes volatiles leaving the reservoir, and may increase the magnitude of the subsidence signal observed due to magma crystallisation, as mass is also being lost. However, in reality volatiles exsolved from a magma often interact with overlying hydrothermal systems (Fournier, 1999), and create complex deformation patterns.

In addition to the added complexity that hydrothermal processes bring, volatiles complicate the study of volcano deformation patterns. Deformation source models typically assume an incompressible reservoir in an elastic halfspace. However, magmatic volatile exsolution significantly affects the compressibility of the magma, particularly H_2O, CO_2, and SO_2 (Rivalta and Segall, 2008; Kilbride et al., 2016). Rivalta and Segall (2008) note that during a dike intrusion, where there is uplift accompanied with subsi-

dence of a source reservoir, there may be a 4–5-fold discrepancy between the modelled positive volume change in the dike, and negative volume change in the source. They explain this due to magma compressibility changes, largely due to volatile exsolution (Rivalta and Segall, 2008). As such, the assumption of an incompressible source can not be applied when considering volatile-bearing magmas, as they have a profound effect on compressibility.

1.2.4 Hydrothermal Depressurisation

Upon leaving an open magmatic system, volatiles may ascend towards the surface. Here, they may interact with a volcanic–hydrothermal system. In volcanic systems, hydrothermal systems have two components, consisting of meteorological- and magma-derived fluids. Meteorological fluids do not directly cause volume change in the magma, however they may act to advect heat as they circulate, altering the cooling rates of magma, and magma-derived fluids (Fournier, 1999; Annen et al., 2008). As these magma-derived fluids ascend, they reach a point where the nature of the crust changes from plastic (caused by increased country rock temperature around a magmatic intrusion), to brittle. At this point, lenses of magmatic fluids may accumulate, and form a hydrothermal system (Figure 1.1C). These lenses are self-sealing, due to plastic flow, and hydrothermal mineral precipitation. As a result, continued fluid accumulation may drive localised uplift, as these lenses inflate (Fournier, 1999; Fournier, 2007). Eventually, this accumulation and pressurisation will cause the lenses to breach, allowing hydrothermal fluids to escape (Figure 1.1C) (Fournier, 1999; Fournier, 2007). As a result, hydrothermal unrest is typified by localised uplift, and rapid subsidence, accompanied by fumarole flux and seismicity between the intruded magma body and the surface. This is particularly evident at established caldera systems, where there may be long-lived magma reservoirs. For example, Lu and Dzurisin (2014) suggest that long-term subsidence at Fisher may be due to fluid migration from a depressurising hydrothermal system. They suggest that a lense of hydrothermal fluid may have breached, and is yet to re-seal, facilitating depressurisation.

1.2.5 Flow Subsidence and Edifice Deformation

During an eruption, magmatic products are extruded from the volcano, and may be deposited onto the flanks of the volcano. These products are typically channelised, either as lava flows (Figure 1.1D), or as gravity-driven pyroclastic density currents. Displacement of these products may be observed by InSAR as they cool (e.g. Parícutin lava field (Chaussard, 2016)). For lava flows, this cooling is thermally driven by conductive heat loss into the underlying country rock, radiative heat loss into the atmosphere, as well as convective heat loss due to wind forcing (Patrick, 2004). The rate of cooling may also be altered by bubble vesiculation and latent heat production within the flow, as well as

cooling due to meteorological precipitation (Patrick, 2004). A cooling, contracting lava flow may be observed via satellite radar as either a subsiding, elongate flow down the flanks of a volcano (e.g. Sierra Negra (Amelung et al., 2000)), or as broader subsidence across a lava field (e.g. Parícutin, Timanfaya (Chaussard, 2016; Purcell et al., 2022)). Subsidence due thermo-elastic contraction may be modelled using Equation 1.7 (e.g. Chaussard (2016)), where Δh is vertical change, t is time, η is the thermal expansion coefficient, ν is Poisson's ratio, and T is Temperature. Though this is best used for modelling long-term contraction as volume change due to pore collapse, crystallisation, and lava flow movement immediately post eruption are not considered.

$$\Delta h(t) = h\eta \frac{1+\nu}{1-\nu} \Delta T(t) \tag{1.7}$$

In addition to deposit cooling, sub-aerial displacement may be observed at volcanoes due to mass movement of the volcanic edifice. Volcanoes often have steep slopes, and are prone to mass movement such as landslides (e.g. Cerro Azul, (Naumann and Geist, 2000)) (Figure 1.1E). Deformation at Arenal volcano, Costa Rica, between 2011–2013 was driven by mass movement of at least 16 landslides on the volcanic edifice (Ebmeier et al., 2014).

1.3 Global Volcanological Settings

In this thesis, I discuss volcanoes from a range of geological settings (Figure 1.2). Though Chapters 2 and 3 focus on the Western Galápagos Islands of Isabela and Fernandina, in Chapter 4 I examine deformation from a variety of geological settings (Table 1.2), such as the Taupo Volcanic Zone, and the Kenyan Rift. Volcanoes here have undergone persistent, long-term subsidence, attributed to the cooling and crystallisation of intruded magma. In the following section, I present a brief introduction to each of these volcanological settings.

1.3.1 The Western Galápagos

The Galápagos are a volcanic archipelago located on the Equator in the East Pacific, approximately 1000 km off of Ecuador's eastern coast (Figure 1.2). They formed as the Nazca plate moves eastwards, over the Galápagos plume. The plume is currently located near the Western Galápagos Islands of Fernandina and Isabela, the youngest islands of the entire archipelago (Harpp and Geist, 2018). Accordingly, the youngest volcanoes are located on the very western edge of the Galápagos; Fernandina is the youngest island (Kurz et al., 2014), while Cerro Azul is still in the Juvenile phase of its development (Harpp and Geist, 2018). The Western Galápagos are less than 500 ka old (Harpp and Geist, 2018), and are home to 7 volcanoes: Alcedo, Cerro Azul, Darwin,

Volcano	Last Eruption	Ground Deformation	Reference
Alcedo[2,3,4]	1993	Steady subsidence from magma crystallisation, with periodic resurgence.	Hooper et al. (2007)
Asama[4]	2019	Erupts regularly, though has undergone phases of subsidence lasting >20 years.	Murase et al. (2007)
Cerro Azul[2,3]	2008	Regular eruptions and off axis unrest.	Baker (2012)
Darwin[2,3]	1813	Eruptive quiescence, with low magnitude deformation and periodic resurgence.	Amelung et al. (2000)
Fernandina[2,3]	2020	Regular eruptions from radial and circumferential fissures.	Bagnardi and Amelung (2012)
Paka[4]	7550 BCE	Alternating uplift and subsidence.	Robertson (2015)
Shasta[4]	1250	Generally inactive.	Siebert et al. (2010)
Sierra Negra[2,3,4]	2018	High magnitude uplift and eruptions, with lateral intrusions.	Bell et al. (2021b)
Silali[4]	5050 BCE	Steady subsidence between 2007–2010.	Robertson (2015)
TVZ[4]	260	Subsidence: Coupled regional extension, magmatic processes, and geothermal activity.	Hamling et al. (2015)
Wolf[2,3]	2022	Steady uplift, with recent eruptions in 2015, and 2022.	Stock et al. (2018)

[2] Volcano discussed in Chapter 2; [3] Volcano discussed in Chapter 3
[4] Volcano discussed in Chapter 4.

Table 1.2: Summary of volcanoes discussed in this thesis.

Ecuador, Fernandina, Sierra Negra, and Wolf. Of these, all but Ecuador have recent eruptions, or observed ground deformation (Siebert et al., 2010). These volcanoes have been described as resembling overturned soup bowls; at lower elevations slopes are gradual, before steepening towards the summit. All of these volcanoes are topped by a broad summit caldera, varying in volume from 3.1 km^3 at Cerro Azul, to 12.4 km^3 at Fernandina (Naumann and Geist, 2000). The large caldera volume at Fernandina can be partially attributed by the 1968 caldera collapse there, when the caldera floor subsided by 300 m — the second largest caldera collapse of the 20^{th} century after the 1912 eruption of Katmai (Simkin and Howard, 1970). Despite their close proximity to one another, there is remarkable diversity in the range of volcanic deformation observed here – Alcedo is typified by steady, low rate subsidence (Hooper et al., 2007), while its southern neighbour, Sierra Negra (approximately 30 km away) undergoes extreme uplift (approximately 6.5 m between its 2005 and 2018 eruptions) (Bell et al., 2021b).

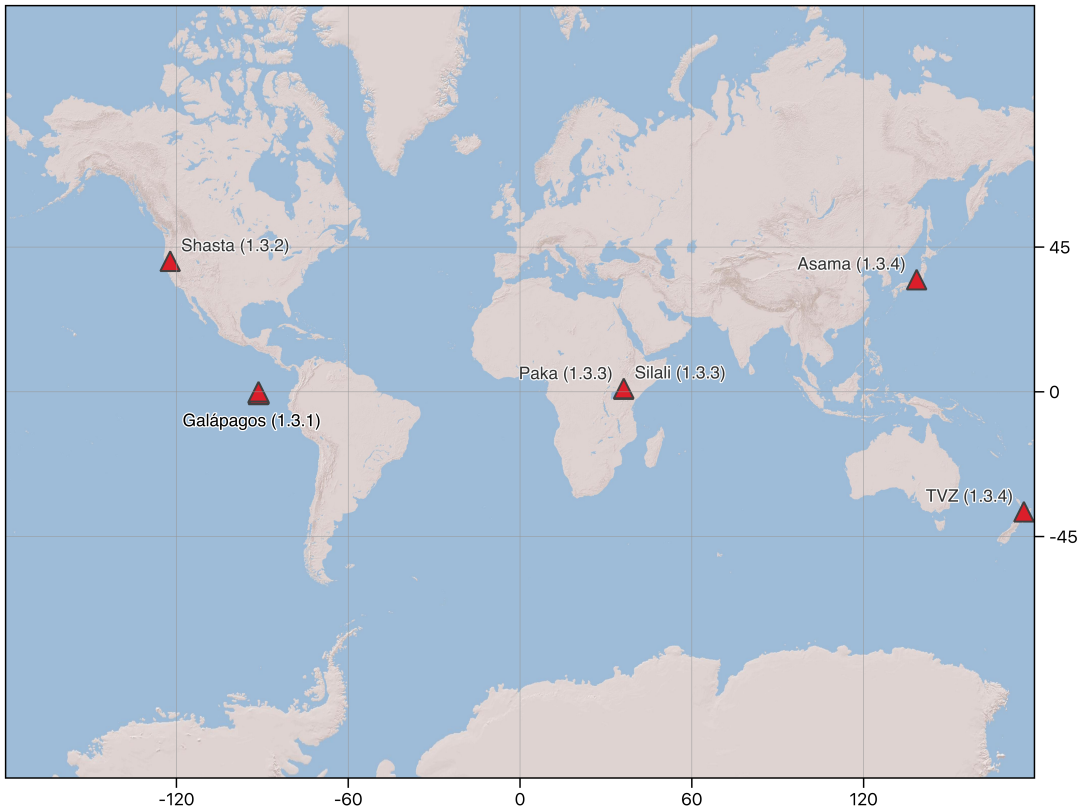

Figure 1.2: Global distribution of volcanic centres studied in this thesis. The numbers correspond to the section where each of these volcanoes are discussed in greater detail, while the underlying map used is the ESRI Shaded Relief basemap, from QGIS QuickMapServices.

1.3.2 The Southern Cascades

The Cascade volcanic arc is located in the Western USA, stretching from Lassen in Northern California, to Mt. Baker near the Canadian Border (Poland et al., 2017).

There are 13 volcanoes here, though in this thesis, I will study those in Californian Section of the Cascades, where long-term subsidence has been previously described. This region marks the interaction between the Cascadia subduction zone, and the Basin and Ridge province (Poland et al., 2017; Parker et al., 2014; Parker et al., 2016). While presently subsiding, Lassen is the only Cascades volcano (other than Mount St. Helens) to have erupted in the 20th Century, while Medicine Lake has not erupted since 1060, and has been steadily subsiding since at least 1954 (Table 1.2) (Parker et al., 2014). Given their location in the Western USA, these volcanoes have been historically well monitored by ground-based instrumentation such as Campaign GPS, Continuous GPS, and EDM (Poland et al., 2017).

1.3.3 The Kenyan Rift

Paka and Silali volcanoes are located in the Kenyan Rift, in East Africa (Figure 1.2). The Kenyan Rift constitutes the eastern branch of the East African Rift System, a diverging plate boundary that is driving the break-up of East Africa, as the Nubia and Somalia plates separate. The East African Rift System extends from Mozambique to the Afar triangle, and has numerous active volcanoes. In the north there have been recent eruptions at Nabro, 2012, Erta Ale, 2023, and Alu-Dalafilla, 2008 (Venzke, 2023). In comparison, Kenyan Rift volcanoes are relatively inactive, with the most recent eruption occurring in 1921, at The Barrier Volcano Complex (Venzke, 2023). However, satellite geodesy has detected ground deformation at multiple Kenyan Volcanoes — Silali subsided between 2007–2010, while Paka uplifted in various phases between 2006–2008, before beginning to subside in February 2008 (Robertson, 2015; Biggs et al., 2009). This subsidence has continued, with Albino et al. (2022) observing subsidence at both Paka and Silali from 2015–2020.

1.3.4 Other Volcanoes

Asama

Asama is an arc volcano located in on the Japanese island of Honshu, formed by the subduction of the Pacific Plate (e.g. Murase et al. (2007)). It is a volcanic complex consisting of the Hotokeiwa, Kurofu, and Maekake volcanoes that has been active for the last 100,000 years (Wang et al., 2019). It is located 160 km northwest of Tokyo, and its regular eruptions (2004, 2008, 2009, 2015, and 2019 (Venzke, 2023)) pose a hazard to the metropolitan area. Despite its extrusive activity, subsidence has been observed there from 1943–1967, and 2014–2018 (Murase et al., 2007; Wang et al., 2019).

Taupo Volcanic Zone

The Taupo Volcanic Zone is located on the north island of New Zealand, stretching 300 km from Lake Taupo in the south, northwards. It forms a back arc basin, as the Pacific Plate subducts beneath the Australian plate. Long-term subsidence has been observed here, with the highest magnitude located around the Wairakei geothermal field, an area that has subsided by 15 m since the 1950s (Hamling et al., 2015).

1.4 Aims and Objectives of this Thesis

The aim of this thesis is to explore the magmatic causes of measurable ground surface displacement. To do this I leverage InSAR data, with which I use a variety of modelling and analysis techniques, to understand the relationship between magma dynamics and surface deformation, and its evolution through time. By doing this, I aim to reconcile observations of volcanic ground displacement with magma dynamics in a vertically extensive trans-crustal magmatic system. My specific objectives are as follows:

1. Link magmatic processes to volcanic ground surface displacement and eruptive activity on the Western Galápagos islands of Fernandina and Isabela.
2. Investigate the prevalence, timings, and causes of correlated deformation in the Western Galápagos.
3. Determine the conditions under which a crystallising magmatic intrusion may result in measurable surface displacement.

1.5 Thesis Structure and Outline

Following this introductory chapter, I present the work that composes the research conducted throughout my PhD. Each chapter was written with the intention of being published in an academic journal. As such, I regularly use plural pronouns throughout (e.g. “we”); however the contribution of each author is detailed at the beginning of this thesis, in the author declaration section. The contents of each chapter is organised as follows:

1. Chapter 2: I present a detailed synthesis of volcanic unrest on the Western Galápagos islands of Isabela and Fernandina. I also present new observations and interpretations of recent unrest at each volcano, as detected using a Sentinel-1 dataset from 2015–2022. This is the most comprehensive island-wide review of volcanic ground displacement in the Western Galápagos to date, and I make the first observations of deformation due to hydrothermal depressurisation, off-caldera sill crystallisation, and offshore sill intrusions.

2. Chapter 3: I make observations of correlated displacements in the Western Galápagos, using Sentinel-1 InSAR data. I prove the presence of these correlated displacements using Independent Component Analysis, and correlation analysis, and show that they occur during periods of heightened magma flux from the Galápagos plume by modelling volume flux at each volcano, from 2017–2022.

3. Chapter 4: I develop a methodology to numerically model long-term volcanic subsidence due to the crystallisation of a shallow magmatic reservoir. I use a petrological model to determine the volume change undergone by a magma during crystallisation, a thermal model to determine the timescale taken for a magma to crystallise, and model corresponding displacement using point Compound Displacement Models. I apply this methodology to time series of deformation for a selection of global volcanoes, to determine the conditions under which crystallisation may cause measurable deformation.

4. Chapter 5: I review and discuss the findings of Chapters 2, 3, and 4, in the context of long-term magma dynamics and ground surface displacement. I then discuss the future of deformation monitoring in the Western Galápagos and globally, and the implications of my findings on Galápagos volcanism on global volcano monitoring.

Chapter 2

Craters of Habit: Patterns of Deformation in the Western Galápagos

Abstract

The Western Galápagos islands of Fernandina and Isabela comprise six closely spaced, historically active volcanoes that have been measurably deforming since the first satellite radar measurements in the 1990s. Here, we analyse new displacement time series (2015-2022) at Alcedo, Cerro Azul, Darwin, Fernandina, Sierra Negra, and Wolf in the context of both deformation since 1992 and eruptive history. Deformation since 2015 has included long-term and episodic uplift (Sierra Negra, Wolf, Darwin), co-eruptive intrusions and subsidence (Fernandina, Sierra Negra, Wolf), and subsidence associated with cooling intrusions, hydrothermal systems and lavas (Alcedo, Sierra Negra, Wolf). Eruptions and unrest in the Western Galápagos all respond to variations in magma flux into the shallow crust from the Galápagos plume. However, the style of eruptions, characteristics of unrest and deformation are distinctive at each volcano. Previous discussion of volcano deformation in the Western Galápagos has focused almost exclusively on either eruptions (e.g. Sierra Negra, 2018, Wolf, 2015) or major intrusive episodes (e.g. Cerro Azul, 2017). In contrast, we discuss the full satellite radar record of deformation, including new higher temporal resolution Sentinel-1 time series from 2015 to 2022. We find that differences in deformation and unrest styles between the volcanoes have persisted over at least the three decades since the first satellite radar measurements, and potentially over the last century. This provides a consistent picture of recent sub-volcanic magmatic zone structures and dynamics, which we use to propose a classification related to current characteristics of activity, which may be useful for designing monitoring strategies.

2.1 Introduction

Both the levels of activity and the magnitude of volcanic deformation in the Western Galápagos are exceptional. Between 1917–2023, Fernandina has averaged an eruption every 5 years (Vasconez et al., 2018), while Sierra Negra averages an eruption every 11–12 years (Vasconez et al., 2018), as well as experiencing metre-scale deformation (Geist et al., 2008; Bell et al., 2021b). The inaccessibility of the Western Galápagos means that much of our knowledge of the volcanoes comes from satellite radar measurement of displacements. Of the seven major volcanoes, six have experienced significant unrest since the 1990s: Alcedo, Cerro Azul, Darwin, Fernandina, Sierra Negra, and Wolf (e.g. Amelung et al. (2000), Baker (2012), Vasconez et al. (2018), and Bell et al. (2021b)).

Major trends in magma flux and the clustering of eruptions in the Galápagos have been attributed to variable melt supply from the mantle plume (Chapter 3). A fundamental control on Galápagos volcanism is the proximity to the centre of the upwelling plume, as implicated by differences in eruption rate (e.g. Fernandina (Kurz et al., 2014)) and thermal state of magmatic reservoirs (Harpp and Geist, 2018). Correlations in deformation are also indicative of deep hydraulic connectivity (Chapter 3), while some eruptions have been attributed to deep-sourced "flushing" events (Stock et al., 2020). However, there is geodetic (Bagnardi and Amelung, 2012) and petrological evidence of shallower differences in magma storage. In particular, the large range in the magnitude and patterns of deformation between neighbouring Western Galápagos volcanoes are a consequence of the edifice and subsurface structures at each volcano.

Habitual deformation trends include sustained periods of uplift on the order of both metres (Sierra Negra) and centimetres (Wolf), interrupted by major eruptions. At Sierra Negra, the intra-caldera fault is located in the southwestern portion of the caldera, and facilitates "trapdoor faulting", where the caldera floor hinges upwards like a trapdoor. Eruptions here in 2005 and 2018 were accompanied by slip along this fault (Jónsson, 2009; Bell et al., 2021b), while it also acts as a conduit for magmatic fluids to the shallow surface fumarole field (Aiuppa et al., 2022). Similar magmatic–tectonic interactions at Alcedo modify displacement patterns during periods of uplift (Galetto et al., 2019). Displacements at Fernandina are associated with frequent eruptions ($\geq$ 5 years) and intrusions (e.g. 2006, and 2007 (Bagnardi and Amelung, 2012)). Cerro Azul experiences an intrusion or eruption about once a decade on its SE flank, while Darwin and Alcedo show lower magnitude subsidence between limited episodes of uplift. Here, we consider the three decades of volcano deformation measurements made at the Western Galápagos volcanoes with satellite radar, and the implications of persistent displacement styles for our understanding of magmatic processes. We first review trends in unrest and eruption in the period for which geodetic data are available (1992-2022, Sections 2.4.1–2.4.6). For each volcano, we then describe previous interpretations of deformation as detected by

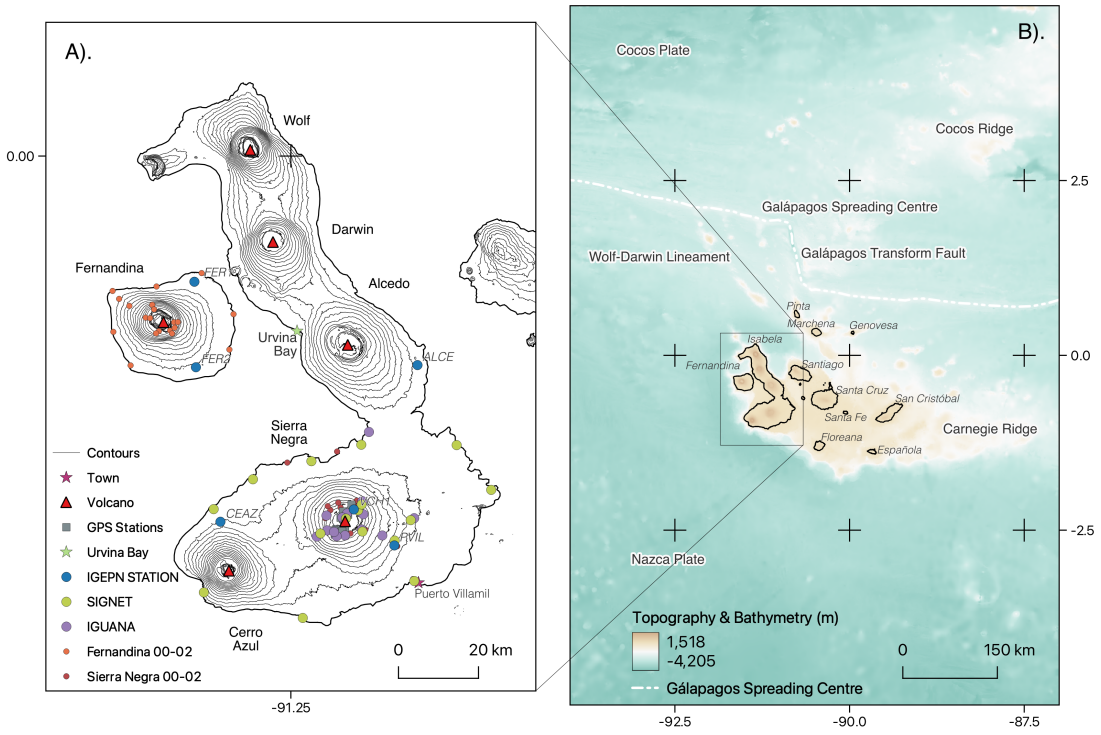

Figure 2.1: Regional view of the Galápagos. A). The Western Galápagos islands of Isabela and Fernandina, showing the volcanoes considered in this study (red triangles). The geographic locations of both continuous and campaign ground-based monitoring systems that are discussed here are annotated, as is the population centre of Puerto Villamil, and Urvina Bay — the location of a major unrest episode in 1954. Each system, with the exceptions of the GPS stations, and Fernandina–Sierra Negra 00-02 (GPS/Gravimeters), are seismometers. B). A broader view of the regional tectonic setting. Sub-aerial islands are labelled, as are major underwater structures, and tectonic plates and faults (e.g. Harpp and Geist (2018)). The colorscale indicates bathymetric and topographic elevation, as discussed in Section 2.3.2.

Interferometric Synthetic Aperture Radar (InSAR) from 1992-2010, as well as those of ground-based surveys, followed by the implications of new displacement time series constructed from Sentinel-1 imagery, spanning 2015-2022. Finally, we summarise the current picture of sub-volcanic magmatic zones from geodesy for each volcano, and contrast the interpretation and resulting classifications of Galápagos volcanism from petrological and geodetic methods.

2.1.1 Western Galápagos Volcanoes

The Galápagos islands straddle the equator in the east Pacific (Figure 2.1). There are 13 major islands here, the westernmost of which (Isabela and Fernandina) are the most volcanically active (Figure 2.1). They are located approximately 250 km south of the Galápagos Spreading Centre (Harpp and Geist, 2018), which is east-west striking, and offset by the Galápagos transform fault. The islands lie on the Nazca plate, and have formed as they move eastwards over the Galápagos mantle plume.

Despite the near-constant volcanism on the islands, monitoring instrumentation is sparse. The Instituto Geofísico de la Escuela Politécnica Nacional (IGEPN) maintain six permanent seismic stations there, two on Sierra Negra, one on Cerro Azul, one to the southeast of Alcedo, and two on Fernandina Island (Figure 2.1). Permanent GPS stations are maintained on Sierra Negra (Figure 2.1), while campaign GPS and gravity surveys have been carried out at Fernandina and Sierra Negra in the early 2000s (Geist et al., 2006a), and 2010s (Davidge et al., 2017). These ground-based systems have prioritised monitoring Fernandina and Sierra Negra volcanoes (Figure 2.1), the former of which is the most frequently erupting Galápagos volcano, and while the latter experiences the highest magnitude eruptions. By comparison, Wolf, which erupted in 2015 and 2022, has no permanent monitoring stations (Figure 2.1). Elevated seismicity during the 2022 Wolf eruption was only detected by the FER1 station, on Fernandina island (Figure 2.1) (*Wolf Volcano Special Report No. 1 - 2022* 2022). The sparse coverage of monitoring stations means that pre-eruptive unrest may be challenging to identify (e.g. Wolf, 2022), and limits the potential of studying volcanic behaviour during periods of effusive quiescence (e.g. Darwin, 2020) from ground-based measurements. The advent of InSAR data has therefore transformed our knowledge of magma storage and movement in the Galápagos .

2.1.2 Satellite Radar Measurements

InSAR is a geodetic technique for monitoring changes in line-of-sight (LOS) displacement from the instrument (usually a satellite) to the Earth's surface. It allows for the measurement of these changes on centimetre to millimetre scales, with a spatial resolution on the order of several metres, across areas of tens to hundreds of kilometres, and return period of several days. It is a powerful tool in Earth system science for the study of the earthquake cycle (e.g. pre-, syn- and post-earthquake), and processes that drive volcanic deformation (e.g. mass movement, hydrothermal activity, magma migration, and eruption). It is particularly useful in the Western Galápagos due to the number of volcanoes across a relatively small area, and good year-round coherence from bare rock. However, Sentinel-1 has a return period of 6–12 days, meaning that InSAR is less useful than ground-based techniques for continuous monitoring of an eruption, but rather measures cumulative change between acquisition dates around the event. Indeed, newly erupted products, and forested areas such as the southern flank of Sierra Negra, are generally incoherent. Satellite-based InSAR missions have been used to measure displacement at Western Galápagos volcanoes since 1992, with multiple platforms used: Amelung et al. (2000) used ERS-1, and ERS-2 to study Isabela and Fernandina from 1992–1998, while Hooper et al. (2007) used the platforms to study Alcedo from 1992–2001. Baker (2012) used the ERS missions, as well as Radarsat-1, Envisat, and AlOS-1 missions to study Galápagos volcanoes from 1992–2011. Pepe et al. (2017) studied 2012–2013 unrest at Fernandina using COSMO-SkyMed, while Galetto et al.

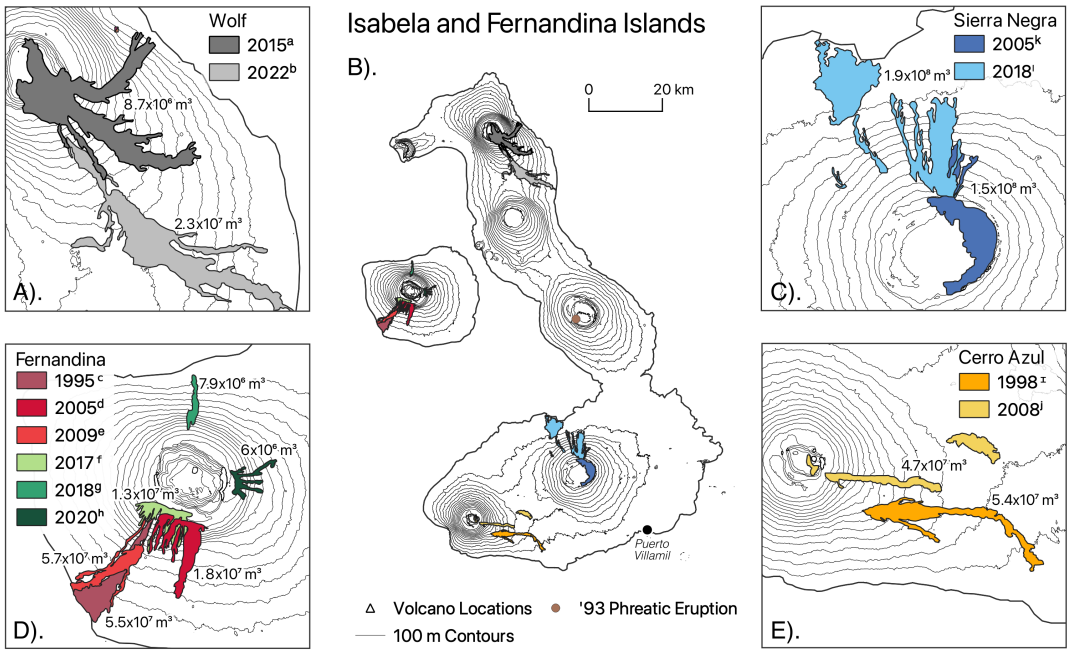

Figure 2.2: Extent of erupted lavas in the Western Galápagos since 1992. A). Extents and volumes of lavas from the 2015, and 2022 eruptions of Wolf. B). Overview of island-wide extent of lavas erupted during the InSAR era. C). Extents and volumes of lavas from the 2005, and 2018 eruptions of Sierra Negra. D). Extents and volumes of lavas from the 1995, 2005, 2009, 2017, 2018, and 2020 eruptions of Fernandina. E). Extents and volumes of lavas from the 1998, and 2008 eruptions of Cerro Azul. Darwin and Alcedo do not have figure panels as they did not effusively erupt over this period. However, the location of a 1993 phreatic eruption at Alcedo is included — though there are no estimates of volumes or extents from this steam explosion (Green, 1994). In each case, the estimated erupted volume is included if known, as presented in Table A2, and annotated beside the relevant lava flow.

(2023) studied the 2017 and 2018 eruptions of Fernandina using COSMO-SkyMed, and Sentinel-1. Xu et al. (2016) used Sentinel-1A and ALOS-2 to study the 2015 eruption of Wolf, while Shreve and Delgado (2023) used Sentinel-1, ALOS-2, and COSMO-SkyMed to study the 2018 eruption of Sierra Negra.

2.1.3 Overview of Eruptions and Unrest in the Western Galápagos 1992-2022

There have been remarkable episodes of eruption and unrest (e.g. Cerro Azul, 2017, Sierra Negra, 2018 (Guo et al., 2019; Bell et al., 2021b)), which have been the focus of previous geodetic work on the Galápagos. The recent eruptive record is well constrained into the early 20th century (Venzke, 2023), and there have been periodic observations of volcanic unrest (e.g. Urvina Bay, 1954), as well as several aerial photography surveys (Rowland and Munro, 1992). However, the systemic detection of volcanic unrest (measurable non-eruptive behaviour) has only been possible in practice since the installation of ground-based networks, and the advent of InSAR — the Western Galápagos volca-

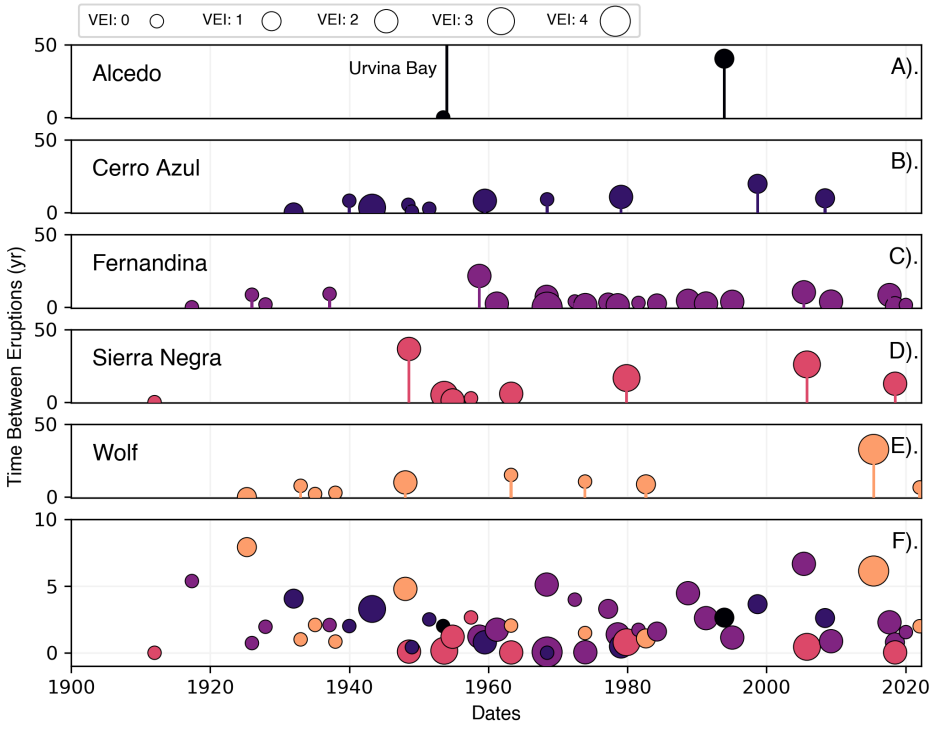

Figure 2.3: Eruptions at the Western Galápagos since the turn of the 20th century. For each volcano, the eruption data is on the x-axis, while the time between the preceding eruption is plotting on the y-axis. The marker size refers to the Volcanic Explosivity index of the given eruptions (as given in the Global Volcanism Program database (Venzke, 2023)). A–E). Eruption date, time between preceding eruption, and VEI for each of Alcedo, Cerro Azul, Fernandina, Sierra Negra, and Wolf. Darwin has not been included as it has not erupted since the early 19th century, while A). includes the 1954 uplift at Urvina Bay. F). Eruptions at all volcanoes, with the time between eruptions referring to all eruptions at any Western Galápagos Volcano. Known non-eruptive unrest (e.g. Urvina Bay 1954, or Cerro Azul, 2017) are not included.

noes have been the subject of extensive InSAR-based geodetic studies (Amelung et al., 2000; Bagnardi, 2014) since 1992. Since then, a variety of eruptive behaviour has been observed across multiple volcanoes.

2.1.4 Characteristics of Western Galápagos volcanoes.

Despite diverse styles of eruption and unrest, there are some common features in Western Galápagos volcanism, including the influence of topographic loading on magma ascent, stacked magmatic reservoirs, very active caldera faulting, and periodic increases in magma flux into the shallow crust ("resurgence" at quiescent systems or "flushing" during eruptions).

The lack of high magnitude regional stress fields associated with rifting or arc settings mean that the impact of topographic loading in local stress field is clearer than

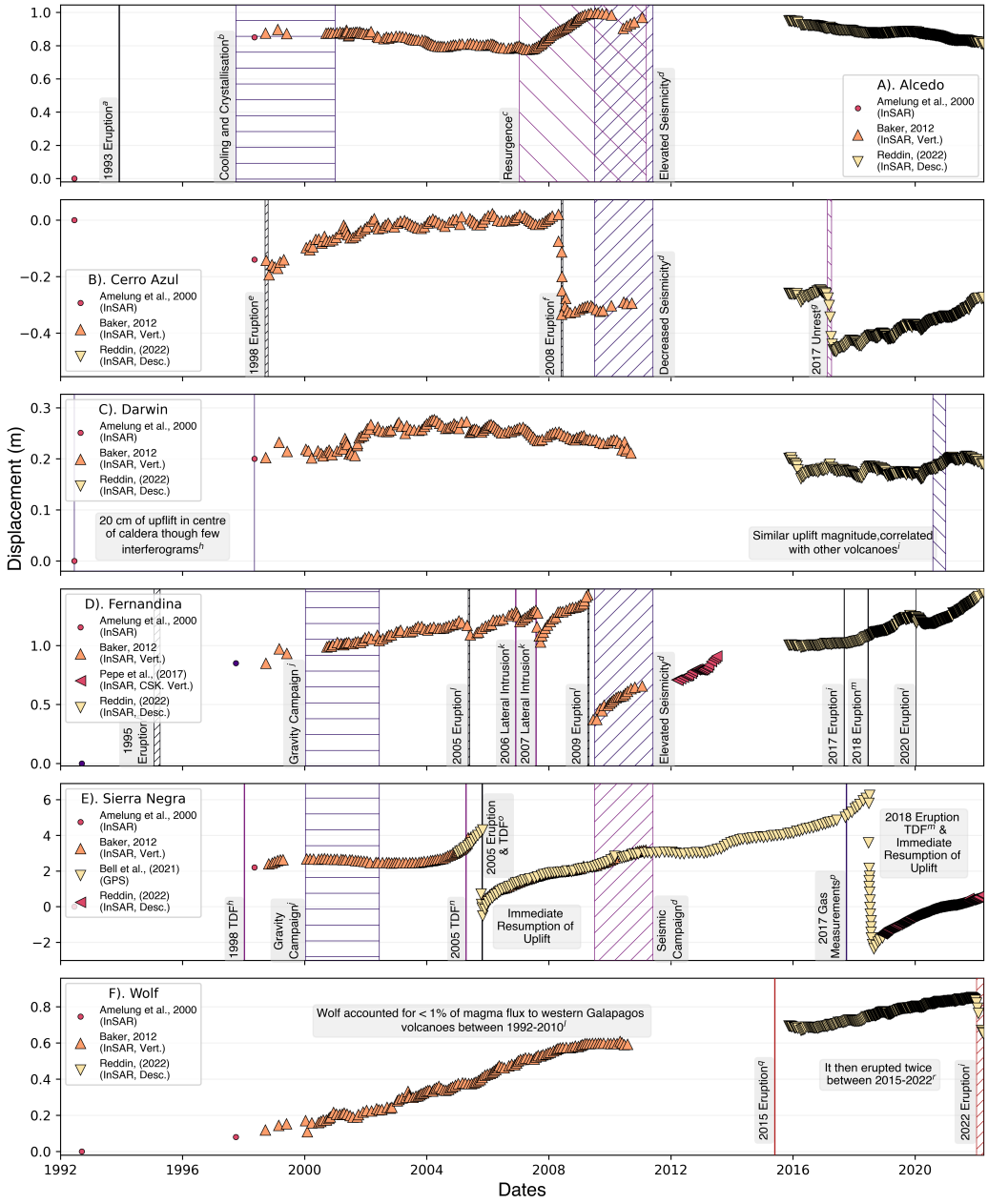

Figure 2.4: Summary of ground surface displacement at each Galápagos volcano, over 30 years from 1992–2022. Displacement in centimetres is given on the y-axis, while time is given on the x-axis. Marker colour denotes the study that the displacement data is taken from, while vertical bars illustrate periods where the volcano was the subject of an unrest-focused study. The nature of the unrest, and the appropriate study is labelled beside each vertical bar. A). Deformation at Alcedo, [a]Green (1994), [b]Hooper et al. (2007), [c]Galetto et al. (2019), [d]Davidge et al. (2017). B). Deformation at Cerro Azul, [e]Baker (2012), [f]Galetto et al. (2020), [g]Bagnardi (2017). C). Deformation at Darwin, [h]Amelung et al. (2000), [i] This Study. D). Deformation at Fernandina, [j]Geist et al. (2006a), [k]Bagnardi and Amelung (2012), [l]Bagnardi (2014), [m]Vasconez et al. (2018). E). Deformation at Sierra Negra, [n]Chadwick et al. (2006), [o]Geist et al. (2008), [p]Aiuppa et al. (2022). F). Deformation at Wolf, [q]Stock et al. (2018), [r] IGEPN.

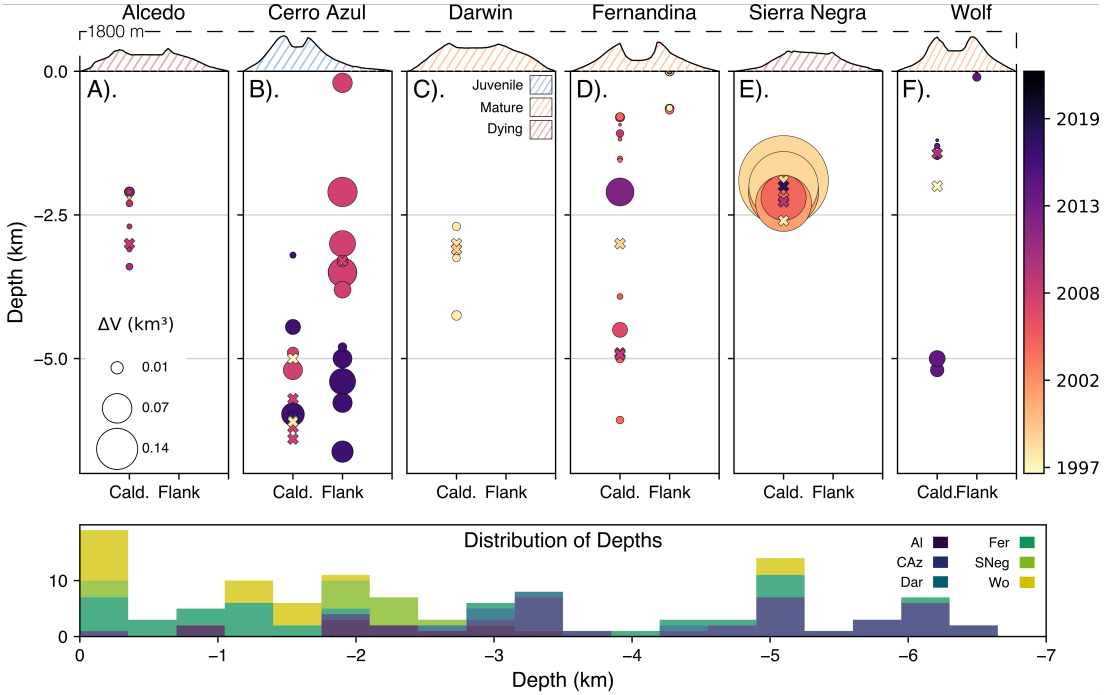

Figure 2.5: Summary of geodetic source depths in the Western Galápagos, derived from InSAR data. Depth, as stated in the corresponding study, is shown on the y-axes and general source location (sub-caldera or flank) topographic cross-sections are shown on the x-axes. Values and corresponding references are provided in Tables A3, A4, A5, A6, A7, A8, A9, and A10. The marker size reflects the relative volume change for each model solution, while colours indicates date that the inferred source was active. Where volume change is not given in the relevant publications, we assume a volume of 1×10^7 m^3, for presentation purposes — these are differentiated by an x marker. The colour of topographic cross sections reflects system maturity according to Harpp and Geist (2018). G). Histogram of the total distribution of depths for all volcanoes.

in other volcanic settings. Eruptions since 1992 (with the exception of the phreatic explosion of Alcedo in 1993 (Green, 1994)) have been fissure eruptions, either radial or circumferential (Figure 2.2). The stress field exerted by the volcanic edifice exerts a primary control on where fissures develop, and their geometry during eruptions (Bagnardi et al., 2013; Davis et al., 2021). Fernandina alternates between radial and circumferential fissures, while all of the recent unrest at Cerro Azul has occurred on the southeastern flank. Similarly, each confirmed eruption at Wolf since 1948 has occurred on the southeastern flank, alternating from circumferential, to radial. This topographic control on eruptive behaviour is also evident at Sierra Negra; a combination of buoyant and topographic forces caused a lateral intrusion there to bend during the 2018 eruption (Davis et al., 2021).

At three volcanoes, there is geodetic and petrological evidence for vertically "stacked" reservoirs (e.g., at Fernandina, Wolf, and Sierra Negra, Figure 2.5). The deeper of these reservoirs acts as a source for shallow and lateral intrusions at Fernandina (at approximately 5 km depth) (Bagnardi and Amelung, 2012), Sierra Negra (at approximately

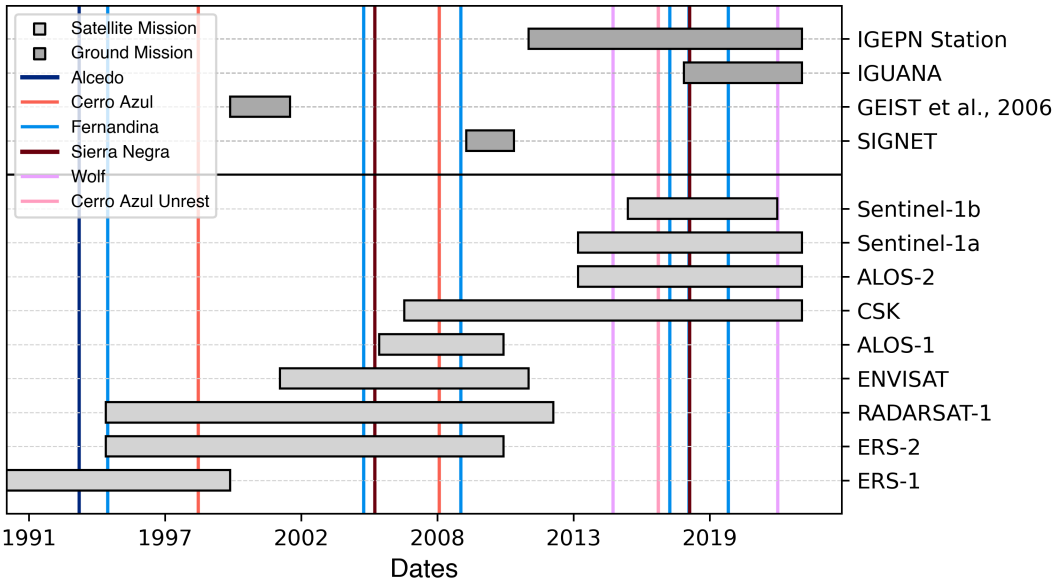

Figure 2.6: Temporal distribution of geodetic measurements since the the first InSAR studies in the Western Galápagos in the 1990s until 2023. Horizontal bars represent the time periods over which satellite missions, and ground-based platforms are active. Vertical bars represent eruptions, or significant unrest. Each included geodetic platform has been used to study unrest in the Western Galápagos. The location where each ground-based system was deployed can be found in Figure 2.1.

7.5 km depth) (Davidge et al., 2017), while a reservoir at 6 km depth acted as a source for the 2017 off-caldera unrest at Cerro Azul (Guo et al., 2019) (Figure 2.5).

Displacements and eruptions at Sierra Negra and Alcedo are controlled by the interaction of a magmatic source and an intra-caldera fault. At Alcedo, this fault exerted a structural control on asymmetric displacement patterns during the volcano's resurgence (Galetto et al., 2019; Bagnardi, 2014). Similarly, slip along the intra-caldera trapdoor fault at Sierra Negra preceded both the 2005 and 2018 eruptions (Geist et al., 2008; Bell et al., 2021b).

Magma periodically fluxes into the shallow reservoir at quiescent volcanoes. Galetto et al. (2019) describe this as a resurgence, at Alcedo volcano. Though this flux manifests as non-eruptive unrest at Alcedo (and Darwin (Section 2.4.3)), similar changes in magma supply (flushing) are the driving force behind eruptions at Fernandina and Wolf (Stock et al., 2020). Additionally, there is evidence that this magma flux from the Galápagos plume is irregular with time, and with the volcanoes to which it partitions (Chapter 3).

2.2 Previous Unrest and Deformation in the Western Galápagos

2.2.1 Alcedo

Alcedo is located on Isabela, directly east of Fernandina Island, between Darwin and Sierra Negra (Figure 2.2). It peaks at 1130 m above sea level, approximately 4 km above the seafloor (Venzke, 2023; Geist et al., 1994). Like all Western Galápagos volcanoes, it is topped by a summit caldera, varying in width between 7–8 km with a maximum depth of 270 m (Figure 2.5) (Geist et al., 1994). Its sub-aerial volume is approximately 200 km^3, though Geist et al. (1994) suggest the majority of the volcano is underwater. Alcedo, alongside Sierra Negra, has a vigorous hydrothermal system, with three fumarole fields (Geyser, Laura and Chantel, and Rhyolite Hill), all located on the southern side of the volcano, within the caldera (Goff et al., 2000; Mayhew et al., 2007) (Figures 2.8 and 2.7). The volcano's gentle slopes and low levels of extrusive activity have made Alcedo home to the highest population of Galápagos tortoises on Earth (De Roy, 2010).

Eruptive History

Alcedo is the only Galápagos volcano known to have erupted rhyolitic lavas in its geological history ($\leq$ 120 ka) (Geist et al., 1994). It has erupted twice in the 20^{th} century, once in 1953, and again in 1993 (Siebert et al., 2010). The 1953 eruption occurred on volcano's SE flank, while the 1993 eruption took place on the southern caldera wall (Siebert et al., 2010). During the 1993 eruption, seismicity, heightened fumarolic activity, and explosions were recorded, due to explosive phreatic activity from two vents (Green, 1994).

Previous Observations of Displacement at Alcedo

Despite its low levels of extrusive activity, Alcedo has been constantly deforming since 1992, and accounted for approximately 11% of intrusive magma flux, as detected by InSAR, of the Western Galápagos between 1992–2010 (Bagnardi, 2014). Amelung et al. (2000) performed an InSAR survey of Isabela and Fernandina from 1992–1999. Alcedo uplifted by $>$ 90 cm over this time, with the majority (approximately 80 cm) occurring between 1992–1997. Following this uplift the direction of deformation inverted to subsidence. Using Persistent Scatterer analysis, Hooper et al. (2007) observe a deflation signal of $>$ 30 mm/yr between 1997–2001, and attribute it to the crystallisation of a pipe-like magma body at 2.2 km depth. It is probable that the majority of uplift observed by Amelung et al. (2000) is related to Alcedos 1993 eruption. However, the sparse temporal spacing of the surrounding acquisitions means that the exact relationship between the timing of the observed uplift and the eruption is unclear. We suggest

that magmas intruded during this uplift crystallised, causing the subsequent subsidence observed by Hooper et al. (2007).

Subsidence continued largely uninterrupted until 2006, with a minor uplift phase in 2004 (Galetto et al., 2019; Baker, 2012). Following this, Alcedo experienced a series of magmatic intrusions, which may represent a component of longer term resurgence (Galetto et al., 2019). Between 2007–2009, sill inflation caused the caldera floor to uplift by approximately 30 cm, at a rate of approximately 8.9 cm/yr (Galetto et al., 2019). This same area then subsided by 8 cm, until June 2010, while the western caldera rim uplifted by 5 cm (Galetto et al., 2019), due to intra-caldera magma migration. Finally, the eastern portion of the caldera resumed uplift between June 2010 to March 2011 (Galetto et al., 2019). In each case, the best-fit sill depth is 2–3 km beneath the caldera floor, while the deformation patterns are asymmetrical, suggesting contribution from the intra-caldera fault (Galetto et al., 2019). Likewise, Bagnardi (2014) suggest deformation trends at Alcedo are due to a combination of magmatic and volcano-tectonic structures, from a Mogi source at 3 km depth and a SSW–NNE striking reverse fault. Part of this episode of resurgence, the period from 2009–2011, is notable for producing higher magnitude seismicity ($M_L \leq 3.3$) than Fernandina ($M_L \leq 2.5$) and Sierra Negra ($M_L \leq 1.5$) (Davidge et al., 2017).

2.2.2 Cerro Azul

Cerro Azul is the southernmost volcano on Isabela, located to the west of Sierra Negra (Figure 2.1). It peaks at 1640 m elevation, with a volume of 172 km^3 (Naumann and Geist, 2000), and has the smallest caldera of all Western Galápagos volcanoes (3.1 km^3). The caldera is the third deepest, at 450 m, but has the smallest area by far (9.5 km^2, less than half Fernandina (20.1 km^2)) (Naumann and Geist, 2000) (Figure 2.5). A lake periodically occupies the caldera floor, and may have contributed to the 1943 hydrovolcanic eruption, causing the only known fatality from a Galápagos eruption (Naumann and Geist, 2000).

Eruptive History

Cerro Azul is one of the more active volcanoes in the Western Galápagos, having erupted 11 times in the past 100 years — only Fernandina erupts more frequently (Venzke, 2023). It erupts, on average, once every 6.6 years (Naumann and Geist, 2000), from its caldera, summit, and flanks (Naumann and Geist, 2000). It has erupted twice since 1992, once in 1998, and again in 2008. During the 1998 eruption, two vents opened within the caldera accompanied by another on on the SE flank (Naumann and Geist, 2000; Teasdale et al., 2005). The eruption lasted 36 days, with eruption plumes, and lava flows along the eastern flank of the caldera — the longest of which was 16 km (Mouginis-Mark et al., 2000). The erupted magma (DRE 5.4 $\pm$ 24 $\times 10^6$ m^3, with mean effusion rate of 17 m^3

s^{-1} (Rowland et al., 2003)) mixed with residual magma from the 1979 eruption during the first 18 days, before changing compositionally as this remnant magma depleted (Teasdale et al., 2005).

Like in 1998, the 2008 eruption also occurred as effusive fissures on the southeastern flank of Cerro Azul (Baker, 2012), initiating on May 29th, and lasting for 19 days (Venzke, 2023). Lava erupted from fissures in the upper part of the cone until June 1st, before erupting from radial fissures along the base of the eastern flank on June 3rd (e.g. Figure 2.2).

Previous Observations of Displacement at Cerro Azul

The 1998 eruption marks the first significant displacement observation at Cerro Azul (Baker, 2012; Galetto et al., 2020). This eruption was accompanied by 15 cm of subsidence, from a source between 5–6.1 km depth, with a radius of 0.2 km (Amelung et al., 2000; Baker, 2012; Bagnardi, 2014). The inter-eruptive period between this and the 2008 eruption was characterised by steady uplift, totalling >20 cm. During the 2008 eruption, the caldera summit subsided by 30 cm (Galetto et al., 2020). Again, this subsidence was modelled as a source at between 5–6.4 km beneath the caldera (Baker, 2012; Galetto et al., 2020) (Tables A4 and A5). It is likely that this is the primary magma reservoir depth at Cerro Azul, though (Naumann et al., 2002) find evidence of tholeiitic magma storage at a range of depths from 3–15 km. However, during this eruption, a dike rooted to the sub-caldera source was also modelled, acting as a conduit between the magma reservoir and the eruptive fissures (Baker, 2012; Galetto et al., 2020) (Tables A4 and A5). Galetto et al. (2020) liken this lateral dike to those at Fernandina, where sills derived from a sub-caldera source bend upwards as they propagate, due to the stress field exerted by the volcano.

Uplift resumed following the 2008 eruption (Baker, 2012). Cerro Azul then underwent a major unrest episode in March 2017, with an uptick in seismicity consistent with an ascending magma body, leading to eruption warnings (*Cerro Azul Special Report No. 1 - 2017* 2017; *Cerro Azul Special Report No. 2 - 2017* 2017). Ultimately, no eruption occurred (*Cerro Azul Special Report No. 3 - 2017* 2017), though there was peak subsidence of -32.9 cm in the caldera, and uplift of 41.8 cm on the southeastern flank (Guo et al., 2019). Like in 1998, and 2008, this deformation was modelled using a geodetic source approximately 5 km beneath the caldera, from which a sill propagated causing surface uplift (Guo et al., 2019) (Tables A4 and A5).

2.2.3 Darwin

Darwin volcano is located on Isabela Island, halfway between Alcedo and Wolf (Figure 2.2). It has an elevation of 1330 m, topped by a broad, shallow caldera (Figure 2.5),

similar to both Alcedo and Sierra Negra. It is the least studied of the six major Western Galápagos volcanoes, due to its extended extrusive quiescence.

Eruptive History

Like Fernandina and Wolf, Darwin is monotonous, though it has infrequently erupted more evolved magmas, such as andesite (Naumann and Krebs, 2003). The Global Volcanism Program lists three Holocene eruptions at Darwin, in 0210 ± 500 C.E, 1150 ± 300 C.E. The most recent eruption took place in 1813, though the source volcano is ambiguous: it was "... more likely Darwin than Wolf, Alcedo" (Venzke, 2023). Evidence of thermal activity is similarly ambiguous, "strong thermal activity" was detected on the eastern flank of the volcano in 1972, via satellite observations (Venzke, 2023). However, a review of this imagery in 1973 suggested that the hotspots occurred on the caldera floor, and could be explained by "normal daytime temperature differences" (Venzke, 2023). Two tuff cones, Tagus and Beagle are located on the coast, to the west of Darwin, indicating some historic hydromagmatic volcanism (Banfield et al., 1956).

Previous Observations of Displacement at Darwin

The strongest evidence that Darwins magmatic system remains active comes from radar displacement studies. There was 20 cm of line-of-sight uplift between 1992–1998, attributed to a point source at between 3.1–4.25 km depth with a positive volume change of between 5×10^6–8×10^6 m^3 (Amelung et al., 2000; Manconi et al., 2007; Bagnardi, 2014). Following this, the caldera uplifted by five centimetres between 1998–2005, before it began to steadily subside until 2010, by a total of 5 cm (Figure 2.4) (Baker, 2012). During this period, there was heightened seismicity between Darwin, Fernandina, and Alcedo (Baker, 2012). From 1992–2010, magma influx at Darwin accounted for 3 % of the magma supplied to Galápagos volcanoes (Bagnardi, 2014).

2.2.4 Fernandina

Fernandina volcano, located on the uninhabited Isla Fernandina, is the westernmost, and most active volcano in the Galápagos. It has the largest caldera, and experienced the second largest global caldera collapse event of the 20^{th} century, after Katmai 1912, in 1968, when the volume of the caldera increased by 1–2 km^3, as the caldera floor fell by approximately 300 m (Simkin and Howard, 1970). Fernandina is the third tallest Western Galápagos volcano, standing at 1476 m, and it erupts frequently — the entire sub-aerial portion of the island has been resurfaced by lava flows in the last 4,300 years, and the island is hypothesised to lie over the centre of the Galápagos hotspot (Kurz et al., 2014).

Eruptive History

Fernandina has erupted 22 times since the turn of the 20th century (Venzke, 2023), with the most recent in January 2020 (at the time of writing) (Venzke, 2023). It has erupted, on average, once every 5.5 years since 1900, with VEI typically varying between 0–2. The largest eruption (VEI 4) occurred in June 1968, in a caldera forming event (Venzke, 2023). This eruption occurred in a series of steps, with major seismicity, ground deformation, trapdoor faulting, ashfall, infrasound detections, fumarole emissions, volcanic lightning, as well as the migration of the caldera lake from the northwestern corner to the southeastern (Simkin and Howard, 1970; Filson et al., 1973; Rowland and Munro, 1992).

Bagnardi et al. (2013) noted that the back and forth pattern of radial–circumferential fissure eruptions at Fernandina is due to stress field perturbations. That is, an intrusion from the shallow sub-volcanic sill can affect the stress field such that the least compressive stress promotes a succeeding intrusion of the opposite geometry (i.e. a radial eruption will be followed by a circumferential one) (Bagnardi et al., 2013). They identify that the 2009 eruption of Fernandina occurred radially along the southwestern flank, and correctly predicted that the next eruption, in 2017 would be circumferential, along the southwestern caldera rim (*Special Report of Fernandina Volcano No. 2 - 2017* 2017). This pattern of alternating radial–circumferential eruptions continued through the 2018 and 2020 eruptions, though the locations varied to the north and eastern flanks (Venzke, 2023). Chestler and Grosfils (2013) suggest that reservoir geometry may also affect which orientation the eruptive fissure takes. Eruption locations at Fernandina have a preferred NW–SE alignment (Rowland and Munro, 1992); during periods of low magma supply, the location of these eruptions is controlled by the regional stress regime, though eruptions may occur outside of this regime if magma supply increases (Rowland and Munro, 1992). The frequent eruptions at Fernandina result in a high degree of resurfacing of Fernandina Island (Kurz et al., 2014). We use maps of lava flow extent between 1995–2020, and suggest that, if these rates are constant through time, then the upper slopes (1200–1300 m) of Fernandina volcano will be resurfaced every 91 years, while the lower slopes (0–100 m) will resurface in approximately 830 years (Figure A2, Table A1).

Previous Observations of Displacement at Fernandina

Between 1992–1999, deformation at Fernandina was concentrated on the southwestern flank of the caldera, the site of the 1995 eruption, totalling almost 1 m (Amelung et al., 2000) of LOS uplift. Since then, displacement here has been non-linear, generally characterised by steady uplift, punctuated by rapid subsidence during episodes of unrest (Figure 2.4). This subsidence accompanied eruptions in 1995, 2005, 2008 (Baker, 2012; Bagnardi and Amelung, 2012; Manconi and Casu, 2012), 2017, 2018 (Galetto et al.,

2023), and 2020, as well as an earthquake in 2007 (Baker, 2012). In each case, the resumption of uplift was immediate. The greatest observed amount of subsidence accompanied the 2009 eruption, when the caldera floor dropped by almost 1 m (Bagnardi and Amelung, 2012). More lava (42.7×10^6 m^3) was effused during this eruption than during the 2005, 2017, 2018 eruptions combined (14.1×10^6 m^3 DRE, $9.1 \pm 4.9 \times 10^6$ m^3, $5.9 \pm 3 \times 10^6$ m^3 DRE, respectively) (Vasconez et al., 2018). Volumetrically, this eruption is comparable the 1995 eruption (42×10^6 m^3 DRE) (Vasconez et al., 2018), though there were not enough SAR acquisitions either side of this eruption to characterise any syn-eruptive subsidence. At Fernandina, the majority of inter-eruptive magma accumulation occurs in the deeper sub-volcanic reservoir (at 5 km depth), and rapidly ascends though the shallow reservoir (1 km) during eruptions (Bagnardi and Amelung, 2012; Galetto et al., 2023). While petrological data also indicate that magma storage occurs at multiple levels within Fernandina's magmatic system (Stock et al., 2020).

2.2.5 Sierra Negra

Sierra Negra is 1124 m tall, and constitutes the entire southeastern corner of Isla Isabela (Reynolds et al., 1995). It is the most voluminous, with the greatest sub-aerial extent, of all Western Galápagos volcanoes (Reynolds et al., 1995). The exposed edifice and lava flows (2.03×10^9 m^2) constitute approximately 44% of the entirety of Isla Isabela (4.6×10^9 m^2). In contrast to the northern volcanoes, Sierra Negra is the best studied volcano in the Western Galápagos, with regular InSAR, GPS, and gravity surveys (Table A9). This is likely due to: a). Its proximity to Puerto Villamil, the primary population centre on Isabela and b). Its extraordinary deformation behaviour (the caldera uplifted by 6.5 m from 2005–2018 (Bell et al., 2021b)). Sierra Negra has probably maintained this high degree of extrusive activity for millennia — 90% of the volcano has been resurfaced in the past 4,500 years, with an average long-term eruptive rate of 1×10^6 m^3 yr^{-1} (Reynolds et al., 1995).

Inflation of a shallow sill, at 2 km depth (Table A9), is the primary cause of uplift at Sierra Negra, with slip along the trapdoor fault (e.g. hinged on one side) contributing to co-eruptive subsidence. Influx of magma into the sill promotes slip along the trapdoor fault, causing asymmetric deformation across the entire caldera floor (Amelung et al., 2000; Jónsson et al., 2005; Jónsson, 2009; Chadwick et al., 2006). Jónsson et al. (2005) suggest that the trapdoor fault inhibits southbound sill growth, and instead promotes eruptions on the northern flank, from a dike rooted to the sill. This hypothesis is supported by observations, with each of the four eruptions since 1963 having taken place in the northern sector of the volcano (Venzke, 2023), and there having been 5 large earthquakes due to fault slip in January 1998, April 2005, October 2005, June 2018, and July 2018 (Amelung et al., 2000; Jónsson et al., 2005; Jónsson, 2009; Chadwick et al., 2006; Geist et al., 2008; Gregg et al., 2018; Bell et al., 2021b).

Sierra Negra, like Alcedo, has an active hydrothermal system, on the western caldera margin (Reynolds et al., 1995; Aiuppa et al., 2022; Goff et al., 2000). Fumaroles here produce magma-derived gases that have exsolved from the shallow sill, and been channeled to the surface by the trapdoor fault (Aiuppa et al., 2022). The trapdoor fault dominates the expression of volcanism at Sierra Negra: it actively promotes fumarolic activity in the west of the caldera (Aiuppa et al., 2022), slip along it can trigger eruptions (Gregg et al., 2018), the location of which is controlled by the accompanying stress field (Gregg et al., 2018), and interplay between the fault and the shallow sill produces asymmetric deformation patterns (Amelung et al., 2000).

Eruptive History

Sierra Negra has erupted twice in the 21^{st} century, first in 2005, and again in 2018. Prior to this it last erupted in 1979, one of seven 20^{th} century eruptions. There was an average eruptive frequency of 13 years between 1911 and 2018 (Venzke, 2023), though our understanding of the sub-volcanic plumbing system is derived from the 2005 and 2018 eruptions .

The 2005 eruption (October 22^{nd}) initiated explosively, with a 13 km plume, followed by three stages of variable lava fountaining (total erupted volume of $1.5 \times 10^8 m^3$, from a sill located at 2.1 km depth (Geist et al., 2008), with a source volume loss of $1.2 \times 10^8\ m^3$ (Manconi and Casu, 2012)). This eruption has a clear top-down seismic control, with no eruptive precursors in cGPS data (Geist et al., 2008). The magmatic reservoir was in a stable state of stress prior to the eruption, and had not reached a critical overpressure threshold (Gregg et al., 2018). Instead, the eruption was "catalyzed" by a mag. 5.5 earthquake three hours prior to its onset (Gregg et al., 2018). This earthquake caused $>$ 1 m of dip-slip displacement on the SW portion of the intra-caldera trapdoor fault (Geist et al., 2008), sufficiently modifying the local static stress to trigger an eruption. As at Fernandina (e.g. Bagnardi et al. (2013)), the location of an event that modifies the local stress field has a major control on the dynamics of the succeeding eruption — the mag. 5.5 earthquake relieved stress along the southern portion of the caldera while increasing tensile stress on the northern section of the caldera and magmatic system (Gregg et al., 2018).

Perhaps the most striking features of the 2018 eruption (June 26^{th}–August 23^{rd}) are the similarities with the 2005 eruption (Bell et al., 2021b; Bell et al., 2021a; Gregg et al., 2022). Lavas again effused from the northern flank of the caldera, following a mag. 5.4 slip on the southwestern section of the trapdoor fault (Bell et al., 2021b). Neither cGPS, nor tilt data, indicated imminent unrest in the hours before eruption (Bell et al., 2021b), though shear wave velocities indicate a pulse of shallow magma intrusion in the preceding 17 days (Ruiz et al., 2022). The earthquake was followed by a seismic swarm on the northwestern trapdoor fault section, eastward migrating seisimicity, and pre- and

co-eruptive tremor (Bell et al., 2021b; Li et al., 2022). The eruption lasted 3 months, and was comprised of 3 phases (Shreve and Delgado, 2023). The caldera floor subsided by $>$ 6 m during the initial eruptive phase (Shreve and Delgado, 2023), as lava effused from both summit, and distal fissures (Figure 2.2), covering an area of 17 km^2 (Vasconez et al., 2018). On July 7^{th}, a M_w 5.0 earthquake subsided the southwestern section of the caldera by up to 71 cm (Bell et al., 2021b; Sandanbata et al., 2021). Following this, the caldera, and lateral sill subsided by 2.5–3 m, and 0.25 m, respectively (Shreve and Delgado, 2023). Lava extrusion during this period was concentrated on the distal fissure, covering an area of 13 km^2 (Vasconez et al., 2018).

Previous Observations of Displacement at Sierra Negra

Amelung et al. (2000) observe 2.4 m of uplift between 1992–1998. Following this, it deflated between 2000–2002, at a rate of approximately 9 $cm\ yr^{-1}$ as observed by GPS data (Geist et al., 2006a), and InSAR data (Baker, 2012). This continued until April 2003, at which point the centre of the caldera uplifted by 2.2 metres preceding its 2005 eruption (Geist et al., 2008), the cumulative uplift from 1992–2005 was approximately 5 m (Geist et al., 2008). The high-magnitude inter-eruptive uplift at Sierra Negra is matched by similar co-eruptive subsidence — the caldera floor subsided by 5 m in 2005, and the entire volcano contracted horizontally by six metres (Geist et al., 2008). Uplift immediately resumed after the 2005 eruption, and was sustained for 13 years (with $>$ 4 sub-phases of deformation) (Bell et al., 2021b; Geist et al., 2008). In total, the caldera inflated by $>$ 6.5 m as magma accumulated at two kilometres depth (Bell et al., 2021b). This depth is consistent with the source of the 2005 eruption (Geist et al., 2008), and agrees with that found by gas composition analysis, as well as magma equilibration depths (Aiuppa et al., 2022; Bell et al., 2021b). The sills that fed the distal fissure are spectacularly observed in the InSAR displacement maps of the eruption (e.g. Davis et al. (2021) and Bell et al. (2021b)). It initiated in the northwestern section of the caldera before separating into two lobes, the larger of which migrates to the west, before deflecting northeast, and surfacing. Davis et al. (2021) show that this curvature is caused by the interaction between the topographic stress gradient, and that of the sill buoyancy. Co-eruptive subsidence in 2018 exceeded the pre-eruptive uplift by 2 m (8.5 m total) (Bell et al., 2021b), with Shreve and Delgado (2023) suggesting that caldera formation at Sierra Negra may be caused by the accumulation of metre-scale subsidence during regular eruptions.

2.2.6 Wolf

Wolf (1710 m) is the northernmost major Western Galápagos volcano, and is the only one found in the northern hemisphere. It is also the most remote, with no ground-based monitoring instrumentation (Bernard, 2022). Wolf's remote location means that

eruptions here are not a threat to human life. However, Wolf is home to the critically endangered pink iguana (*Conolophus marthae*), the only place where these iguanas are native in the world. Following both the 2015 and 2022 eruptions, the response aimed to ensure that these iguanas were not threatened (Bernard, 2022; Communication, 2022).

Eruptive History

Wolf was quiescent for much of the late 20th and early 21st centuries. However, it has recently erupted twice in quick succession, in 2015 and 2022 (Stock et al., 2018; Venzke, 2023). The 2015 eruption (25/05/2015–26/07/2015) was initially explosive, with a 15 km ash column, circumferential lava flows, and lava fountaining — the fountaining was sufficiently vigorous to produce reticulite scoria (Bernard et al., 2019; Bernard, 2022). Following this the eruption transitioned to a phase of intra-caldera lava flows (Bernard et al., 2019; Bernard, 2022) (Figure 2.2). Throughout the eruption, the FER1 station detected 465 earthquakes at Wolf (Bernard et al., 2019).

In comparison, the 2022 eruption was much less explosive during its initiation phase (column was approximately 5.5 km high) (Bernard, 2022), though was sustained for a much longer duration. The eruption started on January 6th, and IGEPN did not report an end to the eruption until May 5th, a period of 119 days (*Wolf Volcano Special Report No. 1 - 2022* 2022). The eruption intensity peaked during its first 5 days, with seismic swarms, tremor, and earthquakes (detected at FER1), gas and ash plumes (up to 3.8 km), and thermal activity from lava flows (*Wolf Volcano Special Report No. 1 - 2022* 2022). By January 11th there were three radial fissures on the southeastern flank, covering an area of 7.4 km^2 (*Wolf Volcano Special Report No. 2 - 2022* 2022). By May 5th, at least 5 fissures had opened, and lava flows covered an area of 30 km^2, with a maximum distance of 18.5 km, almost reaching the sea to the southeastern of the volcano (*Wolf Volcano Special Report No. 3 - 2022* 2022). In total, 60,000 tonnes of SO_2 were emitted, though none had been recorded in the 30 days prior to the eruption end (*Wolf Volcano Special Report No. 3 - 2022* 2022). There were no intra-caldera lava flows, dissimilar from the 2015, and 1982 eruptions, when the thickest lava flows were located within the caldera (9.5–9.7 m) (Bernard et al., 2019).

These are the first eruptions at Wolf since 1982 (Geist et al., 2005) but suggest that Wolf follows the same alternating eruptive fissure pattern as Fernandina (radial-circumferential-radial for the 1982, 2015, and 2022 eruptions respectively (Bernard et al., 2019; *Wolf Volcano Special Report No. 1 - 2022* 2022)), suggesting that, like Fernandina, stress changes during one eruption may affect the geometry of the succeeding eruption (Bagnardi et al., 2013). At Wolf, like Cerro Azul, the most recent eruptions have all taken place on the southeastern flank (as have all confirmed eruptions since 1948 (Siebert et al., 2010)).

Previous Observations of Displacement at Wolf

Wolf has perhaps the best example of variable magma supply rates to volcanoes from the Galápagos plume. Like Fernandina, there is geodetic evidence of stacked magma reservoirs at 1 km depth, and >5 km (Xu et al., 2016; Stock et al., 2018), though there is evidence of even deeper reservoirs — clinopyroxenes erupted during the 2015 eruption equilibrated at 9.9±2.2 km, while glomerocrysts and phenocrysts equilibrated at 11.2±2.8 km (Stock et al., 2018). Bagnardi (2014) made volume flux estimates of magma supply to the six major Galápagos volcanoes, from 1992–2010, when Wolf accounted for approximately 1% of total magma supply, less than both the recently inactive Darwin (3%) and Alcedo (11%). However, there has been a recent uptick in volcanic activity at Wolf, having erupted twice since 2010 (2015, 2022 (Venzke, 2023)). Prior to this pair of eruptions, Wolf erupted eight times since 1900, with an average frequency of approximately 11 years between the 1925 and 2022 eruptions — since 2015, Wolf has been the second most active Western Galápagos volcano, after Fernandina.

2.3 Methods

2.3.1 InSAR Data and Analysis

The InSAR data used in this study was processed using the LiCSAR automatic InSAR processor (Lazecký et al., 2020). In this workflow, interferograms are geocoded with a pixel spacing of approximately 100 m, with minimum temporal baseline of between 6–12 days, when Sentinel-1A, and Sentinel-1B were in constellation. We perform a quality check of the final interferograms, to identify errors (e.g. in the unwrapping process) that may have occurred during the automated workflow. These interferogams are removed, and reproduced. Similarly, we also correct for errors introduced by tropospheric phase delay, using the Generic Atmospheric Correction Online Service (GACOS) (Yu et al., 2018). Here, estimated maps of tropospheric phase delay are constructed, using data from the European Centre for Medium-Range Weather Forecast, and which are then removed from the unwrapped interferogram. We use these corrected data to construct time series of displacement, using the LiCSBAS time series analysis software (Morishita et al., 2020). This small-baseline inversion software utilises phase loop closure, to identify and remove bad interferograms before performing the time series inversion. The final time series are filtered, spatially and temporally, using a Gaussian Kernal. Finally, deformation source modelling is conducted using the MATLAB-Based Geodetic Bayesian Inversion Software (GBIS) (Bagnardi and Hooper, 2018). This software uses a Bayesian approach to estimate the best-fit source geometries, for a given input, in each case we perform 1×10^6 iterations.

2.3.2 Volcanic Areas and Extents

The comparison of areal features was conducted in QGIS. Maps of volcanic features that had been identified in previous studies were imported into QGIS, and georeferenced using the Georeferencer, in the Raster toolbox. The extents of these features were then manually extracted from the georeferenced maps, and converted to polygon vector files, from which variables such as area were calculated (using the EPSG:3857 Coordinate Reference System). This process was carried out for lava fields, bathymetric data, and previously modelled intrusions, using existing maps from published studies (cited in their corresponding sections), or from optical satellite imagery. Maps including bathymethyric data were created using data from the GEBCO Compilation Group (2022) (GEBCO_2022 Grid (doi:10.5285/e0f0bb80-ab44-2739-e053-6c86abc0289c.))

2.3.3 Lava Flow Modelling

We model cooling and subsidence using the PDE Toolbox in MATLAB. We emplace a lava on top of country rock, and allow conductive cooling between these two elements, while imposing a radiative-convective boundary condition on the top surface of the lava. We calculate the temperature distribution in the lava for 10 years after its emplacement, and calculate the corresponding ground displacement as follows (e.g. Chaussard (2016)): $\Delta h(t) = h\eta[(1+\upsilon)/(1-\upsilon)]\Delta T(t)$, where h is thickness, t is time, η is the thermo-elastic expansion coefficient, υ is Poisson's ratio, and T is temperature. The values used for each variable are presented in Table A24. We use a value of 1200°C as the starting temperature of our lava. This simple approach effectively models thermo-elastic contraction due to conductive, convective, and radiative heat loss, though does not account for latent heat release, pose space compaction, bubble vesiculation, convective forcing, or insulating effects. Therefore it is better applied to longer-term deformation (e.g. after Wolf, 2015).

2.3.4 Volatile exsolution at Sierra Negra

We use MELTS Phase equilibria software (Ghiorso and Gualda, 2015; Gualda et al., 2012) to model the changes in phases assemblages for a sill intruded during the 2018 eruption. We assume the sill is intruded at 1 km depth (e.g. Davis et al. (2021)), with a starting composition of 1 $wt\%$ H_2O, after Aiuppa et al. (2022) — the full initial conditions for MELTS modelling are presented in Table A25.

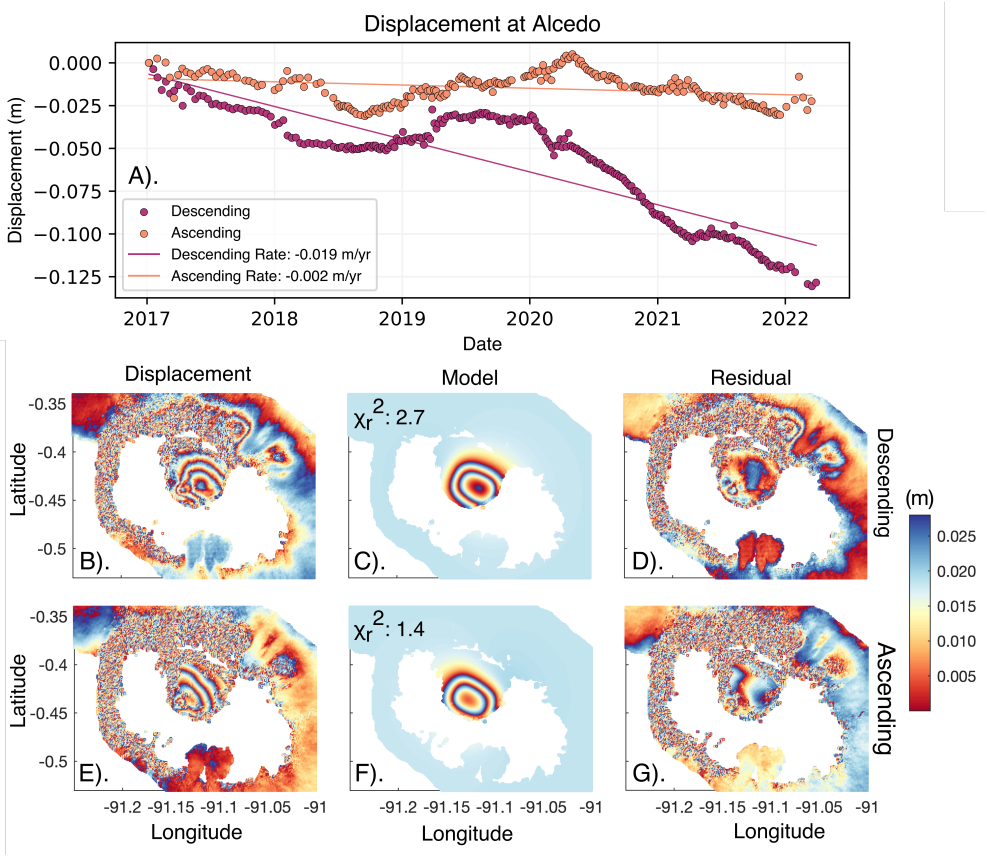

Figure 2.7: Subsidence at Alcedo from 2017–2022. A). Time series in both ascending and descending track directions. The point used in the time series is located at -0.43833° N, and -91.114° E. This subsidence is relative to a reference area between -0.564– -0.548° N, and -91.055– -91.034° E. B–G). Data, model and residual for a contracting sill beneath Alcedo, in descending and ascending track directions, respectively, where each fringe corresponds to 28 mm of LOS displacement. Subsidence in the hydrothermal field is clearly visible in panels B and E, and in the residual panels D and G.

2.4 New observations of Deformation in the Western Galápagos

2.4.1 The Active Hydrothermal System at Alcedo

We observe steady subsidence at Alcedo from 2015–2022 (approximately 14 cm in descending), with a brief period of uplift in 2020 (Figure 2.7A). Using ascending and descending data, we perform a joint geodetic source inversion to model the cumulative caldera subsidence (Section 2.3), over an approximately 5 year period from 26/12/2016–01/10/2021 in descending, and 06/01/2017–30/09/2021 in ascending (We can not use the descending acquisitions from 2015–2017 for a joint inversion, as ascending data were not routinely acquired until 2017). The best-fit sill (Table A11), is approximately 3300 m long, 4700 m wide, at a depth of approximately 1900 m, striking at 207°, and closing by -0.13 m over the modelled period (The 2.5% and 97.5% intervals for length,

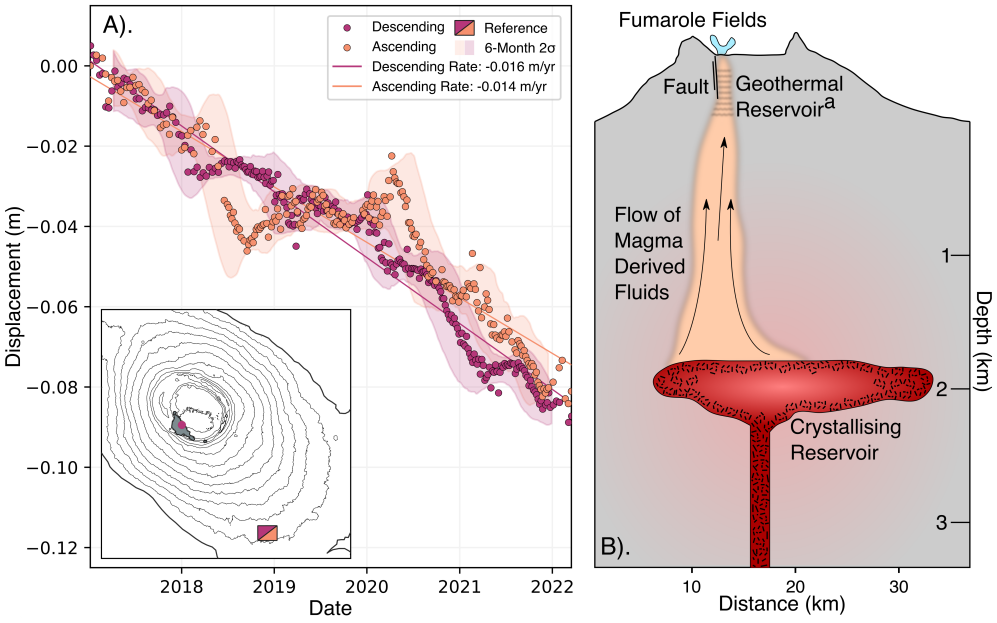

Figure 2.8: Subsidence at the fumarole field at Alcedo volcano from 2017–2022. A). Time series in both ascending and descending track directions. The point used in the time series is located at -0.439° N, and -91.137° E. This subsidence is relative to a reference area between -0.564– -0.548° N, and -91.055– -91.034° E. Inset is a map showing the extent of the hydrothermal field, the plotted point, and reference area, where each line represents 100 m of elevation change. B). Schematic showing a conceptual model of the sub-volcanic structure of Alcedo. [a]The inferred geothermal reservoir is from Goff et al. (2000).

width, depth, strike, and opening are 1466 – 3770 m, 4010 – 5185 m, 1665 – 3137 m, 199 – 220°, and -0.42 – -0.1 m, respectively). The input data, modelled source, and residual, are shown in Figure 2.7B–G, alongside the corresponding reduced χ^2 statistic to indicate the goodness-of-fit between the observation and model (e.g. Li et al. (2021)).

In both Figure 2.7B and Figure 2.7E, there is local modification to the subsidence field at Alcedo. This feature is clear in the residuals (Figure 2.7D and Figure 2.7G), and is located in the hydrothermal field at Alcedo (e.g. Goff et al. (2000), Figure 2.8A). We plot displacements for a point in this hydrothermal zone in Figure 2.8A, observing subsidence of approximately eight centimetres, in both track directions from 2017–2022. The consistent rate in both track directions (approximately 15 mm/yr) suggests that this subsidence is mostly vertical, with consistent LOS change regardless of look direction (Figure 2.8A). This contrasts with the non-vertical caldera subsidence (Figure 2.7A), where, for a point at -0.43833° N, and -91.114° E, the subsidence rate is almost ten times faster in descending (-19 mm/yr) than ascending (-2 mm/yr).

Though the presence of hydrothermal activity has been noted before (at depths of up to 1000 m (Goff et al., 2000)), this is the first time that displacement here has been noted

geodetically. As volatile-bearing magmas crystallise, the residual melt become relatively enriched in volatiles, eventually saturating and exsolving in a process known as second boiling (Caricchi et al., 2014). The volatiles can migrate towards the surface (e.g. along pre-existing faults), prompting unrest in the hydrothermal zone, and fumaroles (e.g. Fournier (1999)). Though the hydrothermal subsidence signal was not noted during Alcedos resurgence (Galetto et al., 2019), magma supplied then may now be undergoing second boiling as it crystallises. These observations suggest that during uplift, deformation at Alcedo is controlled by magma-tectonic interactions between the sill and the intra-caldera fault (Galetto et al., 2019; Bagnardi, 2014), while the fault acts as a conduit for volatiles and the hydrothermal system during periods of subsidence. There may also be more direct interaction between the magmatic and hydrothermal systems — heat supply during magma intrusion can pressurise overlying hydrothermal systems, and cause phreato-magmatic eruptions (e.g. Agung, 2017 (Bemelmans et al., 2023)). This is viable mechanism for unrest at Alcedo, given that the most recent eruption (in 1993) was phreatic, and caused new fumarolic vents to open (Green, 1994). As such, displacement at the hydrothermal field at Alcedo may provide information about future eruptions.

2.4.2 Long-Lived Sources at Cerro Azul

Regular radar acquisitions by Sentinel-1 in both track directions began in January 2017, prior to the March unrest episode. From the IGEPN reports (with eruption warnings), we suggest that this 2017 unrest can be classified as a failed eruption (e.g. *Cerro Azul Special Report No. 3 - 2017* (2017)). Following this, caldera-wide uplift resumed, at a rate of approximately 5 cm yr^{-1}, and continued until the end of this study (Figure 2.9), while the uplifted flank (Figure 2.9) subsided at low rates of between 7–12 mm yr^{-1}, possibly due to crystallisation of the intruded magma (Figure A1).

Petrological, geodetic, and eruptive evidence suggest that the eruptive pathway at Cerro Azul is has persisted from 1979–2017. The 1998 and 2008 eruptions, as well as the 2017 unrest were located on the eastern volcanic flank (Figure 2.2 and Figure 2.9). The magma pathway connecting the sub-caldera source to the eastern flank (the site of fissure eruptions (Figure 2.9)) has probably existed for at least 40 years (given that lavas erupted in 1998 had mixed with residual 1979 magma (Figure 2.9)), and possibly up to 60 years (both the 1979 eruption, and the preceding confirmed eruption in 1959 took place on the eastern flank (Siebert et al., 2010)).

We perform a joint geodetic source inversion to model the post-unrest cumulative uplift (up to 25 cm) at Cerro Azul, over an approximately 5 year period from 05/07/2017–04/01/2022 in ascending, and 06/07/2017–24/12/2021 in descending. We start in July 2017 to avoid any syn-unrest displacement. We perform the source inversion using GBIS (See Section 2.3). The best-fit sill (Table A12), is approximately 9540 m long, 125 m

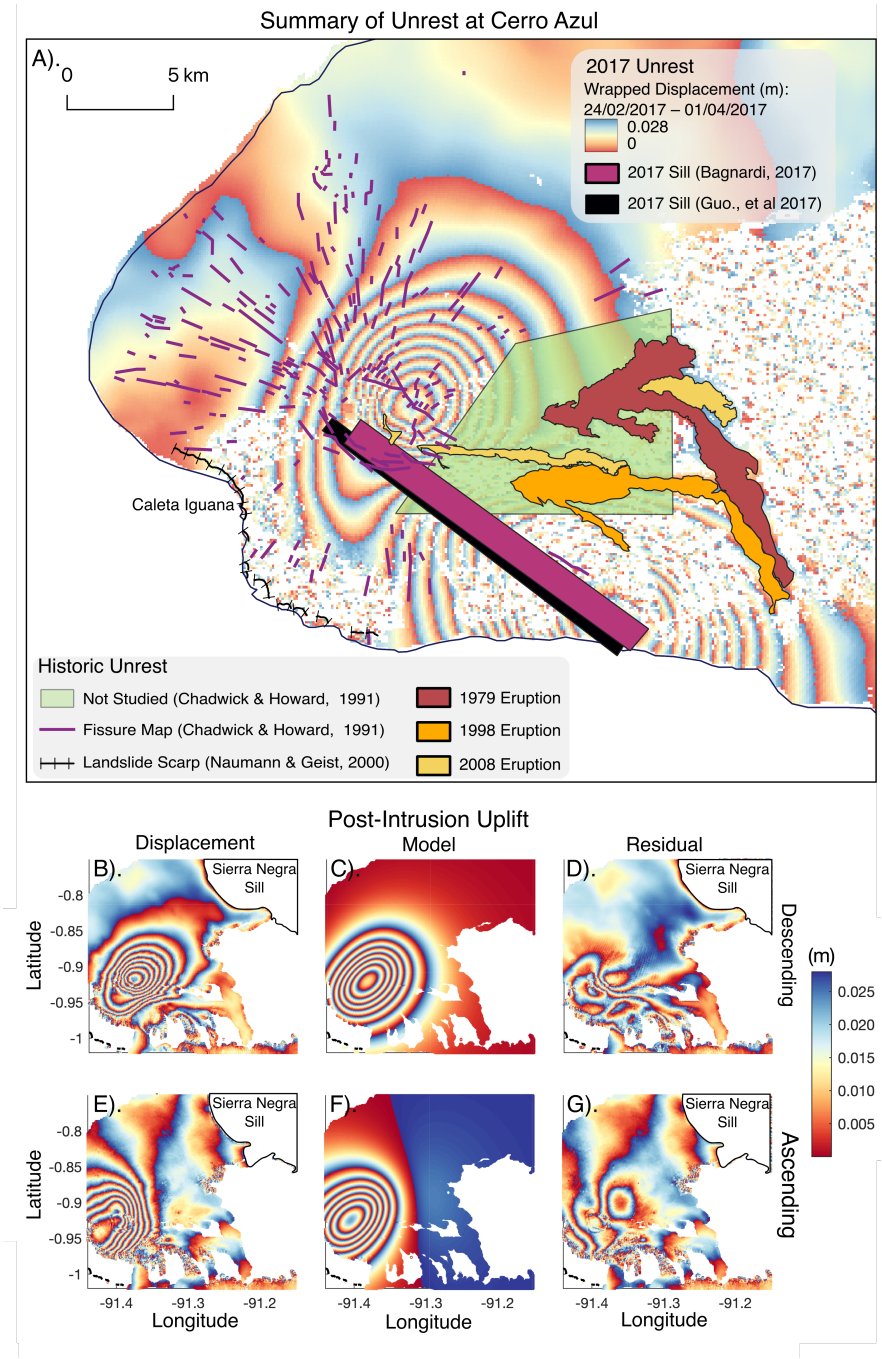

Figure 2.9: Sources at Cerro Azul. A). Map of recently active sources, lavas flows, and historical fissures at Cerro Azul. Fissures, as mapped by Chadwick and Howard (1991), are marked in purple, while recent lava flows on the eastern flank are shown in orange. The underlying interferogram spans the 2017 failed eruption of Cerro Azul in descending direction, from 24/02/2017–01/04/2017. B–D). Data, model and residual, for the best-fit sill for cumulative displacement in the descending track direction from 06/07/2017–24/12/2021. E–G). Data, model and residual, for the best-fit sill for cumulative displacement in the ascending track direction from 05/07/2017–04/01/2022. The best-fit sill is located at 6300 m depth, 9540 m by 125 m wide, and opened by approximately 24 m.

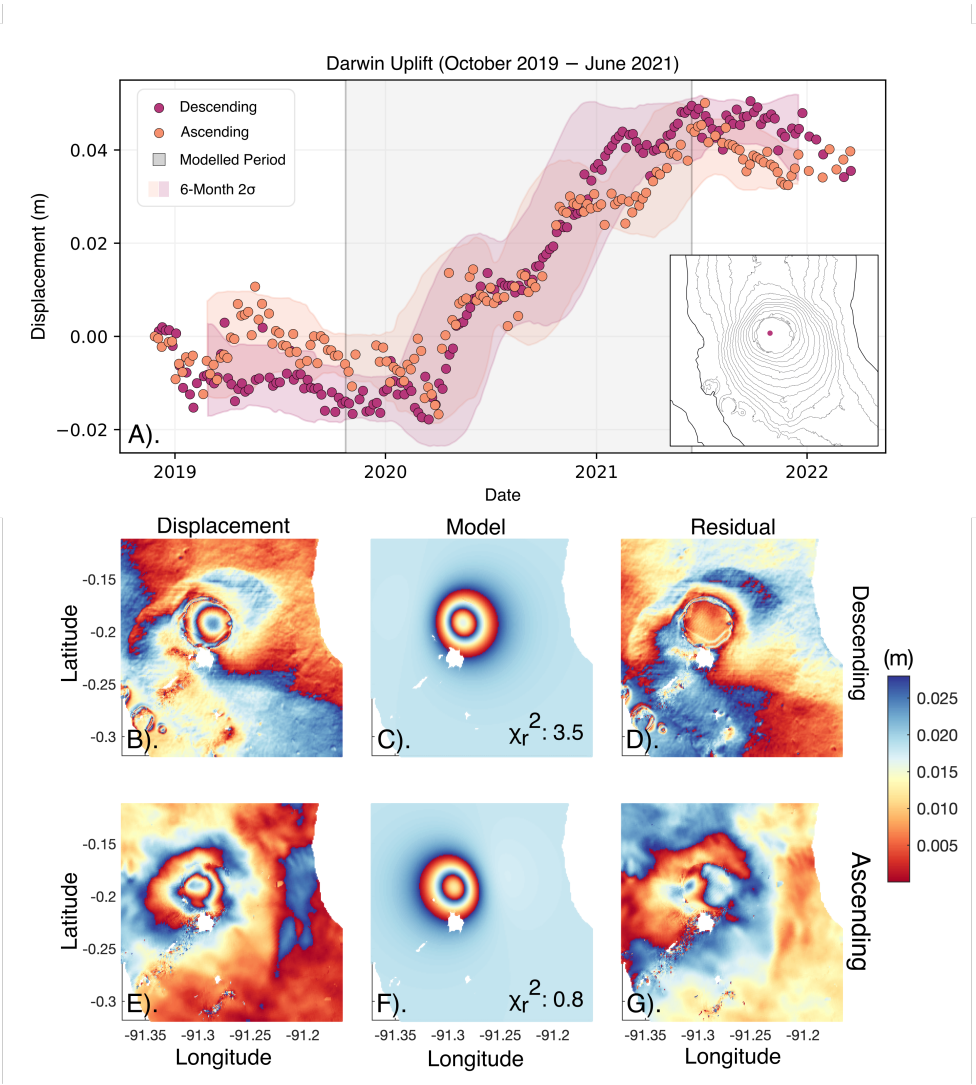

Figure 2.10: Uplift at Darwin volcano from 23/10/2019–14/06/2021, for a point at -0.192° N, and -91.29° E. This unrest is modelled using GBIS (Bagnardi and Hooper, 2018). A). Time series of uplift in descending and ascending track directions, accompanied by the second standard deviation across 6-month rolling windows. B–D). Data, Model and Residual in the ascending track direction. E–G). Data, Model and Residual in the descending track direction. Cumulative displacement across the modelled window is relative to a reference point at -91.32;-0.2974. The best-fit source geometry is as follows: Length: 143.676 m, Width: 2273.56 m, Depth: 3342.57 m, Opening: 4.91 m.

wide, at a depth of approximately 6300 m, striking at 229°, and opening by 24 m over the modelled period (The 2.5% and 97.5% intervals for length, width, depth, strike, and opening are 9350 – 9720 m, 129 – 335 m, 6228 – 6379 m, 228 – 230°, and 9 – 23 m, respectively). The extreme aspect ratio suggests that there may be some trade-off between sill width and opening (e.g. could a wider sill, opening by less, facilitate the same amount of surface displacement?). However, such elongate sills have been modelled at Cerro Azul, both during the 2017 unrest (709 m by 7010 m) (Guo et al., 2019), and the 2008 eruption (1019 m by 7569 m) (Galetto et al., 2020). The input data, modelled

source, and residual, are shown in Figure 2.9B–G. In both track directions, there are features on the displacement field on the upper southwestern flank of Cerro Azul (Figure 2.9B and Figure 2.9E), that remain in the residual (Figure 2.9D and Figure 2.9G). This feature is also observed in cumulative displacement data spanning the 2008 eruption (Galetto et al., 2020), located on the steepest flanks of Cerro Azul ($<30^{o}$), an area susceptible to mass wasting (Naumann and Geist, 2000). There is extensive landsliding at the base of the southwestern flank, at Caleta Iguana, where the volcano meets the Galápagos platform (Naumann and Geist, 2000) (Figure 2.9). We therefore attribute this deformation feature to the influence of extreme topography, and mass wasting (e.g. Arenal, Costa Rica (Ebmeier et al., 2014)).

2.4.3 Resurgence at Darwin

Using Sentinel-1 InSAR data, we see low magnitude (<3 cm) uplift and subsidence from 2017–2022, though we measure an episode of uplift of approximately 6 cm LOS at Darwin, from April 2020 until June 2021 (Figure 2.10).

We modelled the source of this uplift (Bagnardi and Hooper, 2018) (Section 2.3), using both ascending and descending track directions. The best fitting sill is located at 3.3 km depth, and opened by 4.9 metres between April 2020 – June 2021 (Figure 2.10) (The 2.5% and 97.5% intervals for depth and opening are 3220 – 3490 m and 0.93 – 5.6 m). The reduced-chi squared statistic is presented in Figure 2.10, and complete modelling results are presented in Table A13. This depth agrees well with previous studies, and falls within the range of estimates (2.7 – 4.25 km) presented in Table A6, and Figure 2.5. The 2020 episode of uplift at Darwin was similar to the uplift observed there between 1992–1997 (Amelung et al., 2000) and indicates that, despite its eruptive quiescence, magma periodically intrudes into Darwins sub-volcanic system.

2.4.4 The 2020 Eruption at Fernandina

Deformation in the Sentinel-1 era has continued as steady inter-eruptive uplift, varying from 7 cm yr^{-1} between 14/11/2015–01/07/2018, to 34 cm yr^{-1} between 01/07/2018–04/01/2020, and 50 cm yr^{-1} from 21/05/2020–30/03/2020, with syn-eruptive subsidence. During the 2017 and 2018 eruptions, syn-eruptive deformation was short-lived (Figure 2.4). Galetto et al. (2023) observe up to 38 cm of co-eruptive subsidence and uplift in 2017, and < 20 cm of co-eruptive subsidence in 2018, while the caldera floor uplifted by < 14 cm in the inter-eruptive period. However, the 2020 eruption is strikingly different — though the sub-aerial component of the eruption lasted only a day (Venzke, 2023), various locations around Fernandina island continued to deform for a 3 month period from 05/01/2020–14/03/2020 (Figures 2.11 and 2.12). This was accompanied by uplift to the west, and south of the caldera (Section 2.4.4). In November 2021, IGEPN noted heightened fumarolic activity in the caldera, as well as seismic tremor,

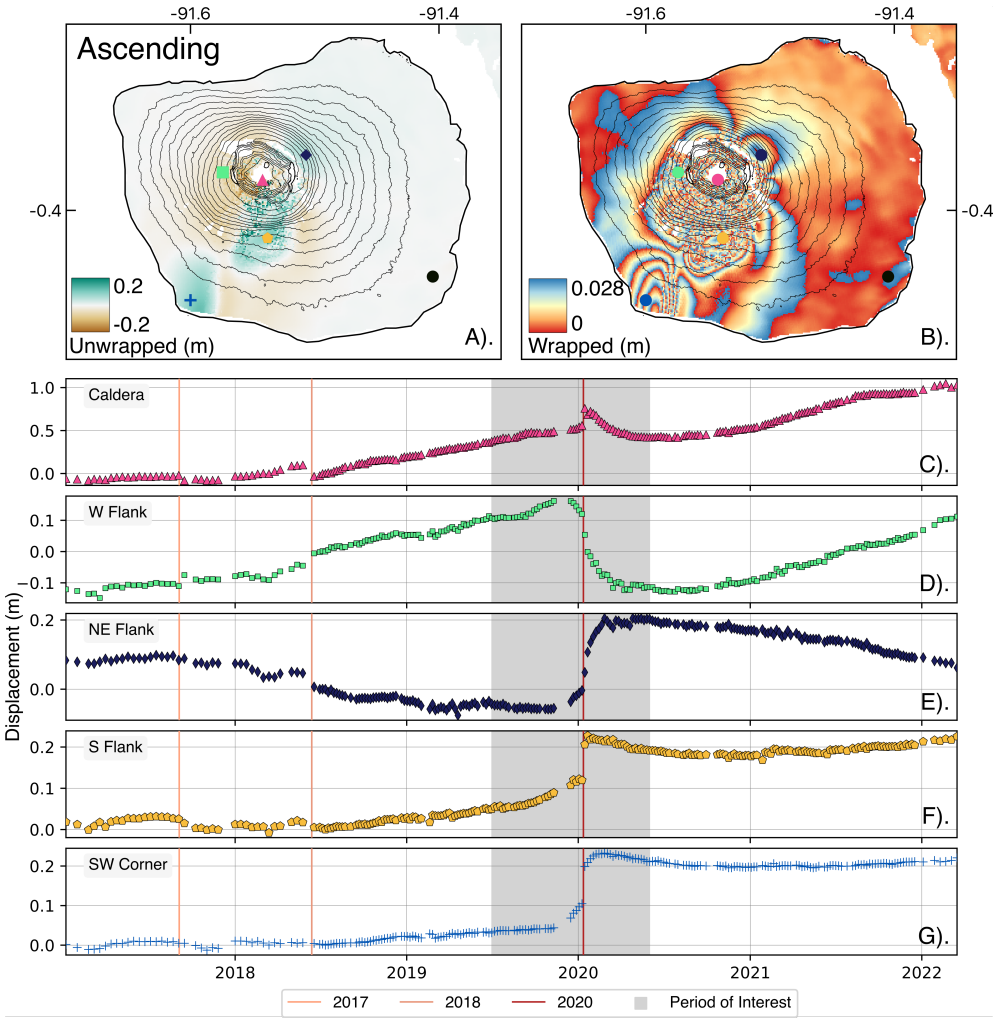

Figure 2.11: Eruptive displacement for the 2020 eruption at Fernandina, in the ascending Track direction, relative to reference point on the east of the island (black dot). A). Unwrapped displacement (m) at Fernandina Island, from 09/01/2020–15/01/2020, spanning the eruption. B). Wrapped displacement (m) at Fernandina Island, from 09/01/2020–15/01/2020, spanning the eruption. C–G). Time series of displacement from 2017–2022 for a point in Fernandinas caldera, western flank, northeastern flank, southern flank, and on the southwestern edge of the island, relative to a point on the SE of the island.

and suggested that they may evolve into an eruption in the medium to long term (*Special Volcanic Report - Fernandina - 2021 - No. 1* 2021). Ultimately, this did not lead to an eruption, though this unrest was accompanied by accelerated uplift, beginning in October (*Special Volcanic Report - Fernandina - 2021 - No. 2* 2021).

Here, we study the 2020 eruption in greater detail. Fernandina erupted on January 12$^{\text{th}}$, 2020. The subaerial component of this eruption was minor — small lava flows effused from an eastern circumferential fissure and it did not exceed VEI 0 (the first VEI 0 eruption at Fernandina in almost 40 years (1981)) (Venzke, 2023). The USGS Seismic Catalogue shows a magnitude 4.6 earthquake occurred on the southern flank

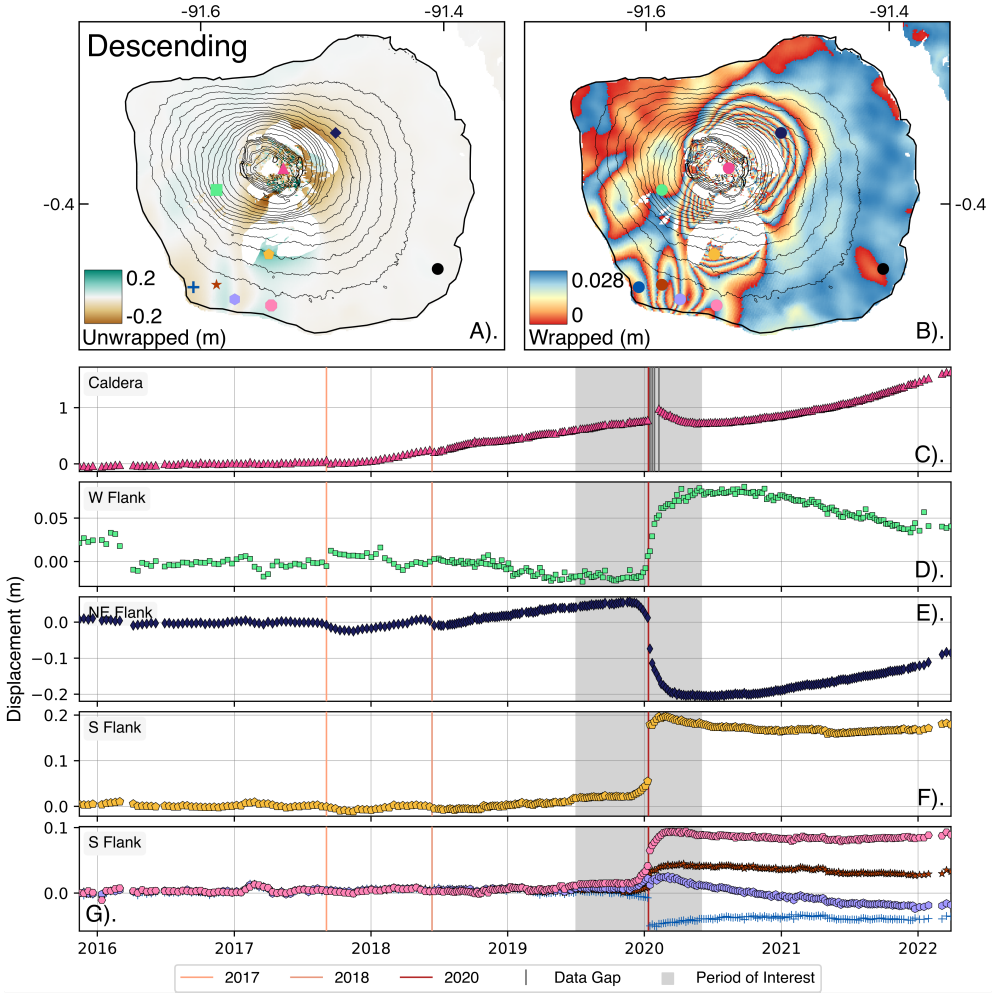

Figure 2.12: Eruptive displacement for the 2020 eruption at Fernandina, in the descending Track direction, relative to reference point on the east of the island (black dot). A). Unwrapped displacement (m) at Fernandina Island, from 10/01/2020–16/01/2020, spanning the eruption. B). Wrapped displacement (m) at Fernandina Island, from 10/01/2020–16/01/2020, spanning the eruption. C). Time series of displacement from 2015–2022 for a point in Fernandinas caldera, western flank, northeastern flank, southern flank, and several points on the southwestern edge of the island, relative to a point on the southeast of the island.

of the volcano on the day of the eruption (Figure 2.14). Sentinel-1 interferograms spanning the eruption show that deformation was widespread; complex interferometric fringes span the entire island, with at least 5 distinct deforming areas (Figure 2.11).

Time-series data reveal further sub-volcanic complexity. The caldera, and southern flanks began inflating immediately following the June 2018 eruption of Fernandina, while the northeastern and western flanks show differing displacement patterns in different LOS directions flank (Figures 2.12 and 2.11), until December 2019. At this point, almost all time series points show an uptick in displacement, until January 12th. During the eruption, all time series points show significant ground deformation, though the most notable change occurred in the southwestern sector of the island. The southwestern flank

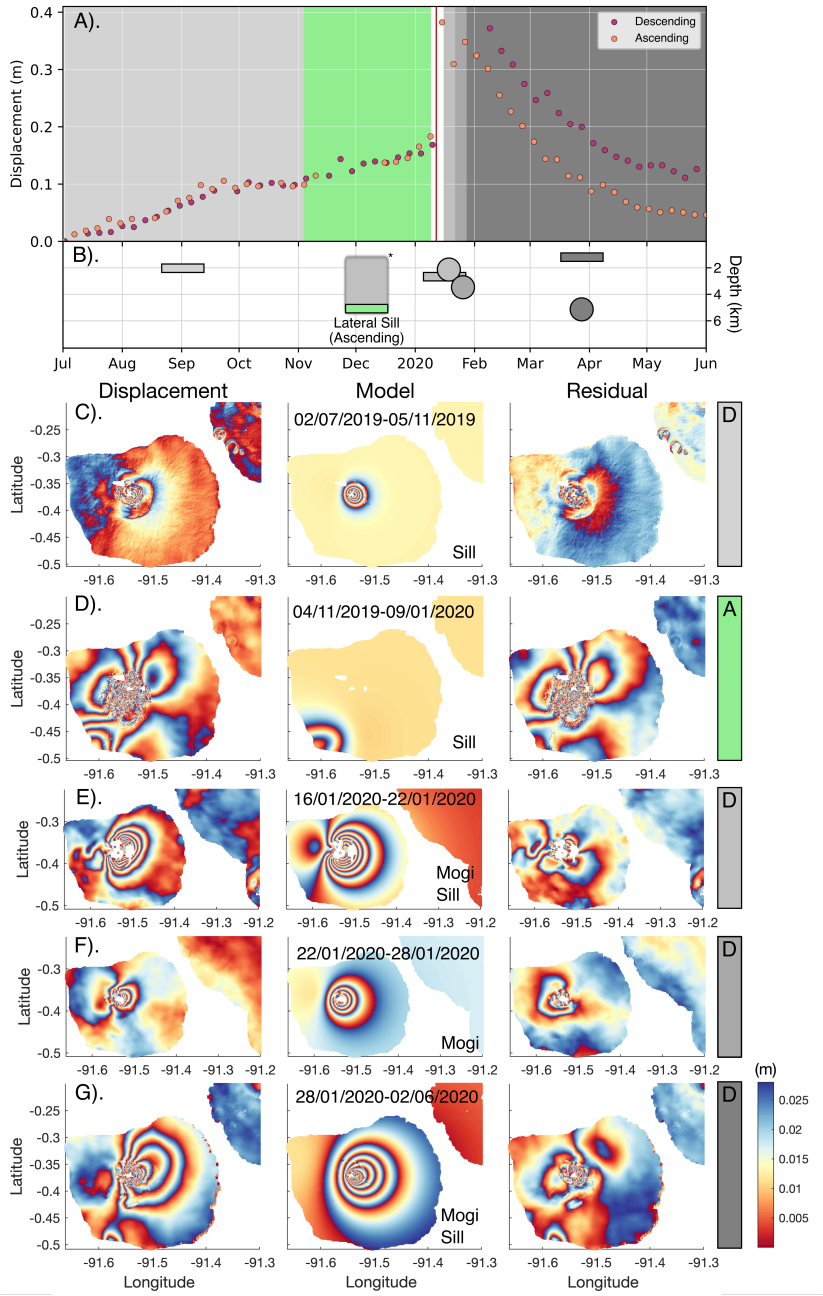

Figure 2.13: Results of geodetic source modelling for the 2020 eruption of Fernandina. Full results in Tables A14– A19. A). Time Series of displacement in the caldera (e.g. Figure 2.11C.), in both track directions, colour indicates each modelled period. B). Indicative schematic of the sources active during each period. * denotes shallow sources that were active during the pre-eruptive period, but that are not modelled here. C), E)–G). Data, model, and residual for cumulative displacement at Fernandina for a joint inversion, presented using descending data. D). Pre-eruptive uplift on the southwestern coast, modelled using only ascending data.

uplifted by 0.1–0.15 m between satellite acquisitions surrounding the eruption, while the southwestern coast uplifted by 0.1 m in ascending, and shows complex uplift-subsidence patterns in descending (Figures 2.11 and 2.12). In both cases, the fringes of deformation

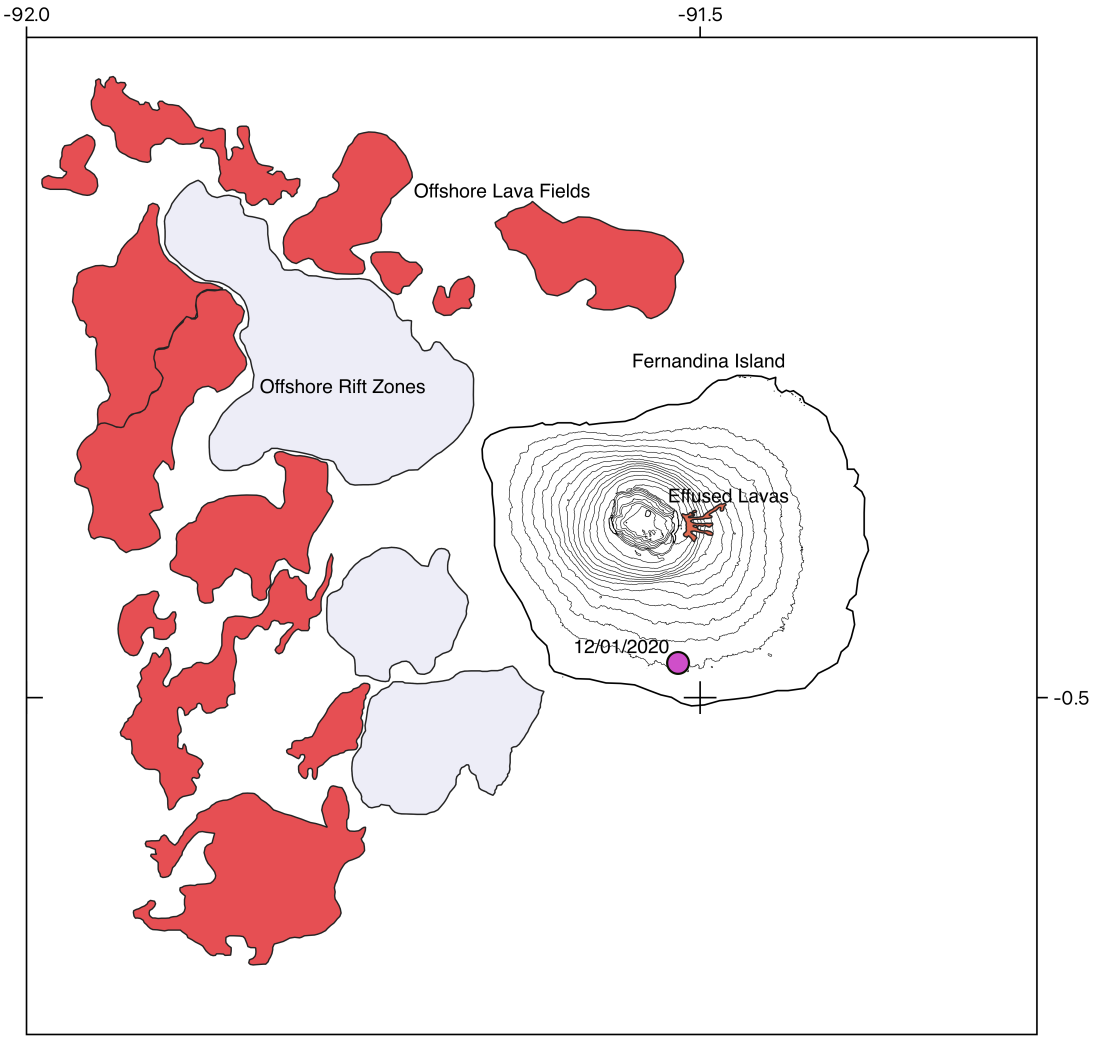

Figure 2.14: Volcanic context of the 2020 eruption of Fernandina. A magnitude 4.6 earthquake occurred on the southern flank of the volcano on the day of the eruption (*U.S. Geological Survey Earthquake Catalogue* 2023). Lavas effused from a circumferential fissure on the eastern caldera rim, covering an area of approximately 3 km^3. Offshore the west coast of Fernandina Island are located extensive rift zones (in grey), and lava fields (in red).

end abruptly at the coast of Fernandina Island, indicating an offshore component to the eruptive unrest. Ground displacement continued for months following the eruption: the caldera, southern flank, and parts of the southwest coast gradually subsided, until June 2020 in both track directions, while the western flank and northeastern flanks continued to deform over this period.

Here, we model the primary features of displacement during the co-eruptive period, and identify the main geodetic source regions (Section 2.3). Bagnardi and Amelung (2012) find that deformation at Fernandina can be explained by a shallow sill overlying a deeper Mogi source. Assuming these sources to be temporally consistent, we

model each of the following periods using either or both of these sources. We perform joint inversions using descending and ascending cumulative displacement data leading up to the eruption, from 01/07/2019–10/11/2019, immediately following it from 16/10/2020–22/01/2020 and from 22/01/2020–28/01/2020, and for the long-term post-eruptive deformation from 28/01/2020–01/06/2020. We find that pre-eruptive inflation, from 01/07/2019–05/11/2019, is due to opening of the shallow sill (2.1 km, 2.5%, 97.5% bounds of 2.1 km – 2.2 km), by 17 m (bounds of 4.2 – 20 m) (Figure 2.13). The ascending track shows ≥ 5 active sources in the immediate pre-eruptive period from 04/12/2019–09/01/2020 (Figure 2.11). We cannot reliably model the multiple pre-eruptive sources using single or joint inversions, and instead model the southwestern coast uplift, in the ascending direction, to get indicative source parameters (Figure 2.13). This part of Fernandina island deforms before, during, and after the eruption, and is similar to previous lateral intrusions, sourced from the deeper reservoir at Fernandina (Bagnardi and Amelung, 2012). We consider this a notable component of the 2020 eruption as the spatial deformation pattern is interrupted by the coastline, indicating a potential offshore component of the eruption. We find that, from 04/11/2019–09/01/2020, uplift of the southwestern corner can be explained by a sill at 5 km depth (fixed to the depth of the deeper source Bagnardi and Amelung (2012)), opening by 0.3 m (bounds of 0.1 – 0.5 m). We also do not model displacement spanning the eruption, given the ≥ 5 active sources (Figure 2.13). Following this, we see that post-eruptive displacement, from 16/10/2020–22/01/2020 is due to the inflation (2.8×10^7 m^3) of a point source at 2.2 km depth, alongside the closing of a sill (-8.5 m, bounds of -8.51 – -4.4 m) at 2.5 km depth (bounds of 2.4 – 2.6 m). The point source (3.1 km, bounds of 3.1 – 3.2 km) continued to inflate (6.5×10^6 m^3) from 22/01/2020–28/01/2020. Deformation in the post-eruptive period can again be explained by stacked reservoirs, a sill at 700 m depth (bounds of 700 – 1200 m) (closing by -0.3 m, bounds of -1.78 – -0.32 m), as well as a point source at 5.4 km depth (bounds of 5.2 – 6.9 km) (deflating by -1.8×10^7 m^3, bounds of -2.55×10^7 m^3 – -1.72×10^7 m^3) (Figure 2.13). However, residual deformation in the ascending track shows an extra source on the northeastern flank, that does not appear in descending (Figure A4), modelling this residual, in the ascending track, shows a deflating source at 4.4 km depth (bounds of 4.2 – 4.5 km) (Figure A5, Table A20). Over the same period, the southwestern corner continued to deflate, this time modelled as a sill at 1.4 km depth (bounds of 1.35 – 1.7 km), closing by -0.09 m (bounds of -1.5 – -0.07). The full data, model and residual for each of these models can be found in Figures A3 and A4, while the full description of sources can be found in Tables A14 to A19.

In total, we see that magma accumulated in the shallow sill for at least 4 months prior to eruption. The uptick in deformation in the month prior to the eruption probably corresponds to heightened magma flux to multiple reservoirs, including one on

the southwestern flank, at 5 km depth. The majority of deformation immediately following the eruption can be explained by magma accumulation between 3.1–2.2 km depth. Both stacked sources continued to deflate from 28/01/2020–01/06/2020, while the southwestern coast of the island inflated. This protracted deformation indicates that the sub-volcanic system of Fernandina was active for months following the eruption, to a much greater degree than indicated by the sub-aerial component. This agrees with seismic data, which shows that seismicity did not return to background levels following the eruption, but continued, with a magnitude 4.2 on January 21st (*Special Volcanic Report - Fernandina - 2020 - No. 3* 2020). Some of the observed deformation can be explained by volume changes in the known sources at Fernandina (Figure 2.13), though there are at least 3 new active sources (Figure 2.11). The instantaneous uplift on the volcano's southern sector on the day of the eruption is consistent with the syn-eruptive opening of a lateral sill, as occurred during the 2018 eruption of Sierra Negra (Davis et al., 2021). The displacement patterns also show that a portion of the southwestern uplift occurred offshore Fernandina, undetectable by satellite-radar. Bathymetric mapping by Geist et al. (2006b) showed that this region of offshore Fernandina consists of multiple rift zones, opening into lava fields (Figure 2.14). Therefore, we speculate that the 2020 eruption of Fernandina may have contained a submarine component, where magma migrated laterally from the sub-volcanic reservoir (e.g. Bagnardi and Amelung (2012)), before intruding, or erupting on offshore Fernandina.

2.4.5 Cooling Related Displacements at Sierra Negra

We observe almost 3 m of LOS uplift in descending Sentinel-1 data in the 4 years following the 2018 eruption (Figure 2.4), with a corresponding intrusive volume of approximately $1{\times}10^8$ m^3 (Chapter 3). The extreme uplift at Sierra Negra is not just confined to the caldera; the coast on the southern flank of the volcano (near Puerto Villamil) uplifted between 0.5–2 m in the late 20^{th} century (Reynolds et al., 1995), while there was a lateral intrusion on the southeastern flank in June 2010, at depths of 5–11 km (Davidge et al., 2017).

There is high-magnitude deformation on Sierra Negra's flanks, due to contraction of effused lavas, and emplaced sills. Amelung et al. (2000) observe 20 cm of subsidence (1992–1998) due to the contraction of lavas effused on the northern flank of the volcano during the 1979 eruption. Similarly, we observe lava flow subsidence immediately following their emplacement during the 2018 eruption. Using Sentinel-1 InSAR, we observe that lava flows at the northern, more active fissure had subsided by 20 cm (Figure 2.15). Lavas emplaced on upper flank in the 2005 eruption did not appear to subside in the Sentinel-1 era, either because they had cooled fully, or were masked by the uplift of the caldera. Lava flows subside as they cool, due to thermo-elastic contraction (from radiative and convective heat transfer), bubble vesiculation, and pore space compaction

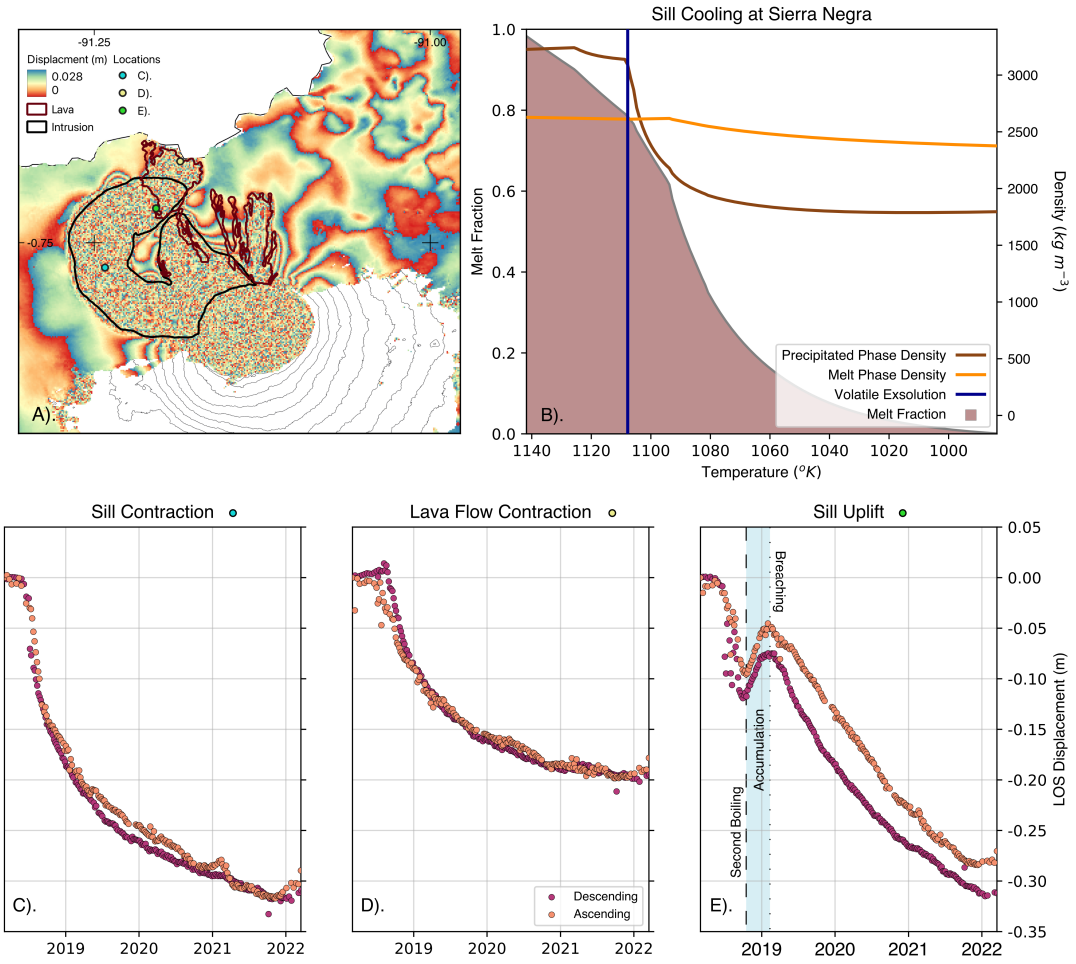

Figure 2.15: Complex post-eruption displacement patterns at Sierra Negra. A). Wrapped cumulative displacement at Sierra Negra from 06/01/2017–30/09/2021, indicated pre- syn-, and post-eruptive deformation. Each fringe corresponds to 2.8 cm of range change. Annotated are the extents of the erupted lava, and intruded sill, as well as the points plotted in individual time series. B). Results of MELTS modelling, showing the change in density of the precipitated, and liquid phases with melt fraction, as well as the point at which volatile exsolution begins (1107 ^{o} K). C). Subsidence due to the cooling and crystallisation of laterally intruded sill. D). Time series of lava flow subsidence at flows derived from the distal fissures. E). Localised area of uplift, towards the terminus of the sill, occurring after the eruption had ceased. This figure shows subsidence due to both contraction of lava flows, and of the sub-volcanic sill. The lava flow subsidence dues not exceed 20 cm, while contraction of the sill, in both time series, is approximately 30 cm.

(Chaussard, 2016; Patrick, 2004).

The lateral sill (Davis et al., 2021) subsided by 30 cm, exceeding that of the lava flow (Figure 2.15). This is most likely due to the cooling, crystallisation, and degassing of the intruded magma. Similar to lava flow subsidence, post-instrusive subsidence is observed as a magma cools and crystallises. The formation of denser-than-melt crystals raises the relative density of the melt, thereby, if no more magma is intruded, decreasing the

volume of the intrusion (e.g. Okmok, USA (Caricchi et al., 2014)). Volatile exsolution during second boiling may alter the rates at which this contraction occurs, and in instances of low magma permeability may actually result in inflation (e.g. Long Valley, USA (Hildreth, 2017)). The subsidence patterns presented in Figure 2.15C is consistent with magma crystallisation (steady long-term subsidence, with the same magnitude in both look directions due to uniform sill contraction). However, an area toward the terminus of the intrusion uplifted by $>$ 5 cm at the end of 2018 (Figure 2.15E), inconsistent with crystallisation. We suggest that this uplift may have been caused by second boiling as exsolved bubbles concentrated at the end of the sill, before escaping in 2019, allowing subsidence to resume. Using MELTS phase equilibria software (Gualda et al., 2012; Ghiorso and Gualda, 2015), we model the change in phase densities within this sill, using a basaltic starting composition with 1 wt% H_2O (after Aiuppa et al. (2022)) (See Section 2.3). We find that second boiling would have occurred in this sill (at 1 km depth) at 1107 ^{o} K, after the intrusion had cooled 35 ^{o} K from liquidus. Once exsolved, these volatiles cause ground deformation analogous to that in a hydrothermal system, where they accumulate in a lens and pressurise, before a critical threshold is met and the lens breaches, causing subsidence (Fournier, 1999). At Fisher, USA, long-term subsidence is attributed to magmatic fluid loss, though an unsealed breach in the hydrothermal system (Lu and Dzurisin, 2014). As such, we suggest that the period of uplift observed at the end of terminus of the lateral sill at Sierra Negra was caused by volatile exsolution, accumulation, and breaching during second boiling.

2.4.6 Inter-Eruptive Flux at Wolf

Table 2.1: Volumes for best fitting sources at Wolf, either sill (S) or Dike (D). In the Expanded ΔV column, the modelled volume has been (96% of inter-eruptive time) has been expanded to estimate the total volume flux over the total eruptive period, assuming a constant intrusion rate. The Volume Fraction column is a measure of how much of the erupted lava is accounted for.

Source	Length (m)	Width (m)	Opening (m)	Depth (m)	Observed ΔV (m^3)	Expanded ΔV (m^3)	Percent. of Erupted Lava	DRE Fraction
S	170	4171	8.8	2600	6.1×10^6	6.4×10^6	27%	36%
D	1454	7748	0.94	1482	1.1×10^7	1.1×10^7	47%	62%
S–S	3508	2189	0.43	1545	1.1×10^7	1.1×10^7	47%	63%
	250	4432	8.3	5295				

We use Sentinel-1 data to observe subsidence of lava flows erupted during the 2015 eruption of Wolf volcano (Figure 2.16). This subsidence is of the same magnitude in both the ascending and descending track directions, consistent with the vertical contraction of lava. We model the subsidence due to thermo-elastic lava flow contraction, using

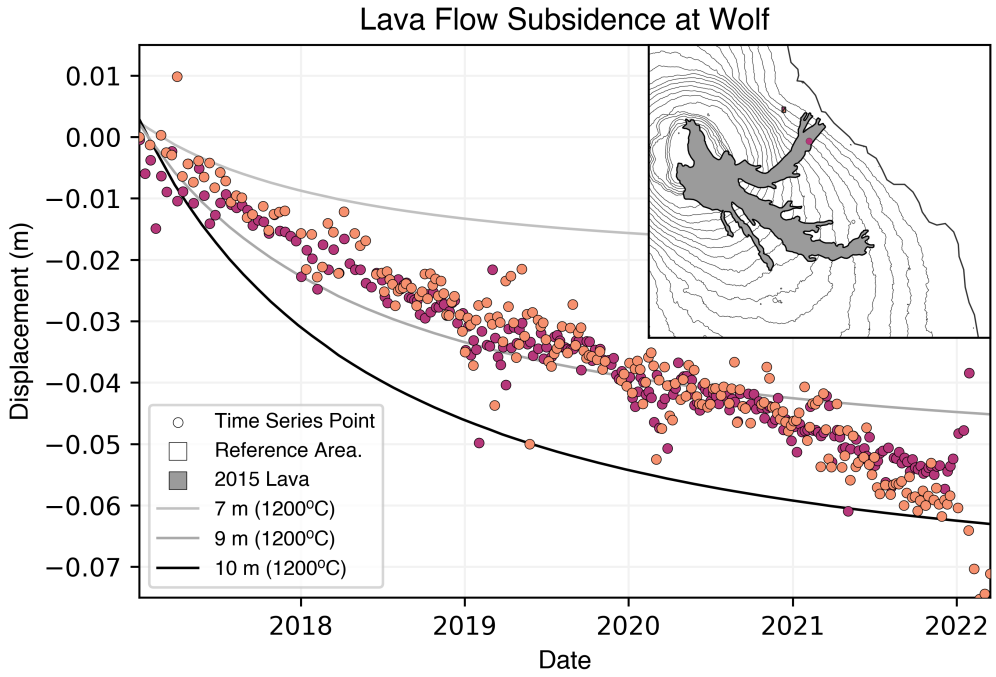

Figure 2.16: Subsidence at Wolf volcano due to contraction of 2015 lava flows. The track directions are annotated in the legend. The point used in the time series is located at 0.0276° N, and -91.279° E. This subsidence is relative to a reference area between 0.044— 0.047° N, and -91.294– -91.292° E. The grey lines indicate subsidence due to thermo-elastic contraction of emplaced lavas of various thicknesses.

the methodology outlined in Section 2.3.3, finding that for a lava emplaced at 1200°C, initial thicknesses of 9–10 m is required to account for the observed subsidence rates. These thicknesses are greater than those measured by Bernard et al. (2019), who find an average thickness of 3.4±1.4 for the flank lavas, with thicknesses of >6.5 m for the lobes closest to our measured point. This, along with higher rate subsidence than expected from thermo-elastic modelling alone, suggests that the cause of subsidence is not solely thermo-elastic, and there is likely contribution from bubble vesiculation and pore space compaction, as well as from latent heat release (Chaussard, 2016; Patrick, 2004).

Wolf had been steadily uplifting since its 2015 eruption, between May–July 2015 (Figure 2.4). There are some Sentinel-1 acquisitions around the eruption (Xu et al., 2016) though continuous monitoring did not begin until 14/11/2015. This monitoring was exclusively in the descending direction until 06/01/2017, when ascending became available. In total, there is data in the descending direction for 96% of the inter-eruptive period. Using this data, we model the intrusive flux into Wolf for cumulative displacement from 14/11/2015 until 24/12/2021, just prior to the 2022 eruption. The results of the best fitting sill, sill–sill combination, and dike, are presented in Table 2.1, and Tables A21–A23, while their data, model and residuals are in Figure 2.17. The

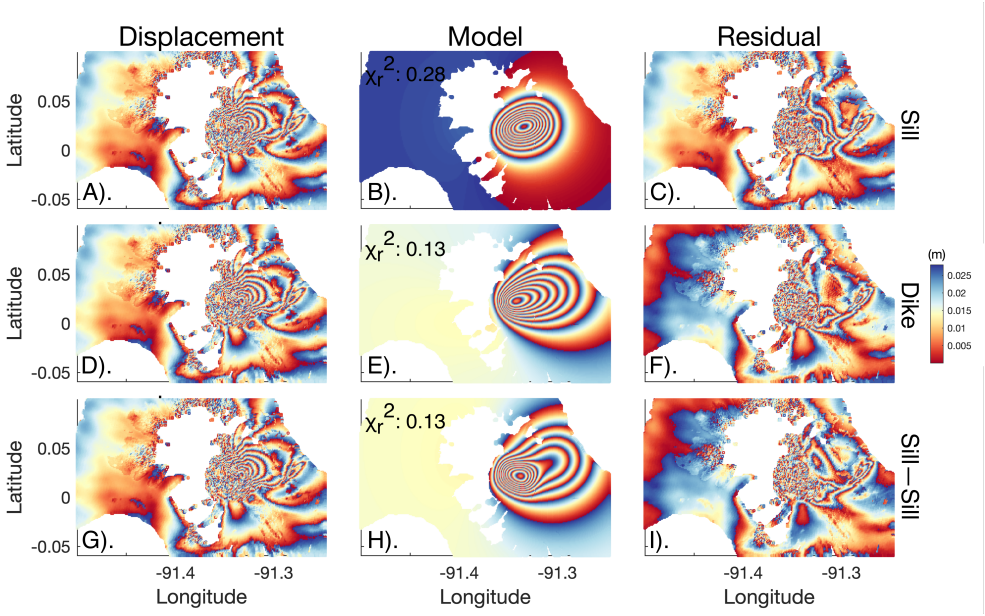

Figure 2.17: Best-fit geometries for source inflation at Wolf from 14/11/2015–24/12/2021, just prior to its 2022 eruption. Each fringe corresponds to 2.8 cm of LOS displacement, in the descending track direction. A–I). Data, model, and residual, for the best fitting sill, dike, and sill-sill geometries.

sill-sill, and dike models fit the data better than single sill, with reduced χ^2 values of 0.13, 0.13, and 0.28, respectively.

These estimates show that, depending on geometry, the inter-eruptive intrusive flux only accounts for between a quarter to a half of the lava that was erupted during Wolf's 2022 eruption. There are several potential explanations for this: (a) Vesiculation and bubble nucleation resulted in lava of much higher volume than the magma reservoir (which is assumed to be incompressible during modelling). For lavas at Fernandina and Sierra Negra, Vasconez et al. (2018) find that DRE volumes are approximately 25% smaller than those of the erupted magmas. When comparing magma influx to a DRE of 25% less than the erupted lavas, we still find that between one and two thirds of the lava is unaccounted for. (b) We assume a constant influx rate from the end of the 2015 eruption to the onset of the 2022 eruption, to account for the period until regular InSAR monitoring began (4% of the total time). Perhaps the influx rate was much higher during this time, and can account for the missing one–two thirds, though we consider this implausible. (c) The missing lava was intruded during the three months of the eruption, rapidly flushing through the subvolcanic system before erupting, as suggested by Stock et al. (2020).

2.5 Discussion

Here, we use our new post-2015 observations as well as historical deformation measurements to summarise the insights that InSAR provides into sub-volcanic structures at Alcedo, Cerro Azul, Darwin, Fernandina, Sierra Negra, and Wolf. We focus on the evidence for either change or endurance of geodetic sources over the past 30 years and discuss the persistence of characteristics in deformation and eruption at different volcanoes in the context of the magma flux into the Western Galápagos and connectivity at the level of melt supply.

2.5.1 Sub-Volcanic Structure of the Western Galápagos:

Alcedo

Deformation patterns at Alcedo are complex, but have been consistently attributed to either inflation (2007–2011) or deflation (2017–2022) of geodetic sources located between 2–3 km depth (point, sill, CDM, and pipe-like sources (e.g. Galetto et al. (2019) in Table A3), indicative of an established reservoir at this depth. Modelling deformation at Alcedo has generally required either contribution from an intra-caldera fault (Bagnardi, 2014; Galetto et al., 2019), or an extreme geometry (Hooper et al., 2007). Faulting seems to dominate displacements during periods of magmatic influx, and may act as a conduit for magma-derived fluids to reach the surface fumarole field. In Section 2.4.1, we observe hydrothermally-driven subsidence at this fumarole field, which overprinted the subsidence due to the cooling of a sill from 2017–2022.

Cerro Azul

Cerro Azul is underlain by a magmatic reservoir consistently located at approximately 5–6 km depth (Tables A4–A5), as detected during the 2008 eruption (Galetto et al., 2020), 2017 unrest (Guo et al., 2019), as well as by our modelling from 2017–2021 (Figure 2.9). This reservoir acts as a source from which fissures extend during unrest/eruptions. We propose that there is an established pathway from this sill to the east of the volcano — each of the 1998, 2008, and 2017 unrest episodes were located in this part of the volcano. That the 1998 eruption was initially mixed with magma from the 1979 eruption (Teasdale et al., 2005) suggests that this pathway may have been important since at least 1979. Eruptions have been confined to the eastern Flank for at least 60 years since the 1959 event. However, hazards are also present on other flanks, with features in the Sentinel-1 deformation field that may capture mass wasting on the western flank, towards Caleta Iguana.

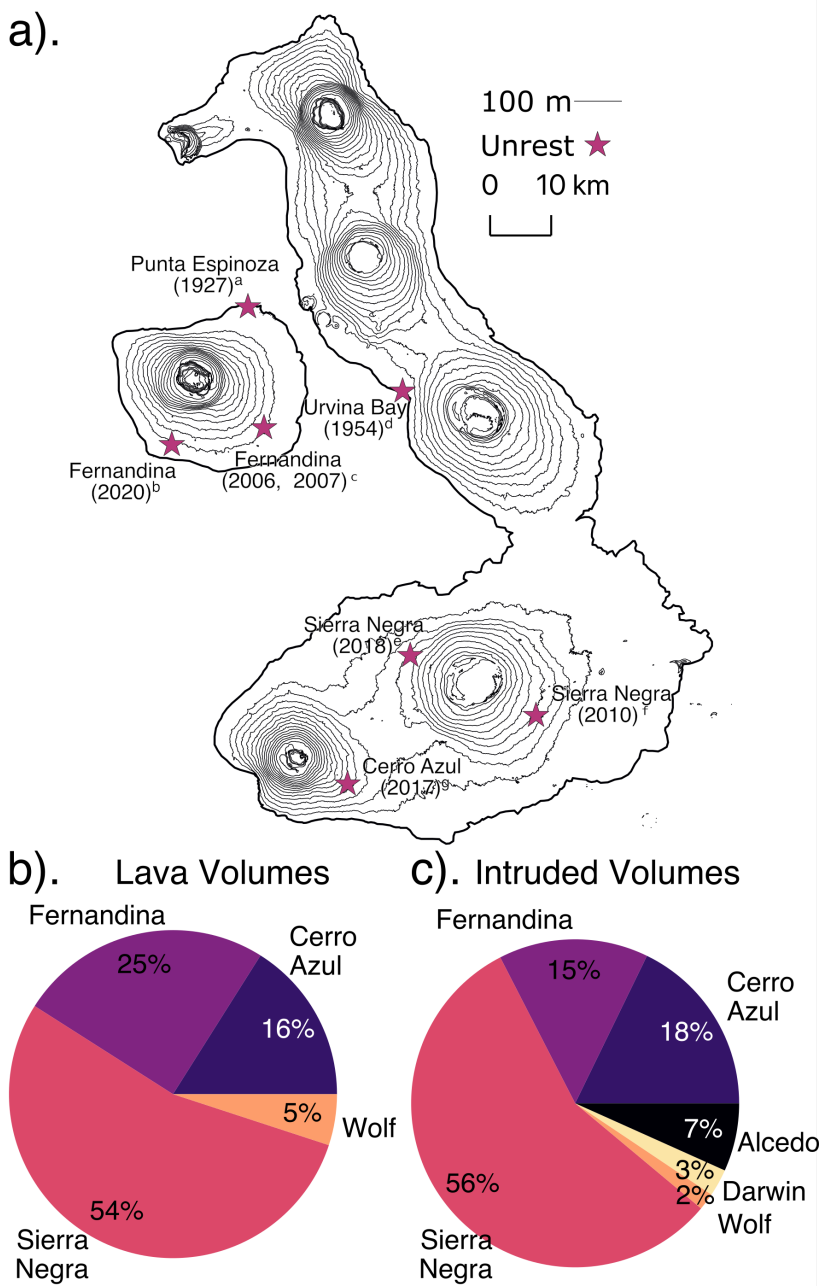

Figure 2.18: Summary of lateral intrusion and magma flux in the Western Galápagos. a). Map of major lateral intrusions, from the following studies: [a] Cullen et al. (1987), [b] Section 2.4.4, [c] Bagnardi and Amelung (2012), [d] Nusbaum et al. (1991), [e] Davis et al. (2021), [f] Davidge et al. (2017), [g] Guo et al. (2019). b). Pie chart of cumulative effused lava volumes from 1995–2025, as presented in Table A2. c). Pie chart of cumulative intrusive volumes from 2000–2010 (Bagnardi, 2014), and 2017–2022 (Chapter 3).

Darwin

Though Darwin is extrusively quiescent, there is clearly active magma supply to the volcano (e.g. Bagnardi (2014)), and it undergoes periodic uplift (e.g. Amelung et al. (2000), Figure 2.10). Both this study and the few previous deformation studies at

Darwin find a geodetic source at around 3 km depth beneath the volcano, with lower depth estimates of 2.7 km, and higher estimates of 4.25 km (Table A6). Why then, despite active magma supply, does Darwin erupt so infrequently? It is possible that the supplied volumes are either insufficient or irregular enough to cause an eruption. However, it is also possible that due to its current quiescence, historic eruptions have not been identified. There is some historic evidence of lateral intrusions near Darwin: Urvina Bay "catastrophically uplifted" by 6 m in 1954, exposing 1.4 km^2 of coral reef

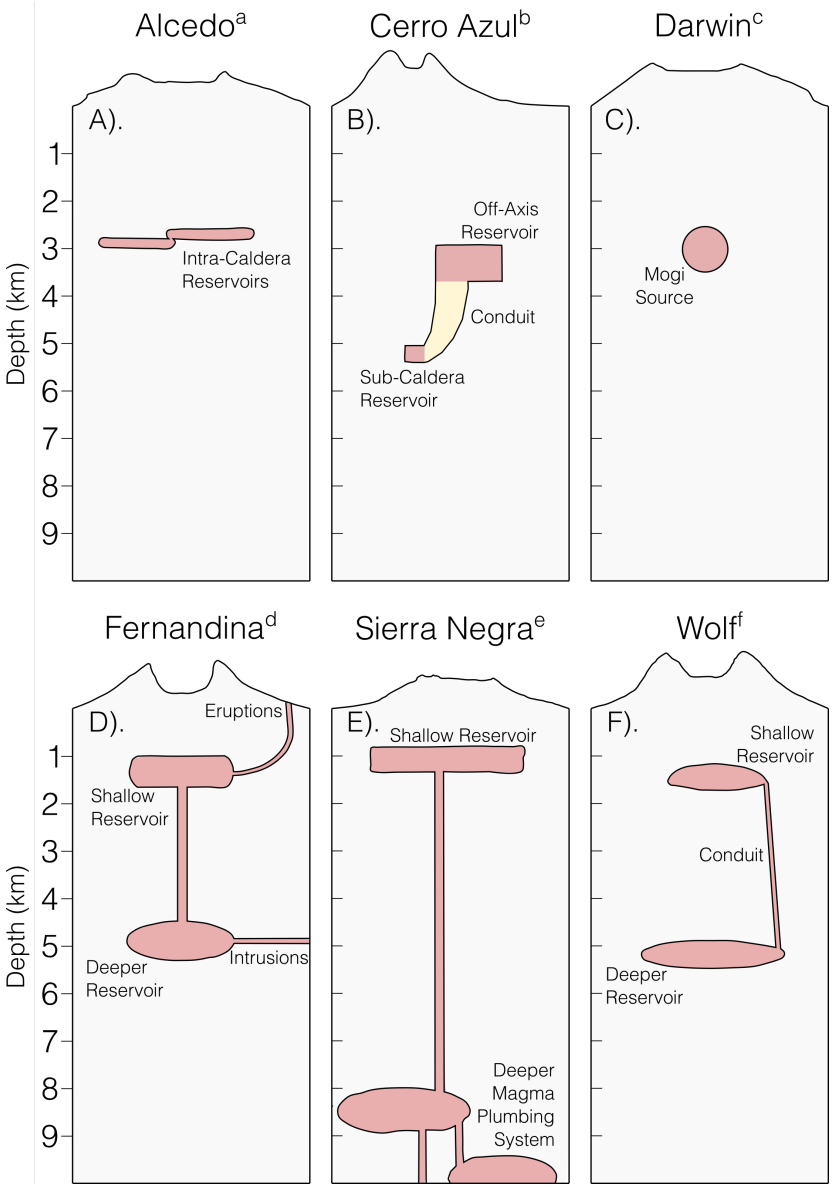

Figure 2.19: Schematic diagrams illustrating the proposed sub-volcanic structure at each volcano. Panels A–F). refer to each of Alcedo, Cerro Azul, Darwin, Fernandina, Sierra Negra, and Wolf, respectively. The studies from which these schematics are modified from are as follows: [a] Galetto et al. (2019)), [b] Galetto et al. (2020), [c] Amelung et al. (2000), [d] Bagnardi and Amelung (2012), [e] Bell et al. (2021b), [f] Xu et al. (2016).

(Nusbaum et al., 1991) (Figure 2.18). The magmatic source of the this uplift is unclear; Urvina Bay is closer to Alcedo than Darwin, but uplift there revealed Darwin-derived basalts, though McBirney et al. (1985) hint that it may be related to a 1954 lava flow at Alcedo.

Though there is so far no geodetic evidence of stacked reservoirs at either Darwin or Alcedo, the 1954 uplift at Urvina Bay suggests that a deeper reservoir may be underlying the shallow one at either volcano. At Fernandina in 2006 and 2007, and Sierra Negra in 2010, the lateral intrusion was sourced from the deeper magmatic system, (Figure 2.18) while the 2017 intrusion at Cerro Azul was intruded from a reservoir at 5–6 km below sea level (Bagnardi and Amelung, 2012; Davidge et al., 2017; Guo et al., 2019).

Fernandina

Fernandina is the most active volcano in the Galápagos, and overlies stacked reservoirs at between 1 km and 5 km depth. These reservoirs drive the near constant ground deformation at Fernandina (Amelung et al., 2000; Baker, 2012; Bagnardi, 2014; Bagnardi et al., 2013; Chadwick et al., 2011; Chandni and Kumar, 2020; Geist et al., 2006a; Jónsson et al., 1999; Pepe et al., 2017), and are particularly evident during eruptions (2005, 2009, 2017, and 2018 (Bagnardi and Amelung, 2012; Galetto et al., 2023)). The shallower of these reservoirs acts as a source for fissure eruptions, while the deeper acts as a source for lateral intrusions. These have been detected at Fernandina, in December 2006, and August 2007 (Bagnardi and Amelung, 2012); likewise, Punta Espinoza, on the NW flank of Fernandina uplifted in 1927 (Figure 2.18), during which a fishing boat was stranded as the ground uplifted by "several feet", and was accompanied by "violent bubbling" of seawater (Cullen et al., 1987). We also observe lateral magma migration during the 2020 eruption of Fernandina. In terms of erupted volume, this was the smallest eruption to have occurred at Fernandina between 1992–2023. However, it was accompanied by major ground deformation, the westward migration of magma, and the opening of a sill off the southwest coast. We speculate that these may have resulted in an offshore eruption into the volcanoes submarine rift zones and lava fields.

Sierra Negra

Like Fernandina and Wolf, Sierra Negra has a stacked magmatic system between, 2 km and 8 km depth (Bell et al., 2021b; Tepp et al., 2014). Extreme uplift at Sierra Negra is driven by magma accumulation in the shallow reservoir, at rates of between 1.06×10^7 m^3 yr^{-1} (Bagnardi, 2014) and 1.3×10^7 m^3 yr^{-1} (Aiuppa et al., 2022). Interaction between this reservoir and the trapdoor fault characterise volcanism here, causing asymmetric deformation patterns, controlling eruption location, and facilitating the vigorous hydrothermal system. The cooling and crystallisation of lateral intrusions (Figure 2.18), and lava flow contraction drives subsidence at the sites of recent eruption. We

observe uplift at the terminus of the lateral intrusion that occurred during the 2018 eruption of Sierra Negra, and suggest that it was caused by second-boiling — this mechanism accounts for the delay in uplift, as magma saturated with volatiles, and the location of uplift as volatiles ascended upslope to the terminus of the sill.

Wolf

Like Fernandina, Wolf overlies stacked reservoirs at approximately 1 km depth (Stock et al., 2018; Xu et al., 2016; De Novellis et al., 2017), and at 5–6 km depth (Stock et al., 2018; Xu et al., 2016) through which magma flushes through during eruptions. Between its 2015 and 2022 eruptions, Wolf is one of the few volcanoes where the entire inter-eruptive cycle was observed. We find that this inter-eruptive inflation is also best-fit by stacked sills at 1.5 and 5.2 km depths. The style of eruptive fissure alternates between eruptions, and we suggest that like Fernandina, the preceding eruption alters the static stress field for the next. As at Cerro Azul, all recent unrest at Wolf has been concentrated on its southeastern flank, though it is unclear how long this pathway has been dominant (no evidence of mixing with historic eruptions as at Cerro Azul). At Wolf, there is little geodetic evidence that the deeper reservoir acts as a source for lateral intrusions, as at Fernandina, though Wolf's remote location and lack of ground-based monitoring may mean that such intrusions have not been detected — the presence of offshore rift zones (Geist et al., 2006b) supports lateral magma migration from Wolf.

2.5.2 Rapid Magma Flux Through Shallow Reservoirs

The flux of melt that supplies the Western Galápagos volcanoes, and to a lesser extent the partitioning of intrusive flux to shallow reservoirs, varies through time (Chapter 3). We compare estimates of intrusive volume change detectable using InSAR, between 2000–2010 (Bagnardi, 2014) and 2017–2022 (Chapter 3). The primary change between these two eras is the decreased melt supply at Alcedo which accounted for 10% of total shallow intrusive flux from 2000–2010 (spanning its resurgence), but subsided between 2017–2022. Comparing total percentages of intrusive volume fluxes to estimates of extruded lava from 1995–2022 (Figure 2.2), we see that the proportion of erupted to intruded lavas is consistent, between Sierra Negra (54%:56%), Cerro Azul (16%:18%), and Wolf (5%:2%) (Figure 2.18). Volcanoes with higher intrusive fluxes also erupted higher volumes of lava, for example, Sierra Negra accounts for more than half of the magma accumulated, and lava erupted, in the Western Galápagos (Figure 2.18). That the ratios of erupted and intruded volumes are similar also agrees with the hypothesis that long-term magma storage in the crust is uncommon, but rather magma rapidly cycles through sub-volcanic systems.

Stock et al. (2020) demonstrated that during eruptions at both Wolf and Fernandina, primitive basalts flush through the sub-volcanic system at the erupting volcano,

overwhelming stored evolved magmas. As a result, these primitive basalts account for the majority of erupted material (> 90 %), at either volcano. This is consistent with the geodetic evidence that at Wolf, magma flux into the shallow reservoir is the lowest of any of the major Western Galápagos volcano (Bagnardi, 2014). In Section 2.4.6, we compare these petrological observations to Sentinel-1 data — there is near complete coverage of inter-eruptive inflation at Wolf from 2015–2022, allowing cumulative intruded magma volumes to be estimated. We find that regardless of source geometry, erupted volumes exceed intruded volumes by almost double. This "missing" intruded volume has been observed at many other volcanoes and attributed variously to data gaps and compressibility of the magma and reservoir (Kilbride et al., 2016). In the Galápagos, this observation, alongside the absence of a significant pre-eruptive uptick in inflation, adds to evidence for magma flushing consistent with the observations of Stock et al. (2020).

2.5.3 Classifying Western Galápagos Volcanoes

The volcanoes of the Western Galápagos have previously been classified as "Juvenile", "Mature", or "Dying", based on the range of the magnesium number of erupted lavas (monotonous or diverse), giving an estimate of magma reservoir temperature, and sub-volcanic structure (Figure 2.20) (Geist et al., 2014; Harpp and Geist, 2018). This classification generally reflects the age of the Western Galápagos volcanoes, as they move eastwards over the Galápagos plume. The youngest, Cerro Azul, is juvenile, it's basalts are simultaneously the most primitive and diverse in the Western Galápagos (Harpp and Geist, 2018). The majority of magma storage occurs at around 5 km depth, as the increasing magma supply constructs the sub-volcanic system (Geist et al., 2014; Harpp and Geist, 2018). Once the magmatic system is established, volcanoes become mature (Fernandina, Darwin, and Wolf), maintaining reservoir temperatures of approximately 1150^{o}C for thousands of years (Figure 2.20). Finally, as the older volcanoes are carried away from the plume, magma supply wanes, and cooler more diverse lavas erupt at dying volcanoes (Alcedo and Sierra Negra) (Figure 2.20). This waning supply means that the system is no longer in a thermal steady-state, and erupts cooler magmas, of less that 1050 ^{o}C.

This classification reflect an evolutionary model that Western Galápagos volcanoes follow across their lifetime. Fernandina is approximately 32,000 years old (Kurz et al., 2014), and has been the subject of geodetic studies for approximately 30 years, or < 0.1 % of its age. As such, interpreting displacements in the context of their evolutionary classification is unhelpful, since the character of activity since geodetic measurements began is ephemeral, compared to the lifespan of the volcano. For example, Sierra Negra is classified as dying from lava Mg numbers, yet it was supplied the most magma (54% of the total magma supply) of any Galápagos volcano between 1992–2010,

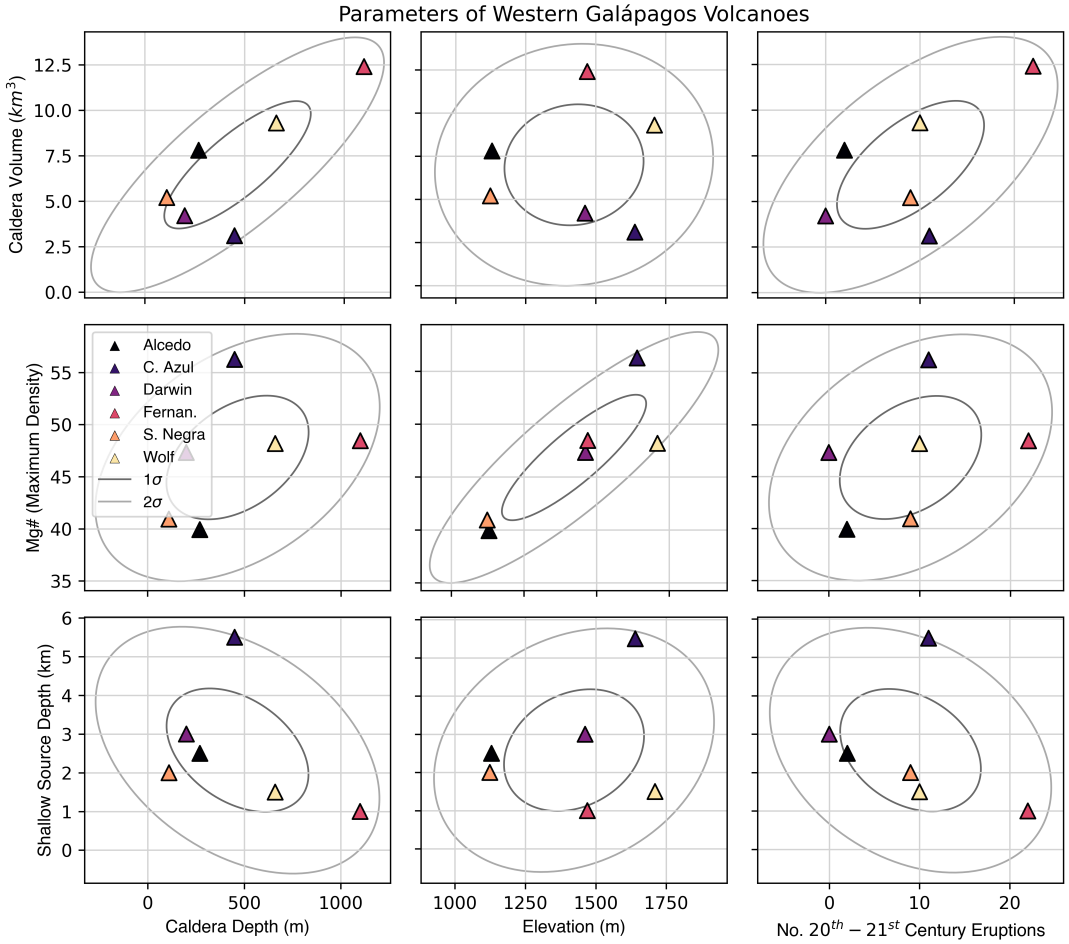

Figure 2.20: Characteristic parameters of Western Galápagos volcanoes. In each plot, a set of key parameters are plotted against one another, from caldera volume, magnesium number, shallow source depth, caldera depth, elevation, and the number of eruptions since the 20^{th} century. The ellipses represent the confidence ellipses for the first and second standard deviations of each dataset.

and 2017–2022. Structurally, the caldera at Darwin ("Mature") better resembles Alcedo and Sierra Negra ("Dying"), with their shallow calderas (Figure 2.18), than the deep calderas of Fernandina, or Wolf ("Mature"), which are similar to Cerro Azuls ("Juvenile") (Figure 2.5 and Figure 2.20). While Fernandina and Wolf erupt through a similar mechanism (Stock et al., 2020), Sierra Negra and Alcedo (both "Dying") deform very differently, the former with spectacular long-term uplift, and the latter with sustained subsidence as the sub-volcanic sill crystallises. Similarly, Fernandina ("Mature") erupted three times between 2010–2022 (2017, 2018, 2020), while Darwin (also "Mature") last erupted in 1813 (Venzke, 2023) (Figure 2.20). Magmatic system maturity, as estimated using Mg numbers, does not bear a clear relationship to either eruption rate or shallow intrusive magma flux over the past three decades.

We therefore suggest the following groupings of Galápagos volcanoes may be more

appropriate for planning monitoring campaigns and analysing current activity.

Basaltic Flushing Through Stacked Reservoirs: Fernandina–Wolf

Fernandina and Wolf are presently in an extrusively active phase, with eruptions in 2017, 2018, and 2020, as well as 2015, and 2022, respectively. These eruptions alternate between radial and circumferential (Bagnardi et al., 2013), from stacked reservoirs at approximately 1 km and 5 km (e.g. Bagnardi and Amelung (2012) and Xu et al. (2016)). These volcanoes share steep slopes and deep calderas, and mechanisms of eruption, in the flushing of primitive basalts through the sub-volcanic systems (Stock et al., 2020) (Figure 2.18 and Figure 2.19).

Episodic Quiescence and Resurgence: Alcedo–Darwin

Both of these volcanoes maintain shallow magma reservoirs between 2–3 km depth (Figure 2.19). Significant unrest is uncommon at either volcano, though both periodically resurge (Figure 2.10, Galetto et al. (2019)). Eruptions are also rare — Darwin last erupted in 1813 (Venzke, 2023), and Alcedo in 1993, though the 1993 eruption was a phreatic explosion, rather than an effusive eruption typical of Western Galápagos volcanoes. They also have shallow, broad calderas, distinct from Cerro Azul, Fernandina, and Wolf.

Exceptional Magma Flux: Sierra Negra

The extreme uplift and intrusive flux at Sierra makes it unique globally. Like Fernandina and Wolf it has stacked reservoirs, has experienced sustained long-term uplift like Wolf, as well as sustained subsidence (between 2000–2004) like Alcedo. The shape of Sierra Negra volcano is similar to Alcedo, and Darwin (Figure 2.19), though it is likewise distinct from these volcanoes due to its extreme uplift.

Juvenile Magmatic System: Cerro Azul

Cerro Azul does not have stacked reservoirs, is more active than Darwin and Alcedo, and maintains a deeper reservoir (6 km), and smaller caldera than any other Western Galápagos volcano. Cerro Azul has a similar shape to Fernandina and Wolf, though the differences in its eruptive style, and sub-volcanic architecture distinguish it.

2.6 Conclusions

The Western Galápagos islands of Fernandina and Isabela are striking in the diversity of volcanism that exists there. By integrating new and historical observations of volcanic unrest we show that a range of volcanic displacement patterns are controlled by the varying magma dynamics between volcanoes. We synthesise published literature, and present new InSAR interpretations for each volcano. Alcedo has two discrete zones of subsidence, one magmatic and one hydrothermal; Cerro Azul has an established pathway for eruptions an unrest on the eastern flank of the volcano that has existed for at least 30 years; Darwin has resurged, like Alcedo, but shows no evidence of hydrothermal emissions or subsidence; Fernandina rapidly inflates and deflates more than any other volcano, and may have had a submarine eruption in 2020; Sierra Negra uplifts by extreme magnitudes for sustained periods, and there is evidence of volcanic deformation on its flanks as well as its caldera; Wolf uplifts by low magnitudes for sustained periods, and magma rapidly flushes through there during eruption. We suggest an unrest-based classification for these volcanoes, based on rapid magma flux through stacked reservoirs, periodic resurgence and quiescence, juvenile magmatic systems, and exceptional magma flux.

Chapter 3

Magmatic Connectivity among Six Galápagos Volcanoes Revealed by Satellite Geodesy

Abstract

Shallow magmatic reservoirs that produce measurable volcanic surface deformation are often considered as discrete independent systems. However, petrological analyses of erupted products suggest that these may be the shallowest expression of extensive, heterogeneous magmatic systems, that we show may be interconnected. Here, we analyse new time series of satellite-radar-measured displacements at Western Galápagos volcanoes, from 2017 through 2022, and revisit historical displacements since 1998. We demonstrate that these volcanoes consistently experience correlated displacements during periods of heightened magma supply to the shallow crust. We rule out changes in static stress, shallow hydraulic connections, and artefacts associated with data processing and analysis. We instead propose that episodic surges of magma into an interconnected trans-crustal magmatic system, affect neighbouring volcanoes simultaneously causing correlations in both volcanic uplift and subsidence. While expected to occur globally, such processes are uniquely observable at the dense cluster of Western Galápagos volcanoes, thanks to the high rate of surface displacements and the wealth of geodetic measurements.

3.1 Introduction

Volcanic unrest and eruption may be initiated by processes at the Earth's surface (Albino et al., 2010; Gregg et al., 2018), or by changes in deeper supplies of magma (Poland et al., 2012; Caricchi et al., 2014). At oceanic hotspots, thin crust promotes the frequent

effusive eruption of basaltic lavas, that rapidly flush through crustal magmatic systems (Stock et al., 2020) or accumulate at shallow depths (e.g. <2 km from the surface) (Bell et al., 2021b). This thin oceanic crust facilitates the rapid ascent of magma through multiple trans-crustal pathways, instead of through a few established magmatic storage zones in thicker crust (González et al., 2013). Therefore, oceanic hotspots with multiple sub-aerial volcanoes (Figure 3.1i) are excellent sites to identify and study rapid magma migration through connected magmatic systems. At the Western Galápagos islands of Isabela and Fernandina (Ecuador), there are six active volcanoes atop oceanic crust with a maximum thickness of 18 km (Feighner and Richards, 1994). This high spatial density of volcanoes, alongside the high-magnitude deformation and eruption rates routinely observed there, make the islands an excellent site to understand the relationship between volcanic deformation, magma flux, and the underlying trans-crustal magmatic systems.

The six major volcanic centres of the Western Galápagos (Alcedo, Cerro Azul, Darwin, Fernandina, Sierra Negra, and Wolf (Figure 3.1)) have their magma supplied by the Galápagos plume, and are each separated from their neighbour by lateral distances of only 30–45 km. These volcanoes are underlain by vertically extensive magmatic systems, with discrete levels of magma storage (Harpp and Geist, 2018; Geist et al., 2014). Magma supply through each system varies according to the maturity of the volcano (Harpp and Geist, 2018; Geist et al., 2014). The shallowest magmatic storage zones lie in the upper 4 km of the crust (Bagnardi and Amelung, 2012; Xu et al., 2016; Bell et al., 2021b; Stock et al., 2018), where volume changes produce displacement patterns that are easily measured by satellite radar thanks to high phase coherence (Guo et al., 2019; Bagnardi and Hooper, 2018). Here, we use satellite radar data to produce new time series of volcanic displacements and show that there are correlations between deformation at all six volcanoes during various periods of eruption and quiescence, and that these correlations are especially strong during episodes of elevated magma flux.

Using Interferometric Synthetic Aperture Radar (InSAR), we construct new displacement time series for Isla Fernadina and Isla Isabela from January 2017, until March 2022. These time series (Methods) capture displacements associated with major unrest episodes (e.g. Cerro Azul, 2017) as well as five eruptions (Fernandina in 2017, 2018, and 2020, Sierra Negra, 2018, and Wolf, 2022). There are obvious associations between displacement trends before and after eruptions (Figure 3.1 and Figure B1). For example, Darwin began to subside as Fernandina and Sierra Negra erupted in 2018. After these eruptions, Alcedo switched to uplift at the same time as Sierra Negra resumed inflation. Additionally, Fernandina, Cerro Azul, and Darwin all showed simultaneous changes in displacement direction and rate in mid-2021, approximately 3 months prior to the Wolf 2022 eruption. Cross correlation analysis (Walter et al., 2014) showed that time lag is close to zero (Figure B2) at the temporal resolution of our InSAR

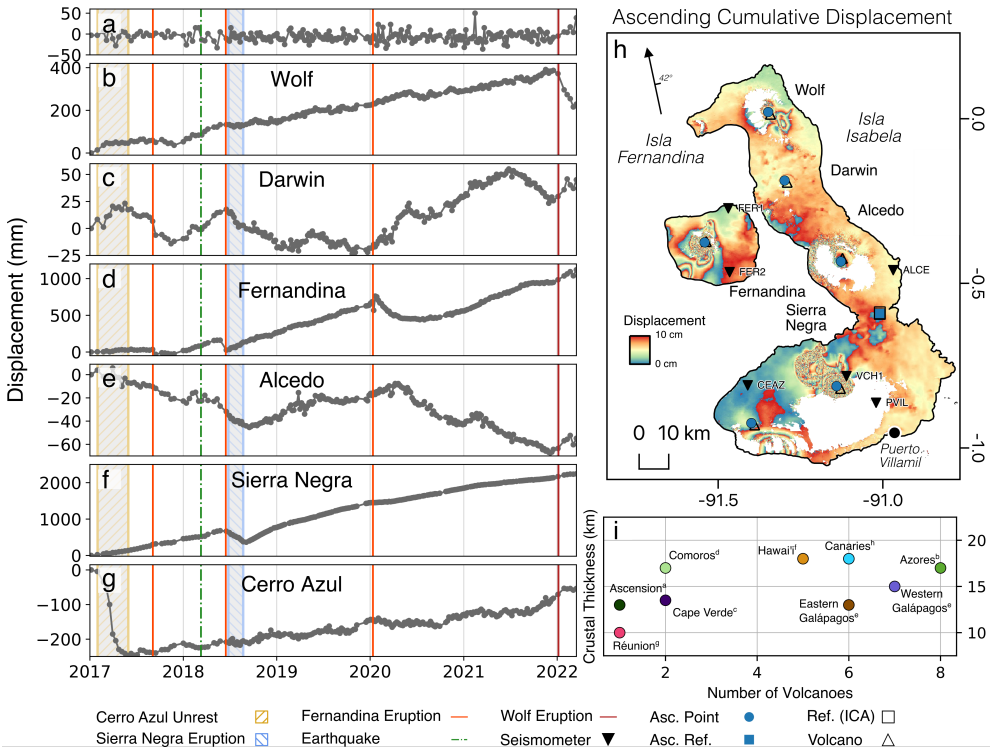

Figure 3.1: Ascending Sentinel-1 cumulative displacement time series for the Western Galápagos, from 06/01/2017–17/03/2022. **a**, Time series of average displacement of the reference pixel (annotated by the blue square in panel h). **b**–**g**, Displacement time series at each of the major volcanoes of the Western Galápagos. Periods of significant unrest, including unrest at Cerro Azul, and eruptions at Fernandina, Sierra Negra, and Wolf are annotated. Displacement values may differ from previous studies due to choice of point plotted. For example, Sierra Negra subsided by a maximum of 8 m during the 2018 eruption (Bell et al., 2021b), resulting in phase-decorrelation in our dataset. Therefore, we plot a point that may not capture this maximum displacement in order to prevent time series gaps. **h**, Wrapped cumulative displacement map of the Western Galápagos, across the entire time series (2017–2022). Each fringe corresponds to 10 cm of displacement in the satellite line-of-sight direction. The arrow shows the satellite heading, as well as the average incidence angle. The annotated points refer to pixels used during correlation analysis, while the reference area is used during Independent Component Analysis (Figure 3.2). **i**, Crustal thickness and number of volcanoes at oceanic hotspots. References for crustal thicknesses are as follows: a (Klingelhöfer et al., 2001), b (Spieker et al., 2018), c (Mata et al., 2017), d (Dofal et al., 2021), e (Feighner and Richards, 1994), f (Furumoto et al., 2013), g (Fontaine et al., 2015),h (Lodge et al., 2012).

observations, implying strong vertical connectivity in magmatic systems, or that any differences in ascent rate to reach the interconnected magmatic zones are short relative to InSAR acquisition spacing. This is consistent with earlier observations of simultaneous unrest at each of Fernandina, Wolf and Alcedo (Figure B3). Fernandina and Alcedo showed changes in surface displacement during a sequence of local earthquakes (each $<$ M5.0) between 2006–2007 (Baker, 2012). During the April 2009 eruption of Fernandina, Alcedo switched from uplift to subsidence (Baker, 2012), while the uplift rate at Wolf slowed. This ended 10 yrs of steady uplift at Wolf (Figure B3). The uplift rate at Fernandina decayed during sudden deflation at Alcedo in May 2010 (Baker, 2012).

Similarly, GPS data show that the rate of inflation at Sierra Negra slowed during the May 2008 eruption of Cerro Azul (Baker, 2012). Some isolated petrological data also hints at magmatic connectivity here, as isotopically similar magmas have erupted at adjacent volcanoes (Geist et al., 1999). However, these similar samples are rare; there is evidence that Galápagos volcanoes have been erupting magmas of distinct compositions for the last 10 Ka, each sampling a distinct part of a geochemically heterogenous plume (Kurz and Geist, 1999).

The increased temporal density of interferometric data provided by the European Spaces Agency's Sentinel-1 satellite relative to previous SAR sensors, allows a more systematic approach to testing the relationships between time series. We use three independent methods to do this (Methods): identification of turning or inflection points in time series (Figure 3.1), calculation of correlation coefficients between time series pairs using temporal Independent Component Analysis (ICA), as a robust test of the statistical independence of signals (Figure 3.2), as well as a rolling windowed approach (Figure 3.3a). In combination, these approaches demonstrate that correlated displacements occur persistently between all pairs of volcanoes in the Western Galápagos, and are not only associated with eruptions (spanning days–weeks) but also episodes of inter-eruptive unrest (weeks–months). This suggests a high degree of complex, inter-magmatic system connectivity in the Western Galápagos.

3.1.1 Shared Displacements in InSAR Time Series

Fernandina, Wolf, Alcedo, Cerro Azul, and Sierra Negra showed correlated displacement multiple times, during several unrest episodes between 2006–2011 (Baker, 2012). We observe similar patterns in the Sentinel-1 time series, particularly before and during the 2018 eruptions of Fernandina and Sierra Negra, and preceding the 2022 eruption of Wolf (Figure 3.1). Figure 3.2 shows independent temporal components, and their weighting, derived for both of these phases of activity. Between 2017–2018, we retrieve an independent component of deformation associated with shared uplift. This component is strongest at Fernandina and Sierra Negra, and also present at Wolf. Similarly, correlation analysis shows that this period had the highest number of strongly correlated time series of the entire study period (57% of possible time series combinations had a correlation coefficient of $>|\ 0.9\ |$) (Figure 3.3a and 3.3b). When applied to time series during the 2022 eruption of Wolf, as well as the preceding year, we retrieve a single independent component that describes deformation at each of Wolf, Fernandina, and Sierra Negra. Correlation analysis shows that this period had the second highest number of strongly correlated time series, with 53% of all possible time series combinations having a correlation coefficient of $>|\ 0.9\ |$. In these two periods, visual inspection of the time series, Independent Component Analysis, and correlation analysis all indicate that Galápagos volcanoes are deforming in a correlated manner. From late 2020 to 2021, Darwin up-

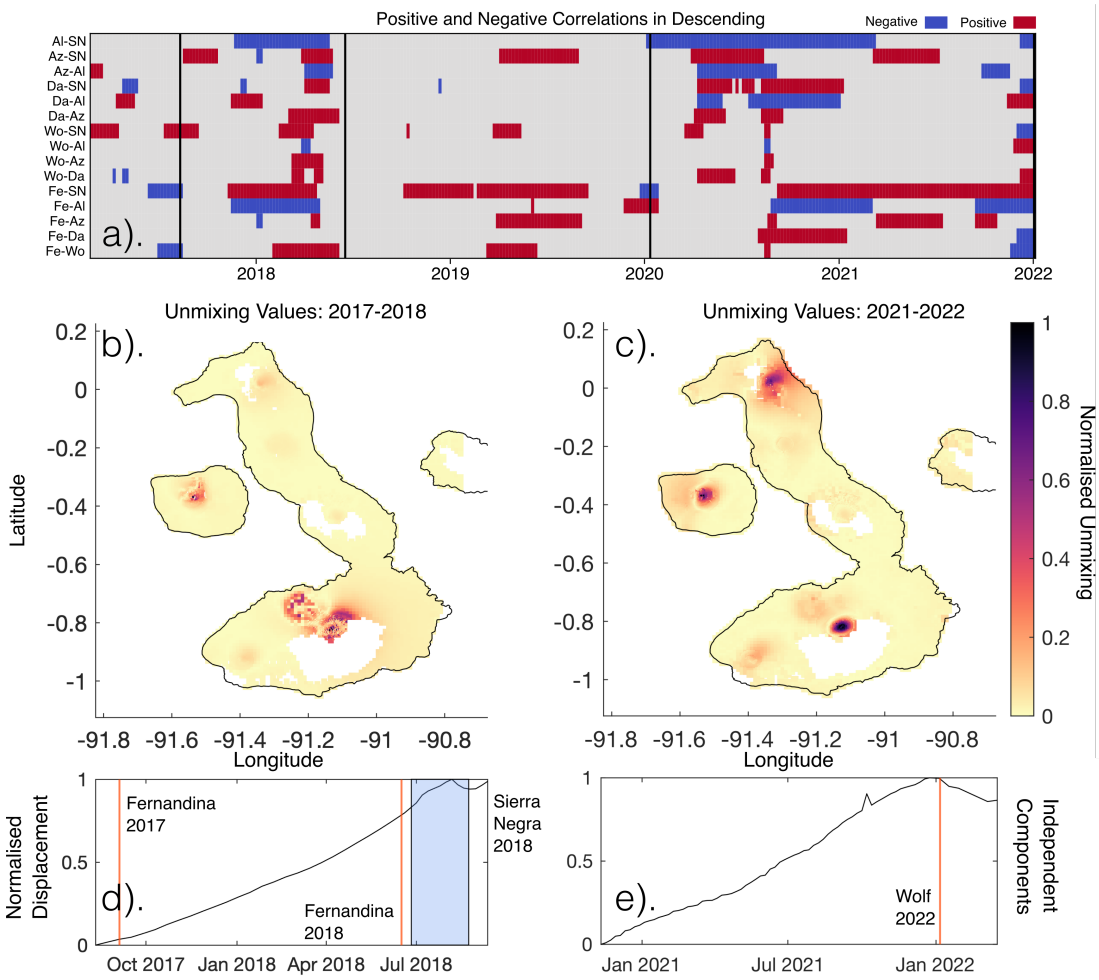

Figure 3.2: Results of Independent Component Analysis, and comparison with correlation analysis, on Descending Data (ICA results in both track directions for all periods can be found in Figure B4, and Figure B5). **a**, Results of Correlation Analysis for each pair of volcano time series, in descending track direction. Grid color indicates if the correlation is positive (red), or negative (blue), and >| 0.9 |. **b**, Spatially reconstructed unmixing values for the corresponding independent component (panel d), for the Fernandina eruptions in 2017, 2018, and the Sierra Negra eruption in 2018, from 11/08/2017–17/09/2018. The color indicates the relative strength of the unmixing value. **c**, Spatially reconstructed unmixing values for the corresponding independent component (panel e), prior to the 2022 eruption of Wolf, from 11/11/2020–30/03/2022. **d**, Independent component corresponding to the unmixing values in panel b. Displacement is normalised on the y-axis. **e**, Independent component corresponding to the unmixing values in panel c. Note that the independent component does not necessarily mirror the shape of the original time series. For example, the contribution of the independent component shown in e) results in rate changes at Wolf, Sierra Negra, Fernandina and Cerro Azul (Figure B1.)

lifted, as Alcedo began to subside. Though we do not clearly retrieve an independent component for this event (Figures B4, and B5), we find that 43% of possible time series combinations show strongly correlated deformation, the third highest number of the study period. These periods have the highest number of strong correlations of the en-

tire time series, showing clear changes in displacement behaviour at multiple volcanoes, with two of them showing shared independent components between multiple volcanoes. Most of the correlations between pairs of displacement time series are positive (Figure 3.3a and Figure B10), indicating that volcanoes were deforming in the same direction. We use a change point algorithm and assume a Poisson distribution for the number of rate changes, to estimate the probability of two volcanoes with random rate changes having correlated turning points. We identify an average of 4 change points in each volcanic deformation time series (Figures B7, B8), and find the probability of just two volcanoes randomly experiencing a major change in deformation rate in the same month to be 0.21%, and even lower for correlated changes at > 2 volcanoes. Similarly, using eruption rates since the early 20^{th} century, we find that the probability of Fernandina and Sierra Negra erupting in the same 6 month period (as occurred in 2005, and 2018) would be 0.3%, if eruptions were randomly spaced in time. Therefore, we conclude that Galápagos volcanoes routinely deform, and even erupt, in a correlated manner.

While coupled volcanic unrest has been reported globally (Biggs et al., 2016; Brothelande et al., 2018; Hildreth, 1991; Ji et al., 2018), quantitative proof of relationships between markers of unrest, such as displacements, are rare (Walter et al., 2014; Poland et al., 2012; Baker, 2012) and were previously limited by scarcity of ground-based infrastructure, and the lower temporal resolution of satellite geodetic measurements (e.g. ERS-1/2, Envisat, and ALOS-1 had repeat times varying from 35 to 46 days, while Sentinel-1 has a repeat time of six days when in a two satellite constellation). Observations from the Galápagos are unique in that they demonstrate temporally consistent correlated displacements due to changes in shallow magmatic system pressures over multiple decades (as determined by semi-continuous space geodetic coverage between 2006–2011, and 2017–2022), including during inter-eruptive periods. We rule out the possibility that the correlations in our time series are InSAR measurement artefacts by systematically testing the impact of reference pixel selection (Figure 3.1a, Figure B6). We also test the impact of island-wide atmospheric phase contributions by making corrections from weather models, and assessing the seasonality of our time series (Methods).

3.1.2 Interpreting Correlated Deformation

Observations of correlated deformation and eruptions at other volcanic centres have been attributed variously to the impact of tectonic or magmatic static stress changes (Pritchard et al., 2013; Takada and Fukushima, 2013; Przeor et al., 2022), hydraulic magmatic connections between volcanic systems (Ji et al., 2018; Hildreth, 1991; Walter et al., 2014), or pore-pressure diffusion (Gonnermann et al., 2012). No recorded earthquakes or magmatic intrusions that occurred during our observation period were sufficient to cause such persistent correlations in displacement. A seismic station on

Sierra Negra's caldera rim (VCH1) recorded no earthquakes greater than magnitude 5.4 between 2012 and 2022, with the largest events due to slip along intra-caldera faults preceding and during eruptions (Bell et al., 2021a; Bell et al., 2021c). Among all eruptions that occurred during this study, the largest was the 2018 eruption at Sierra Negra (Figure 3.3c). The erupted volume here was $147 \pm 71 \times 10^6$ m^3 DRE (at least 14 times more than that of the 2017 eruption of Fernandina ($9.7 \pm 4.9 \times 10^6$ m^3 DRE) (Vasconez et al., 2018)). However, even the pressure drop caused by this eruption only produced significant dilational strain (e.g. $> 4 \times 10^{-5}$) within 10 km of the volcano (Figure B9), and therefore not sufficient to explain correlated deformation seen at Fernandina and Wolf. This leaves the possibility that dynamic stress changes from a magmatic intrusion at a location unobservable from InSAR or the existing seismic network (Figure 3.1) (e.g., below the seafloor between Isabela and Fernandina) could cause similar changes in shallow reservoirs. However, the lack of a simple spatial relationship between the locations where correlated deformation occurs (Figure 3.2), and the switching between episodes of positive and negative correlation (Figure 3.3a and 3.3b), are inconsistent with such a mechanism.

There is also no evidence for extensive, persistent shallow hydraulic connections between Western Galápagos volcanoes. Vertical magma migration in the shallow crust occurs during both unrest and eruption (Bagnardi and Amelung, 2012), and is more consistent with distinct stacked sub-volcanic systems than lateral magma movements. Shallow reservoirs at < 4 km, lie above deeper storage zones at > 5 km (Geist et al., 2014) at Fernandina (Chadwick et al., 2011; Bagnardi and Amelung, 2012; Stock et al., 2020; Geist et al., 2014), Sierra Negra (Bell et al., 2021b) and Wolf (Stock et al., 2020; Stock et al., 2018; Geist et al., 2014). The lateral migration of magma through shallow sills is a common phenomenon in the Galápagos, and it produces high magnitude deformation when it does occur (e.g. Cerro Azul, 2017 (Guo et al., 2019), Sierra Negra, 2018 (Davis et al., 2021; Bell et al., 2021b) (Figure 3.1h), and Fernandina 2006, and 2007 (Bagnardi and Amelung, 2012)). However, the extensive episodes of positively correlated deformation that we observe during inter-eruptive periods do not show measurable deformation associated with shallow magma movements.

In Hawai'i, like the Western Galápagos, Mauna Loa and Kīlauea show correlated deformation, yet erupt isotopically distinct magmas (Poland et al., 2012; Gonnermann et al., 2012; Przeor et al., 2022). An asthenospheric melt layer is proposed to facilitate coupling between these volcanoes, across distances of 34 km (Gonnermann et al., 2012). Pore-pressure diffusion through this layer affects magma supply rate to the shallow reservoirs, and allows coupled deformation between the volcanoes, while maintaining their isotopic heterogeneity (Gonnermann et al., 2012). Such a layer, the Pāhala Sill Complex, has been seismically imaged at Hawai'i, a collection of sills between 36–43 km depth, with seismicity indicating magmatic pathways to both Mauna Loa and Kīlauea

(Wilding et al., 2023). A similar structure in the Galápagos may reconcile our observations of correlated deformation with the isotopic evidence of distinct magmas between each volcano (Kurz and Geist, 1999).

This structure would exist at depths beyond geodetic detection, at the base of the crust (ranging from 12 km at Fernandina, to 18 km at Sierra Negra (Feighner and Richards, 1994)). We consider the simplest explanation for correlations in Galápagos displacements to be temporally variable melt supply from the plume into an asthenospheric melt layer, that causes neighbouring sub-volcanic reservoirs to simultaneously pressurise via pore-pressure diffusion. A variable melt supply would explain our observations of correlations in shallow magmatic reservoir pressure that are dominantly positive, but with some modifications due to (1) the impact of eruptions and resulting shallow stress changes on individual sub-volcanic systems, and (2) variations in partitioning of melt entering the shallow crust due to differences in ascent mechanisms (Figure 3.4).

There are multiple strands of evidence for a time-varying melt flux into the Western Galápagos. We know that magma flux into the shallower crust there is periodic (Galetto et al., 2020; Galetto et al., 2019), and that historical eruptions have occurred in clusters (e.g. there were pauses between Galápagos eruptions from 1998–2005, and 2009–2015). There have also been discrete episodes of exceptionally high rate uplift (e.g., Sierra Negra 2005–2018 (Bell et al., 2021b; Guo et al., 2019)). Periods of elevated magma flux may result in magmatic "flushing" (the rapid migration of primitive magmas through the sub-volcanic system, at Fernandina and Wolf) (Stock et al., 2020), or the resurgence (repressurisation of a formerly contracting or inactive intrusion) of quiescent systems over months to years (Alcedo, 2007 (Figure B3); Darwin, 2020, (Figure 3.1)) (Galetto et al., 2020; Galetto et al., 2019)). We compare correlation coefficients over windows of 25 SAR acquisitions (approximately 5 months) with published volumetric estimates (Guo et al., 2019; Vasconez et al., 2018) and with new estimates of intrusive volume flux at each volcano between 2017–2022 (Methods). Our estimates of intrusive magma flux (Figure 3.3, Figure 3.4) use inversions of InSAR-derived displacements spanning either an eruption or inter-eruptive windows of three months (Methods). We observe that the periods with the highest number of strong correlations between pairs of time series occur during an eruption (e.g. Fernandina, Sierra Negra, 2018, and Wolf, 2022), or when there is an increase of magma supply (e.g. as Darwin uplifted in 2020) (Figure 3.1). For example, Cerro Azul, Fernandina, Sierra Negra, and Wolf show only positively correlated deformation in 2019 (Figure 3.2a, Figure B10), corresponding with the greatest intrusive volume flux of the entire time series (1.9×10^7 m^3 from January–March, 2019). Similarly, a period of positive volume flux to all volcanoes in late 2020 (Figure 3.3), resulted in a high number of positive correlations (Figure 3.3a). This supply in-

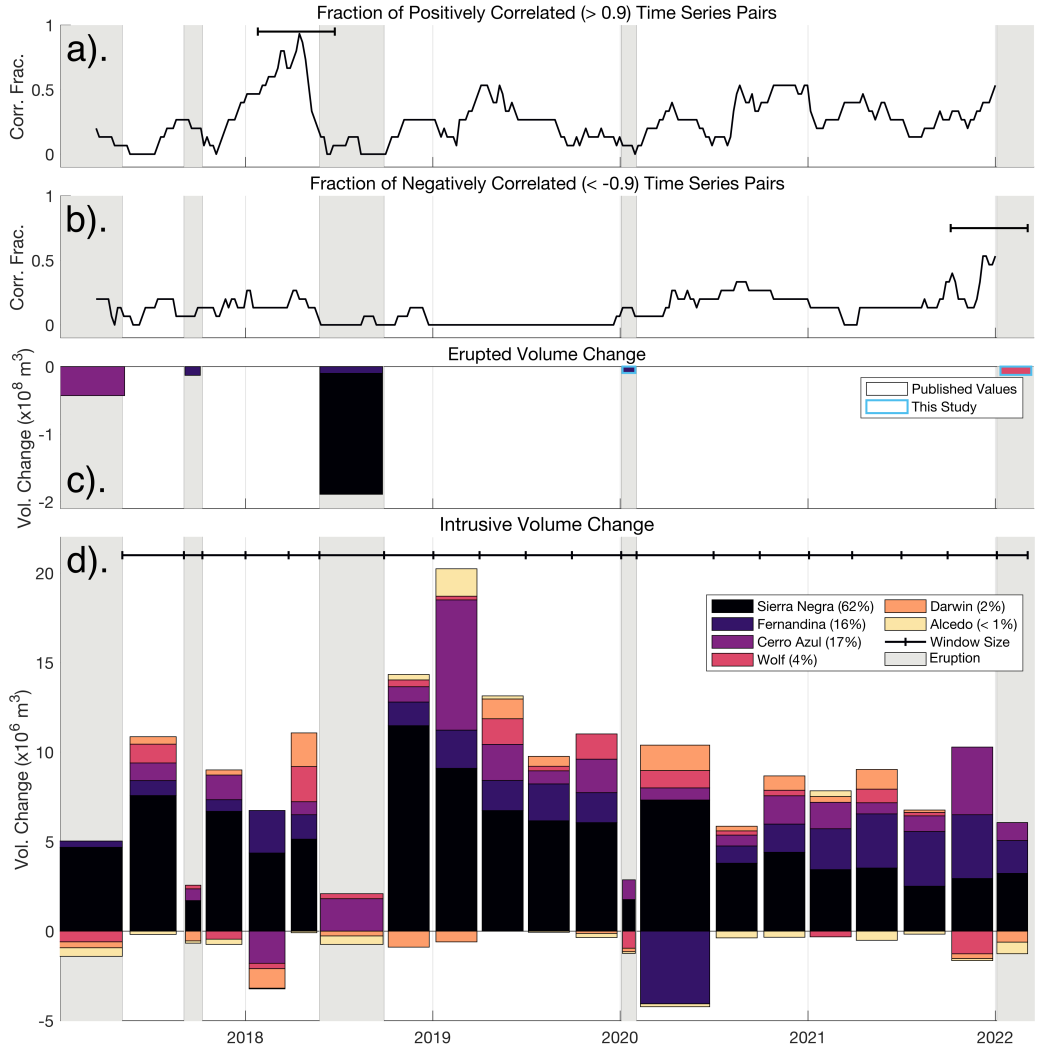

Figure 3.3: Change in the number of strong pair-wise correlation coefficients with time, as well as volume flux into each Western Galápagos volcano. **a**, Number of strong positive correlations between each pair of time series, determined using windowed correlation analysis (Methods). The correlation coefficient is calculated between each pair of volcanoes (Figure B10), and the number of values that are > 0.9 are counted. The count for each window is plotted at the centre of the window (5 months), the size of which is annotated by the horizontal black bar. **b**, Number of strong negative correlations between each pair of time series, determined using windowed correlation analysis (Methods). The correlation coefficient is calculated between each pair of volcanoes (Figure B10), and the number of values that are < -0.9 are counted. **c**, Estimates of volume flux for each unrest period, either from published analysis, or estimated here. **d**, Volume change with time at each Western Galápagos volcano, for a sill source. The spatial coordinates (X, Y, and Z values) of a sill are determined for each volcano, then held constant while the variables that control volume change (length, width, and opening) are allowed to vary. The width of each bar corresponds to the length of the period modelled, as does the horizontal black line, while different colours represent each volcano. Periods of significant unrest (e.g. eruptions) have been masked out (vertical grey bars) for the corresponding volcano (e.g. Sierra Negra 2018). In the Galápagos, eruptions typically comprise multiple sources, at different levels in the crust, that cannot be accurately modelled by a single, fixed source.

crease was observed on the surface with the uplift of Darwin, the highest magnitude uplift measured at the volcano throughout our time series (Figure 3.1). This observation of correlated displacement occurring during episodes of increased magmatic flux agrees with observations from between 2007–2011 (Baker, 2012). Then, heightened magma flux, evidenced by Alcedo's resurgence (Galetto et al., 2019), caused similar displacements at five volcanoes. This demonstrates that the correlated unrest discussed here, from 2006–2022, capture a representative rather than anomalous period of Galápagos volcanism.

The majority positive correlations is consistent with a common response to variation in melt supply from a deeper source. The positive correlation at Cerro Azul, Fernandina, Sierra Negra, and Wolf in 2019 (Figure 3.2a), and at Cerro Azul, Darwin, Fernandina, Sierra Negra, and Wolf in late 2020 (Figure 3.2a) occurred during a period of increased melt supply to each volcano (Figure 3.3d), and as Darwin resurged (Figure 3.1). This supply increase caused pressurisation of shallow reservoirs across the Galápagos resulting in correlated uplift (Figure 3.1). During periods of heightened supply, magma ascends either slowly via porous flow, or rapidly through dike propagation (Turcotte, 1987). Episodes of positively correlated subsidence were more unusual (e.g. Fernandina–Sierra Negra, 2018) and shorter in duration, but can similarly be attributed to simultaneous eruptions, or a drop in magma supply allowing cooling processes such crystallisation to dominate the shallowest parts of the magmatic system. For example, subsidence at both Alcedo (1997–2001 (Hooper et al., 2007)), and Sierra Negra (2000-2002 (Geist et al., 2006a)) may be due to cooling of intruded products during a period of decreased magma supply.

Negative correlations may also be explained by pore pressure diffusion, where increased magma supply to one volcano creates a pressure gradient throughout the asthenospheric melt layer. For example, in the six months prior to the 2022 eruption of Wolf, the the uplift rate and time series turning points were correlated between multiple volcanoes, while deformation trends were anti-correlated. Specifically, displacements in the descending satellite track, at Cerro Azul (at -0.900 E, -91.356 N) increased to an average of 0.1 m yr^{-1}, from 0.04 m yr^{-1} in the previous six months (Figure B1). This was accompanied by subsidence at Darwin (Figure 3.1), and a decrease in the uplift rate at Sierra Negra (Figure 3.1).

Our modelling of shallow intrusive flux into a sub-volcanic sill (Figure 3.3d) shows that from 2021, magma supply to Cerro Azul steadily increased, while steadily decreasing at Sierra Negra. This negative correlation is also seen during the 2008 eruption of Cerro Azul, when the inflation rate at Sierra Negra slowed (Baker, 2012). The GPS station GV02 was closest to the centre of the shallow reservoir at Sierra Negra, and showed the greatest change in vertical displacement of all Sierra Negra stations during the eruption of Cerro Azul, again indicating a magmatic response (Baker, 2012). An-

other explanation for negatively correlated deformation is the transient response of a magmatic system to eruption, when stress drop in shallow reservoirs temporarily alter the rate of magma ascent from background values in a "top-down" process (Baker and Amelung, 2012).

3.1.3 Conceptual Model for Common Magmatic Systems

Our conceptual model of volcanism in the Western Galápagos (Figure 3.4 and (Figure 5)) is of distinct, vertically extensive sub-volcanic magmatic zones that all respond to dynamic magma supply from the Galápagos plume.

This dynamic supply causes dynamic pore pressure changes throughout an asthenospheric melt layer, similar to the Pāhala Sill Complex beneath Hawai'i (Wilding et al., 2023), varying supply to the shallow crust. This melt layer is likely composed of geochemically distinct sills, allowing dynamic stress transfer, while preserving isotopic homogeneity between volcanoes (Figure 5). Melt flux from the plume varies temporally, flushing through different sub-volcanic systems during eruptions (Stock et al., 2020), allowing subsiding volcanoes to resurge (Galetto et al., 2019), and creating periods of elevated eruptive activity (e.g. 2005–2009, 2015–2022). However, magma is not supplied equally to each Galápagos volcano, with Sierra Negra receiving >50% of the total supply from 2000–2022 (Figure 3.4). Subsidence (indicative of limited magma supply to the shallow crust) has been observed twice at Sierra Negra, between 2000–2002 (Geist et al., 2006a), and 2011–2012 (Bell et al., 2021b), in both instances during a quiescent period of decreased eruptive activity across the Galápagos. At Kīlauea, local compositional heterogeneities at the plume alter the degree of partial melting, affecting magma supply to the shallow crust and the eruption rate (Pietruszka and Garcia, 1999). Therefore, we speculate that variations in magma supply at Sierra Negra, caused by local plume heterogeneities, are primarily responsible for driving dynamic stress through an interconnected asthenospheric sill complex. Supply variations to other Galápagos volcanoes will also affect pore pressure stresses, though to a lesser extent than at Sierra Negra, as will major eruptions or morphological changes at specific volcanoes cause deviations from these general trends.

The tight grouping of active, deforming volcanoes in the Western Galápagos makes their connectivity uniquely observable using geodetic data. However, multi-volcano cycles of unrest and eruption driven by a common source are likely to exist globally, as has been discussed in Hawai'i.

We speculate that the thin crust beneath the Western Galápagos (and potentially the Azores (Figure 3.1i)) is underlain by a melt layer comprising geochemically distinct sills, each sampling a different part of the Galápagos plume, and allowing stress interactions at the point of supply to sub-volcanic magmatic zones (Figure 3.5). This

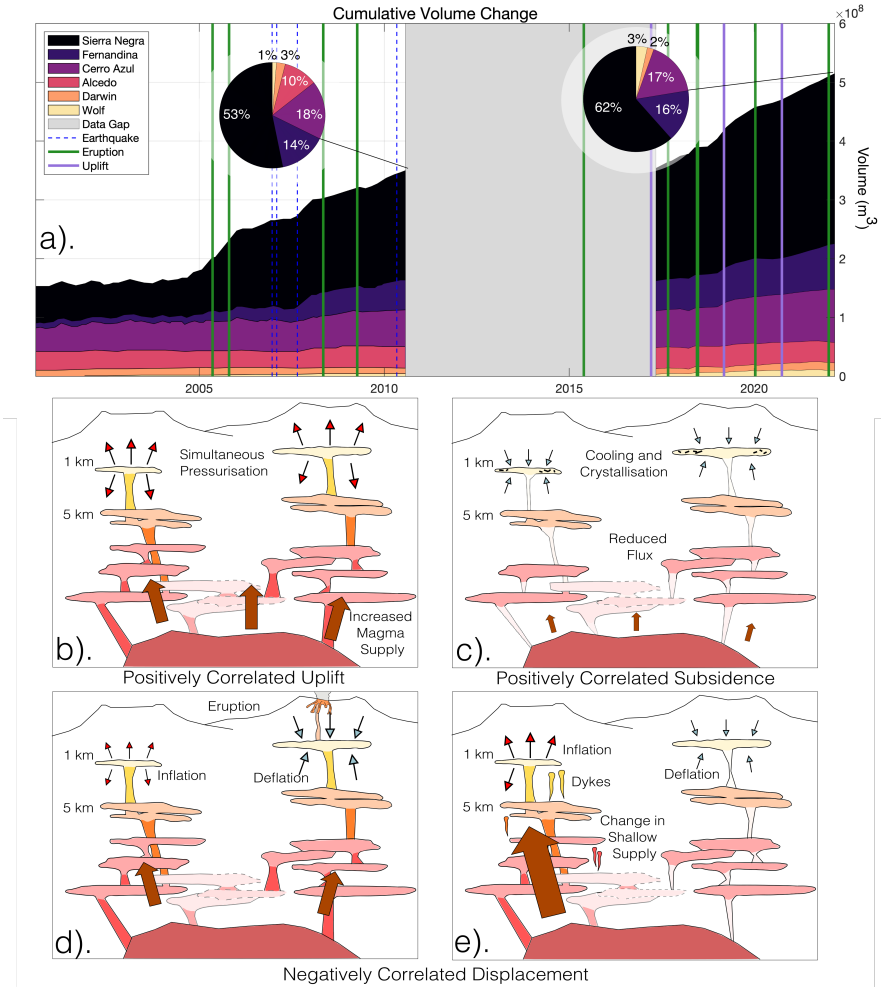

Figure 3.4: Mechanism of correlated displacements in the Western Galápagos. **a**, Cumulative intrusive volume in the Western Gaálapagos from 2000–2022 (modified from (Bagnardi, 2014)), with periods of correlated displacements annotated (this study, and modified from (Baker, 2012)). Each coloured area correspond to a different volcanic system, while the coloured vertical bars denote the observed evidence of related displacement (e.g. during an eruption, or volcanic unrest) — eruptions that occurred, but did not result in observed related displacements are faintly marked. The grey area marks periods where there was a lack of enough satellite data to perform modelling (Methods). The embedded pie charts show the cumulative distribution of magma at each volcano, firstly for the period from 2000–2010 (modified from (Bagnardi, 2014)), and secondly for the from 2017–2022 (i.e. not including volumes from 2000–2010). Alcedo is not included as it subsided over this period, and neither are volumes lost during an eruption (e.g. those that were removed in Figure 3.3). **b**, Schematic diagram of a proposed mechanism of correlated uplift. Neighbouring volcanic systems are supplied from the same deeper source, periodic changes in magma supply from this source cause these volcanoes to uplift simultaneously. These systems may be hydraulically connected at some depth, to facilitate correlated displacements during an eruption. **c**, Schematic diagram of a proposed mechanism of correlated subsidence. As magma supply wanes, cooling and crystallisation dominates, decreasing reservoir volume, and allowing neighbouring volcanic systems to deform simultaneously. **d**, Schematic diagram of a proposed mechanism of negatively correlated unrest. One of these then erupts while the other continues to inflate, causing subsidence, while the neighbour continues to inflate. **e**, Negatively correlated displacement due to a change in magma supply.

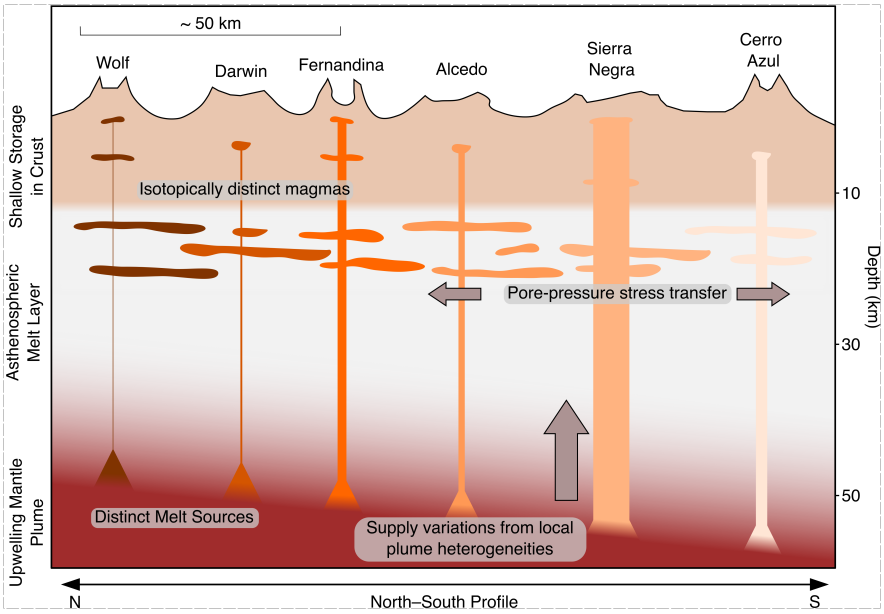

Figure 3.5: Schematic illustration of our proposed bottom-up mechanism for correlated deformation at Galápagos volcanoes. The recent melt flux to each volcano (Figure 3.3) is represented by the width of hatched areas, with Sierra Negra accounting for an average of 55% of total supply since 2000 (Figure 3.4). Each volcano samples a geochemically distinct area of the Galápagos plume, where local compositional variations control supply (Pietruszka and Garcia, 1999), though there may be occasional mingling between heterogeneous magma batches (Geist et al., 1999). Connectivity occurs at the base of the crust through pore pressure stress transfer between geochemically distinct sills (e.g. the Pāhala Sill Complex) (Gonnermann et al., 2012; Wilding et al., 2023). Flux of magma to the shallow crust, causing measurable deformation, varies in magnitude and partitioning according to a combination of plume supply variations and eruption, as illustrated in Figure 3.4.

promotes multiple ascent pathways within close proximity, and feeds six actively deforming Galápagos volcanoes within 100 km of one another. We anticipate that at other ocean hotspot systems, such as Ascension, Cape Verde, Reunion, or Comoros (Figure 3.1i)), magma flux is also ultimately driven by deep melt supply, but that fewer active volcanic centres inhibit observations of direct connections between surface displacements and deeper magmatic source zones. With this study, we show that volcanic displacement in the Western Galápagos, and beyond, should be viewed as a window into deeper, interconnected transcrustal magmatic systems.

3.2 Methods

In both this Chapter, and in Chapter 2, I use the same time series dataset in both ascending and descending track directions, but vary the subsequent analysis. Here, I detail these subsequent analyses, and again describe the steps in time series processing of InSAR data for clarity.

3.2.1 InSAR

We use approximately 2,000 interferograms spanning January 2017 (the first date from which regular satellite acquisitions were available in both track directions), until March 2022, towards the culmination of the 2022 eruption of Wolf Volcano (Figure 3.1). These interferograms are automatically constructed using the LiCSAR Sentinel-1 InSAR Processor (Lazecký et al., 2020). This is a fully automated chain for processing Sentinel-1 InSAR data (Lazecký et al., 2020). Image pairs have a minimum temporal spacing of between 6 or 12 days when S1-A and S1-B are in constellation, and are geocoded to pixel spacing of approximately 100 m. The network, and perpendicular baselines are presented in Figure B11. As these interferograms are automatically produced, we manually perform a quality check, and then re-make those interferograms containing gaps or unwrapping errors. We use the Generic Atmospheric Correction Online Service (GACOS) (Yu et al., 2018b) to minimise the error introduced by tropospheric noise. This correction reduced the standard deviation of the unwrapped phase in the descending track, from a dataset mean of 3.2 radians, to 2.7 (Figure B12). However, standard deviation slightly increased in the ascending track, from 4.12 radians, to 4.27 (Figure B12). Here, maps of tropospheric delay are created using data from the European Centre for Medium-Range Weather Forecast, then subtracted from the LiCSAR generated interferograms. Finally, we use these corrected interferograms to construct time series of displacement using the LiCSBAS time series inversion software (Morishita et al., 2020). This is an open-source software package designed for time series analysis of LiCSAR products, using a small baseline inversion. LiCSBAS utilises a phase closure technique to identify and remove bad interferograms, such as those with unwrapping errors (Morishita et al., 2020). The final time series are filtered using a Gaussian kernel, with a spatial width of 2 km, and a temporal width of 24 days (three times the average acquisition spacing).

3.2.2 Correlation Analysis

We perform rolling correlation analysis to identify periods of correlated displacements between representative time series for each volcano. For this analysis, and for the later Independent Component Analysis, we use time series previously produced using LiCSBAS. The primary criteria for the time series selected for analysis is that they must be representative of displacements at the caldera across the time series, and that the time series contains no data gaps (e.g. due to decorrelation during an eruption), as such gaps may present as false positive or negative correlation. The locations of the time series selected for presentation can be found in Figure 3.1, and Figure B1. We then discretise time series into temporal windows, where each window is offset by one acquisition from the previous window. To assure that each window has consistent temporal coverage, we linearly interpolate each time series, keeping a constant separation of 6 days between

each data point. We use windows of 150 days, or approximately five months; eruptions in the Western Galápagos frequently last months (e.g. in 2018 Sierra Negra erupted for two months, while in 2022, Wolf erupted for five months). With this window size, we ensure that we can compare multiple windows across entire eruptions, as well as any immediate pre- and post-eruptive correlation. We also ensure that we are comparing time series where the source of deformation is magmatic, rather than shorter term processes such as brittle failure, and slip along trapdoor faults. We test the impact of window size and find that windows of between 90–150 days produce consistent correlations. An example of using an 3-month window can be seen in Figure B13. We then calculate the correlation coefficient for each window, to retrieve a rolling correlation coefficient, pair-wise, for each set of volcanic time series. The correlation coefficient is a measure of the strength of the linear relationship between two variables, given between a range of -1 to 1. Correlation increases closer to either -1 or 1, while values closer to zero are more independent. The sign indicates whether the values are positively or negatively correlated. The correlation coefficient of two random variables, A and B (ρ_{AB}), be expressed through Equation 3.1.

$$\rho_{AB} = \frac{cov(A, B)}{\sigma_A \sigma_B} \tag{3.1}$$

Where *cov* is the covariance of A and B, and σ is their respective standard deviation. We identify strongly correlated displacement periods between volcanoes when absolute windowed correlation coefficients are > 0.9. We visualise these periods in Figure 3.3, which represents the number of these strong correlations at each date. We plot both the sum of the absolute correlation coefficients, and the non-absolute coefficients as a means of visualising when positive or negative correlations are active.

3.2.3 Independent Component Analysis

We select episodes of high correlation for further analysis using Independent Component Analysis (ICA) (e.g. Ebmeier (2016)). ICA is a blind source separation technique that is used to retrieve independent sources from a mixed signal. ICA is based on the principle that a mixed signal, X, is composed of a linear mixture of multiple components, S ($X = AS$), where A is a mixing matrix. Using the fastICA algorithm (Hyvärinen and Oja, 1997) we iterate to find an unmixing matrix, W, the inverse of A, such that $S = WX$, and the non-Gaussinity of W is maximised. An initial random value for W is selected before iteration. Therefore, global convergence is not assured, and the retrieved independent components may vary between each run. For each selected time interval, we perform ICA using approximately 8000 time series across the island (a total of 16,000 points). To ensure reasonable computation times, we downsample the number of time series based on the radial distance to each caldera centre (Figure B14),

on the assumption that the majority of displacement occurs within the caldera. This step provides three levels of resolution; the caldera floor is downsampled to 0.4 of it's original resolution, the caldera flanks to 0.25. Once downsampled, we use a k-means algorithm to identify independent components that appear consistently between different iterations, ensuring we converge on all W values. For each selected time period (as identified through correlation analysis), we run fastICA 100 times, and save the output. We identify unique independent components by calculating the sum of the squares of each one returned, and cluster similar time series using this value, using k-means. We calculate the mean independent component and unmixing value for each cluster. We visualise where these Independent components are active by plotting the absolute of each W value with its corresponding latitude and longitude (e.g. Figure 3.2). With this approach we can accurately reconstruct known displacement patterns (e.g. Cerro Azul 2017, and Sierra Negra 2018), and robustly identify the volcanoes that are affected by the same independent component. In addition to Figure 3.2, more results of this analysis can be found in supplementary material.

3.2.4 Estimation of intrusive flux

We estimate the volume flux with time into a shallow sill (Bagnardi and Amelung, 2012; Stock et al., 2018) at each volcano, from 2017 to 2022. While Descending data is available from 14/11/2015, Ascending is only available from 06/01/2017. As we perform a joint inversion, we use this latter date as a starting point. To do this, we perform a Bayesian inversion for best-fit source parameters, using the MATLAB-based Geodetic Bayesian Inversion Software (GBIS) (Bagnardi and Hooper, 2018). We first crop the spatial extent of the displacement map, such that only one volcano is considered in each inversion. We then pick a representative time period for each volcano, and model the best-fit source, using a joint inversion of the Ascending and Descending tracks. This representative period is selected such that there is no eruptions at the volcano, and that the observed displacement is from inflation or deflation of the sub-volcanic reservoir. We then slice our cumulative displacement time series into approximately three month windows. However, this window size is not constant during periods of significant unrest; windows are cropped to include all of an unrest period, such that the effect of volume loss only occurs in a single modelled window. This results in 21 windows of cumulative displacement for each volcano, or 126 total windows to be modelled. For each of these, we characterise the spatial variance using a semi-variogram (Bagnardi and Hooper, 2018), and ensure that the degree of quadtree downsampling is similar in both track directions. When slicing the cumulative displacement windows in either track direction, the dates do not exactly overlap, as the Descending acquisition typically occurs the day after the Ascending. Therefore, the inputs for our joint inversion are typically offset by one day, though we assume that interim displacement is negligible compared to the three month period studied. Once the best fit source has been constrained for each volcano,

we hold the X, Y and Z coordinates constant, and allow the opening, length, and width of the sill to vary for each window. The data, model, residual, and retrieved parameters can be found in Figures B15–B20. In each case, we verify that the retrieved depth of the sill agrees with what has been determined by previous studies, if available. We then calculate associated volume change to determine the change in volume with time (e.g. Figure 3.3, Figure 3.4). Though we model volume change in the best-fit source during eruptions and unrest (Cerro Azul, 2017, Fernandina, 2017, 2018, 2020, Sierra Negra 2018, and Wolf 2022), these volumes may not agree with previous observations. Many sources may be active during a volcanic eruption, making volume change estimates unreliable for our single source. To deal with this, draw on published results for eruptive episodes, and use single sources for the inter-eruptive periods. Finally, the dilational change during an eruption, as presented in Figure B9 was modelled with Coulomb 3.1 (Lin and Stein, 2004). We modelled this using a point source at Sierra Negra, with a volume change of $-2x10^8\ m^3$ (Vasconez et al., 2018).

Chapter 4

The Contribution of Crystallisation to Decadal Volcano Subsidence

Abstract

Persistent, low-rate ($< 3\,cm\,yr^{-1}$) subsidence has been observed at >27 volcanoes since the advent of satellite radar deformation measurements. Understanding the origin of this long-term subsidence is important for distinguishing between scenarios with different implications for volcanic hazard. Here, we assess the maximum contribution that the simplest of these potential origins — the cooling-driven crystallisation of magmatic intrusions — could conceivably have on long-term subsidence rates. We do this using simple numerical models, to describe the crystallisation of a sill due to conductive heat loss. We find that crystallisation best accounts for long-term subsidence signals in cases where magmatic sills intrude into country rock (e.g. Sierra Negra, 2018). We determine this by comparing Sentinel-1 displacement time series with modelled crystallisation curves, calculated using phase equilibria, thermal, and displacement models. We find that cooling and crystallisation-driven volume changes may generate measurable surface displacements for decades, requiring intrusions varying in thickness on the order of tens to hundreds of metres. At caldera systems with mature Trans-Crustal Magmatic Systems, crystallisation of individual intrusions cannot account for long-term subsidence, and is instead a combination of volatile and hydrothermal activity, magmatic replenishment, mush rheology, and, in cases of low magma supply, thermo-elastic contraction.

4.1 Introduction

Ground deformation data are essential in modern volcano monitoring. Deformation patterns are frequently used to estimate the depth, geometry and, in some cases, volume of magmatic intrusions (Pritchard and Simons, 2004). In the simplest conceptual

deformation cycle, magma accumulation in elastic crust preceding an eruption causes instantaneous uplift, while its expulsion causes subsidence (Biggs and Pritchard, 2017). Residual magma, or magma stalled following a non-eruptive intrusion, will contract as it cools in the absence of a persistent hot source. However, in reality many deformation observations reflect more complex processes. Magmatic signals may be modified by the response of the surrounding country rock (e.g. in a viscoelastic setting response signals are time-dependent (Nooner and Chadwick, 2009)) or by the superposition of secondary deformation from overlying hydrothermal systems, or faulting. Understanding the mechanisms that drive volcanic deformation at all stages of the eruption cycle improves our ability to interpret it, especially if we can distinguish between magma movement and volume changes taking place within a stationary body of magma. Here, we test the potential of cooling-driven crystallisation of a stalled body of magma to generate measurable surface displacements (Figure 4.1), with the aim of understanding the extent to which crystallisation can cause observed patterns of deformation. The crystallisation of an intrusion will occur whenever a magma stalls in the shallow crust, and is routinely proposed as a cause of long-term volcanic subsidence (e.g. Medicine Lake, Lassen (Parker et al., 2014; Parker et al., 2016)). Our approach combines phase equilibria models of magmatic phase changes between liquidus and solidus, numerical thermal modelling, and analytical elastic deformation models to explore the parameter space over which crystallisation of a cooling sill can produce measurable deformation at the Earths surface.

4.1.1 Interferometric Synthetic Aperture Radar Measurements of Volcano Subsidence

Volcano deformation that persists for multiple years to decades is commonly attributed to processes within a stalled magma (e.g. an intrusion that is stored in the upper crust rather than immediately erupting). Such deformation is characterised by low displacement rates and long durations (e.g. Lu and Dzurisin (2014) observe subsidence of 6–10 mm yr^{-1} at Aniakchak, USA, from 1992–2010 (Figure 4.2)), and by occurrence during post- or inter-eruptive periods (e.g. Lu and Dzurisin (2014) and Parker et al. (2014)). Examples of such subsidence, as found in the geodetic record and detected by Interferometric Synthetic Aperture Radar (InSAR), are presented in Figure 4.2, with the majority (>80%) deforming at rates of <20 mm/yr, for periods of >1 yr.

There are 8 instances in Figure 4.2 where this long-term subsidence occurs immediately following magma intrusion in the shallow crust, during an eruption. For example, eruptions at Kupreanof, Akutan, and Makushin, USA, occurred before, or during the early stages of observed subsidence (1987, 1992, and 1995 respectively (Figure 4.2) (Lu and Dzurisin, 2014; Venzke, 2023)). Alcedo, Galápagos, has undergone two distinct episodes of subsidence following an eruption in 1993 (Green, 1994), and after a period

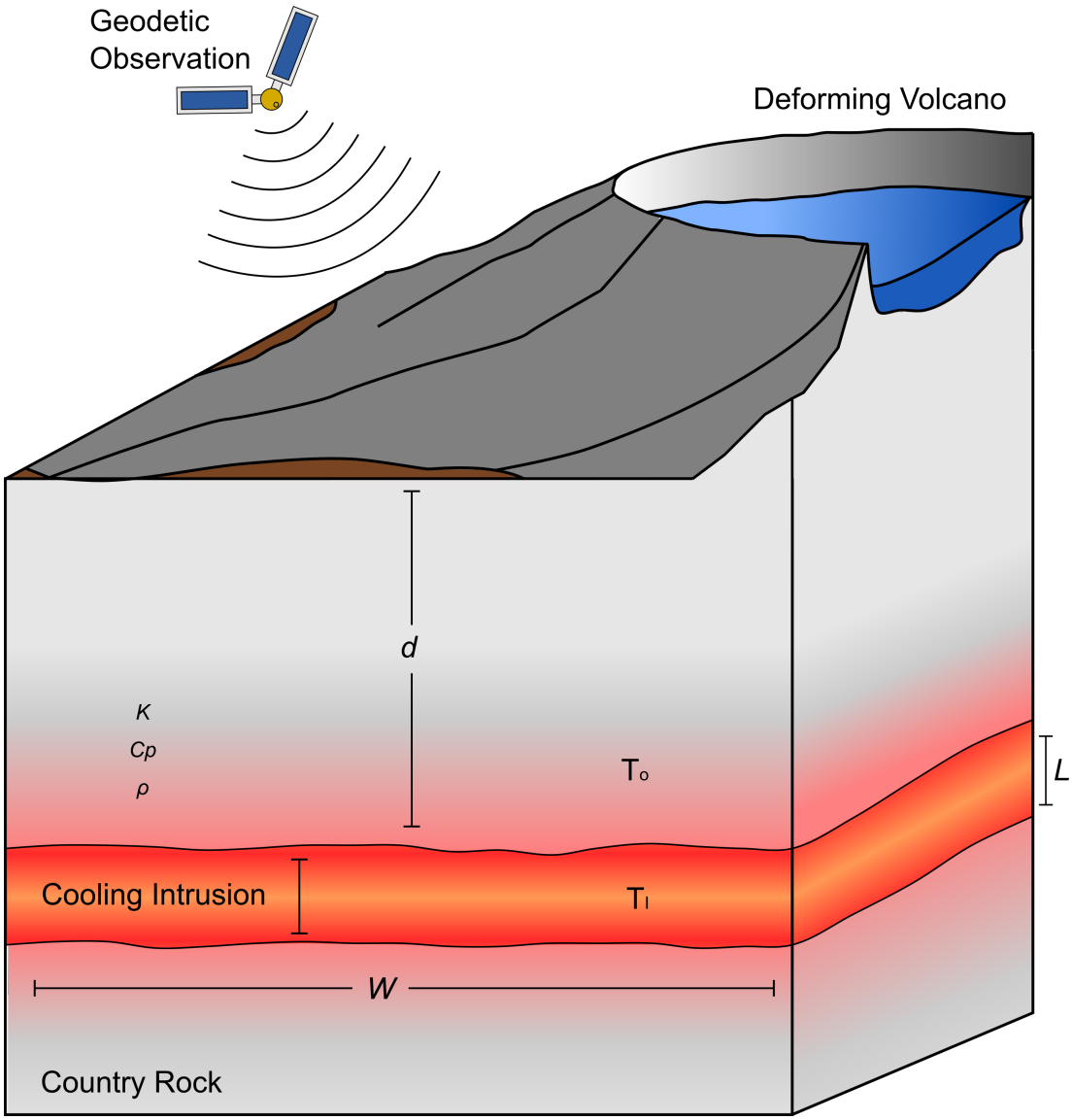

Figure 4.1: Conceptual model of the scenario being explored in this paper. Magma has stalled beneath a volcanic centre, where it is cooling and causing measurable deformation. K, C_p, and ρ are thermal conductivity, specific heat capacity, and density, respectively. T_o is country rock temperature, T_I is intrusion temperature, while d, W, and L are intrusion depth, width, and thickness, respectively.

of resurgent behaviour from 2007–2011 (Galetto et al., 2019). However, long-term subsidence is also widely observed as an inter-eruptive process, and is sometimes the only indication of an active volcanic system at an otherwise quiescent volcano. Medicine Lake, USA, subsided by approximately 10 mm/yr between 1954–2011 despite no confirmed eruption since 1060 (Parker et al., 2014; Venzke, 2023) (Figure 4.2). Likewise Aniakchak, Lassen, Fisher (USA), and Taupo, New Zealand, have been subsiding at rates of >6 mm yr^{-1}, despite not erupting since 1931, 1917, 1830, and 260, respectively. At each of these examples, crystallisation of stalled, sub-volcanic magma has been proposed as either the primary or secondary mechanism of deformation. For example, deformation at Fisher Caldera, USA, has been attributed to crystallisation coupled with volatile exsolution and migration from the magma (Lu and Dzurisin, 2014). At Askja, Iceland, crystallisation has been discussed as a potential contributing factor, alongside magmatic "drainback" (Sturkell et al., 2006), and at Nabro with a post-intrusion relaxation of a viscoelastic shell surrounding the magma chamber, or CO_2 outgassing (Hamlyn et al., 2018).

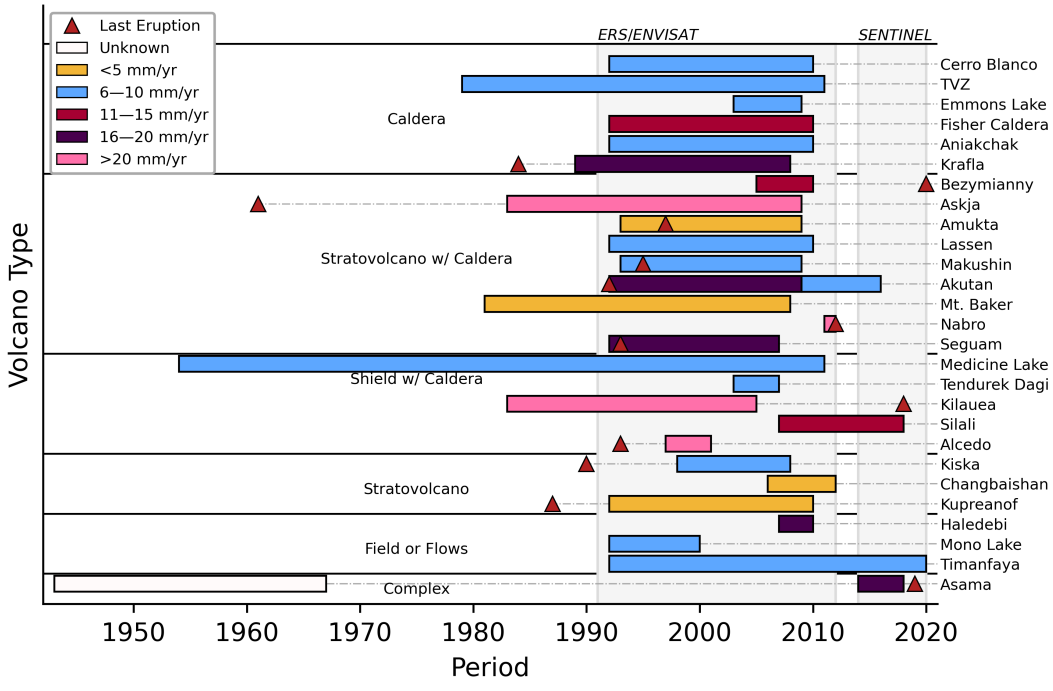

Figure 4.2: Instances of deformation either attributed to a cooling magma body or with deformation properties (long-duration, low-rate) characteristic of a cooling intrusion. Shown is the duration of observed deformation at each volcano, grouped by type (Venzke, 2023). Red triangles denote the most recent eruption at each centre, and colours indicate the observed rate of deformation. Areas of grey hatching illustrate the operational periods of major satellite geodesy missions. The references for each volcano can be found in Table C1.

4.1.2 Volume Change in a Cooling Magma

Long-term subsidence due to crystallisation occurs due to cooling of non-erupted, subvolcanic magma. This magma may be remaining from a previous co-eruptive intrusion (e.g. Kupreanof, USA (Lu and Dzurisin, 2014)), be injected during a lateral sill intrusion (Bell et al., 2021b), or be a constituent part of a vertically extensive, established magmatic system (Parker et al., 2014). Following emplacement, heat is conducted into the surrounding country rock as the magma cools, and crystals form. Progressive crystallisation of the intruded magma as it changes phase between the liquidus and solidus raises the relative density of the melt, and decreases its volume (e.g. Caricchi et al. (2014)). This density increase is caused by the formation of denser-than-melt minerals (e.g. Hall (1996)). This process can cause subsidence for as long as the magma is above the solidus, and if the magnitude of volume decrease from crystallisation is greater than any increase from other processes (e.g. volatile exsolution).

In volatile bearing melts, this subsidence may be punctuated by periods of uplift as bubbles nucleate and expand in the magma, or as they accumulate and pressurise in an overlying carapace (e.g. Fournier (1999)). Volatile and hydrothermal processes (or reservoir viscoelasticity) may result in long-term deformation, either alone or in combination. However, here we focus solely on the effect of crystallisation on volcanic deformation. We do this because cooling and crystallisation will consistently occur where magma has been intruded into cooler country rock, regardless of magmatic volatile content, or country rock properties. We aim to assess whether this process of magmatic crystallisation can reasonably contribute to the long-term displacements presented in Figure 4.2, and evaluate the fraction of observed signal that it can account for.

4.1.3 Detecting Long-Term Deformation

Observing long-term deformation historically required established monitoring networks. These networks were found almost exclusively at historically active, accessible, volcanoes, in developed countries (e.g. Kilauea, USA, and Asama, Japan (Johnson et al., 2010; Murase et al., 2007)). The advent of satellite-based monitoring techniques, such as InSAR, allow for remote monitoring of volcanoes where in-situ ground based techniques are not viable (e.g. Aleutian Arc, USA (Lu and Dzurisin, 2014)). The surge in observations of long-term subsidence between 1992–2010 coincides with the lifetime of the ERS and ENVISAT satellite missions (Figure 4.2), and reflects an increase in observations, rather than an increase in deforming volcanoes.

The detectable threshold of these measured volcano subsidence rates depends on the signal-noise ratio, with noisier data limiting the lowest measurable rate. This noise may be spatially limiting (e.g. snow/vegetation affect the coherence (change

in ground backscatter characteristics) of an observation (Bürgmann et al., 2000)), or spatially/temporally correlated (e.g. atmosphere (Ebmeier et al., 2013)). At Cascade volcanoes, Parker et al. (2015) resolve deformation rates of <1 cm/yr using atmospheric uncertainty models (e.g GACOS (Yu et al., 2018a)). Multi-temporal approaches may also lower the threshold of detectable deformation; González and Fernández (2011) detect subsidence at rates as low as 3–4 mm/yr on Lanzarote, while Purcell et al. (2022) observe subsidence of 6 mm/yr between 1992–2020, using small baseline time series analysis (e.g. Morishita et al. (2020)).

4.1.4 Previous Modelling of Cooling Magma

Previous studies have used both analytical and numerical modelling approaches to investigate how crystallisation may influence both magma chamber volume change and surface deformation. Tallarico (2003) propose an analytical approach to model volume change in a cooling spherical magma chamber where the impact of crystallisation is represented by allowing the radius of the source to change with time. They apply this model to Basiluzzo Island, Italy, and propose that a cooling magma chamber there has contracted and caused deformation since emplacement 50 ka ago. Hamlyn et al. (2018) apply this model to investigate post-eruptive deformation over a 15 month period at Nabro, Eritrea, and suggest that displacement could not be attributed to crystallisation alone. Similarly Townsend (2022) present an analytical model to study crystallisation, volatile exsolution, and viscoelastic-driven deformation, from a spherical source. These models (Tallarico, 2003; Townsend, 2022) have the advantage of being analytical.

In contrast, Parker (2015) use a combination of numerical thermal modelling and analytical source modelling to study the impact of crystallisation on 65 years of subsidence at Medicine Lake, USA. They find that this subsidence requires a sill between 150–800 m thick. Similarly, Caricchi et al. (2014) use a numerical approach to investigate the effect of crystallisation and degassing during successive uplift and subsidence events over an 11 year period at Okmok, USA. They use MELTS phase equilibria software (Gualda et al., 2012; Ghiorso and Gualda, 2015a) to predict the volume change associated with evolving phase assemblages for various intrusions. They then use a thermal model to evaluate volume change as a function of time. They find that crystallisation alone cannot replicate the observed volume loss, and as such, Okmok has been excluded from Figure 4.2.

Here, we also take a numerical approach to predict volume change from crystallisation in order to understand the effect of such volume loss on ground deformation. We use MELTS to predict volume change with temperature and evaluate timescales using a finite difference thermal model. We use point Compound Dislocation Models to convert

volume change to displacement. This approach allows us to consider time-dependent deformation in realistic intrusion geometries.

4.2 Methods

We consider crystallisation for the simple case of an anhydrous magma to estimate volume loss from liquid to solid phase transitions. We do not consider volatiles as they have a significant impact on magma density changes and compressibilty. We select our initial magma compositions from published literature, assuming that erupted whole rock compositions represent those in an intruded reservoir. We also make the following considerations: Heat flux is controlled by thermal gradient, meaning that sills emplaced in cool country rock will cool faster than those emplaced in established magmatic systems. As such, the geothermal gradient (and corresponding ambient temperature) is varied to approximate these different cooling scenarios. A crystallising stalled magma loses volume in all directions, so volume change is modelled as isotropic along all axes.

We use MELTS (rhyolite-MELTS v 1.0.2, as part of the alphaMELTS2 package (Gualda et al., 2012; Ghiorso and Gualda, 2015a)), alongside thermal and displacement models to predict surface deformation for various melt compositions (e.g. Purcell et al. (2022)). We first model the phase assemblages from an initial composition (Section 4.2.1), to determine volume change as a function of temperature. We then use a finite difference thermal model to predict cooling (Section 4.2.2), and thus volume change, time series. Finally, displacement over time is determined through numerical integration of point Compound Dislocation Models (pCDMs (Nikkhoo et al., 2017)) in Section 4.2.3. The major controls on the rate of surface deformation following intrusion of a volume of magma are the changing density of the magma as it cools, the temperature of the country rock, and latent heat release during crystallisation.

There are numerous examples of subsidence at volcanoes due to thermo-elastic contraction of erupted products (e.g. Parícutin Lava Field (Chaussard, 2016)). However, here we only consider volume change due to crystallisation, and neglect the effects of such thermo-elastic contraction on the following basis. We examine the temperature change in and around a sill as it cools from liquidus to solidus, with a 1-dimensional finite difference thermal model, using a thermal expansivity value of 2×10^{-5} (e.g. Wang and Aoki (2019)). Figure C1 shows that contraction will be offset by expansion of the surrounding country rock. Latent heat release from magmatic phase changes causes the country rock temperature to increase more than the temperature decrease in the intrusion, with the corresponding increase in country rock volume offsetting any contraction (Figure C1). Though thermal contraction clearly plays a role in sub-solidus subsidence

(e.g. lava flow contraction (Patrick, 2004; Chaussard, 2016)), it should be negligible for an intrusion between the solidus and the liquidus. Therefore, we evaluate the changing density of the cooling magma to evaluate surface deformation, and systematically test the effect of thermal setting and intrusion thickness. These parameters are considered in detail as they represent a variety of volcanic settings and intrusion types (Figure 4.3).

We perform systematic parameter space testing, and real-world data comparison using our model, and make the following assumptions. We consider a magma body that has stalled at a level of neutral buoyancy (Lister and Kerr, 1991), and is not replenished by a subsequent intrusion during the modelled period of cooling or tapped during an eruption (e.g. Cashman et al. (2017)). This stalled sill has a low aspect ratio, being much more laterally extensive than thick (Figure 4.4). Therefore, in a thermal sense, the sill is treated as laterally infinite, and is modelled using the one-dimensional heat equation (Equation 4.1). We consider an anhydrous melt, such that volatile exsolution is neglected. We assume that this intrusion is relatively shallow, and that the surrounding country rock behaves elastically (e.g. Pritchard and Simons (2004)). Finally, we also assume that there is no overlying hydrothermal activity. These choices mean that we determine the highest rates of deformation that could reasonably be attributed to crystallisation; hence, our estimates express the maximum likely contribution of crystallisation. We investigate cooling time in a range of thermal settings by intruding the sill into a geothermal gradient between 0.02 – 0.098 $^oCm^{-1}$ (Reverdatto et al., 2019).

4.2.1 Modelling Volume Change

MELTS models the evolving phase assemblages in a melt of a given composition by minimising the appropriate thermodynamic potential (Ghiorso and Gualda, 2015b). In this study, we assume that the magma undergoes isobaric crystallisation following intrusion at the liquidus. We consider the case of a closed system (no magma gain/loss, and no volatile phases present). We iterate from the initial intrusion temperature to the solidus, calculating magma density at 1^{o}C increments. Real magmas consist of both solid and liquid phases, but by assuming that all of the magma is intruded at the liquidus temperature, we calculate the maximum volume change due to crystallisation. By assuming that the intrusions do not mix with pre-existing magma, we avoid considering volume changes during re-melting, as well as the well as the effect of re-melting on cooling times, due to latent heat absorption. We predict volume change as a function of temperature and express this as a function of time using a thermal model.

4.2.2 Cooling Scenarios

We construct time series of temperature using a finite-difference approach to model conductive heat loss in a crystallising sill. We assume that all heat loss occurs via

conductive heat diffusion through its upper and lower surfaces. While convection will increase magmatic heat transfer (thereby increasing cooling rate) (Annen, 2017), it is not considered here. The governing one-dimensional heat equation is expressed in Equation 4.1 (e.g. Annen (2017)).

$$\rho C_p \frac{\partial T}{\partial t} + \rho L \frac{\partial X}{\partial t} = K \frac{\partial^2 T}{\partial x^2} \tag{4.1}$$

Where ρ is density, Cp is specific heat capacity, T is temperature, t is time, X is melt fraction, K is conductivity, and x is distance. We account for latent heat (L) release by assuming a linear relationship between temperature and melt fraction. We assume a melt fraction of one above the liquidus, and zero below the solidus. Between the liquidus and solidus, the relationship between X and T is expressed by Equation 4.2 (e.g. Annen (2017)). Cp is set to 1000 $Jkg^{-1o}C^{-1}$, K is set to 2.5 $Wm^{-1o}C^{-1}$, and L is set to $3{\times}10^5$ $Jkg^{-1o}C^{-1}$ after Annen (2017).

$$X = \frac{T - T_s}{T_l - T_s} \tag{4.2}$$

To estimate volume change with time, we emplace a magma into our model domain at time 0. Following this, we iterate using the Forward Euler method to calculate conductive heat flux until the intrusion has cooled below the solidus. Spatial steps of 1 m are used, with a dynamic timestep to ensure numerical stability. We use the results of the thermal model, and those of the phase assemblage model, to convert volume change as a function of temperature to volume change as a function of time (Figure C2). The final step uses the predicted volume changes to calculate the corresponding surface deformation using point Compound Dislocation Models. (Nikkhoo et al., 2017).

4.2.3 Calculating Displacement

The geometry of our modelled intrusion is comparable to a rectangular dislocation (Okada, 1985), where opening along the major axis is accompanied by closing along the minor axes (Segall, 2010). However, crystallisation contracts isotropically. We therefore use a numerical approach, approximating the intrusion as a network of isotropically contracting point sources.

We compared this numerical approach to an analytical horizontal rectangular dislocation to evaluate the difference between isotropic and Okada-type contraction. To do this we first created a synthetic interferogram of displacement for a 4 km wide square sill, 25 m thick, at 4 km depth. This displacement was calculated by numerical integration of a discrete mesh of pCDMs that lost approximately 10 % of its volume. The best fit horizontal rectangular dislocation for these interferograms was determined using

the Geodetic Bayesian Inversion Software (GBIS (Bagnardi and Hooper, 2018)). We fixed source depth at 4 km, and tested all other parameters to find the optimum model after 1,000,000 iterations. These synthetic wrapped and unwrapped interferograms are presented in Figure C3.A. The modelled interferogram, and pCDM–Okada misfit are shown in Figure C3. The best-fit horizontal rectangular dislocation is 5980 m long, 6050 m wide, with an opening of approximately -0.44 m. This is a total volume change of -1.6×10^{-7} m^3. For comparison the total volume change using the pCDM approach is -4×10^{-7} m^3. The comparative volume change is on the same order, though volume change using the pCDM method is approximately 2.5 times greater than that in the rectangular dislocation. Therefore, a rectangular dislocation is inappropriate when considering crystallisation, as it both fails to model the isotropic process and underestimates the volume loss.

Displacement Model Setup

We discretise the intrusion volume into a uniform three-dimensional grid, such that every point has equal volume. We consider our input volume change to be the cubed intrusion thickness (e.g thickness, width and length are equal) by calculated volume loss (from MELTS), such that each pCDM approximates an equal volume of the intrusion. We then equally space these throughout the intrusion, such that the entire volume of the intrusion is considered. Therefore, when referring to intrusion thickness in relation to displacement calculations, we are referring to the equivalent cubic volumes of such a thickness for each individual pCDM. We place a point Compound Dislocation Model (pCDM) (Nikkhoo et al., 2017) at each of these points. The pCDM is composed of three mutually orthogonal point tensile dislocations (Nikkhoo et al., 2017; Okada, 1985). Here, each of these orthogonal tensile dislocations lose volume equally. Alternative approaches to model this volume change include using a rectangular dislocation (Section 4.2.3), or alternative point sources such as Mogi (Mogi, 1958), or cuboid (Barbot et al., 2017). See Figure C4 for a comparison of sources.

$$U_{tot} = \iint_{-\frac{1}{2}W}^{+\frac{1}{2}W} U_{pCDM}(x, y)\, dx\, dy \tag{4.3}$$

We calculate the superposition of displacement from each pCDM in the grid via numerical integration. The general approach is described in Equation 4.3, where U_{tot} is the matrix of total displacement, U_{pCDM} is the predicted matrix of displacement for a single pCDM, x and y are coordinates, and W is width. Limits are set to $-\frac{1}{2}W$ and $+\frac{1}{2}W$ such that centre of the sill is at 0. For computational efficiency, we use matrix convolution with a weighted kernel of the displacement matrix from the pCDM at the centre of the sill. This gives the total displacement produced by our cooling intrusion. This allows us to express the time series of volume loss in terms of displacement over

time (Figure C2).

4.2.4 Parameter Selection and Initial Conditions

We carry out sensitivity tests for the impact of initial conditions of the cooling sill, and our choice of physical parameters on deformation at the Earth's surface. To test the effect of each parameter, we define the expected ranges over which these parameters are found. We use widely cited values for physical properties of magma, such as thermal conductivity, and latent heat of crystallisation (e.g. Annen (2017)), and select representative values for parameters such as sill thickness and area, that may vary on a volcano-by-volcano basis.

Table 4.1: Parameters used as model inputs. Thickness and Geothermal Gradient are systematically varied while the rest are held constant.

Parameter	Unit	Value	Reference
Thermal Conductivity	$W\ m^{-1o}\ C^{-1}$	2.5	Annen (2017)
Specific Heat	$J\ kg^{-1o}C^{-1}$	1000	Annen (2017)
Thickness	m	5–75 (Figure 4.4)	
Representative Depth	m	4,000	Ebmeier et al. (2018)
Latent Heat	$J\ kg^{-1}$	3e5	Annen (2017)
Geothermal Gradient	$^oC\ m^{-1}$	0.02–0.098	Reverdatto et al. (2019)
Width	m	4,000 (Figure 4.4)	
Initial Melt Fraction		1	

In order to determine reasonable thicknesses and areas, source inversions from the geodetic record were reviewed for boundary conditions that bracket the likely natural range. Values for each parameter used are presented in Table 4.1. Figure 4.4.A presents the distribution of sill openings from rectangular dislocations, determined by inversion of InSAR measurements. Standard deviation of opening is approximately two metres, significantly less than the field observations of thicknesses presented in Figure 4.4.B, as expected. This figure shows the distribution of sill thicknesses within the Transvaal Supergroup, as found by Button and Cawthorn (2015), one of just a few studies with a significant number of field measurements of sill thicknesses. These sills have a mean thickness of approximately 34 m, and standard deviation of approximately 75 m, once extreme outliers have been removed (Button and Cawthorn, 2015). Modelled openings (Figure 4.4.A) and exposed thickness (Figure 4.4.B) relate to different stages of sill development. Rectangular dislocations represent change in thickness rather than absolute thickness, such as Figure 4.4.B, and only represent a fraction of sill thickness at the time of intrusion, since volume change is not equivalent to total volume (aside from the very first first intrusion). Figure 4.4.C presents modelled sill areas for penny shaped cracks

and rectangular dislocations. Also included are the dips, where stated, of modelled sills. We consider a sill with sides of 4 km, such that the area of our modelled intrusion is the median value (16 km^2) of the data presented in Figure 4.4.C.

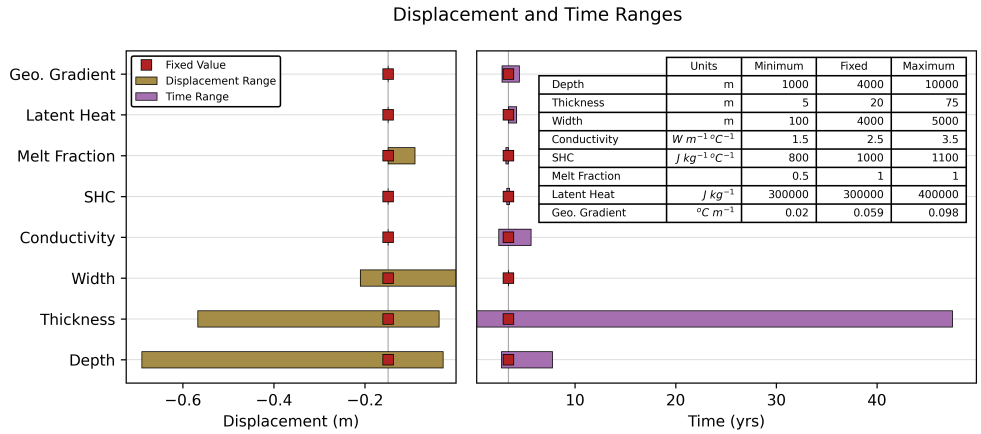

	Units	Minimum	Fixed	Maximum
Depth	m	1000	4000	10000
Thickness	m	5	20	75
Width	m	100	4000	5000
Conductivity	$W\,m^{-1}\,°C^{-1}$	1.5	2.5	3.5
SHC	$J\,kg^{-1}\,°C^{-1}$	800	1000	1100
Melt Fraction		0.5	1	1
Latent Heat	$J\,kg^{-1}$	300000	300000	400000
Geo. Gradient	$°C\,m^{-1}$	0.02	0.059	0.098

Figure 4.3: Results of initial parameter testing. The displacement and cooling time for parameter maximum and minimum are calculated while the other parameters are held constant at an indicative value — these values are presented in Table 4.1. The inset table shows the maximum, minimum, and fixed values (Table 4.1) for every parameter tested. Initial compositional data for testing is from Busa et al. (2002)

.

We use our simple crystallisation model to predict time series of displacement for sill intrusions into country rock. Preliminary testing showed that intrusion depth has the most significant effect on the magnitude of displacement, followed by thickness, with width also having a major influence (Figure 4.3).

4.3 Time Series of Long Duration Volcano Subsidence

We use interferograms from the LiCSAR automatic interferometric processor (Lazecký et al., 2020). LiCSAR generates interferograms with temporal resolution of up to 6 days (when Sentinel-1A and 1B were in constellation), geocoded to approximately 100 m pixel spacing (Lazecký et al., 2020). Each acquisition forms an interferogram with the three preceding and succeeding acquisitions, for subsequent use in small baseline time series analysis (Lazecký et al., 2020). These interferograms are corrected for atmospheric contributions to phase using the Generic Atmospheric Correction Service (GACOS) (Yu et al., 2018b). Here, maps of tropospheric phase delay are calculated using ECMWF weather maps, and subtracted from the uncorrected interferogram. The average change in standard deviation for each time series can be found in Tables C2–C8. Finally, we construct time series of ground displacement using the small baseline subset (SBAS) LiCSBAS time series python package (Morishita et al., 2020). Prior to performing a time-series inversion, LiCSBAS allows for coherence-based masking, spatial cropping, coherence and extent-based quality checks, before identifying and removing "bad" in-

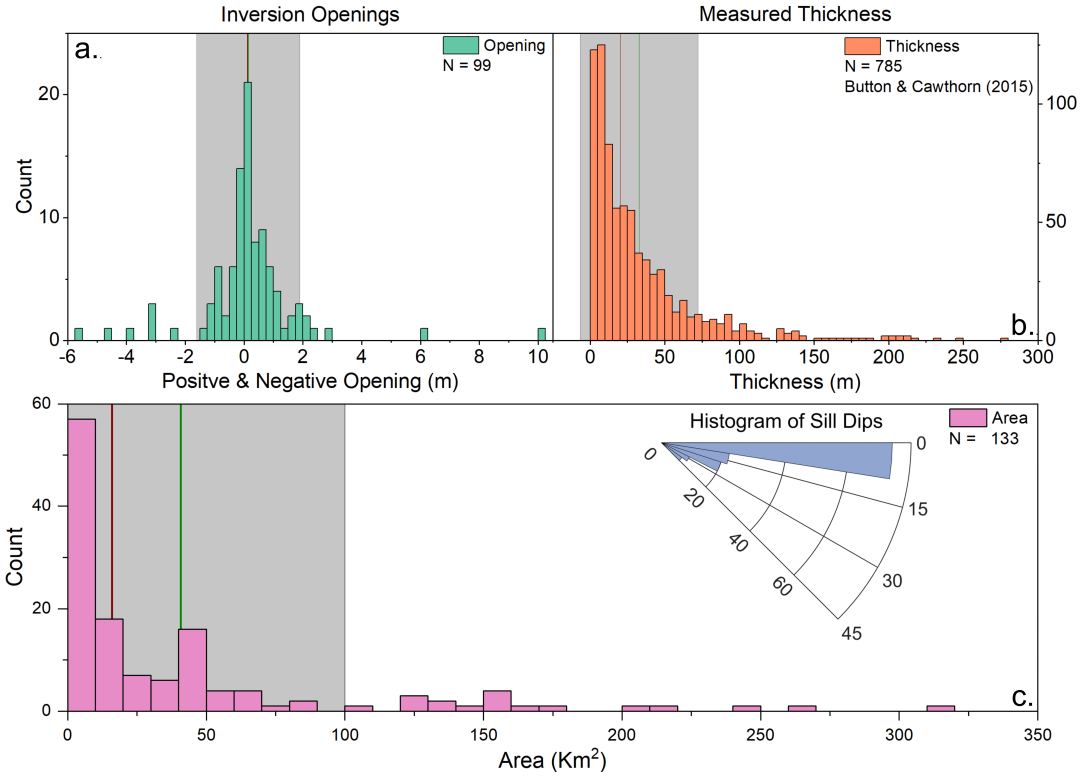

Figure 4.4: Distribution of sill opening, thickness, and area. a. Distribution of positive and sill openings from published geodetic inversions. Openings from near horizontal rectangular dislocations are included. b. Distribution of sill thickness within the Transvaal Supergroup, South Africa, as measured by Button and Cawthorn (2015). c. Distribution of sill areas from published geodetic inversions. Rectangular dislocations, penny shaped cracks, and estimates of area are all included. Modelled sill dips are also presented, a dip of zero is assumed if not stated.

terferograms from the processing chain using phase loop closure checks. The final time series have are presented in Section 4.4, while the satellite track, and processing parameters for each volcano presented in Section 4.4 can be found in Supplementary Tables C2–C8. For each volcano, we plot deformation relative to multiple reference points to test for the influence of phase bias (Section 4.3.1). As noted in Section 4.2, thermoelastic contraction of lava flows can cause long-term subsidence signals (Purcell et al., 2022; Chaussard, 2016). These signals are also characterised by low-rates (mm–cm yr^{-1}), but typically occur off the volcanic summit, with spatial displacement patterns matching the spatial extent of the lava flow (e.g. Chaussard (2016)). To ensure that we are not observing subsidence due to lava flow contraction here, we only plot points at volcanoes where the displacement field does not overlap with any lava fields that are observable in optical satellite imagery, or where there was no ongoing subsidence prior to magma intrusion (as is the case at Sierra Negra). We model crystallisation either since the first observation of long-term subsidence (e.g. 2003 at TVZ (Hamling et al., 2015)), or since the most recent unrest (e.g. Sierra Negra, following its 2018 eruption), such that we model the maximum possible rate attributable to crystallisation. To compare our model outputs we resample both the model and time series to daily frequencies, and linearly interpolate the intervening data. We then calculate the Residual Sum of Squares (RSS) between the data and model. For each of Figures 4.5–C9, this calculation is performed between the model data, and the first legend entry time series.

4.3.1 Assessing the Impact of Fading Signal on Decadal Subsidence Time series

Phase-Bias, or "Fading Signal" is an apparent signal, caused by cumulative errors in time-series processing, resulting in apparent long term trends in deformation, that do not reflect reality (e.g. Purcell et al. (2022) and Maghsoudi et al. (2022)). This bias is particularly evident in time series constructed from networks of short interval, multi-looked interferograms, as spatial filtering introduces error terms. This has a minor contribution to the observed signal in each interferogram relative to other terms such as ground movement and atmospheric noise, but can propagate through time series to have a measurable influence on ground deformation. The value of the error term introduced through multi-looking varies with ground cover type, with Maghsoudi et al. (2022) showing a minor contribution at urban settings compared to cropland and forests, that mimic subsidence and alternating subsidence and uplift, respectively. Here, we are considering long-term subsidence due to crystallisation, a phenomenon that may be mistaken with phase bias. As such, when we are considering candidate volcanoes, we plot subsidence relative to a reference pixel at varying ground-cover types, and disregard those where the rate of subsidence varies with reference pixel (an alternative approach is to increase the temporal interferogram length, though this may result in coherence

loss (Purcell et al., 2022)). For example, we observe 15 cm of apparent subsidence at Mt. Shasta from 2015–2023, on a point on the western flank of the volcano (Figure C5, Table C5). However, Mt. Shasta is a well monitored Cascade volcano, with no geodetic evidence of recent unrest or deformation, making it unclear when a magma intruded prior to crystallising. To test for potential phase bias, we varied reference pixel location from a forested reference area SSE of Mt. Shasta (Figure C5), to a mountainous reference area at Castle Crag dome SW of Mt. Shasta, to an urban reference area NW of Mt. Shasta, at Yreka (Figure C5). We see a clear discrepancy in the magnitude of subsidence with each reference location, with the lowest magnitude occurring relative to the urban setting (Figure C5), indicating phase bias may be present (e.g. (Maghsoudi et al., 2022)). As such we discount the potential of a crystallising signal, and vary reference locations at each candidate volcano before considering crystallisation.

4.4 Results

To determine the impact of crystallisation on long-term subsidence, we compare our model to Sentinel-1 displacement time series (ranging from 2014–2022 (Section 4.4)), from volcanoes presented in Figure 4.2. We select six of these volcanoes as case studies to test if long-term rates are consistent with crystallisation. These volcanoes were selected as they are from diverse global settings, have varied historical activity, and have been either previously suggested as undergoing crystallisation or long-term subsidence. Here, we present detailed results from Alcedo and Sierra Negra, and summarise the results of the remaining volcanoes in Table 4.2 (detailed in Appendix C).

4.4.1 Alcedo

Alcedo is located on the Western Galápagos Island of Isabela, in the east Pacific Ocean. It has a large summit caldera, and usually erupts basaltic lavas, though rhyolitic lavas have been sampled here (Geist et al., 1994). Alcedo most recently erupted in 1993, from a phreatic explosion on its southwestern flank (Green, 1994). Interferograms spanning this eruption, from 1992–1997, showed that the volcano uplifted by almost 1 m during this time (Amelung et al., 2000). Following this uplift, Alcedo steadily subsided (-<30 mm yr^{-1}) until 2007; Hooper et al. (2007) suggest this this subsidence was caused by the cooling and crystallisation of magma, possibly intruded during the uplift observed by Amelung et al. (2000). From 2007–2011 Alcedo underwent a period of unsteady uplift (>30 cm), which Galetto et al. (2019) attribute to caldera resurgence, and a new influx of magma into a sill geometry. Following this, from 2016–2022, Alcedo subsided by approximately 20 cm (Figure 4.5) at a point in the centre of its caldera. Displacement is consistent between reference areas at Cerro Azul and Sierra Negra volcanoes, as well as at Puerto Villamil. This subsidence (initially -0.026 m yr^{-1}) was interrupted by a

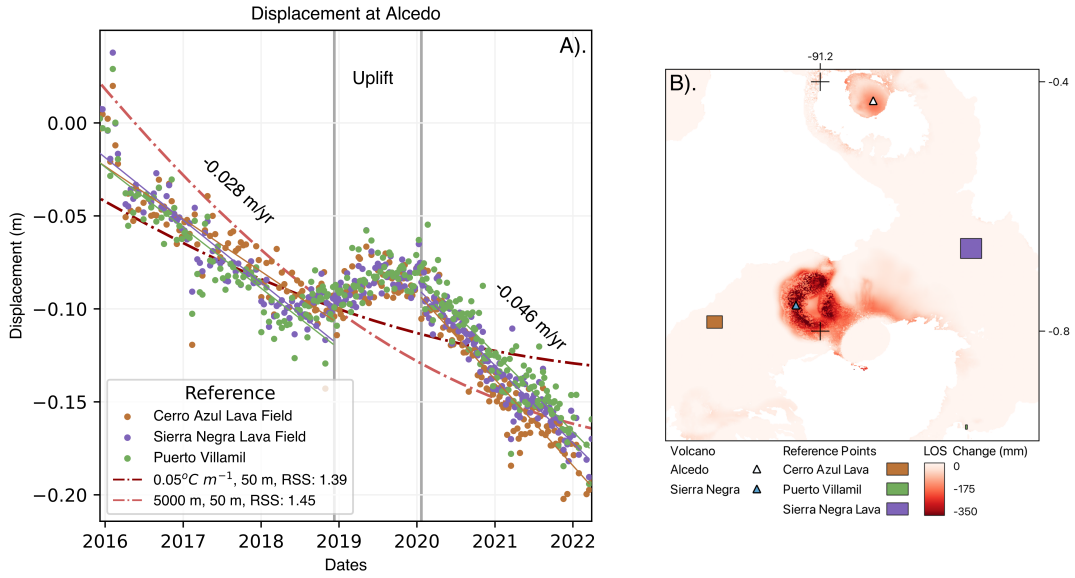

Figure 4.5: Time Series of subsidence at Alcedo from 08/12/2015–30/03/2022. A). Subsidence at Alcedo relative to various reference areas, and associated linear regressions. The hatched red lines indicate crystallisation driven subsidence, and the vertical grey lines illustrate uplift at Alcedo from 2019–2020. The subsidence rates before and after the uplift are annotated. B). Map of cumulative displacement at Alcedo. Annotated is the plotted pixel and the reference areas, while crosses indicate the grid of latitude and longitude.

minor uplift phase from 2019-2020 ($<$ 5 cm), and resumed afterwards at a greater rate (-0.046 m yr^{-1}). Like the subsidence observed by Hooper et al. (2007), it is probable that this deflation is driven by the magma intruded during Alcedos resurgence (Galetto et al., 2019).

We model maximum subsidence rates due to crystallisation at Alcedo under two scenarios, for an intrusion at 3 km depth (Table C2), varying the intrusion thickness and geothermal gradient, as well as the intrusion width and thickness (Table C2). We assume that magma cooling began in 2007, the onset of resurgence here (Galetto et al., 2019). This is the earliest evidence of recent magma influx at Alcedo, though resurgence, and magma influx, continued until 2011, and the volcano was not geodetically monitored from 2011–2015. Though there is evidence of magma intrusion in 2019, we do not include this intrusion in the model. This event would have added mass to the crystallising reservoir, and caused remelting of crystallising magma (e.g. Okmok (Caricchi et al., 2014)), and following it there would have been at least two magmatic zones, crystallising at different rates — scenarios not considered this model. Instead, we approximate these sills as a single large intrusion, 50 m thickness, emplaced at either $0.05^oC\ M^{-1}$ (RSS: 1.39) or of 5000 m width (RSS: 1.45). This may reveal a model limitation, as crystallisation of the 2019 intrusion may have increased the subsidence rate by 0.018 m/yr (from -0.028 m/yr to -0.046 m/yr (Figure 4.5)). Additionally, fumarolic activity

at Alcedo suggests that volatiles may affect subsidence rates here (Sections 4.5.2 and 4.5.3).

4.4.2 Sierra Negra

Sierra Negra forms the southeastern portion of Isabela Island in the Western Galápagos, and regularly experience high-volume effusive basaltic eruptions (Vasconez et al., 2018). Sierra Negras large caldera experiences extreme uplift due to magma accumulation in a shallow reservoir at 2 km depth, inflating by 6.5 m between its 2005 and 2018 eruption (Bell et al., 2021b). During this eruption, distal fissures were fed by a laterally propagating sill, sourced from the caldera, located to the northwest of the volcano. This sill was located at 1,000 m below sea level (Davis et al., 2021). We construct time series for a point on the ground above this sill from 2016–2022, and see that it deflated at a non-linear rate by $>$ 35 cm from its emplacement in 2018 (Figure 4.6). This intrusion is a unique in that crystallisation is occurring in an off-volcano intrusion into country rock, rather than within a Trans-Crustal Magmatic System.

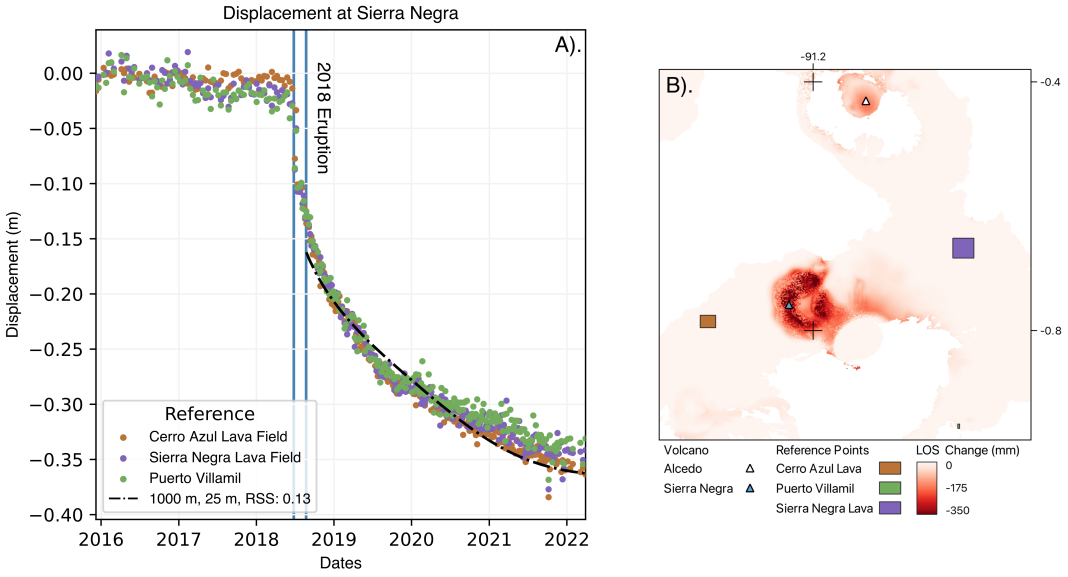

Figure 4.6: Post-eruptive crystallisation at Sierra Negra. A). Time series at Sierra Negra extending from 08/12/2015–30/03/2022. The vertical blue lines denote the onset (June 26$^{\text{th}}$) and end of the 2018 eruption (August 23$^{\text{th}}$). Each set of coloured scatter points show deformation, at the blue triangle, relative to the indicated reference areas. The hatched red lines show estimated model predictions, while time, and displacement in metres are given on the x- and y-axes, respectively. B). Cumulative displacement map showing the location of the plotted points and reference areas, the crosses on the map indicate the grid of latitude and longitude.

At Sierra Negra, we find that maximum subsidence rates from a 25 m thick by 1000 m wide sill, intruded at 1 km (Table C6), agree with subsidence observations following the sill emplacement (RSS: 0.13), after the conclusion of the eruption. Unlike other volca-

noes in this section, there is little ambiguity about the timing of the magmatic intrusion, with the eruption lasting from 26/06/2018–23/08/2018. We model displacement from August 24th, attributing the initial 16 cm of subsidence to syn-eruptive lava effusion from fissures at the terminus of the intrusion, over the 58 days of the eruption (Vasconez et al., 2018).

4.4.3 Global Volcanoes

We also model crystallisation for each of Asama, Paka, Silali, and TVZ, the results of which are outlined in Table 4.2, and Appendix C. In these examples, we find that while we can model this subsidence as crystallisation, the required model parameters do not agree with observations, and other mechanisms may be present (e.g. hydrothermal activity.)

Table 4.2: Summary of modelled parameters for crystallisation at various volcanoes (detailed results in Appendix C).

Volcano	Eruption	Depth	Width	Thickness	RSS	Intrusion Date	Fig.
Asama	2019	5 km	5000 m	50 m	0.74	2003	C6
Paka	7550 BCE	2.8 km	5000 m	40 m	0.19	2008	C7
Silali	5050 BCE	3.9 km	4000 m	50 m	0.22	2006	C8
TVZ	260 CE	6 km	6000 m	200 m	0.6	2003	C9

4.4.4 Parameter Space

We calculate maximum displacement, cooling time and average subsidence rate in Figure 4.7. Here we vary intrusion width using values of 1000 m, 2000 m, 3000 m, 4000 m, 5000 m, 6000 m, 7000 m, 8000 m, 9000 m, and 10000 m, and thickness using values of 10 m, 20 m, 25 m, 40 m, 50 m, 100 m, 125 m, 200 m, 250 m, and 500 m. Petrological input values are found in Table C2, and we model for an intrusion at 3 km depth (e.g. that at Alcedo). In Figure 4.7, we plot on contours of average displacement rate at -5 $mm\ yr^{-1}$, -10 $mm\ yr^{-1}$, -20 $mm\ yr^{-1}$, -50 $mm\ yr^{-1}$, -100 $mm\ yr^{-1}$, and -250 $mm\ yr^{-1}$, to illustrate the subsidence rates of the volcanoes presented in Figure 4.2. We find that each of the rates presented in Figure 4.2 fall within our parameter space, with a clear relationship between intrusion thickness and width; for example, the subsidence rate of -5 $mm\ yr^{-1}$ at Mt. Baker can be modelled using values of 1000 m width and approximately 50 m thick, as well as 4000 m width and 500 m thick.

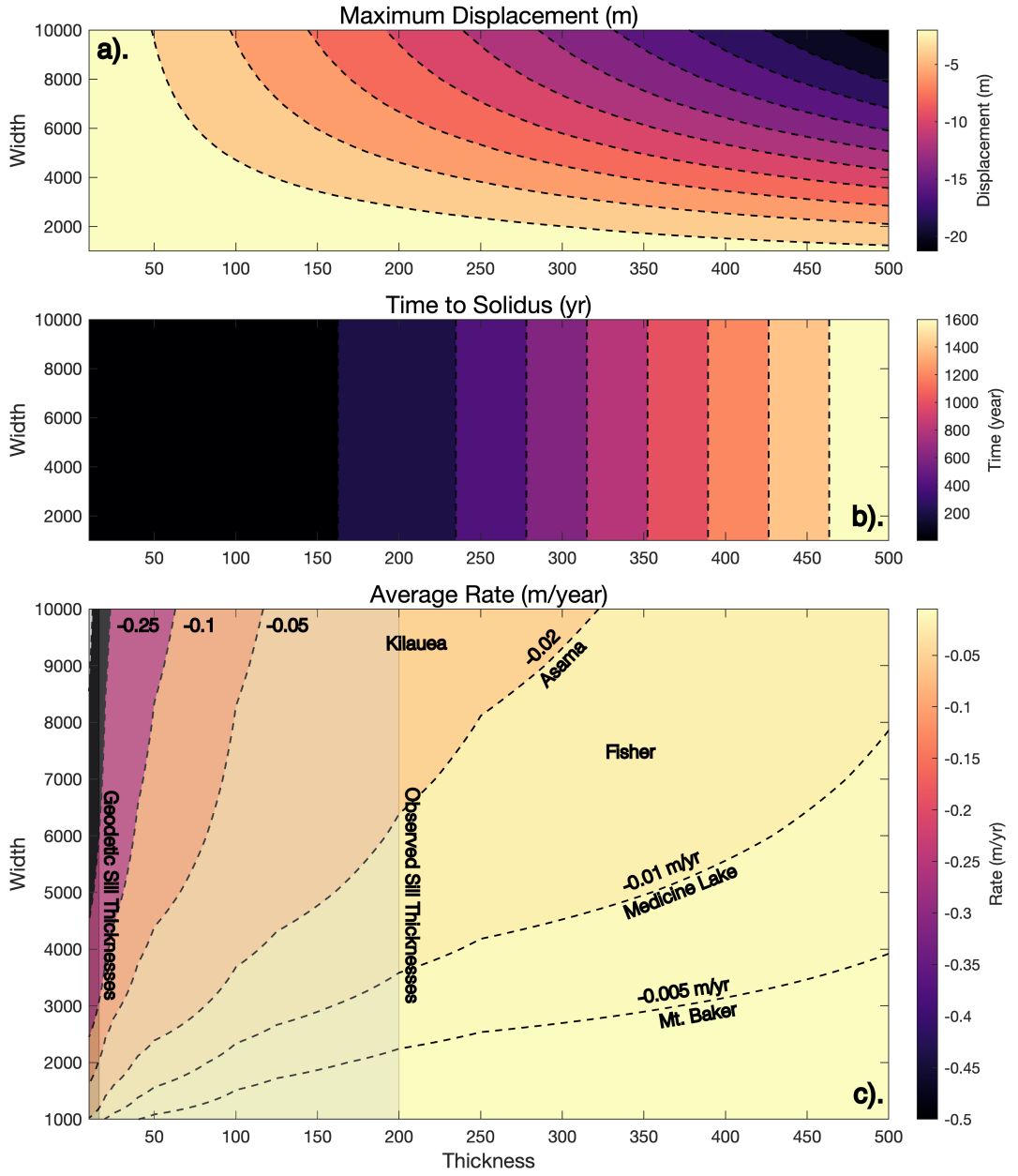

Figure 4.7: Parameter space plots testing the effect of varying width versus thickness in a crystallising intrusion. We use the parameters in Table C2, varying width between 1000–10000 m, and thickness from 10–500 m. a). Contours of maximum displacement when varying width versus thickness. b). Contours of maximum time to crystallise when varying width versus thickness. c). Contours of average rate when varying width versus thickness. Average rate is taken across the whole post-intrusion period (e.g. from the time of intrusion, until solidus is reached). Plotted are the contours for rates of -5, -10, -20, -50, -100, and -250 $mm\ yr^{-1}$, representing the rates plotted in Figure 4.2. These are also annotated with the relevant volcanoes where these rates have been observed, while the grey boxes denote ranges of common sill thicknesses, as presented in Figure 4.4.

4.5 Discussion: Crystallisation as an Origin for Long-Term Subsidence

As shown in Figures 4.5–4.7, crystallisation can cause long-term subsidence at volcanic centres. However, there are several factors that alter the observed deformation profiles such that they differ from that modelled.

Of the volcanoes tested in Section 4.4, Sierra Negra is the only instance where the exact time of intrusion is known, and where we can be near-certain that there was no magmatic replenishment once the eruption ended. This scenario most closely represents that of our model; a single sill intruded in one go into an elastic medium, that immediately begins to cool and crystallise. Under these conditions, we find that our model performs well, with the lowest RSS value (0.13) of any volcano, and we match the post-eruptive deformation trends with crystallisation of a 25 m thick sill (Figure 4.6). However, during this eruption, there was almost no pre- or syn-eruptive uplift at the intruded sill, inconsistent with the intrusion of a 25 m thick sill. This may be suggest that is heavily overprinted by co-eruptive subsidence as magma flowed through the sill to the eruptive fissures. Therefore, while we can well model post-intrusive subsidence due to cooling and crystallisation, in reality, the eruption dynamics are more complex than we capture with our model.

At Alcedo, we can estimate when magmas were intruded by it's recent volcanic activity. We find that our observations of subsidence can be modelled by crystallisation of a 50 m thick sill, intruded at 3 km. However, this model has the worst fit of any case studies (RSS of 1.39), suggesting additional complexity than is considered by our model. The crystallising magma is located within the sub-volcanic TCMS, and the surrounding mush is unlikely to transmit stresses elastically, but rather in a time-dependent manner (e.g. poroviscoelastically (Castelino et al., 2021)), such that we may underestimate long-term deformation by only considering the elastic component. There is likely to be pre-existing magma already crystallising here (e.g. Alcedo was subsiding prior to its resurgence, attributed to magmatic crystallisation (Hooper et al., 2007)). Therefore, while we consider instantaneous emplacement of large sills, at Alcedo subsidence is rather likely a combination of volume loss in a pre-existing reservoir, that periodically get replenished, rather than of a large individual sill, intruded in one go (e.g. Sierra Negra). Despite these complexities, our model can approximate intrusions at active volcanoes to give an estimate of the volume of magma crystallising there.

This approximation allows us to plot the parameter space across which rate varies with intrusion thickness and width, as shown in Figure 4.7, where we plot rates from Figure 4.2. There is a clear relationship between intrusion thickness and width. How-

ever, as at Alcedo, the rates presented in Figure 4.7 and Figure 4.2 may be modified by processes such as magma replenishment, as well as thermoelastic contraction, volatile exsolution, and hydrothermal activity.

4.5.1 Crystallisation and Thermoelastic Contraction

None of Paka, Silali or the TVZ have erupted since at least 260 CE. While we can model observed displacement as crystallisation (RSS values of 0.5, 0.21, and 0.6, respectively) (Figures C7–C9), doing so requires thick sills (40–200 m) that intruded between 2003–2008. Aside from Paka (Biggs et al., 2009) (where subsidence due to crystallisation is a poor fit with the data (Figure C7)), there is no evidence at TVZ or Silali that such intrusions occurred. Indeed, the millenia-scale gap in extrusive volcanism suggests that large magmatic intrusions do not routinely occur. As such, it is difficult to attribute observed subsidence signals to magmatic crystallisation. These are mature volcanoes with caldera structures, likely underlain by trans-crustal magmatic systems. We suggest that rather than invoking intrusions that there is little evidence for, long-term subsidence may instead be explained by thermo-elastic contraction of the sub-solidus mush that composes the magmatic system as it cools (Figure 4.8, Table 4.4).

We estimate vertical contraction in a mush due to thermo-elastic contraction using Equation 4.4 (e.g. Chaussard (2016)), where Δh is thickness change, η is the thermo-elastic expansion coefficient of magma (2×10^{-5} (Wang and Aoki, 2019)), ν is Poisson's Ratio (0.25), ΔT is temperature change, and t is time.

$$\Delta h(t) = h\eta\frac{1+\nu}{1-nu}\Delta T(t) \tag{4.4}$$

To calculate the minimum expected vertical contraction, we use the TCMS at Fernandina as an example. This is one of the few locations where the distance between stacked sills has been geodetically observed, which we take as an indicative value for minimum TCMS thickness. Here, the TCMS is at least 4 km thick, with reservoirs detected at depths of 1 km and 5 km (Bagnardi, 2014; Geist et al., 2014). Taking this value for h, we find that average cooling of just $0.5^oC\ yr^{-1}$ would result in almost 7 cm of vertical contraction of the TCMS. Such contraction allows volume loss to continue in the absence of liquid magma, and likely contributes to the majority of examples of long term deformation: 21 out of 27 examples in Figure 4.2 are mature, caldera volcanoes.

4.5.2 Volatile Exsolution and Long-Term Subsidence

In this study we modelled deformation from an anhydrous magma as the simplest case for understanding the effect of crystallisation on deformation. In nature, such compo-

sitions are uncommon — volatile bearing magmas are ubiquitous at convergent boundaries, and low concentrations of H_2O (e.g. < 1 wt% (Sigurdsson et al., 2015)) are routinely found in both ocean island basalts, and mid-ocean ridge basalts (Sigurdsson et al., 2015). These magmas have the potential to produce higher magnitude volume changes, and deformation, under certain conditions. As solid, anhydrous crystalline phases form during cooling, the magmatic melt fraction relatively enriches in volatiles (e.g. Caricchi et al. (2014)). This relative increase in concentration, and corresponding vapour pressure increase, allows magma-borne volatiles to saturate, and exsolve in homogeneous second boiling (Cashman, 2004; Caricchi et al., 2014; Hildreth, 2017). These exsolved volatiles may then generate surface displacements depending on the volatile fraction and permeability of the melt (Table 4.4).

We performed order of magnitude tests using MELTS, as presented in section 4.2, to illustrate the effect of volatiles on surface displacement by calculating volume changes in a cooling basalt with incrementally increasing H_2O (Table 4.3). We see that volatile exsolution dramatically affects the magnitude of volume change in a cooling magma. Exsolution will increase the magnitude of volume change in an open system, and counteract volume change due to crystallisation in a closed system. Even 0.5 $wt\%$ H_2O causes an extra 2% volume change in an open system, and 5% less volume change in a closed system, while 1 $wt\%$ H_2O in a closed reservoir resulted in positive volume change. Though systems that are fully open or closed to fluid escape are unlikely in nature, these end-member values (Table 4.3) illustrate the potential effect that volatiles may have on deformation in a crystallising magma.

In addition to changes in volume, volatile exsolution could have an affect on the crystallisation models presented in Section 4.4. Volatiles increase magmatic compressibilty, altering the relationship between volume change in the reservoir and corresponding deformation (analytical source models assume incompressibility)(Rivalta and Segall, 2008). Volatiles act as network breakers in silicate melts, lowering the solidus temperature (Green, 1973), thereby increasing the thermal range across which crystallisation can occur. In open reservoirs, volatiles may advect heat, increasing the rate of cooling, as they ascend to shallow hydrothermal systems, causing uplift and seismicity. Though we assume anhydrous magmas in our modelling, clearly the role of volatiles is substantial, and would affect our results if considered. Of the volcanoes studied in Section 4.4, the TVZ has extensive geothermal activity, Alcedo has a vigorous caldera fumarole field, while both Asama and Paka have evidence of hydrothermal activity. As such, the stalled source magma must be somewhat open, and volatile exsolution must change the observed subsidence rate, by increasing the magnitude of volume loss, and altering the rates at which it occurs by increasing the range between liquidus and solidus, and by thermal advection.

Table 4.3: Modelled volume change for a basaltic composition illustrating the effect of varying initial H_2O. Volume change for each composition is modelled using MELTS, with the corresponding displacement calculated using the pCDM approach outlined in Section 4.2.3. Modelled intrusion is approximately 25 m thick, 2 km wide, at 4 km depth.

H_2O Amount	Behaviour	ΔV
Anhydrous	N/A	-8.5%
0.5 $wt\%$	Escaped	-10.6%
	Trapped	-3.2%
1 $wt\%$	Escaped	-12.4%
	Trapped	$+2\%$
2 $wt\%$	Escaped	-15%
	Trapped	$+11\%$

4.5.3 Hydrothermal Activty and Long-Duration Subsidence

An active volcanic hydrothermal system (e.g. Fisher Caldera, USA, Alcedo, Ecuador) may generate phases of uplift when magma-derived fluids become trapped in a carapace above an intrusion (Fournier, 1999). This carapace will increase in volume, generating uplift until a critical pressure is met, at which point it will depressurise and deflate. This style of deformation is distinct from that of crystallisation and volatile exsolution by periodic uplift and subsidence, seismicity, and fumarole release (Pritchard et al., 2019). While easily distinguishable from purely crystallisation-driven deformation, a purely meteorological hydrothermal system above the intrusion may contribute to crystallisation-driven deformation without any obvious changes in deformation direction. Like volatiles escaping a reservoir, this occurs by the advection of heat from the country above the intrusion, thus increasing the cooling rate within the intrusion (Table 4.4).

Hydrothermal and volatile activity are distinguishable from crystallisation through seismicity, gas emissions, and may be detected via gravimetric techniques (Pritchard et al., 2019). In cases where these occur alongside long-term volcanic deformation, volatile activity plays a role in long-term deformation. However, in cases where long-term deformation occurs without these observations (e.g. Medicine Lake, USA), then crystallisation may be dominant in driving deformation.

4.6 Conclusions

We compare modelled time-series of crystallisation with real InSAR observations at six volcanoes, and evaluate the impact of crystallisation on long-term subsidence under three scenarios.

The effect of crystallisation on surface subsidence is most evident during a magmatic sill intrusion into country rock. Here, the timing of intrusion (and onset of crystallisation)

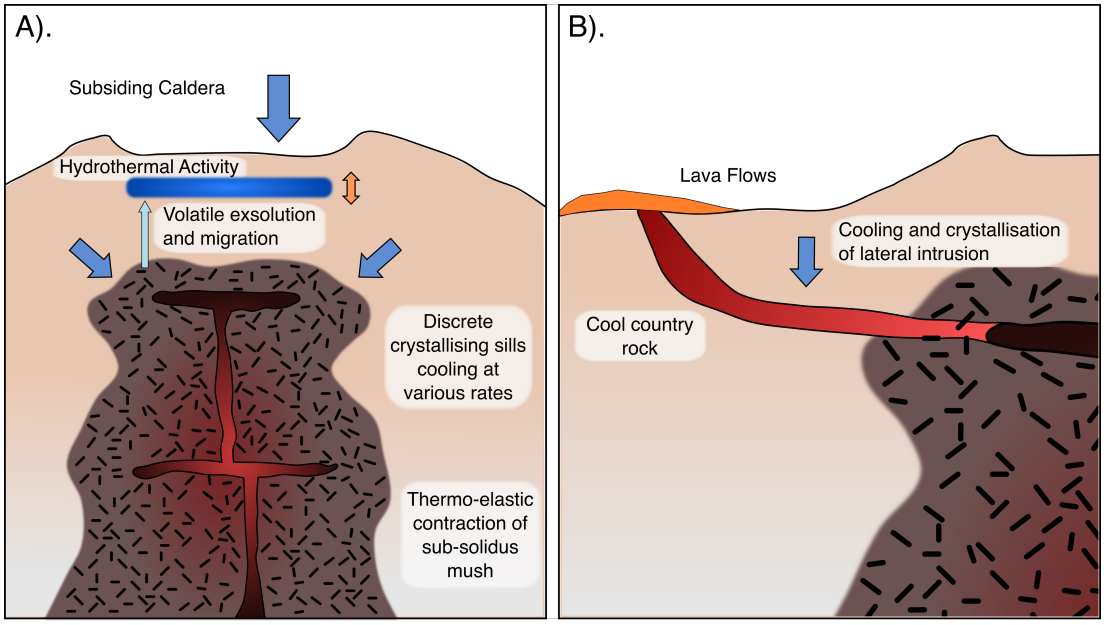

Figure 4.8: Factors that can affect subsidence rates at caldera volcanic systems. A). Cooling and contraction of a TCMS. Discrete lenses distributed vertically lose volume as they undergo crystallisation and contract. As magma supply wanes, thermo-elastic contraction of the surrounding mush may sustain long-term subsidence, even in the absence of active volcanism. Volatiles may alter the observed deformation profiles, and interact with an overlying hydrothermal system. B). Crystallisation of a sill, intruded into country rock. Once magmatic influx has stopped, crystallisation will be the dominant cause of volume loss and subsidence, as the magma cools from liquidus to solidus.

is well constrained, the country rock responds elastically, and there is no overlying processes (i.e. hydrothermal) that can contribute to subsidence rates. However, modelled subsidence here should be considered carefully in the context of pre- and syn-eruptive deformation, e.g. if a thick sill is required for crystallisation patterns, is there any evidence of such an intrusion?

At active volcanoes, crystallisation of magma in the TCMS contributes to subsidence though is altered by several factors. The rheology of the surrounding mush facilitates time-dependent rather than instantaneous subsidence. The time at which crystallisation starts is more ambiguous, altered by pre-existing magmas and subsequent magmatic replenishment. Volatile and hydrothermal activity widely occur at active volcanoes, and significantly affect both the magnitude and rate at which volume loss occurs. In these settings, rather than individual intrusions, we suggest that most observations of long term-subsidence are explicable by the combination of crystallisation-driven contraction of multiple intrusions cooling at discrete intervals in the crust, overprinted by mush rheology as well as volatile and hydrothermal effects .

Long-term subsidence at historically quiescent volcanoes is unlikely to be driven by crystallisation. This would require recent magmatic intrusions at volcanoes that have not erupted, in some cases, for millennia. Instead, we speculate that thermo-elastic contraction of the cooling TCMS may explain these observations, though further research is required to investigate this hypothesis.

Table 4.4: Factors that influence deformation rate

Variable	Value	Cooling Time Change	Volume Change
Hydrothermal	Pressurisation	-	Increase
	Depressurisation	-	Decrease
	Advection	Decrease	-
Volatiles[a]	Closed System Exsolution	-	Increase
	Open System Exsolution	-	Decrease
	Open System Advection	Increase	-
TCMS	Thermo-elastic Contraction	-	Increase
	Pre-existing Magma	Increase	Increase
	Subsequent Intrusion	Increase	Increase
	Time dependent response to intrusion	-	Increase
	Time dependent response to crystallisation	-	Decrease

[a] Magmatic volatiles increase compressibility and lowers the solidus

Chapter 5

Discussion and Conclusions

This PhD thesis investigated the controls on long-term magmatic processes, and the role of InSAR in their study. I have considered these processes across multiple temporal ranges, from months, when looking at resurgence at Darwin volcano (Chapter 2), to years, as neighbouring Galápagos volcanoes deformed in a correlated manner (Chapter 3), to decades, as magma crystallisation driven subsidence (e.g. at the Taupo Volcanic Zone). I have also varied the scale of our studies, from a volcano-by-volcano consideration in Chapter 2, to all of the major Western Galápagos volcanoes in Chapter 3, to studying multiple global volcanoes from diverse geological settings (from the Kenyan Rift, to the North Island of New Zealand), in Chapter 4. Throughout this work, I have demonstrated the utility of InSAR for the study of volcanism across varying temporal and spatial scales, with an emphasis on understanding the underlying magma dynamics.

In the following chapter, I first (Section 5.1) summarise and discuss the outcomes of each preceding thesis chapter. I then discuss the future of volcano monitoring in the Western Galápagos, and on long-term volcanic subsidence, in Section 5.2. Finally, I conclude I this thesis in Section 5.3.

5.1 Magmatic processes and Satellite InSAR

In Chapter 1, I outlined the aims of this PhD thesis, and the academic questions that I hoped to address. Here, I explain the significance of my findings, and how they address the aims of this project.

5.1.1 Shallow Unrest in the Western Galápagos

In Chapter 2, I presented a synthesis of recent volcanic unrest in the Western Galápagos, in the context of volcanic ground deformation. Using Sentinel-1 InSAR data, I made new observations at each Western Galápagos volcano, and show how they relate to

previous geodetic, seismic, and petrological studies at each volcano.

At Alcedo, I make the first observation of subsidence at the hydrothermal zone, in the southwestern corner of the caldera. This may be one of the best examples in the global geodetic record of subsidence due to the cooling of a sill, overprinted by hydrothermal subsidence. In previous studies, and in Chapter 4, subsidence at Alcedo has been assumed to be driven by magmatic crystallisation (Hooper et al., 2007). Clearly, this magma is volatile-bearing (Goff et al., 2000), and actively contributes to the deformation field at Alcedo (Chapter 2). All together, I show that deformation at Alcedo is complex, with magmatic, tectonic, and hydrothermal components. Like Sierra Negra, the intra-caldera fault at Alcedo is a major control on deformation there (Galetto et al., 2019; Bagnardi, 2014), with magma–tectonic interactions during periods of uplift (Figure 5.1). At both volcanoes, fumarolic activity is concentrated on the area on top of the intra-caldera fault, which I believe raises an interesting question: Are these the only Galápagos volcanoes with fumarole fields because they are "dying" (e.g. shallow magma is cooling and degassing), or because they are the volcanoes with easy conduits to the surface, along the intra-caldera fault?

The 2017 unrest at Cerro Azul there has been studied multiple times (Guo et al., 2019; Bagnardi, 2017), though Chapter 2 is the first time it considered in the context of previous unrest. I find that volcanism has been concentrated on the eastern flank of Cerro Azul, going back as far as 1979, and possibly earlier (Figure 5.1). I also make new observations of deformation on the western flank of the volcano, and suggest that mass wasting, in the direction of the Caleta Iguana landslide scarps is responsible (Figure 5.1). While the area around Cerro Azul is uninhabited, and eruptions there occur as effusive fissures, it is still the only Western Galápagos volcano with a known loss of human life during eruption (Naumann and Geist, 2000). As such, this observation may be important for future eruption hazard mitigation.

Like all Western Galápagos volcanoes, Darwin has a summit caldera, exposed lava flows, and experiences regular magma flux (Chapter 2). However, it is the only Galápagos volcano to have not erupted in the 20^{th} century, and, at the time of writing, has not erupted in over 200 years. Indeed, there are only three recorded eruptions at Darwin on the Global Volcanism Program. Why then, when I see evidence of magma intrusion there in 2020 (Figure 5.1), and other studies do between 1992–1995 (Amelung et al., 2000), does Darwin erupt so infrequently? Perhaps the volumes intruded are insufficient to trigger an eruption, though further work such as seismic and petrological surveys (e.g. melt inclusion analysis), should be carried out to better answer this question.

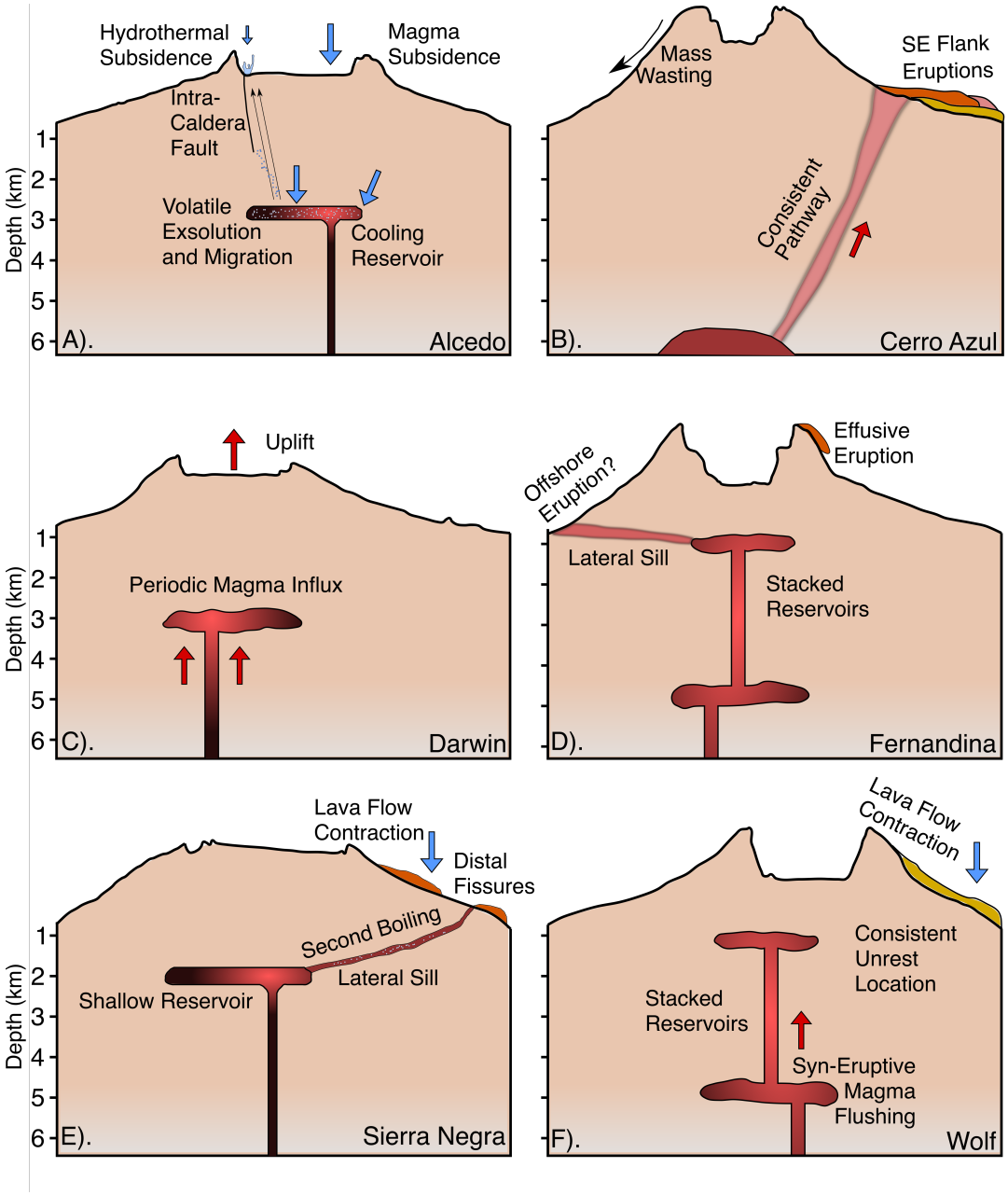

Figure 5.1: Shallow magmatic processes in the Western Galápagos. A). Alcedo: Hydrothermal and magma driven subsidence, influenced by the intra-caldera fault. B). Cerro Azul: Consistent pathway from the magma reservoir at 6 km depth to unrest locations on the eastern flank, as well as mass wasting on the western flank. C). Darwin: Occasional magma influx into the magma reservoir at 3 km depth, driving uplift. D). Fernandina: The 2020 eruption had both an effusive component at the caldera, as well as a potential offshore eruption. E). Sierra Negra: The 2018 eruption was followed by second boiling at the lateral sill, as well as lava flow contraction on the northern flanks of the volcano. F). Wolf: Magma flushing during eruptions and consistent eruption location, as well as subsidence of effused lava flows.

Fernandina erupts regularly, and has been well studied by multiple disciplines (Bagnardi and Amelung, 2012; Geist et al., 2006a). However, I show in Chapter 2 that

eruptions there may be more nuanced than previously thought, by presenting evidence for submarine eruptions off of the western coast of Fernandina Island (Figure 5.1). I see evidence that the 2020 eruption had a lateral component that migrated westwards towards offshore rifts and lava fields (Geist et al., 2006b). This style of lateral intrusion is one of many at Fernandina, with similar intrusions occurring on the southeastern corner in 2006 and 2007, and on the northeastern corner in 1927 (Bagnardi and Amelung, 2012). These observations emphasise the complex magmatic architecture of Fernandina. There are a series of stacked reservoirs there, though which primitive basalts flush through during eruptions (Galetto et al., 2023). From these reservoirs radiate lateral intrusions, in multiple directions, some of which may culminate in an offshore eruption. Fully constraining the dynamics of such underwater eruptions is challenging using satellite InSAR, but improved seismic monitoring would be useful to study future offshore eruptions, while optical satellite imagery may shed further light on the 2020 eruption.

Sierra Negra is the best studied volcano in the Western Galápagos, and underwent a major eruption in 2018 (Bell et al., 2021b). Here, I make several novel observations of post-eruptive deformation. Lavas on both the flank and distal fissures contracted and subsided, as did the lateral sill connecting the caldera and fissures (Chapter 4). The sill contraction is also notable, given the period of uplift at the terminus of the lateral intrusion in late 2018 (Figure 5.1). This is somewhat of an unintuitive observation — what processes in a crystallising sill could cause uplift? Volatile-driven unrest during second boiling has been observed at numerous volcanoes (e.g. Okmok (Caricchi et al., 2014)), and I consider it as a viable mechanism here as it accounts for the delay in uplift (e.g. magma saturation during second boiling), and the uplift at the terminus of the sill — e.g. volatile ascent upslope through the intrusion. In Chapter 2, I show the temperatures at which volatile exsolution would occur for a Sierra Negra magma intruded at 1 km depth, though further work should be carried out to constrain the time taken to reach these temperatures, and the impact of volatiles on magma compressibilty.

At Wolf, I make the first observations of subsidence due to lava flow contraction at the volcano (Figure 5.1). This subsidence is significant in that it is the same magnitude in both track directions. Lava flows should contract isotropically as they cool, meaning that line-of-sight change should be the same regardless of look direction, as is seen here. However, for every time series at a Galápagos volcano, there is significant magnitude differences between ascending and descending tracks. The fact that lava flow contraction is the same proves that this discrepancy is not a systemic issue, but rather a feature of Galápagos deformation. Therefore, the presence of trapdoor faults (e.g. hinged at one side) at Galápagos calderas may facilitate different line-of-sight changes, and shows the importance of considering both track directions when studying deformation here.

5.1.2 Bottom-Up Volcanism

In Chapter 3 of my thesis, I show evidence for correlated deformation at multiple Galápagos volcanoes. This observation showcases the utility of InSAR when considering volcanic unrest over extended spatial areas. Ground-based systems are effective in monitoring the areas local to their deployment (e.g. Sierra Negra). In cases where there are multiple active volcanoes, but limited ground-based systems (as at the Western Galápagos), then such systems are insufficient to identify correlated unrest between volcanoes. This is why, in Chapter 3, and in Baker (2012), InSAR is so effective at detecting correlated deformation. These observations again show why unrest at groups of volcanoes should be considered holistically, rather than as individual systems.

Magma is stored as lenses of melt that are vertically distributed throughout the crust at discrete intervals (Cashman et al., 2017). These lenses are surrounded by a crystalline mush, which develops as the volcano matures (Geist et al., 2014). At the Galápagos, there is evidence that these systems are vertically extensive (e.g. Wolf (Stock et al., 2018)), and laterally extensive (e.g. Fernandina (Bagnardi and Amelung, 2012)), and periodically have magma flush through them during eruptions (Stock et al., 2020). Each volcano of the Western Galápagos is underlain by an extensive magmatic system derived from the Galápagos plume. Volcanoes here do show individual unrest characteristics; the neighbouring Sierra Negra and Alcedo deform in almost exactly the opposite manner (long-term uplift vs long-term subsidence), as do Darwin and Fernandina (quiescent vs regularly erupting) (Chapter 3). However, the surging style of eruptions, the phases of eruptive activity and quiescence that the entire islands go though, as well the correlated deformation patterns, shows that the degree of volcanism here is periodic, and multiple volcanoes within the larger volcanic system, respond to temporal variations in magma flux (Chapter 3). This phenomenon is easily observed in the Western Galápagos, due to the utility of InSAR there, though has been suggested at Hawai'i (Poland et al., 2012), and is likely to occur at the Azores, as well as at other global volcanoes (Figure 5.6).

In Hawai'i, Gonnermann et al. (2012) show that correlated unrest between Mauna Loa and Kīlauea can be explained by pore pressure changes in an asthenospheric melt layer. Recently, Wilding et al. (2023) seismically image such a layer, the Pāhala Sill Complex, and depths of between 36–41 km. Given the similarities between Hawai'i and the Western Galápagos (ocean island hotspot volcanoes, with correlated deformation), I invoke a similar layer here in Chapter 3 to account for our observations of correlated deformation. This layer facilitates dynamic stress transfer between volcanoes, while allowing each to remain isotopically distinct. It may also explain the observations of illegitimate magma by Geist et al. (1999). These magmas account for a small fraction of all erupted in the Galápagos, and I suggest that they can likened to glomyrocrsyts or xenoliths, e.g. a distinct composition that a magma picks up as it moves from the plume to surface, passing through this melt layer (Figure 5.3). Additionally, I

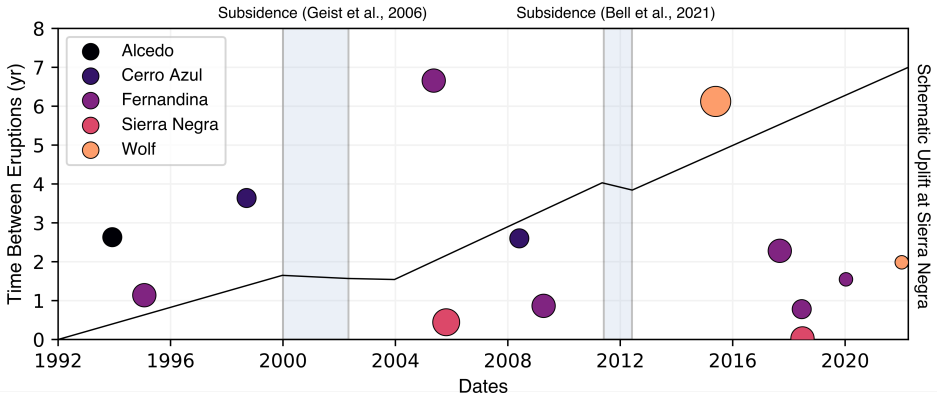

Figure 5.2: Time between eruption and eruption date, for each Western Galápagos volcano, from 1992–2022. A schematic illustrating uplift at Sierra Negra is plotted over this, and noted periods of subsidence are annotated.

consider this correlated deformation in the context of the work on the lateral extent of volcanic connectivity by Biggs et al. (2016) in Figure 5.4. Every combination of pairs of Galápagos volcanoes plot in the "deep source" zone, corresponding with my hypothesised sub-crustal melt layer.

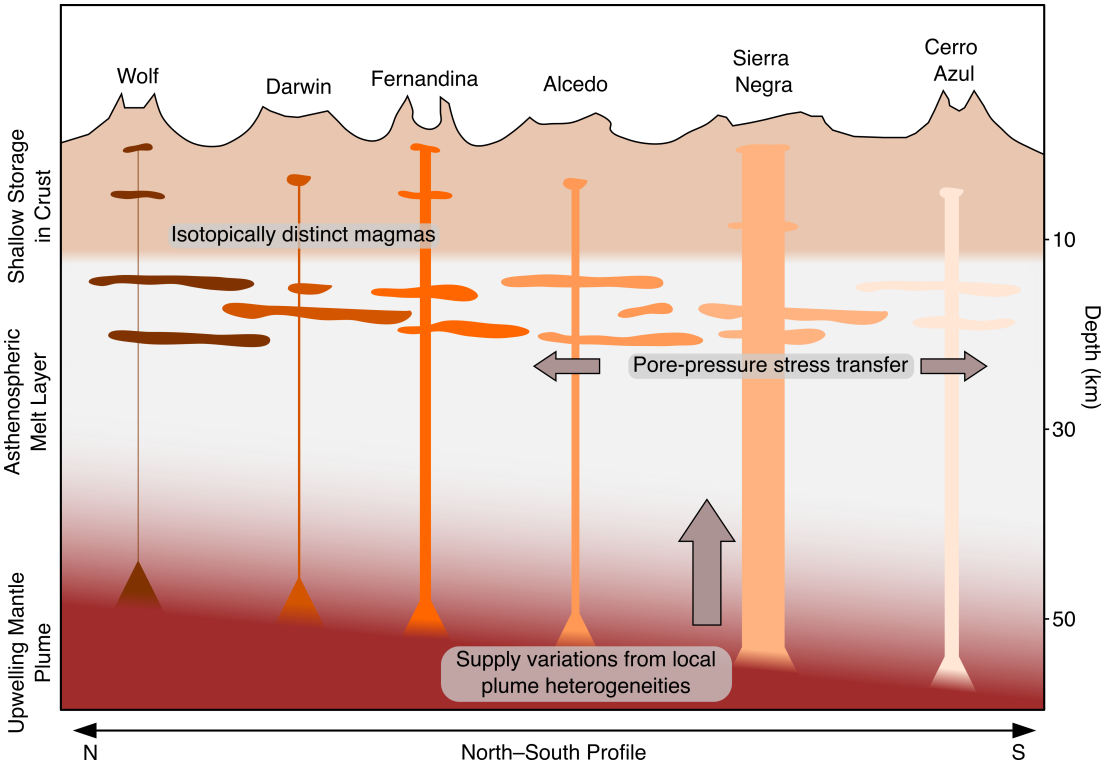

Figure 5.3: Mechanism by which Sierra Negra affects regional volcanism in the Western Galápagos. Local compositional heterogeneities in the plume affect magma supply to Sierra Negra. Dynamic stresses during periods of heightened supply transfer through an asthenospheric melt layer to neighbouring volcanoes.

However, I also show in Chapter 3 that magma supply to each volcano is not equal, with the shallow reservoir at Sierra Negra receiving more magma than all the other volcanoes combined (Figure 5.3). As such, it should have the greatest impact on pore pressure changes in the asthenospheric melt layer. Magma supply from an ascending plume is driven by decompressive partial melting, and Pietruszka and Garcia (1999) show that magma supply changes to Kīlauea can be explained by local heterogeneities in the sampled plume region causing temporally varying rates of partial melting. I suggest that such heterogeneities in the region of the plume sampled by Sierra Negra also cause magma supply variations there. Sierra Negra has uplifted, on the order of metres, more or less steadily since it was first observed by InSAR in 1992. However, there are two notable exceptions, when it subsided in 2002, and in 2012 (Geist et al., 2006a; Bell et al., 2021b), indicating a decrease in magma supply rate. In both instances, this subsidence occurs during a period of eruptive quiescence, with no eruptions in the surrounding years — simply put, since InSAR observation began here in 1992, if Sierra Negra is uplifting, other volcanoes erupt, and when it is not, they don't (Figure 5.2). There are hints of this occurring historically too, the 1954 uplift of Urvina Bay occurred during the same year as an eruption at Sierra Negra. Though each volcano samples a distinct region of the plume, I suggest that large volumes intruded at Sierra Negra may sufficiently pressurise its neighbours, via dynamic stress transfer, to trigger eruptions. Therefore, I propose that local heterogeneities in the region of the plume sampled by Sierra Negra cause temporally varying magma supply to the shallow reservoir, that ultimately exerts a primary control on regional volcanic unrest in the Western Galápagos. Magma supply to other volcanoes is also controlled by plume heterogeneities, though the lower volumes supplied to each indicates that dynamic stress changes may be more local-scale than Sierra Negra. This may be seen during the 2009 eruption of Fernandina, when both Alcedo and Wolf cease uplifting (Baker, 2012).

5.1.3 Long-Term Subsidence

In Chapter 4, I investigate the potential for magma crystallisation as a mechanism for globally observed long-term volcanic subsidence. To do this, I develop a model that uses an initial magmatic composition to predict volume change with time, for an isotropically contracting sill. This approach allowed me to model volume change due to mineral phase changes, as the magma cooled from the liquidus to the solidus, and did not consider the effects of thermo-elastic contraction, renewed magma influx, or volatile exsolution. I use this model to predict subsidence time series for multiple global volcanoes. I show that while crystallisation can account for this displacement, it typically requires recent intrusions and large volumes of magma, that there is little evidence of, to do so. Though the purpose of this chapter was to specifically investigate the impact of crystallisation, I will now discuss alternative mechanisms for long-term subsidence.

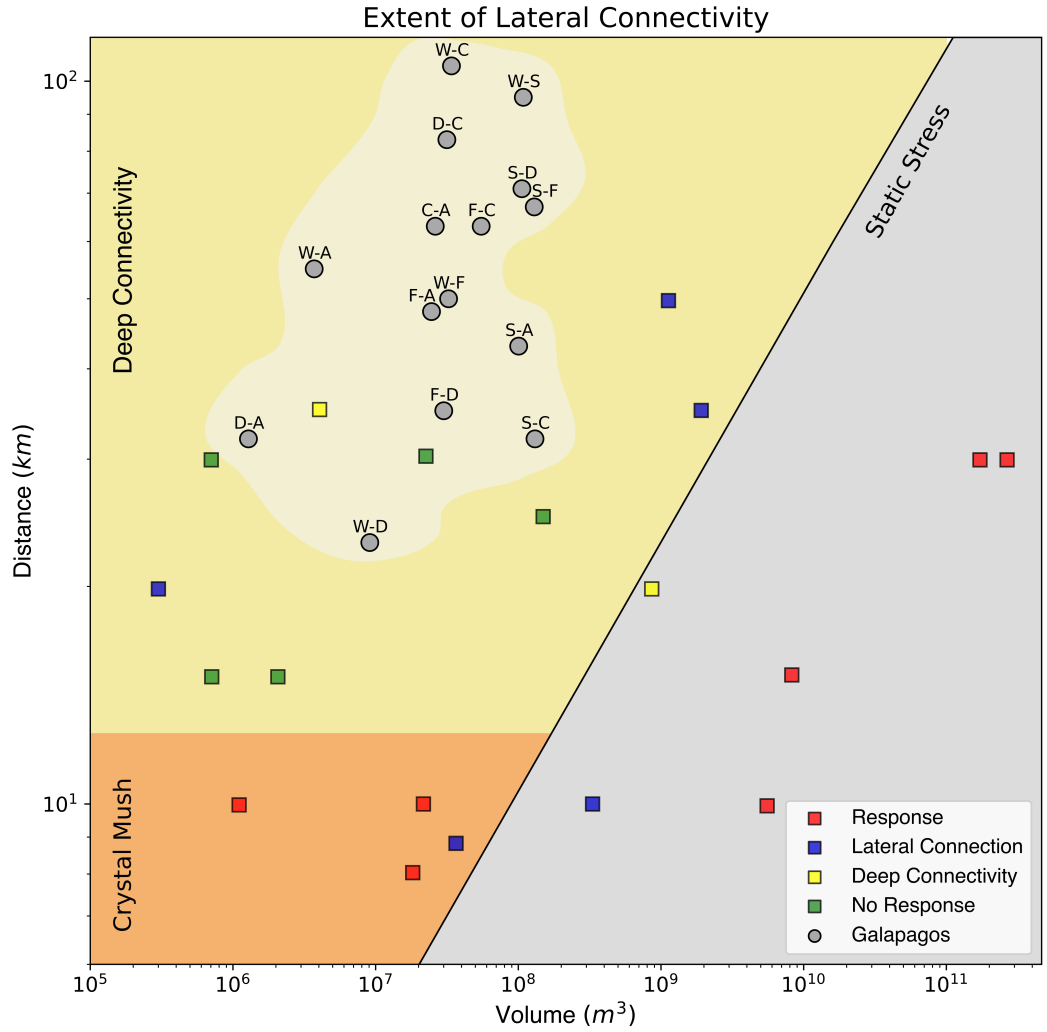

Figure 5.4: Relationship between volume and distance for coupled volcanic activity, modified from Biggs et al. (2016). Previous examples of coupled volcanism (from Biggs et al. (2016)) are plotted in coloured squares, response refers to examples where activity at one volcano had an affect on another, lateral connection refers to examples where there is evidence of a hydraulic link between volcanoes, deep source refers to examples where volcanoes share a deep source, and no response to examples where responses did not occur; grey circles represent values from this study (volumes are from 2017–2022, as found in Chapter 3). The coloured zones correspond to deformation mechanism (Biggs et al., 2016).

Volatiles have a major impact on volcanic displacement patterns. The associated volume change following second boiling can cause uplift (e.g. Long Valley (Hildreth, 2017)), interact with a shallow hydrothermal system (Fournier, 1999), and affects magma compressibility (Rivalta and Segall, 2008). Additionally, volatiles act as network breakers in silicate melts, lowering the solidus temperature and extending the temperature range over which crystallisation occurs (Green, 1973). As such, even if I assumed, while modelling crystallisation, that exsolved volatiles did not cause any uplift, or shallow hydrothermal interaction, or have any effect on magmatic compressibility, I would ex-

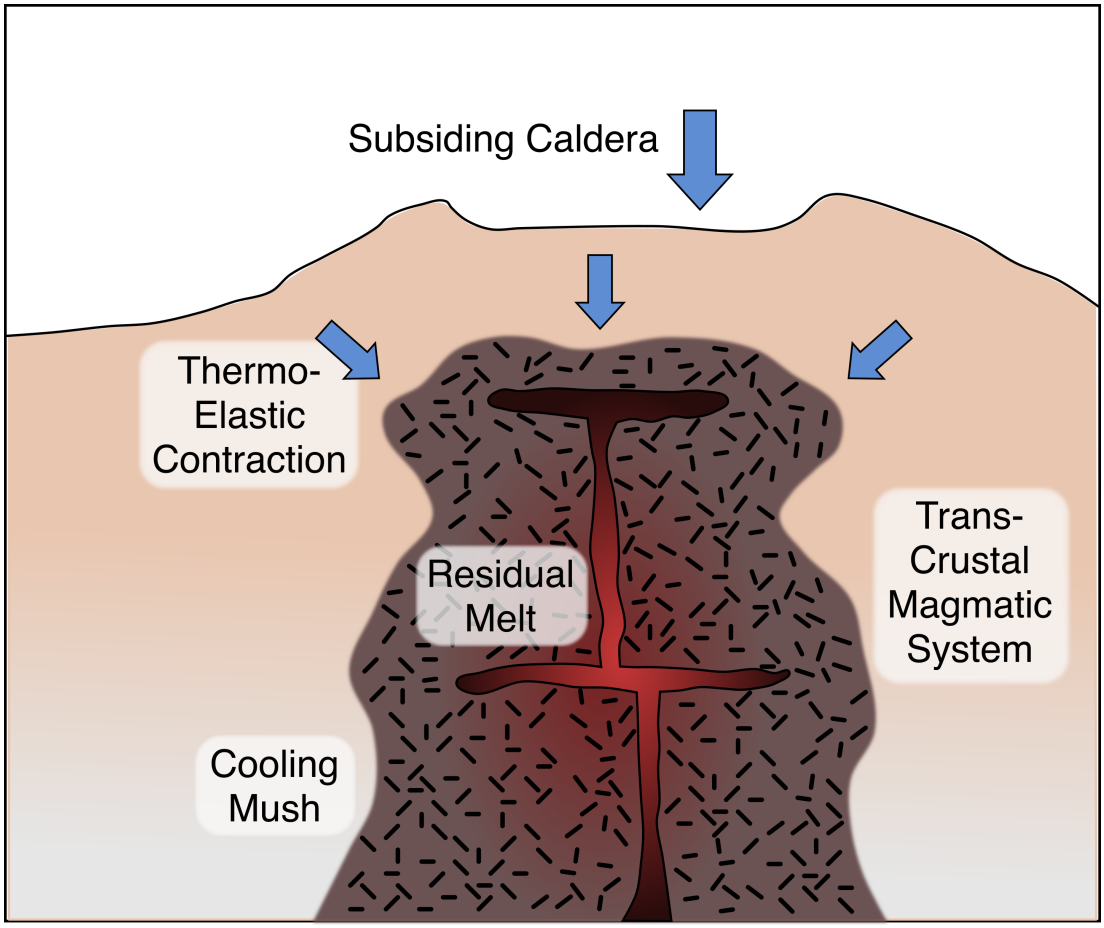

Figure 5.5: Alternative mechanism of long-term subsidence. Cooling-driven thermo-elastic contraction of the sub-caldera mush that composes the TCMZ may drive subsidence in the absence of renewed magma influx.

pect the time taken to cool from liquidus to solidus to be longer, and for crystallisation to occur over a longer time period. This is particularly noteworthy given the extensive evidence of volatiles in the volcanoes considered here — both the Taupo Volcanic Zone and Paka have geothermal plants, while Alcedo has an active hydrothermal system (Chapter 2), and I suspect that second boiling occurred following the 2018 eruption of Sierra Negra (Chapter 3).

However, even with the extended time to crystallisation provided by the presence of volatiles, I find it unlikely that magmatic crystallisation can account for long-term subsidence at volcanoes where there has not been a recent intrusion. Of the volcanoes presented in Figure 4.2, 15 have little evidence of recent eruptive activity. For example, Fisher last erupted in 1830 CE, Medicine Lake in 1060 CE, Taupo in 260 CE, Silali in 5050 BCE, and Paka in 7550 BCE (Venzke, 2023). Each of these, alongside the majority in Figure 4.2, are topped by a summit caldera indicating significant historical volcanism. In Chapter 4 I do not consider the influence of thermo-elastic contraction,

as it negligible during crystallisation due to latent heat release. However, below the solidus, latent heat release no longer occurs, and is a viable mechanism of volume loss. In Lanzarote, there is evidence of thermo-elastically contraction of lava flows for hundreds of years (Purcell et al., 2022). Therefore, I suggest that long-term subsidence at caldera systems that have not experienced recent magma intrusion may be driven by thermo-elastic contraction of the sub-solidus mush that composes the Trans-Crustal Magmatic System, after magma supply has decreased. This mechanism may account for the low rates of subsidence, the lack of recent volcanism, as well of the type of volcanoes that undergo this deformation. I did not explore this mechanism in Chapter 4 in detail, as I did not consider thermo-elastic contraction, and sub-solidus volume loss relevant when modelling subsidence due to crystallisation.

5.2 Future Work

5.2.1 Continued Monitoring of the Western Galápagos

In Chapter 2 I make new observations of deformation at each of the major Western Galápagos volcanoes. I believe that this work would be best complemented by ground-based investigation of the presented results. At Alcedo, fumarole sampling and continuous gas flux analysis, as well as uplift rate, and seismic data, would be useful to study the role of the intra-caldera fault here, how it interacts with the deformation field during periods of uplift, and whether it acts as a conduit for volatiles from the magma reservoir. At Cerro Azul, the presence of an existing pathway from the magma reservoir to the eastern flank could be validated by locating seismic and GPS stations there, as well as looking for further evidence of magma mingling between eruptions (e.g. 1979 and 1998). GPS stations would also be useful on the western flank to further constrain the mass wasting there. At Darwin, monitoring should be continued to look for further periods of magma influx, and a detail field study of it's eruptive history should be carried out. At Fernandina, a submarine component to the 2020 eruption could be confirmed by a retrospective analysis of optical satellite data. Submarine eruptions are often accompanied by an increase in the organic content surrounding seawater, which is detectable by optical satellites. Reviewing offshore southwestern Fernandina from January 2020 for such an increase may be useful to confirm an offshore component. Sierra Negra is well monitored, both by satellites and ground-based techniques. However, I believe that magma supply variations here may affect volcanism across the Western Galápagos, an idea I expand upon in Section 5.1.2. Wolf is the second most active Galápagos volcano since 2015. Despite this, there are no ground-based systems there — the closest seismometers are tens of kilometres away, on Fernandina island and Alcedo. While eruptions in the Western Galápagos rarely pose a risk to human life, there are critically endangered animal species that exist only here (such as the Pink Iguana on Wolf), and

enhanced seismic monitoring may help mitigate against their loss.

5.2.2 Correlated Deformation in the Western Galápagos

In Section 5.1.2, I outline a mechanism whereby volcanism in the Western Galápagos may be affected by dynamic stresses in an asthenospheric melt layer (Gonnermann et al., 2012), caused by temporally varying magma supply changes at Sierra Negra (Figure 5.3). There are several steps to test this hypothesis. First, the existence of this melt layer should be validated. Wilding et al. (2023) record 200,000 seismic events to image the Pahāla Sill Complex. As such, the installation of a dense seismic network with the purpose of imaging the asthenosphere is required. Following this, once the location of this melt layer has been constrained, a model should be developed (after Gonnermann et al. (2012)) to study how such a layer would transmit dynamic pore-pressure stresses. The volume of magma partitioned to the shallow crust at each volcano has been determined in Chapter 3, to provide baseline values for magma supply.

Though extensive ground-based monitoring is necessary to fully complement the satellite work done here, such research is both logistically and financially challenging. However, the Western Galápagos are but one of numerous global volcanic groupings (Figure 5.6). Applying InSAR to these other systems is a resource effective way of expanding the scope of the work carried out here, by studying the effect of bottom-up magmatism, and shared magma dynamics, globally (Figure 5.6). There is already evidence of interaction between Mauna Loa and Kīlauea volcanoes in Hawai'i, an oceanic hotspot similar to the Galápagos, albeit with thicker crust, and fewer sub-aerial volcanoes. In 2002, Mauna Loa switched from prolonged subsidence to uplift, as the rate of magma supply to Kīlauea increased, this was detected by both deformation and seismic data (Poland et al., 2012; Przeor et al., 2022). Of similar volcanic systems, I suggest that the Azores may have the best potential for further identifying correlated volcanic behaviour, due to the thin crust and high number of sub-aerial volcanoes. Similarly, Icelandic volcanoes may also be suitable for detecting correlated volcanic unrest. Though the climatic conditions are much less favourable for InSAR monitoring, the thorough ground-based monitoring networks present there may provide alternate means of monitoring.

5.2.3 Long-term Subsidence

As outlined in Section 5.1.3, I believe that thermo-elastic contraction of magmatic mush at mature volcanic setting may play a greater role in long-term subsidence than previously thought (Figure 5.5). To investigate this, I would develop a model that accounts for thermo-elastic contraction of a large sub-volcanic body. To do this would require volume estimates of a TCMZ in the upper 10 km of the crust (the depth which is resolvable by InSAR), and estimates of the temperature gradient across such a zone. Like

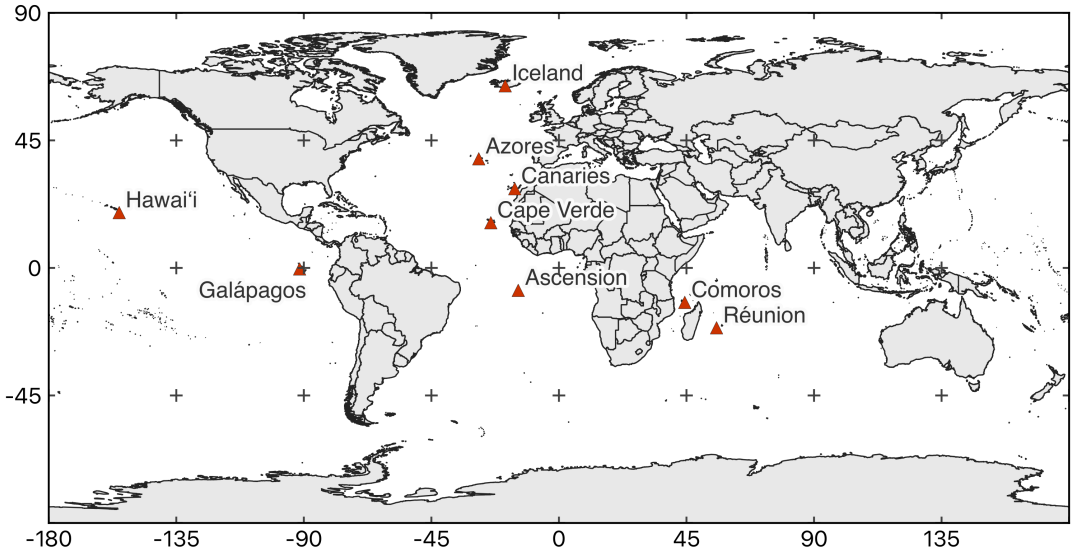

Figure 5.6: Candidate volcanoes for study of periodic magma flux and volcanic unrest.

crystallisation modelling, an isotropically contracting point source would be required, as well as estimates of renewed magma supply rates. I hypothesise that high temperatures throughout this zone would mean that cooling rates (and thermo-elastic contraction rates) would be slow, though the large volumes of contracting material would allow deformation to continue long after crystallisation has finished (Figure 5.5). Once developed, this model could be used alongside the crystallisation model presented in Chapter 4, to fully capture the subsidence due to volume loss in a TCMS, from initial magma intrusion to late-stage mush contraction.

5.3 Concluding remarks

In this thesis, I have used satellite InSAR data to investigate magma dynamics in the Western Galápagos and beyond. The Western Galápagos are an excellent natural laboratory for studying volcanic ground displacement, and I have shown that these volcanoes deform in response to common bottom-up processes. I speculate that this correlated deformation is caused by magma supply variations at Sierra Negra, and believe that Western Galápagos volcanism should be considered holistically, from correlated unrest, to local plume heterogeneities, to temporally varying eruption clusters. I outline future steps, such as the analysis of optical satellite imagery during the 2020 eruption of Fernandina, and improved ground-based monitoring at Wolf, that would complement the work presented in Chapter 2. Future seismic surveys, and pore pressure modelling that may be use to test the hypothesis of an asthenospheric melt layer presented in Chapter 3. Though this layer has not been previously detected at the Galápagos, and should be rigorously examined, the presence of such a zone at Hawai'i, a comparable volcanic

setting, suggests that future research may yield compelling results. I also investigate how crystallisation, a widely proposed mechanism, can affect long-term displacement. I suggest that its role may be overemphasised in long-term subsidence, and that the role of mush contraction needs more investigation. I have outlined an approach by which further work can explore the influence of thermo-elastic mush contraction on these patterns. I believe this thesis demonstrates the utility of satellite InSAR when studying volcanoes, and shows the importance of considering observations of deformation in the context of the historical unrest of the volcano, as well as that of its neighbours.

Bibliography

Aiuppa, Alessandro, Patrick Allard, Benjamin Bernard, Francesco Maria Lo Forte, Roberto Moretti, and Silvana Hidalgo (Feb. 2022). "Gas Leakage From Shallow Ponding Magma and Trapdoor Faulting at Sierra Negra Volcano (Isabela Island, Galápagos)". en. In: *Geochemistry, Geophysics, Geosystems* 23.2. ISSN: 1525-2027, 1525-2027. DOI: 10.1029/2021GC010288. URL: https://onlinelibrary.wiley.com/doi/10.1029/2021GC010288 (visited on 03/21/2022).

Albino, F., V. Pinel, and F. Sigmundsson (Apr. 2010). "Influence of surface load variations on eruption likelihood: application to two Icelandic subglacial volcanoes, Grímsvötn and Katla". en. In: *Geophysical Journal International*. ISSN: 0956540X, 1365246X. DOI: 10.1111/j.1365-246X.2010.04603.x. URL: https://academic.oup.com/gji/article-lookup/doi/10.1111/j.1365-246X.2010.04603.x (visited on 08/30/2022).

Albino, Fabien, Juliet Biggs, Milan Lazecký, and Yasser Maghsoudi (Nov. 2022). "Routine Processing and Automatic Detection of Volcanic Ground Deformation Using Sentinel-1 InSAR Data: Insights from African Volcanoes". en. In: *Remote Sensing* 14.22, p. 5703. ISSN: 2072-4292. DOI: 10.3390/rs14225703. URL: https://www.mdpi.com/2072-4292/14/22/5703 (visited on 04/28/2023).

Albino, Fabien, Juliet Biggs, and Devy Kamil Syahbana (Feb. 2019). "Dyke intrusion between neighbouring arc volcanoes responsible for 2017 pre-eruptive seismic swarm at Agung". en. In: *Nature Communications* 10.1, p. 748. ISSN: 2041-1723. DOI: 10.1038/s41467-019-08564-9. URL: https://www.nature.com/articles/s41467-019-08564-9 (visited on 06/12/2023).

Amelung, Falk, Sigurjón Jónsson, Howard Zebker, and Paul Segall (Oct. 2000). "Widespread uplift and 'trapdoor' faulting on Galápagos volcanoes observed with radar interferometry". en. In: *Nature* 407.6807, pp. 993–996. ISSN: 0028-0836, 1476-4687. DOI: 10.1038/35039604. URL: http://www.nature.com/articles/35039604 (visited on 02/17/2021).

Annen, Catherine (Oct. 2017). "Factors Affecting the Thickness of Thermal Aureoles". In: *Frontiers in Earth Science* 5, p. 82. ISSN: 2296-6463. DOI: 10.3389/feart.2017.

00082. URL: http://journal.frontiersin.org/article/10.3389/feart.2017.00082/full (visited on 05/26/2020).

Annen, Catherine, Michel Pichavant, Olivier Bachmann, and Alain Burgisser (July 2008). "Conditions for the growth of a long-lived shallow crustal magma chamber below Mount Pelee volcano (Martinique, Lesser Antilles Arc)". en. In: *Journal of Geophysical Research* 113.B7, B07209. ISSN: 0148-0227. DOI: 10.1029/2007JB005049. URL: http://doi.wiley.com/10.1029/2007JB005049 (visited on 05/26/2020).

Bagnardi, Marco (2014). "Dynamics of Magma Supply, Storage and Migration at Basaltic Volcanoes: Geophysical Studies of the Galápagos and Hawaiian Volcanoes". en. PhD thesis. Coral Gables, Florida: University of Miami.

— (Mar. 2017). *Intrusive Activity at Cerro Azul Volcano, Galápagos Islands (Ecuador).* Tech. rep. 01. University of Leeds: COMET. URL: https://comet.nerc.ac.uk/intrusive-activity-cerro-azul-volcano-galapagos-islands-ecuador/?platform=hootsuite.

Bagnardi, Marco and Falk Amelung (Oct. 2012). "Space-geodetic evidence for multiple magma reservoirs and subvolcanic lateral intrusions at Fernandina Volcano, Galápagos Islands". en. In: *Journal of Geophysical Research: Solid Earth* 117.B10. ISSN: 01480227. DOI: 10.1029/2012JB009465. URL: http://doi.wiley.com/10.1029/2012JB009465 (visited on 02/17/2021).

Bagnardi, Marco, Falk Amelung, and Michael P. Poland (Sept. 2013). "A new model for the growth of basaltic shields based on deformation of Fernandina volcano, Galápagos Islands". en. In: *Earth and Planetary Science Letters* 377-378, pp. 358–366. ISSN: 0012821X. DOI: 10.1016/j.epsl.2013.07.016. URL: https://linkinghub.elsevier.com/retrieve/pii/S0012821X13003919 (visited on 02/17/2021).

Bagnardi, Marco and Andrew Hooper (July 2018). "Inversion of Surface Deformation Data for Rapid Estimates of Source Parameters and Uncertainties: A Bayesian Approach". en. In: *Geochemistry, Geophysics, Geosystems* 19.7, pp. 2194–2211. ISSN: 1525-2027, 1525-2027. DOI: 10.1029/2018GC007585. URL: https://onlinelibrary.wiley.com/doi/10.1029/2018GC007585 (visited on 10/18/2022).

Baker, Michael Scott (2012). "Investigating the Dynamics of Basaltic Volcano Magmatic Systems with Space Geodesy". en. PhD thesis. Coral Gables, Florida: University of Miami.

Baker, Scott and Falk Amelung (Dec. 2012). "Top-down inflation and deflation at the summit of Kīlauea Volcano, Hawai'i observed with InSAR". en. In: *Journal of Geophysical Research: Solid Earth* 117.B12, n/a–n/a. ISSN: 01480227. DOI: 10.1029/2011JB009123. URL: http://doi.wiley.com/10.1029/2011JB009123 (visited on 12/07/2022).

Banfield, A F, Chas H Behre, and David St Clair (1956). "Geology of Isabela (Albemarle) Island, Archipielago de Colon (Galapagos)". en. In: *Geological Society of America Bulletin* 67.2, pp. 215–234.

Barbot, Sylvain, James D. P. Moore, and Valère Lambert (Apr. 2017). "Displacement and Stress Associated with Distributed Anelastic Deformation in a Half-Space". en. In: *Bulletin of the Seismological Society of America* 107.2, pp. 821–855. ISSN: 0037-1106, 1943-3573. DOI: 10.1785/0120160237. URL: https://pubs.geoscienceworld.org/bssa/article/107/2/821-855/354173 (visited on 10/05/2023).

Bathke, H., H. Sudhaus, E.P. Holohan, T. R. Walter, and M. Shirzaei (Aug. 2013). "An active ring fault detected at Tendürek volcano by using InSAR: INSAR SOURCE STUDY AT TENDÜREK VOLCANO". en. In: *Journal of Geophysical Research: Solid Earth* 118.8, pp. 4488–4502. ISSN: 21699313. DOI: 10.1002/jgrb.50305. URL: http://doi.wiley.com/10.1002/jgrb.50305 (visited on 08/01/2023).

Bell, Andrew F., Stephen Hernandez, John McCloskey, Mario Ruiz, Peter C. LaFemina, Christopher J. Bean, and Martin Möllhoff (Sept. 2021a). "Dynamic earthquake triggering response tracks evolving unrest at Sierra Negra volcano, Galápagos Islands". en. In: *Science Advances* 7.39, eabh0894. ISSN: 2375-2548. DOI: 10.1126/sciadv.abh0894. URL: https://www.science.org/doi/10.1126/sciadv.abh0894 (visited on 02/01/2022).

Bell, Andrew F., Peter C. La Femina, Mario Ruiz, Falk Amelung, Marco Bagnardi, Christopher J. Bean, Benjamin Bernard, Cynthia Ebinger, Matthew Gleeson, James Grannell, Stephen Hernandez, Machel Higgins, Céline Liorzou, Paul Lundgren, Nathan J. Meier, Martin Möllhoff, Sarah-Jaye Oliva, Andres Gorki Ruiz, and Michael J. Stock (Dec. 2021b). "Caldera resurgence during the 2018 eruption of Sierra Negra volcano, Galápagos Islands". en. In: *Nature Communications* 12.1, p. 1397. ISSN: 2041-1723. DOI: 10.1038/s41467-021-21596-4. URL: http://www.nature.com/articles/s41467-021-21596-4 (visited on 07/22/2021).

Bell, Andrew Forbes, Stephen Hernandez, Peter Christopher La Femina, and Mario Calixto Ruiz (July 2021c). "Uplift and Seismicity Driven by Magmatic Inflation at Sierra Negra Volcano, Galápagos Islands". en. In: *Journal of Geophysical Research: Solid Earth* 126.7. ISSN: 2169-9313, 2169-9356. DOI: 10.1029/2021JB022244. URL: https://onlinelibrary.wiley.com/doi/10.1029/2021JB022244 (visited on 10/28/2022).

Bemelmans, M. J. W., J. Biggs, M. Poland, J. Wookey, S. K. Ebmeier, A. K. Diefenbach, and D. Syahbana (May 2023). "High-Resolution InSAR Reveals Localized Pre-Eruptive Deformation Inside the Crater of Agung Volcano, Indonesia". en. In: *Journal of Geophysical Research: Solid Earth* 128.5, e2022JB025669. ISSN: 2169-9313, 2169-9356. DOI: 10.1029/2022JB025669. URL: https://agupubs.onlinelibrary.wiley.com/doi/10.1029/2022JB025669 (visited on 05/17/2023).

Berardino, P., G. Fornaro, R. Lanari, and E. Sansosti (Nov. 2002). "A new algorithm for surface deformation monitoring based on small baseline differential SAR interferograms". en. In: *IEEE Transactions on Geoscience and Remote Sensing* 40.11,

pp. 2375–2383. ISSN: 0196-2892. DOI: 10.1109/TGRS.2002.803792. URL: http://ieeexplore.ieee.org/document/1166596/ (visited on 10/26/2022).

Bernard, Benjamin (2022). "Volcanic event management in the Galápagos Islands, Ecuador". en. In: 5, p. 17.

Bernard, Benjamin, Michael J. Stock, Diego Coppola, Silvana Hidalgo, Marco Bagnardi, Sally Gibson, Stephen Hernandez, Patricio Ramón, and Matthew Gleeson (Apr. 2019). "Chronology and phenomenology of the 1982 and 2015 Wolf volcano eruptions, Galápagos Archipelago". en. In: *Journal of Volcanology and Geothermal Research* 374, pp. 26–38. ISSN: 03770273. DOI: 10.1016/j.jvolgeores.2019.02.013. URL: https://linkinghub.elsevier.com/retrieve/pii/S0377027318305110 (visited on 06/28/2022).

Biggs, J., I. D. Bastow, D. Keir, and E. Lewi (Sept. 2011). "Pulses of deformation reveal frequently recurring shallow magmatic activity beneath the Main Ethiopian Rift: DEFORMING VOLCANOES IN THE MER". en. In: *Geochemistry, Geophysics, Geosystems* 12.9, n/a–n/a. ISSN: 15252027. DOI: 10.1029/2011GC003662. URL: http://doi.wiley.com/10.1029/2011GC003662 (visited on 11/02/2017).

Biggs, Juliet, E. Y. Anthony, and C. J. Ebinger (2009). "Multiple inflation and deflation events at Kenyan volcanoes, East African Rift". In: *Geology* 37.11, pp. 979–982.

Biggs, Juliet and Matthew E. Pritchard (Feb. 2017). "Global Volcano Monitoring: What Does It Mean When Volcanoes Deform?" en. In: *Elements* 13.1, pp. 17–22. ISSN: 1811-5209, 1811-5217. DOI: 10.2113/gselements.13.1.17. URL: http://elements.geoscienceworld.org/lookup/doi/10.2113/gselements.13.1.17 (visited on 11/26/2017).

Biggs, Juliet, Elspeth Robertson, and Katharine Cashman (Apr. 2016). "The lateral extent of volcanic interactions during unrest and eruption". en. In: *Nature Geoscience* 9.4, pp. 308–311. ISSN: 1752-0894, 1752-0908. DOI: 10.1038/ngeo2658. URL: http://www.nature.com/articles/ngeo2658 (visited on 10/05/2021).

Blake, S., C. J. N. Wilson, I. E. M. Smith, and G. P. L. Walker (Mar. 1992). "Petrology and dynamics of the Waimihia mixed magma eruption, Taupo Volcano, New Zealand". en. In: *Journal of the Geological Society* 149.2, pp. 193–207. ISSN: 0016-7649, 2041-479X. DOI: 10.1144/gsjgs.149.2.0193. URL: https://www.lyellcollection.org/doi/10.1144/gsjgs.149.2.0193 (visited on 02/21/2023).

Brothelande, E., F. Amelung, Z. Yunjun, and S. Wdowinski (Dec. 2018). "Geodetic evidence for interconnectivity between Aira and Kirishima magmatic systems, Japan". en. In: *Scientific Reports* 8.1, p. 9811. ISSN: 2045-2322. DOI: 10.1038/s41598-018-28026-4. URL: http://www.nature.com/articles/s41598-018-28026-4 (visited on 11/02/2021).

Bürgmann, Roland, Paul A. Rosen, and Eric J. Fielding (May 2000). "Synthetic Aperture Radar Interferometry to Measure Earth's Surface Topography and Its Deformation". en. In: *Annual Review of Earth and Planetary Sciences* 28.1, pp. 169–

209. ISSN: 0084-6597, 1545-4495. DOI: 10.1146/annurev.earth.28.1.169. URL: http://www.annualreviews.org/doi/10.1146/annurev.earth.28.1.169 (visited on 05/26/2018).

Busa, T., R. Clochiatti, and R. Cristofolini (Jan. 2002). "The role of apatite fractionation and REE distribution in alkaline rocks from Mt. Etna, Sicily". In: *Mineralogy and Petrology* 74.1, pp. 95–114. ISSN: 0930-0708, 1438-1168. DOI: 10.1007/s710-002-8217-3. URL: http://link.springer.com/10.1007/s710-002-8217-3 (visited on 05/26/2020).

Button, A. and R. G. Cawthorn (May 2015). "Distribution of mafic sills in the Transvaal Supergroup, northeastern South Africa". en. In: *Journal of the Geological Society* 172.3, pp. 357–367. ISSN: 0016-7649, 2041-479X. DOI: 10.1144/jgs2014-101. URL: http://jgs.lyellcollection.org/lookup/doi/10.1144/jgs2014-101 (visited on 05/26/2020).

Caricchi, Luca, Juliet Biggs, Catherine Annen, and Susanna Ebmeier (Feb. 2014). "The influence of cooling, crystallisation and re-melting on the interpretation of geodetic signals in volcanic systems". en. In: *Earth and Planetary Science Letters* 388, pp. 166–174. ISSN: 0012821X. DOI: 10.1016/j.epsl.2013.12.002. URL: http://linkinghub.elsevier.com/retrieve/pii/S0012821X13006985 (visited on 11/15/2017).

Cashman, Katharine V. (2004). "Volatile controls on magma ascent and eruption". en. In: *Geophysical Monograph Series*. Ed. by Robert Stephen John Sparks and Christopher John Hawkesworth. Vol. 150. Washington, D. C.: American Geophysical Union, pp. 109–124. ISBN: 978-0-87590-415-3. DOI: 10.1029/150GM10. URL: http://www.agu.org/books/gm/v150/150GM10/150GM10.shtml (visited on 08/25/2018).

Cashman, Katharine V., R. Stephen J. Sparks, and Jonathan D. Blundy (Mar. 2017). "Vertically extensive and unstable magmatic systems: A unified view of igneous processes". en. In: *Science* 355.6331, eaag3055. ISSN: 0036-8075, 1095-9203. DOI: 10.1126/science.aag3055. URL: https://www.sciencemag.org/lookup/doi/10.1126/science.aag3055 (visited on 05/26/2020).

Castelino, Jennifer, Susanna Ebmeier, Sam Pegler, and Oliver Harlen (Dec. 2021). "Poroviscoelastic Dynamics of Mushy Magmatic Systems". In: 2021. Conference Name: AGU Fall Meeting Abstracts ADS Bibcode: 2021AGUFM.V15D0114C, pp. V15D–0114. URL: https://ui.adsabs.harvard.edu/abs/2021AGUFM.V15D0114C (visited on 06/08/2023).

Cerro Azul Special Report No. 1 - 2017 (Mar. 2017). Special 01. Campus "Ing. José Rubén Orellana", Facultad de Ingeniería Civil 6to. Piso. Av. Ladrón de Guevara E11-253: Instituto Geofísico Escuela Politécnica Nacional. URL: https://www.igepn.edu.ec/servicios/noticias/1468-informe-especial-cerro-azul-no-1-2017.

Cerro Azul Special Report No. 2 - 2017 (Mar. 2017). Special 02. Campus "Ing. José Rubén Orellana", Facultad de Ingeniería Civil 6to. Piso. Av. Ladrón de Guevara E11-

253: Instituto Geofísico Escuela Politécnica Nacional. URL: https://www.igepn.edu.ec/servicios/noticias/1473-informe-especial-cerro-azul-no-2-2017.

Cerro Azul Special Report No. 3 - 2017 (Apr. 2017). Special 02. Campus "Ing. José Rubén Orellana", Facultad de Ingeniería Civil 6to. Piso. Av. Ladrón de Guevara E11-253: Instituto Geofísico Escuela Politécnica Nacional. URL: https://www.igepn.edu.ec/servicios/noticias/1477-informe-especial-cerro-azul-n-3-2017.

Chadwick, William W and Keith A Howard (May 1991). "The pattern of circumferential and radial eruptive fissures on the volcanoes of Fernandina and Isabela islands, Galapagos". en. In: *Bulletin of Volcanology* 53.4, pp. 259–275. ISSN: 0258-8900, 1432-0819. DOI: 10.1007/BF00414523. URL: http://link.springer.com/10.1007/BF00414523 (visited on 03/10/2022).

Chadwick, William W., Dennis J. Geist, Sigurjón Jónsson, Michael Poland, Daniel J. Johnson, and Charles M. Meertens (2006). "A volcano bursting at the seams: Inflation, faulting, and eruption at Sierra Negra volcano, Galápagos". en. In: *Geology* 34.12, p. 1025. ISSN: 0091-7613. DOI: 10.1130/G22826A.1. URL: https://pubs.geoscienceworld.org/geology/article/34/12/1025-1028/129426 (visited on 03/18/2022).

Chadwick, William W., Sigurjon Jónsson, Dennis J. Geist, Michael Poland, Daniel J. Johnson, Spencer Batt, Karen S. Harpp, and Andres Ruiz (Aug. 2011). "The May 2005 eruption of Fernandina volcano, Galápagos: The first circumferential dike intrusion observed by GPS and InSAR". en. In: *Bulletin of Volcanology* 73.6, pp. 679–697. ISSN: 0258-8900, 1432-0819. DOI: 10.1007/s00445-010-0433-0. URL: http://link.springer.com/10.1007/s00445-010-0433-0 (visited on 02/17/2021).

Chandni, C. K. and Shashi Kumar (Dec. 2020). "DInSAR based Analysis of January 2020 Eruption of Fernandina Volcano, Galapagos". en. In: *2020 IEEE India Geoscience and Remote Sensing Symposium (InGARSS)*. Ahmedabad, India: IEEE, pp. 250–253. ISBN: 978-1-72813-114-6. DOI: 10.1109/InGARSS48198.2020.9358954. URL: https://ieeexplore.ieee.org/document/9358954/ (visited on 03/10/2022).

Chaussard, Estelle (June 2016). "Subsidence in the Parícutin lava field: Causes and implications for interpretation of deformation fields at volcanoes". en. In: *Journal of Volcanology and Geothermal Research* 320, pp. 1–11. ISSN: 03770273. DOI: 10.1016/j.jvolgeores.2016.04.009. URL: http://linkinghub.elsevier.com/retrieve/pii/S0377027316300415 (visited on 11/16/2017).

Chestler, Shelley R. and Eric B. Grosfils (Sept. 2013). "Using numerical modeling to explore the origin of intrusion patterns on Fernandina volcano, Galapagos Islands, Ecuador". en. In: *Geophysical Research Letters* 40.17, pp. 4565–4569. ISSN: 00948276. DOI: 10.1002/grl.50833. URL: http://doi.wiley.com/10.1002/grl.50833 (visited on 03/10/2022).

Communication, Directorate of (Jan. 2022). *Overflight shows that Wolf's volcanic activity continues*. Governmental. URL: https://www.ambiente.gob.ec/sobrevuelo-

evidencia-que-la-actividad-volcanica-de-wolf-se-mantiene/ (visited on 06/29/2022).

Crider, Juliet G., David Frank, Stephen D. Malone, Michael P. Poland, Cynthia Werner, and Jacqueline Caplan-Auerbach (Mar. 2011). "Magma at depth: a retrospective analysis of the 1975 unrest at Mount Baker, Washington, USA". en. In: *Bulletin of Volcanology* 73.2, pp. 175–189. ISSN: 0258-8900, 1432-0819. DOI: 10.1007/s00445-010-0441-0. URL: http://link.springer.com/10.1007/s00445-010-0441-0 (visited on 08/01/2023).

Cullen, Andrew B., Alexander R. McBirney, and Ralph D. Rogers (Dec. 1987). "Structural controls on the morphology of Galapagos shields". en. In: *Journal of Volcanology and Geothermal Research* 34.1-2, pp. 143–151. ISSN: 03770273. DOI: 10.1016/0377-0273(87)90099-0. URL: https://linkinghub.elsevier.com/retrieve/pii/0377027387900990 (visited on 01/27/2023).

Davidge, Lindsey, Cynthia Ebinger, Mario Ruiz, Gabrielle Tepp, Falk Amelung, Dennis Geist, Dustin Coté, and Juan Anzieta (Mar. 2017). "Seismicity patterns during a period of inflation at Sierra Negra volcano, Galápagos Ocean Island Chain". en. In: *Earth and Planetary Science Letters* 462, pp. 169–179. ISSN: 0012821X. DOI: 10.1016/j.epsl.2016.12.021. URL: http://linkinghub.elsevier.com/retrieve/pii/S0012821X16307348 (visited on 11/16/2017).

Davis, Timothy, Marco Bagnardi, Paul Lundgren, and Eleonora Rivalta (July 2021). "Extreme Curvature of Shallow Magma Pathways Controlled by Competing Stresses: Insights From the 2018 Sierra Negra Eruption". en. In: *Geophysical Research Letters* 48.13. ISSN: 0094-8276, 1944-8007. DOI: 10.1029/2021GL093038. URL: https://onlinelibrary.wiley.com/doi/10.1029/2021GL093038 (visited on 08/27/2021).

De Novellis, V., R. Castaldo, C. De Luca, S. Pepe, I. Zinno, F. Casu, R. Lanari, and G. Solaro (Sept. 2017). "Source modelling of the 2015 Wolf volcano (Galápagos) eruption inferred from Sentinel 1-A DInSAR deformation maps and pre-eruptive ENVISAT time series". en. In: *Journal of Volcanology and Geothermal Research* 344, pp. 246–256. ISSN: 03770273. DOI: 10.1016/j.jvolgeores.2017.05.013. URL: https://linkinghub.elsevier.com/retrieve/pii/S0377027317302962 (visited on 02/18/2021).

De Roy, Tui (2010). *Galapagos: Islands Born of Fire*. 10th anniversary edition. Princeton, New Jersey: Princeton University Press. ISBN: 978-0-691-14637-9.

Dofal, A., F.R. Fontaine, L. Michon, G. Barruol, and H. Tkalčić (Dec. 2021). "Nature of the crust beneath the islands of the Mozambique Channel: Constraints from receiver functions". en. In: *Journal of African Earth Sciences* 184, p. 104379. ISSN: 1464343X. DOI: 10.1016/j.jafrearsci.2021.104379. URL: https://linkinghub.elsevier.com/retrieve/pii/S1464343X21002806 (visited on 01/18/2023).

Dualeh, E.W., S.K. Ebmeier, T.J. Wright, M.P. Poland, R. Grandin, A.J. Stinton, M. Camejo-Harry, B. Esse, and M. Burton (Feb. 2023). "Rapid pre-explosion increase in

dome extrusion rate at La Soufrière, St. Vincent quantified from synthetic aperture radar backscatter". en. In: *Earth and Planetary Science Letters* 603, p. 117980. ISSN: 0012821X. DOI: 10.1016/j.epsl.2022.117980. URL: https://linkinghub.elsevier.com/retrieve/pii/S0012821X22006161 (visited on 06/01/2023).

Ebmeier, S. K. (Dec. 2016). "Application of independent component analysis to multitemporal InSAR data with volcanic case studies: ICA Analysis of InSAR Data". en. In: *Journal of Geophysical Research: Solid Earth* 121.12, pp. 8970–8986. ISSN: 21699313. DOI: 10.1002/2016JB013765. URL: http://doi.wiley.com/10.1002/2016JB013765 (visited on 03/11/2021).

Ebmeier, S. K., B. J. Andrews, M. C. Araya, D. W. D. Arnold, J. Biggs, C. Cooper, E. Cottrell, M. Furtney, J. Hickey, J. Jay, R. Lloyd, A. L. Parker, M. E. Pritchard, E. Robertson, E. Venzke, and J. L. Williamson (Dec. 2018). "Synthesis of global satellite observations of magmatic and volcanic deformation: implications for volcano monitoring & the lateral extent of magmatic domains". en. In: *Journal of Applied Volcanology* 7.1, p. 2. ISSN: 2191-5040. DOI: 10.1186/s13617-018-0071-3. URL: https://appliedvolc.biomedcentral.com/articles/10.1186/s13617-018-0071-3 (visited on 05/26/2020).

Ebmeier, S. K., J. Biggs, T. A. Mather, and F. Amelung (2013). "Applicability of InSAR to tropical volcanoes: insights from Central America". en. In: *Geological Society, London, Special Publications* 380.1, pp. 15–37. ISSN: 0305-8719, 2041-4927. DOI: 10.1144/SP380.2. URL: http://sp.lyellcollection.org/lookup/doi/10.1144/SP380.2 (visited on 05/25/2018).

Ebmeier, Susanna K., Juliet Biggs, Cyril Muller, and Geoffroy Avard (Dec. 2014). "Thin-skinned mass-wasting responsible for widespread deformation at Arenal volcano". en. In: *Frontiers in Earth Science* 2. ISSN: 2296-6463. DOI: 10.3389/feart.2014.00035. URL: http://journal.frontiersin.org/article/10.3389/feart.2014.00035/abstract (visited on 04/05/2023).

Feighner, Mark A. and Mark A. Richards (1994). "Lithospheric structure and compensation mechanisms of the Galápagos Archipelago". en. In: *Journal of Geophysical Research* 99.B4, p. 6711. ISSN: 0148-0227. DOI: 10.1029/93JB03360. URL: http://doi.wiley.com/10.1029/93JB03360 (visited on 11/21/2022).

Filson, John, Tom Simkin, and Lei-kuang Leu (Dec. 1973). "Seismicity of a caldera collapse: Galapagos Islands 1968". en. In: *Journal of Geophysical Research* 78.35, pp. 8591–8622. ISSN: 01480227. DOI: 10.1029/JB078i035p08591. URL: http://doi.wiley.com/10.1029/JB078i035p08591 (visited on 03/08/2022).

Fontaine, Fabrice R., Guilhem Barruol, Hrvoje Tkalčić, Ingo Wölbern, Georg Rümpker, Thomas Bodin, and Méric Haugmard (Oct. 2015). "Crustal and uppermost mantle structure variation beneath La Réunion hotspot track". en. In: *Geophysical Journal International* 203.1, pp. 107–126. ISSN: 0956-540X, 1365-246X. DOI: 10.1093/gji/

ggv279. URL: https://academic.oup.com/gji/article-lookup/doi/10.1093/gji/ggv279 (visited on 11/21/2022).

Fournier, Robert O. (Dec. 1999). "Hydrothermal processes related to movement of fluid from plastic into brittle rock in the magmatic-epithermal environment". en. In: *Economic Geology* 94.8, pp. 1193–1211. ISSN: 1554-0774, 0361-0128. DOI: 10.2113/gsecongeo.94.8.1193. URL: http://pubs.geoscienceworld.org/economicgeology/article/94/8/1193/21899/Hydrothermal-processes-related-to-movement-of (visited on 05/26/2020).

— (2007). "Hydrothermal systems and volcano geochemistry". en. In: *Volcano Deformation*. Berlin, Heidelberg: Springer Berlin Heidelberg, pp. 323–341. ISBN: 978-3-642-51763-1. DOI: 10.1007/978-3-540-49302-0_10. URL: http://link.springer.com/10.1007/978-3-540-49302-0_10 (visited on 08/18/2020).

Furumoto, Augustine S., George P. Woollard, J. F. Campbell, and D. M. Hussong (Mar. 2013). "Variation in the Thickness of the Crust in the Hawaiian Archipelago". en. In: *Geophysical Monograph Series*. Ed. by Leon Knopoff, Charles L. Drake, and Pembroke J. Hart. Washington, D. C.: American Geophysical Union, pp. 94–111. ISBN: 978-1-118-66373-8. DOI: 10.1029/GM012p0094. URL: http://doi.wiley.com/10.1029/GM012p0094 (visited on 01/18/2023).

Gaddes, M. E., A. Hooper, and M. Bagnardi (Nov. 2019). "Using Machine Learning to Automatically Detect Volcanic Unrest in a Time Series of Interferograms". en. In: *Journal of Geophysical Research: Solid Earth* 124.11, pp. 12304–12322. ISSN: 2169-9313, 2169-9356. DOI: 10.1029/2019JB017519. URL: https://onlinelibrary.wiley.com/doi/10.1029/2019JB017519 (visited on 03/22/2022).

Galetto, Federico, Marco Bagnardi, Valerio Acocella, and Andrew Hooper (Apr. 2019). "Noneruptive Unrest at the Caldera of Alcedo Volcano (Galápagos Islands) Revealed by InSAR Data and Geodetic Modeling". en. In: *Journal of Geophysical Research: Solid Earth* 124.4, pp. 3365–3381. ISSN: 2169-9313, 2169-9356. DOI: 10.1029/2018JB017103. URL: https://onlinelibrary.wiley.com/doi/10.1029/2018JB017103 (visited on 02/17/2021).

Galetto, Federico, Andrew Hooper, Marco Bagnardi, and Valerio Acocella (Feb. 2020). "The 2008 Eruptive Unrest at Cerro Azul Volcano (Galápagos) Revealed by InSAR Data and a Novel Method for Geodetic Modelling". en. In: *Journal of Geophysical Research: Solid Earth* 125.2. ISSN: 2169-9313, 2169-9356. DOI: 10.1029/2019JB018521. URL: https://onlinelibrary.wiley.com/doi/abs/10.1029/2019JB018521 (visited on 02/19/2021).

Galetto, Federico, Diego Reale, Eugenio Sansosti, and Valerio Acocella (June 2023). "Implications for Shallow Magma Transfer During the 2017 and 2018 Eruptions at Fernandina (Galápagos) Inferred From InSAR Data". en. In: *Journal of Geophysical Research: Solid Earth* 128.6, e2022JB026174. ISSN: 2169-9313, 2169-9356. DOI: 10.

1029/2022JB026174. URL: https://agupubs.onlinelibrary.wiley.com/doi/10.1029/2022JB026174 (visited on 06/01/2023).

Geist, Dennis, William Chadwick, and Daniel Johnson (Feb. 2006a). "Results from new GPS and gravity monitoring networks at Fernandina and Sierra Negra Volcanoes, Galápagos, 2000–2002". en. In: *Journal of Volcanology and Geothermal Research* 150.1-3, pp. 79–97. ISSN: 03770273. DOI: 10.1016/j.jvolgeores.2005.07.003. URL: https://linkinghub.elsevier.com/retrieve/pii/S037702730500260X (visited on 03/10/2022).

Geist, Dennis, Keith A Howard, A Mark Jellinek, and Scott Rayder (Jan. 1994). "The volcanic history of Volcán Alcedo, Galápagos Archipelago: A case study of rhyolitic oceanic volcanism". en. In: *Bulletin of Volcanology* 56, pp. 243–260.

Geist, Dennis, William White, Terry Naumann, and Robert Reynolds (1999). "Illegitimate magmas of the Galápagos: Insights into mantle mixing and magma transport". en. In: *Geology* 27.12, p. 4.

Geist, Dennis J., George Bergantz, and William W. Chadwick (Aug. 2014). "Galápagos Magma Chambers". en. In: *Geophysical Monograph Series*. Ed. by Karen S. Harpp, Eric Mittelstaedt, Noémi d'Ozouville, and David W. Graham. Hoboken, New Jersey: John Wiley & Sons, Inc, pp. 55–69. ISBN: 978-1-118-85253-8. DOI: 10.1002/9781118852538.ch5. (Visited on 08/12/2021).

Geist, Dennis J., Daniel J. Fornari, Mark D. Kurz, Karen S. Harpp, S. Adam Soule, Michael R. Perfit, and Alison M. Koleszar (Dec. 2006b). "Submarine Fernandina: Magmatism at the leading edge of the Galápagos hot spot". en. In: *Geochemistry, Geophysics, Geosystems* 7.12, n/a–n/a. ISSN: 15252027. DOI: 10.1029/2006GC001290. URL: http://doi.wiley.com/10.1029/2006GC001290 (visited on 03/10/2022).

Geist, Dennis J., Karen S. Harpp, Terry R. Naumann, Michael Poland, William W. Chadwick, Minard Hall, and Erika Rader (Apr. 2008). "The 2005 eruption of Sierra Negra volcano, Galápagos, Ecuador". en. In: *Bulletin of Volcanology* 70.6, pp. 655–673. ISSN: 0258-8900, 1432-0819. DOI: 10.1007/s00445-007-0160-3. URL: http://link.springer.com/10.1007/s00445-007-0160-3 (visited on 02/23/2021).

Geist, Dennis J., Terry R. Naumann, Jared J. Standish, Mark D. Kurz, Karen S. Harpp, William M. White, and Daniel J. Fornari (Nov. 2005). "Wolf Volcano, Galápagos Archipelago: Melting and Magmatic Evolution at the Margins of a Mantle Plume". en. In: *Journal of Petrology* 46.11, pp. 2197–2224. ISSN: 1460-2415, 0022-3530. DOI: 10.1093/petrology/egi052. URL: http://academic.oup.com/petrology/article/46/11/2197/1433599/Wolf-Volcano-Gal%C3%A1pagos-Archipelago-Melting-and (visited on 03/10/2022).

Ghiorso, Mark S. and Guilherme A. R. Gualda (June 2015a). "An H2O–CO2 mixed fluid saturation model compatible with rhyolite-MELTS". en. In: *Contributions to Mineralogy and Petrology* 169.6, p. 53. ISSN: 0010-7999, 1432-0967. DOI: 10.1007/

s00410-015-1141-8. URL: http://link.springer.com/10.1007/s00410-015-1141-8 (visited on 05/26/2020).

— (2015b). "Chemical Thermodynamics and the Study of Magmas". en. In: *The Encyclopedia of Volcanoes*. Elsevier, pp. 143–161. ISBN: 978-0-12-385938-9. DOI: 10.1016/B978-0-12-385938-9.00006-7. URL: https://linkinghub.elsevier.com/retrieve/pii/B9780123859389000067 (visited on 05/26/2020).

Goff, Fraser, Gary M. McMurtry, Dale Counce, James A. Simac, Alfredo R. Roldán-Manzo, and David R. Hilton (May 2000). "Contrasting hydrothermal activity at Sierra Negra and Alcedo volcanoes, Galapagos Archipelago, Ecuador". en. In: *Bulletin of Volcanology* 62.1, pp. 34–52. ISSN: 0258-8900, 1432-0819. DOI: 10.1007/s004450050289. URL: http://link.springer.com/10.1007/s004450050289 (visited on 02/24/2021).

Goitom, Berhe, Clive Oppenheimer, James O. S. Hammond, Raphaël Grandin, Talfan Barnie, Amy Donovan, Ghebrebrhan Ogubazghi, Ermias Yohannes, Goitom Kibrom, J- Michael Kendall, Simon A. Carn, David Fee, Christine Sealing, Derek Keir, Atalay Ayele, Jon Blundy, Joanna Hamlyn, Tim Wright, and Seife Berhe (Oct. 2015). "First recorded eruption of Nabro volcano, Eritrea, 2011". en. In: *Bulletin of Volcanology* 77.10. ISSN: 0258-8900, 1432-0819. DOI: 10.1007/s00445-015-0966-3. URL: http://link.springer.com/10.1007/s00445-015-0966-3 (visited on 12/14/2017).

Gonnermann, Helge M., James H. Foster, Michael Poland, Cecily J. Wolfe, Benjamin A. Brooks, and Asta Miklius (Nov. 2012). "Coupling at Mauna Loa and Kīlauea by stress transfer in an asthenospheric melt layer". en. In: *Nature Geoscience* 5.11, pp. 826–829. ISSN: 1752-0894, 1752-0908. DOI: 10.1038/ngeo1612. URL: http://www.nature.com/articles/ngeo1612 (visited on 01/25/2022).

González, Pablo J. and José Fernández (Oct. 2011). "Error estimation in multitemporal InSAR deformation time series, with application to Lanzarote, Canary Islands". en. In: *Journal of Geophysical Research* 116.B10, B10404. ISSN: 0148-0227. DOI: 10.1029/2011JB008412. URL: http://doi.wiley.com/10.1029/2011JB008412 (visited on 05/26/2020).

González, Pablo J., Sergey V. Samsonov, Susi Pepe, Kristy F. Tiampo, Pietro Tizzani, Francesco Casu, José Fernández, Antonio G. Camacho, and Eugenio Sansosti (Aug. 2013). "Magma storage and migration associated with the 2011-2012 El Hierro eruption: Implications for crustal magmatic systems at oceanic island volcanoes". en. In: *Journal of Geophysical Research: Solid Earth* 118.8, pp. 4361–4377. ISSN: 21699313. DOI: 10.1002/jgrb.50289. URL: http://doi.wiley.com/10.1002/jgrb.50289 (visited on 12/19/2022).

Grapenthin, Ronni, Jeffrey T. Freymueller, and Sergey S. Serovetnikov (Aug. 2013). "Surface deformation of Bezymianny Volcano, Kamchatka, recorded by GPS: The eruptions from 2005 to 2010 and long-term, long-wavelength subsidence". en. In: *Journal of Volcanology and Geothermal Research* 263, pp. 58–74. ISSN: 03770273.

DOI: 10.1016/j.jvolgeores.2012.11.012. URL: https://linkinghub.elsevier.com/retrieve/pii/S0377027312003423 (visited on 08/01/2023).

Green, D.H. (May 1973). "Experimental melting studies on a model upper mantle composition at high pressure under water-saturated and water-undersaturated conditions". en. In: *Earth and Planetary Science Letters* 19.1, pp. 37–53. ISSN: 0012821X. DOI: 10.1016/0012-821X(73)90176-3. URL: https://linkinghub.elsevier.com/retrieve/pii/0012821X73901763 (visited on 06/08/2023).

Green, Jonathan R (Nov. 1994). "Recent activity in Alcedo Volcano, Isabela Island". en. In: *Noticias De Galapagos*, p. 3.

Gregg, P. M., H. Le Mével, Y. Zhan, J. Dufek, D. Geist, and W. W. Chadwick (Dec. 2018). "Stress Triggering of the 2005 Eruption of Sierra Negra Volcano, Galápagos". en. In: *Geophysical Research Letters* 45.24. ISSN: 0094-8276, 1944-8007. DOI: 10.1029/2018GL080393. URL: https://onlinelibrary.wiley.com/doi/10.1029/2018GL080393 (visited on 03/21/2022).

Gregg, Patricia M., Yan Zhan, Falk Amelung, Dennis Geist, Patricia Mothes, Seid Koric, and Zhang Yunjun (June 2022). "Forecasting mechanical failure and the 26 June 2018 eruption of Sierra Negra Volcano, Galápagos, Ecuador". en. In: *Science Advances* 8.22, eabm4261. ISSN: 2375-2548. DOI: 10.1126/sciadv.abm4261. URL: https://www.science.org/doi/10.1126/sciadv.abm4261 (visited on 10/18/2022).

Gualda, G. A. R., M. S. Ghiorso, R. V. Lemons, and T. L. Carley (May 2012). "Rhyolite-MELTS: a Modified Calibration of MELTS Optimized for Silica-rich, Fluid-bearing Magmatic Systems". en. In: *Journal of Petrology* 53.5, pp. 875–890. ISSN: 0022-3530, 1460-2415. DOI: 10.1093/petrology/egr080. URL: https://academic.oup.com/petrology/article-lookup/doi/10.1093/petrology/egr080 (visited on 05/26/2020).

Guo, Qian, Caijun Xu, Yangmao Wen, Yang Liu, and Guangyu Xu (Aug. 2019). "The 2017 Noneruptive Unrest at the Caldera of Cerro Azul Volcano (Galápagos Islands) Revealed by InSAR Observations and Geodetic Modelling". en. In: *Remote Sensing* 11.17, p. 1992. ISSN: 2072-4292. DOI: 10.3390/rs11171992. URL: https://www.mdpi.com/2072-4292/11/17/1992 (visited on 02/19/2021).

Hall, Anthony (1996). *Igneous petrology.* 2. ed., 4. Harlow: Prentice Hall. ISBN: 978-0-582-23080-4.

Hamling, I. J., S. Hreinsdóttir, and N. Fournier (June 2015). "The ups and downs of the TVZ: Geodetic observations of deformation around the Taupo Volcanic Zone, New Zealand". en. In: *Journal of Geophysical Research: Solid Earth* 120.6, pp. 4667–4679. ISSN: 21699313. DOI: 10.1002/2015JB012125. URL: http://doi.wiley.com/10.1002/2015JB012125 (visited on 05/26/2020).

Hamlyn, Joanna, Tim Wright, Richard Walters, Carolina Pagli, Eugenio Sansosti, Francesco Casu, Susi Pepe, Marie Edmonds, Brendan McCormick Kilbride, Derek Keir, Jürgen Neuberg, and Clive Oppenheimer (Dec. 2018). "What causes subsidence following

the 2011 eruption at Nabro (Eritrea)?" en. In: *Progress in Earth and Planetary Science* 5.1. ISSN: 2197-4284. DOI: 10.1186/s40645-018-0186-5. URL: https://progearthplanetsci.springeropen.com/articles/10.1186/s40645-018-0186-5 (visited on 11/28/2018).

Hanssen, Ramon F. (2001). *Radar interferometry: data interpretation and error analysis*. Remote sensing and digital image processing v. 2. Dordrecht ; Boston: Kluwer Academic. ISBN: 978-0-7923-6945-5.

Harpp, Karen S. and Dennis J. Geist (May 2018). "The Evolution of Galápagos Volcanoes: An Alternative Perspective". en. In: *Frontiers in Earth Science* 6, p. 50. ISSN: 2296-6463. DOI: 10.3389/feart.2018.00050. URL: http://journal.frontiersin.org/article/10.3389/feart.2018.00050/full (visited on 03/04/2021).

Henderson, S. T. and M. E. Pritchard (May 2013). "Decadal volcanic deformation in the Central Andes Volcanic Zone revealed by InSAR time series: DECADAL INSAR TIME SERIES SURVEY-CVZ". en. In: *Geochemistry, Geophysics, Geosystems* 14.5, pp. 1358–1374. ISSN: 15252027. DOI: 10.1002/ggge.20074. URL: http://doi.wiley.com/10.1002/ggge.20074 (visited on 08/01/2023).

Hildreth, Wes (Aug. 1991). "The timing of caldera collapse at Mount Katmai in response to magma withdrawal toward Novarupta". en. In: *Geophysical Research Letters* 18.8, pp. 1541–1544. ISSN: 00948276. DOI: 10.1029/91GL01083. URL: http://doi.wiley.com/10.1029/91GL01083 (visited on 01/19/2022).

— (July 2017). "Fluid-driven uplift at Long Valley Caldera, California: Geologic perspectives". en. In: *Journal of Volcanology and Geothermal Research* 341, pp. 269–286. ISSN: 03770273. DOI: 10.1016/j.jvolgeores.2017.06.010. URL: http://linkinghub.elsevier.com/retrieve/pii/S0377027317300434 (visited on 08/31/2018).

Hooper, A., P. Segall, and H. Zebker (July 2007). "Persistent scatterer interferometric synthetic aperture radar for crustal deformation analysis, with application to Volcán Alcedo, Galápagos". en. In: *Journal of Geophysical Research* 112.B7, B07407. ISSN: 0148-0227. DOI: 10.1029/2006JB004763. URL: http://doi.wiley.com/10.1029/2006JB004763 (visited on 10/13/2020).

Hutchison, William, Juliet Biggs, Tamsin A. Mather, David M. Pyle, Elias Lewi, Gezahegn Yirgu, Stefano Caliro, Giovanni Chiodini, Laura E. Clor, and Tobias P. Fischer (Aug. 2016). "Causes of unrest at silicic calderas in the East African Rift: New constraints from InSAR and soil-gas chemistry at Aluto volcano, Ethiopia". en. In: *Geochemistry, Geophysics, Geosystems* 17.8, pp. 3008–3030. ISSN: 15252027. DOI: 10.1002/2016GC006395. URL: http://doi.wiley.com/10.1002/2016GC006395 (visited on 02/05/2021).

Hyvärinen, Aapo and Erkki Oja (July 1997). "A Fast Fixed-Point Algorithm for Independent Component Analysis". In: *Neural Computation* 9.7, pp. 1483–1492. ISSN:

0899-7667. DOI: 10.1162/neco.1997.9.7.1483. URL: https://doi.org/10.1162/neco.1997.9.7.1483 (visited on 10/26/2021).

Ji, Lingyun, Pavel Izbekov, Sergey Senyukov, and Zhong Lu (2018). "Deformation patterns, magma supply, and magma storage at Karymsky Volcanic Center, Kamchatka, Russia, 2000-2010, revealed by InSAR". en. In: *Journal of Volcanology and Geothermal Research*, p. 11.

Johnson, Daniel J., Albert A. Eggers, Marco Bagnardi, Maurizio Battaglia, Michael P. Poland, and Asta Miklius (Dec. 2010). "Shallow magma accumulation at Kīlauea Volcano, Hawai'i, revealed by microgravity surveys". en. In: *Geology* 38.12, pp. 1139–1142. ISSN: 1943-2682, 0091-7613. DOI: 10.1130/G31323.1. URL: http://pubs.geoscienceworld.org/geology/article/38/12/1139/130151/Shallow-magma-accumulation-at-K%C4%ABlauea-Volcano (visited on 05/26/2020).

Jónsson, Sigurjón (June 2009). "Stress interaction between magma accumulation and trapdoor faulting on Sierra Negra volcano, Galápagos". en. In: *Tectonophysics* 471.1-2, pp. 36–44. ISSN: 00401951. DOI: 10.1016/j.tecto.2008.08.005. URL: https://linkinghub.elsevier.com/retrieve/pii/S0040195108003880 (visited on 03/18/2022).

Jónsson, Sigurjón, Howard Zebker, and Falk Amelung (June 2005). "On trapdoor faulting at Sierra Negra volcano, Galápagos". en. In: *Journal of Volcanology and Geothermal Research* 144.1-4, pp. 59–71. ISSN: 03770273. DOI: 10.1016/j.jvolgeores.2004.11.029. URL: https://linkinghub.elsevier.com/retrieve/pii/S0377027304004160 (visited on 02/23/2021).

Jónsson, Sigurjón, Howard Zebker, Peter Cervelli, Paul Segall, Harold Garbeil, Peter Mouginis-Mark, and Scott Rowland (Apr. 1999). "A shallow-dipping dike fed the 1995 flank eruption at Fernandina Volcano, Galápagos, observed by satellite radar interferometry". en. In: *Geophysical Research Letters* 26.8, pp. 1077–1080. ISSN: 00948276. DOI: 10.1029/1999GL900108. URL: http://doi.wiley.com/10.1029/1999GL900108 (visited on 02/17/2021).

Kang, Ya, Chaoying Zhao, Qin Zhang, Zhong Lu, and Bin Li (Oct. 2017). "Application of InSAR Techniques to an Analysis of the Guanling Landslide". en. In: *Remote Sensing* 9.10, p. 1046. ISSN: 2072-4292. DOI: 10.3390/rs9101046. URL: http://www.mdpi.com/2072-4292/9/10/1046 (visited on 06/01/2023).

Kilbride, Brendan McCormick, Marie Edmonds, and Juliet Biggs (Dec. 2016). "Observing eruptions of gas-rich compressible magmas from space". en. In: *Nature Communications* 7.1, p. 13744. ISSN: 2041-1723. DOI: 10.1038/ncomms13744. URL: http://www.nature.com/articles/ncomms13744 (visited on 07/20/2020).

Klingelhöfer, F., T.A. Minshull, D.K. Blackman, P. Harben, and V. Childers (July 2001). "Crustal structure of Ascension Island from wide-angle seismic data: implications for the formation of near-ridge volcanic islands". en. In: *Earth and Planetary Science Letters* 190.1-2, pp. 41–56. ISSN: 0012821X. DOI: 10.1016/S0012-821X(01)00362-

4. URL: https://linkinghub.elsevier.com/retrieve/pii/S0012821X01003624 (visited on 11/21/2022).

Kurz, Mark D and D Geist (Dec. 1999). "Dynamics of the Galapagos hotspot from helium isotope geochemistry". en. In: *Geochimica et Cosmochimica Acta* 63.23-24, pp. 4139–4156. ISSN: 00167037. DOI: 10.1016/S0016-7037(99)00314-2. URL: https://linkinghub.elsevier.com/retrieve/pii/S0016703799003142 (visited on 05/10/2023).

Kurz, Mark D, Scott K Rowland, Joshua Curtice, Alberto E Saal, and Terry Naumann (2014). "Eruption Rates for Fernandina Volcano: A New Chronology at the Galápagos Hotspot Center". en. In: p. 14.

Lazecký, Milan, Karsten Spaans, Pablo J. González, Yasser Maghsoudi, Yu Morishita, Fabien Albino, John Elliott, Nicholas Greenall, Emma Hatton, Andrew Hooper, Daniel Juncu, Alistair McDougall, Richard J. Walters, C. Scott Watson, Jonathan R. Weiss, and Tim J. Wright (July 2020). "LiCSAR: An Automatic InSAR Tool for Measuring and Monitoring Tectonic and Volcanic Activity". en. In: *Remote Sensing* 12.15, p. 2430. ISSN: 2072-4292. DOI: 10.3390/rs12152430. URL: https://www.mdpi.com/2072-4292/12/15/2430 (visited on 05/20/2021).

Li, Ka Lok, Christopher J. Bean, Andrew F. Bell, Mario Ruiz, Stephen Hernandez, and James Grannell (May 2022). "Seismic tremor reveals slow fracture propagation prior to the 2018 eruption at Sierra Negra volcano, Galápagos". en. In: *Earth and Planetary Science Letters* 586, p. 117533. ISSN: 0012821X. DOI: 10.1016/j.epsl.2022.117533. URL: https://linkinghub.elsevier.com/retrieve/pii/S0012821X22001698 (visited on 10/18/2022).

Li, Siqi, Freysteinn Sigmundsson, Vincent Drouin, Michelle M. Parks, Benedikt G. Ófeigsson, Kristín Jónsdóttir, Ronni Grapenthin, Halldór Geirsson, Andrew Hooper, and Sigrún Hreinsdóttir (Mar. 2021). "Ground Deformation After a Caldera Collapse: Contributions of Magma Inflow and Viscoelastic Response to the 2015–2018 Deformation Field Around Bárðarbunga, Iceland". en. In: *Journal of Geophysical Research: Solid Earth* 126.3. ISSN: 2169-9313, 2169-9356. DOI: 10.1029/2020JB020157. URL: https://onlinelibrary.wiley.com/doi/10.1029/2020JB020157 (visited on 03/20/2023).

Lin, Jian and Ross S. Stein (Feb. 2004). "Stress triggering in thrust and subduction earthquakes and stress interaction between the southern San Andreas and nearby thrust and strike-slip faults". en. In: *Journal of Geophysical Research: Solid Earth* 109.B2. ISSN: 01480227. DOI: 10.1029/2003JB002607. URL: http://doi.wiley.com/10.1029/2003JB002607 (visited on 08/24/2021).

Lister, John R. and Ross C. Kerr (1991). "Fluid-mechanical models of crack propagation and their application to magma transport in dykes". en. In: *Journal of Geophysical Research* 96.B6, p. 10049. ISSN: 0148-0227. DOI: 10.1029/91JB00600. URL: http://doi.wiley.com/10.1029/91JB00600 (visited on 05/26/2020).

Lodge, A., S.E.J. Nippress, A. Rietbrock, A. García-Yeguas, and J.M. Ibáñez (Dec. 2012). "Evidence for magmatic underplating and partial melt beneath the Canary Islands derived using teleseismic receiver functions". en. In: *Physics of the Earth and Planetary Interiors* 212-213, pp. 44–54. ISSN: 00319201. DOI: 10.1016/j.pepi.2012.09.004. URL: https://linkinghub.elsevier.com/retrieve/pii/S0031920112001653 (visited on 01/18/2023).

López-Quiroz, Penélope, Marie-Pierre Doin, Florence Tupin, Pierre Briole, and Jean-Marie Nicolas (Sept. 2009). "Time series analysis of Mexico City subsidence constrained by radar interferometry". en. In: *Journal of Applied Geophysics* 69.1, pp. 1–15. ISSN: 09269851. DOI: 10.1016/j.jappgeo.2009.02.006. URL: https://linkinghub.elsevier.com/retrieve/pii/S0926985109000251 (visited on 10/26/2022).

Lu, Zhong and Daniel Dzurisin (2014). "InSAR Imaging of Aleutian Volcanoes". en. In: *InSAR Imaging of Aleutian Volcanoes*. Berlin, Heidelberg: Springer Berlin Heidelberg, pp. 87–345. ISBN: 978-3-642-00347-9. DOI: 10.1007/978-3-642-00348-6_6. URL: http://link.springer.com/10.1007/978-3-642-00348-6 (visited on 05/26/2020).

Macdonald, R., G. R. Davies, B. G. J. Upton, P. N. Dunkley, M. Smith, and P. T. Leat (July 1995). "Petrogenesis of Silali volcano, Gregory Rift, Kenya". en. In: *Journal of the Geological Society* 152.4, pp. 703–720. ISSN: 0016-7649, 2041-479X. DOI: 10.1144/gsjgs.152.4.0703. URL: https://www.lyellcollection.org/doi/10.1144/gsjgs.152.4.0703 (visited on 02/21/2023).

Maghsoudi, Yasser, Andrew J. Hooper, Tim J. Wright, Milan Lazecky, and Homa Ansari (June 2022). "Characterizing and correcting phase biases in short-term, multilooked interferograms". en. In: *Remote Sensing of Environment* 275, p. 113022. ISSN: 00344257. DOI: 10.1016/j.rse.2022.113022. URL: https://linkinghub.elsevier.com/retrieve/pii/S0034425722001365 (visited on 04/11/2023).

Manconi, A., T. R. Walter, and F. Amelung (Aug. 2007). "Effects of mechanical layering on volcano deformation". en. In: *Geophysical Journal International* 170.2, pp. 952–958. ISSN: 0956540X, 1365246X. DOI: 10.1111/j.1365-246X.2007.03449.x. URL: https://academic.oup.com/gji/article-lookup/doi/10.1111/j.1365-246X.2007.03449.x (visited on 02/28/2022).

Manconi, Andrea and Francesco Casu (July 2012). "Joint analysis of displacement time series retrieved from SAR phase and amplitude: Impact on the estimation of volcanic source parameters". en. In: *Geophysical Research Letters* 39.14, n/a–n/a. ISSN: 00948276. DOI: 10.1029/2012GL052202. URL: http://doi.wiley.com/10.1029/2012GL052202 (visited on 03/10/2022).

Massonnet, Didier and Kurt L. Feigl (Nov. 1998). "Radar interferometry and its application to changes in the Earth's surface". en. In: *Reviews of Geophysics* 36.4, pp. 441–500. ISSN: 87551209. DOI: 10.1029/97RG03139. URL: http://doi.wiley.com/10.1029/97RG03139 (visited on 10/25/2022).

Mata, J., S. Martins, N. Mattielli, J. Madeira, B. Faria, R.S. Ramalho, P. Silva, M. Moreira, R. Caldeira, M. Moreira, J. Rodrigues, and L. Martins (Sept. 2017). "The 2014–15 eruption and the short-term geochemical evolution of the Fogo volcano (Cape Verde): Evidence for small-scale mantle heterogeneity". en. In: *Lithos* 288-289, pp. 91–107. ISSN: 00244937. DOI: 10.1016/j.lithos.2017.07.001. URL: https://linkinghub.elsevier.com/retrieve/pii/S0024493717302402 (visited on 11/21/2022).

Mayhew, Lisa E., Dennis J. Geist, Susan E. Childers, and Jacob D. Pierson (Dec. 2007). "Microbial Community Comparisons as a Function of the Physical and Geochemical Conditions of Galápagos Island Fumaroles". en. In: *Geomicrobiology Journal* 24.7-8, pp. 615–625. ISSN: 0149-0451, 1521-0529. DOI: 10.1080/01490450701672133. URL: https://www.tandfonline.com/doi/full/10.1080/01490450701672133 (visited on 03/01/2022).

McBirney, A.R., A.B. Cullen, D. Geist, E.P. Vicenzi, R.A. Duncan, M.L. Hall, and M. Estrella (Oct. 1985). "The Galapagos volcano Alcedo: A unique ocean caldera". en. In: *Journal of Volcanology and Geothermal Research* 26.1-2, pp. 173–177. ISSN: 03770273. DOI: 10.1016/0377-0273(85)90052-6. URL: https://linkinghub.elsevier.com/retrieve/pii/0377027385900526 (visited on 02/28/2022).

Mibei, Geoffrey, Enikő Bali, Halldór Geirsson, Guðmundur H. Gudfinnsson, Björn S. Hardarson, and Hjalti Franzson (Nov. 2021). "Partial melt generation and evolution of magma reservoir conditions at the Paka volcanic complex in Kenya: Constraints from geochemistry, petrology and geophysics". en. In: *Lithos* 400-401, p. 106385. ISSN: 00244937. DOI: 10.1016/j.lithos.2021.106385. URL: https://linkinghub.elsevier.com/retrieve/pii/S0024493721004217 (visited on 02/21/2023).

Mibei, Geoffrey, Björn S. Harðarson, Hjalti Franzson, Enikő Bali, Halldór Geirsson, Guðmundur H. Guðfinnsson, Charles Lichoro, and John Lagat (Jan. 2022). "Reservoir characterization of the Paka geothermal system in Kenya: Insights from borehole PK-01". en. In: *Geothermics* 98, p. 102293. ISSN: 03756505. DOI: 10.1016/j.geothermics.2021.102293. URL: https://linkinghub.elsevier.com/retrieve/pii/S0375650521002509 (visited on 05/08/2023).

Mogi, Kiyoo (1958). "Relations between the eruption of various volcanoes and the deformations of the ground surfaces around them". In: *Bulletin of the Earthquake Research Institute* 36, pp. 99–134.

Morishita, Yu, Milan Lazecky, Tim Wright, Jonathan Weiss, John Elliott, and Andy Hooper (Jan. 2020). "LiCSBAS: An Open-Source InSAR Time Series Analysis Package Integrated with the LiCSAR Automated Sentinel-1 InSAR Processor". en. In: *Remote Sensing* 12.3, p. 424. ISSN: 2072-4292. DOI: 10.3390/rs12030424. URL: https://www.mdpi.com/2072-4292/12/3/424 (visited on 03/11/2021).

Mouginis-Mark, Peter J., Howard Snell, and Rachel Ellisor (Aug. 2000). "GOES satellite and field observations of the 1998 eruption of Volcan Cerro Azul, Galápagos Islands".

In: *Bulletin of Volcanology* 62.3, pp. 188–198. ISSN: 0258-8900, 1432-0819. DOI: 10.1007/s004450000078. URL: http://link.springer.com/10.1007/s004450000078 (visited on 03/01/2022).

Murase, Masayuki, Koji Ono, Takeo Ito, Rikio Miyajima, Hitoshi Mori, Hiroshi Aoyama, Hiromitu Oshima, Yuka Yoshida, Akihiko Terada, Eturo Koyama, Toyotarou Takeda, Hidefumi Watanabe, Fumiaki Kimata, and Naoyuki Fujii (July 2007). "Time-dependent model for volume changes in pressure sources at Asama volcano, central Japan due to vertical deformations detected by precise leveling during 1902–2005". en. In: *Journal of Volcanology and Geothermal Research* 164.1-2, pp. 54–75. ISSN: 03770273. DOI: 10.1016/j.jvolgeores.2007.04.001. URL: https://linkinghub.elsevier.com/retrieve/pii/S0377027307000856 (visited on 05/26/2020).

Naumann, T. and D. Geist (2000). "Physical volcanology and structural development of Cerro Azul Volcano, Isabela Island, Galµpagos: implications for the development of Galµpagos-type shield volcanoes". en. In: *Bulletin of Volcanology* 61, pp. 497–514.

Naumann, T., Dennis J. Geist, and Mark Kurz (May 2002). "Petrology and Geochemistry of Volcan Cerro Azul: Petrologic Diversity among the Western Galapagos Volcanoes". en. In: *Journal of Petrology* 43.5, pp. 859–883. ISSN: 14602415. DOI: 10.1093/petrology/43.5.859. URL: https://academic.oup.com/petrology/article-lookup/doi/10.1093/petrology/43.5.859 (visited on 08/12/2021).

Naumann, T. R. and L. K. Krebs (Dec. 2003). "Petrology and Geochemistry of Volcan Darwin, Isabela Island, Galapagos Archipelago". In: 2003. Conference Name: AGU Fall Meeting Abstracts ADS Bibcode: 2003AGUFM.V12D0618N, pp. V12D–0618. URL: https://ui.adsabs.harvard.edu/abs/2003AGUFM.V12D0618N (visited on 08/19/2022).

Nikkhoo, Mehdi, Thomas R. Walter, Paul R. Lundgren, and Pau Prats-Iraola (Feb. 2017). "Compound dislocation models (CDMs) for volcano deformation analyses". en. In: *Geophysical Journal International* 208.2, pp. 877–894. ISSN: 0956-540X, 1365-246X. DOI: 10.1093/gji/ggw427. URL: https://academic.oup.com/gji/article-lookup/doi/10.1093/gji/ggw427 (visited on 05/26/2020).

Nooner, Scott L. and William W. Chadwick (Feb. 2009). "Volcanic inflation measured in the caldera of Axial Seamount: Implications for magma supply and future eruptions". en. In: *Geochemistry, Geophysics, Geosystems* 10.2, n/a–n/a. ISSN: 15252027. DOI: 10.1029/2008GC002315. URL: http://doi.wiley.com/10.1029/2008GC002315 (visited on 05/26/2020).

Nusbaum, Robert L, Mitchell W Colgan, Donna E Lawton, and Michael D Glascock (1991). "Mineralogic constraints on the magmatic history of Volcán Darwin flank lava at Urvina Bay, Islá Isabela, Galápagos". In: *Journal of volcanology and geothermal research* 47, pp. 359–366.

Okada, Yoshimitsu (1985). "Surface deformation due to shear and tensile faults in a half-space". In: *Bulletin of the seismological society of America* 75.4, pp. 1135–1154.

Parker, Amy L (2015). "InSAR Observations of Ground Deformation: Application to the Cascades Volcanic Arc". en. PhD Thesis. Bristol: University of Bristol.

Parker, Amy L., Juliet Biggs, and Zhong Lu (Nov. 2014). "Investigating long-term subsidence at Medicine Lake Volcano, CA, using multitemporal InSAR". en. In: *Geophysical Journal International* 199.2, pp. 844–859. ISSN: 1365-246X, 0956-540X. DOI: 10.1093/gji/ggu304. URL: http://academic.oup.com/gji/article/199/2/844/623102/Investigating-longterm-subsidence-at-Medicine-Lake (visited on 09/04/2018).

— (June 2016). "Time-scale and mechanism of subsidence at Lassen Volcanic Center, CA, from InSAR". en. In: *Journal of Volcanology and Geothermal Research* 320, pp. 117–127. ISSN: 03770273. DOI: 10.1016/j.jvolgeores.2016.04.013. URL: http://linkinghub.elsevier.com/retrieve/pii/S0377027316300452 (visited on 02/07/2018).

Parker, Amy L., Juliet Biggs, Richard J. Walters, Susanna K. Ebmeier, Tim J. Wright, Nicholas A. Teanby, and Zhong Lu (Dec. 2015). "Systematic assessment of atmospheric uncertainties for InSAR data at volcanic arcs using large-scale atmospheric models: Application to the Cascade volcanoes, United States". en. In: *Remote Sensing of Environment* 170, pp. 102–114. ISSN: 00344257. DOI: 10.1016/j.rse.2015.09.003. URL: https://linkinghub.elsevier.com/retrieve/pii/S0034425715301267 (visited on 10/13/2020).

Patrick, M. R. (2004). "Numerical modeling of lava flow cooling applied to the 1997 Okmok eruption: Approach and analysis". en. In: *Journal of Geophysical Research* 109.B3, B03202. ISSN: 0148-0227. DOI: 10.1029/2003JB002537. URL: http://doi.wiley.com/10.1029/2003JB002537 (visited on 05/31/2021).

Patrick, Matthew, Tim Orr, Kyle Anderson, and Don Swanson (Feb. 2019). "Eruptions in sync: Improved constraints on Kīlauea Volcano's hydraulic connection". en. In: *Earth and Planetary Science Letters* 507, pp. 50–61. ISSN: 0012821X. DOI: 10.1016/j.epsl.2018.11.030. URL: https://linkinghub.elsevier.com/retrieve/pii/S0012821X18306897 (visited on 08/03/2023).

Pepe, S., R. Castaldo, V. De Novellis, L. D'Auria, C. De Luca, F. Casu, E. Sansosti, and P. Tizzani (Nov. 2017). "New insights on the 2012–2013 uplift episode at Fernandina Volcano (Galápagos)". en. In: *Geophysical Journal International* 211.2, pp. 673–685. ISSN: 0956-540X, 1365-246X. DOI: 10.1093/gji/ggx330. URL: http://academic.oup.com/gji/article/211/2/673/4060698/New-insights-on-the-20122013-uplift-episode-at (visited on 02/18/2021).

Pietruszka, Aaron J and Michael O Garcia (1999). "A Rapid Fluctuation in the Mantle Source and Melting History of Kilauea Volcano Inferred from the Geochemistry of its Historical Summit Lavas (1790–1982)". en. In: 40.8.

Poland, Michael P., Michael Lisowski, Daniel Dzurisin, Rebecca Kramer, Megan McLay, and Ben Pauk (Aug. 2017). "Volcano geodesy in the Cascade arc, USA". en. In:

Bulletin of Volcanology 79.8. ISSN: 0258-8900, 1432-0819. DOI: 10.1007/s00445-017-1140-x. URL: http://link.springer.com/10.1007/s00445-017-1140-x (visited on 11/09/2017).

Poland, Michael P., Asta Miklius, A. Jeff Sutton, and Carl R. Thornber (Apr. 2012). "A mantle-driven surge in magma supply to Kīlauea Volcano during 2003–2007". en. In: *Nature Geoscience* 5.4, pp. 295–300. ISSN: 1752-0894, 1752-0908. DOI: 10.1038/ngeo1426. URL: http://www.nature.com/articles/ngeo1426 (visited on 01/19/2022).

Pritchard, M. E., J. A. Jay, F. Aron, S. T. Henderson, and L. E. Lara (Aug. 2013). "Subsidence at southern Andes volcanoes induced by the 2010 Maule, Chile earthquake". en. In: *Nature Geoscience* 6.8, pp. 632–636. ISSN: 1752-0894, 1752-0908. DOI: 10.1038/ngeo1855. URL: http://www.nature.com/articles/ngeo1855 (visited on 05/11/2021).

Pritchard, M. E., T. A. Mather, S. R. McNutt, F. J. Delgado, and K. Reath (Feb. 2019). "Thoughts on the criteria to determine the origin of volcanic unrest as magmatic or non-magmatic". en. In: *Philosophical Transactions of the Royal Society A: Mathematical, Physical and Engineering Sciences* 377.2139, p. 20180008. ISSN: 1364-503X, 1471-2962. DOI: 10.1098/rsta.2018.0008. URL: https://royalsocietypublishing.org/doi/10.1098/rsta.2018.0008 (visited on 05/26/2020).

Pritchard, M. E. and M. Simons (Feb. 2004). "An InSAR-based survey of volcanic deformation in the central Andes". en. In: *Geochemistry, Geophysics, Geosystems* 5.2, n/a–n/a. ISSN: 15252027. DOI: 10.1029/2003GC000610. URL: http://doi.wiley.com/10.1029/2003GC000610 (visited on 08/07/2018).

Przeor, Monika, Luca D'Auria, Susi Pepe, Pietro Tizzani, and Iván Cabrera-Pérez (Nov. 2022). "Elastic interaction between Mauna Loa and Kīlauea evidenced by independent component analysis". en. In: *Scientific Reports* 12.1, p. 19863. ISSN: 2045-2322. DOI: 10.1038/s41598-022-24308-0. URL: https://www.nature.com/articles/s41598-022-24308-0 (visited on 11/21/2022).

Purcell, Victoria, Eoin Reddin, Susanna Ebmeier, Pablo J. González, Andrew Watson, Yu Morishita, and John Elliott (Oct. 2022). "Nearly Three Centuries of Lava Flow Subsidence at Timanfaya, Lanzarote". en. In: *Geochemistry, Geophysics, Geosystems* 23.10. ISSN: 1525-2027, 1525-2027. DOI: 10.1029/2022GC010576. URL: https://onlinelibrary.wiley.com/doi/10.1029/2022GC010576 (visited on 10/24/2022).

Reverdatto, Vladimir V, Igor I Likhanov, Oleg P Polyansky, Valentin S Sheplev, and Vasiliy Yu Kolobov (2019). *The Nature and Models of Metamorphism*. English. ISBN: 978-3-030-03029-2. URL: https://doi.org/10.1007/978-3-030-03029-2 (visited on 05/26/2020).

Reynolds, Robert W., Dennis Geist, and Mark D. Kurz (Dec. 1995). "Physical volcanology and structural development of Sierra Negra volcano, Isabela Island, Gal´apagos archipelago". en. In: *Geological Society of America Bulletin* 107.12, pp. 1398–1410.

ISSN: 00167606. DOI: 10.1130/0016-7606(1995)107<1398:PVASDO>2.3.CO;2. URL: https://pubs.geoscienceworld.org/gsabulletin/article/107/12/1398-1410/182997 (visited on 10/19/2022).

Rivalta, Eleonora and Paul Segall (Feb. 2008). "Magma compressibility and the missing source for some dike intrusions". en. In: *Geophysical Research Letters* 35.4, p. L04306. ISSN: 0094-8276. DOI: 10.1029/2007GL032521. URL: http://doi.wiley.com/10.1029/2007GL032521 (visited on 07/20/2020).

Robertson, E. A. M. (Feb. 2015). "Magma storage and transport at Kenyan Rift volcanoes: a remote sensing perspective". en-gb. PhD Thesis. Bristol, UK: University of Bristol.

Rowland, Scott K and Duncan C Munro (Dec. 1992). "The caldera of Volcan Fernandina: a remote sensing study of its structure and recent activity". en. In: *Bulletin of Volcanology* 55.1-2, pp. 97–109. ISSN: 0258-8900, 1432-0819. DOI: 10.1007/BF00301123. URL: http://link.springer.com/10.1007/BF00301123 (visited on 03/08/2022).

Rowland, Scott K., Andrew J. L. Harris, Martin J. Wooster, Falk Amelung, Harold Garbeil, Lionel Wilson, and Peter J. Mouginis-Mark (July 2003). "Volumetric characteristics of lava flows from interferometric radar and multispectral satellite data: the 1995 Fernandina and 1998 Cerro Azul eruptions in the western Galapagos". en. In: *Bulletin of Volcanology* 65.5, pp. 311–330. ISSN: 0258-8900, 1432-0819. DOI: 10.1007/s00445-002-0262-x. URL: http://link.springer.com/10.1007/s00445-002-0262-x (visited on 03/01/2022).

Ruiz, Mario Z., Francesco Civilini, Cynthia J. Ebinger, Sarah J. Oliva, Mario C. Ruiz, Gabriela Badi, Peter C. La Femina, and José A. Casas (Mar. 2022). "Precursory Signal Detected for the 2018 Sierra Negra Volcanic Eruption, Galápagos, Using Seismic Ambient Noise". en. In: *Journal of Geophysical Research: Solid Earth* 127.3. ISSN: 2169-9313, 2169-9356. DOI: 10.1029/2021JB022990. URL: https://onlinelibrary.wiley.com/doi/10.1029/2021JB022990 (visited on 10/18/2022).

Sandanbata, Osamu, Hiroo Kanamori, Luis Rivera, Zhongwen Zhan, Shingo Watada, and Kenji Satake (June 2021). "Moment Tensors of Ring-Faulting at Active Volcanoes: Insights Into Vertical-CLVD Earthquakes at the Sierra Negra Caldera, Galápagos Islands". en. In: *Journal of Geophysical Research: Solid Earth* 126.6. ISSN: 2169-9313, 2169-9356. DOI: 10.1029/2021JB021693. URL: https://onlinelibrary.wiley.com/doi/10.1029/2021JB021693 (visited on 10/18/2022).

Segall, Paul (Jan. 2010). *Earthquake and Volcano Deformation:* Princeton University Press. ISBN: 978-1-4008-3385-6. URL: https://www.dawsonera.com:443/abstract/9781400833856.

Shreve, T. and F. Delgado (May 2023). "Trapdoor Fault Activation: A Step Toward Caldera Collapse at Sierra Negra, Galápagos, Ecuador". en. In: *Journal of Geophysical Research: Solid Earth* 128.5, e2023JB026437. ISSN: 2169-9313, 2169-9356. DOI:

10.1029/2023JB026437. URL: https://agupubs.onlinelibrary.wiley.com/doi/10.1029/2023JB026437 (visited on 05/18/2023).

Siebert, Lee, Tom Simkin, and Paul Kimberly (2010). *Volcanoes of the world*. 3rd ed. OCLC: ocn647772311. Washington, D.C. : Berkeley ; University of California Press: Smithsonian Institution. ISBN: 978-0-520-26877-7.

Sigurdsson, Haraldur, Stephen McNutt, Hazel Rymer, and John Stix (2015). *The Encyclopedia of Volcanoes*. London: Academic Press.

Simkin, Tom and Keith A. Howard (July 1970). "Caldera Collapse in the Galápagos Islands, 1968: The largest known collapse since 1912 followed a flank eruption and explosive volcanism within the caldera." en. In: *Science* 169.3944, pp. 429–437. ISSN: 0036-8075, 1095-9203. DOI: 10.1126/science.169.3944.429. URL: https://www.science.org/doi/10.1126/science.169.3944.429 (visited on 03/08/2022).

Special Report of Fernandina Volcano No. 2 - 2017 (Sept. 2017). Special 02. Campus "Ing. José Rubén Orellana", Facultad de Ingeniería Civil 6to. Piso. Av. Ladrón de Guevara E11-253: Instituto Geofísico Escuela Politécnica Nacional. URL: https://www.igepn.edu.ec/servicios/noticias/1512-informe-especial-del-volcan-fernandina-n-2-2017.

Special Volcanic Report - Fernandina - 2020 - No. 3 (Jan. 2020). Special 03. Campus "Ing. José Rubén Orellana", Facultad de Ingeniería Civil 6to. Piso. Av. Ladrón de Guevara E11-253: Instituto Geofísico Escuela Politécnica Nacional. URL: https://igepn.edu.ec/servicios/noticias/1792-informe-especial-del-volcan-fernandina-n-3-2020.

Special Volcanic Report - Fernandina - 2021 - No. 1 (Nov. 2021). Special 01. Campus "Ing. José Rubén Orellana", Facultad de Ingeniería Civil 6to. Piso. Av. Ladrón de Guevara E11-253: Instituto Geofísico Escuela Politécnica Nacional. URL: https://www.igepn.edu.ec/servicios/noticias/1899-informe-volcanico-especial-fernandina-2021-n-01.

Special Volcanic Report - Fernandina - 2021 - No. 2 (Nov. 2021). Special 02. Campus "Ing. José Rubén Orellana", Facultad de Ingeniería Civil 6to. Piso. Av. Ladrón de Guevara E11-253: Instituto Geofísico Escuela Politécnica Nacional. URL: https://www.igepn.edu.ec/servicios/noticias/1900-informe-volcanico-especial-fernandina-2021-n-02.

Spieker, Kathrin, Stéphane Rondenay, Ricardo Ramalho, Christine Thomas, and George Helffrich (May 2018). "Constraints on the structure of the crust and lithosphere beneath the Azores Islands from teleseismic receiver functions". en. In: *Geophysical Journal International* 213.2, pp. 824–835. ISSN: 0956-540X, 1365-246X. DOI: 10.1093/gji/ggy022. URL: https://academic.oup.com/gji/article/213/2/824/4819286 (visited on 11/21/2022).

Stock, Michael J., Marco Bagnardi, David A. Neave, John Maclennan, Benjamin Bernard, Iris Buisman, Matthew L. M. Gleeson, and Dennis Geist (Dec. 2018). "Integrated

Petrological and Geophysical Constraints on Magma System Architecture in the Western Galápagos Archipelago: Insights From Wolf Volcano". en. In: *Geochemistry, Geophysics, Geosystems* 19.12, pp. 4722–4743. ISSN: 15252027. DOI: 10.1029/2018GC007936. URL: http://doi.wiley.com/10.1029/2018GC007936 (visited on 02/18/2021).

Stock, Michael J., Dennis Geist, David A. Neave, Matthew L. M. Gleeson, Benjamin Bernard, Keith A. Howard, Iris Buisman, and John Maclennan (Dec. 2020). "Cryptic evolved melts beneath monotonous basaltic shield volcanoes in the Galápagos Archipelago". en. In: *Nature Communications* 11.1, p. 3767. ISSN: 2041-1723. DOI: 10.1038/s41467-020-17590-x. URL: http://www.nature.com/articles/s41467-020-17590-x (visited on 08/12/2021).

Sturkell, Erik, Freysteinn Sigmundsson, and Ragnar Slunga (May 2006). "1983–2003 decaying rate of deflation at Askja caldera: Pressure decrease in an extensive magma plumbing system at a spreading plate boundary". en. In: *Bulletin of Volcanology* 68.7-8, pp. 727–735. ISSN: 0258-8900, 1432-0819. DOI: 10.1007/s00445-005-0046-1. URL: http://link.springer.com/10.1007/s00445-005-0046-1 (visited on 05/26/2020).

Takada, Youichiro and Yo Fukushima (Aug. 2013). "Volcanic subsidence triggered by the 2011 Tohoku earthquake in Japan". en. In: *Nature Geoscience* 6.8, pp. 637–641. ISSN: 1752-0894, 1752-0908. DOI: 10.1038/ngeo1857. URL: http://www.nature.com/articles/ngeo1857 (visited on 09/04/2018).

Tallarico, A. (2003). "Modeling long-term ground deformation due to the cooling of a magma chamber: Case of Basiluzzo island, Aeolian Islands, Italy". en. In: *Journal of Geophysical Research* 108.B12, p. 2568. ISSN: 0148-0227. DOI: 10.1029/2002JB002376. URL: http://doi.wiley.com/10.1029/2002JB002376 (visited on 05/28/2020).

Teasdale, Rachel, Dennis Geist, Mark Kurz, and Karen Harpp (Feb. 2005). "1998 Eruption at Volcan Cerro Azul, Galapagos Islands: I. Syn-Eruptive Petrogenesis". en. In: *Bulletin of Volcanology* 67.2, pp. 170–185. ISSN: 0258-8900, 1432-0819. DOI: 10.1007/s00445-004-0371-9. URL: http://link.springer.com/10.1007/s00445-004-0371-9 (visited on 03/01/2022).

Tepp, Gabrielle, Cynthia J. Ebinger, Mario Ruiz, and Manahloh Belachew (Jan. 2014). "Imaging rapidly deforming ocean island volcanoes in the western Galápagos archipelago, Ecuador". en. In: *Journal of Geophysical Research: Solid Earth* 119.1, pp. 442–463. ISSN: 21699313. DOI: 10.1002/2013JB010227. URL: http://doi.wiley.com/10.1002/2013JB010227 (visited on 02/24/2021).

Tizzani, P, P Berardino, F Casu, P Euillades, M Manzo, G Ricciardi, G Zeni, and R Lanari (June 2007). "Surface deformation of Long Valley caldera and Mono Basin, California, investigated with the SBAS-InSAR approach". en. In: *Remote Sensing of Environment* 108.3, pp. 277–289. ISSN: 00344257. DOI: 10.1016/j.rse.2006.11.015.

URL: https://linkinghub.elsevier.com/retrieve/pii/S0034425706004688 (visited on 08/01/2023).

Townsend, Meredith (Jan. 2022). "Linking surface deformation to thermal and mechanical magma chamber processes". en. In: *Earth and Planetary Science Letters* 577, p. 117272. ISSN: 0012821X. DOI: 10.1016/j.epsl.2021.117272. URL: https://linkinghub.elsevier.com/retrieve/pii/S0012821X21005288 (visited on 03/02/2023).

Tsuya, Hiromichi (1933). "30. Petrology of Some Lavas of Volcano Asama, Sinano Province, Japan." In: *Bulletin of the Earthquake Research Institute* 11.25, pp. 575–595.

Turcotte, Donald L (1987). "Physics of magma segregation processes". In: *Magmatic processes: physicochemical principles*. Vol. 1. The Geochemical Society, University Park Pennsylvania, pp. 69–74.

U.S. Geological Survey Earthquake Catalogue (Mar. 2023). English. URL: https://earthquake.usgs.gov/earthquakes/search/.

Vasconez, Francisco, Patricio Ramón, Stephen Hernandez, Silvana Hidalgo, Benjamin Bernard, Mario Ruiz, Alexandra Alvarado, Peter La Femina, and Gorki Ruiz (2018). "The different characteristics of the recent eruptions of Fernandina and Sierra Negra volcanoes (Galápagos, Ecuador)". en. In: *Volcanica* 1.2, pp. 127–133. ISSN: 26103540. DOI: 10.30909/vol.01.02.127133. URL: https://www.jvolcanica.org/ojs/index.php/volcanica/article/view/18 (visited on 03/08/2022).

Venzke, E. (Aug. 2023). *Global Volcanism Program, 2023. Volcanoes of the World (v. 5.1.1)*. [Database]. Smithsonian Institution. DOI: https://doi.org/10.5479/si.GVP.VOTW5-2023.5.1. URL: https://volcano.si.edu/search_volcano.cfm.

Walter, T.R., M. Shirzaei, A. Manconi, G. Solaro, A. Pepe, M. Manzo, and E. Sansosti (June 2014). "Possible coupling of Campi Flegrei and Vesuvius as revealed by InSAR time series, correlation analysis and time dependent modeling". en. In: *Journal of Volcanology and Geothermal Research* 280, pp. 104–110. ISSN: 03770273. DOI: 10.1016/j.jvolgeores.2014.05.006. URL: https://linkinghub.elsevier.com/retrieve/pii/S0377027314001413 (visited on 08/27/2021).

Wang, Xiaowen and Yosuke Aoki (Jan. 2019). "Posteruptive Thermoelastic Deflation of Intruded Magma in Usu Volcano, Japan, 1992–2017". en. In: *Journal of Geophysical Research: Solid Earth* 124.1, pp. 335–357. ISSN: 2169-9313, 2169-9356. DOI: 10.1029/2018JB016729. URL: https://onlinelibrary.wiley.com/doi/abs/10.1029/2018JB016729 (visited on 05/26/2020).

Wang, Xiaowen, Yosuke Aoki, and Jie Chen (Dec. 2019). "Surface deformation of Asama volcano, Japan, detected by time series InSAR combining persistent and distributed scatterers, 2014–2018". en. In: *Earth, Planets and Space* 71.1, p. 121. ISSN: 1880-5981. DOI: 10.1186/s40623-019-1104-9. URL: https://earth-planets-

space.springeropen.com/articles/10.1186/s40623-019-1104-9 (visited on 04/28/2023).

Watson, Andrew R., John R. Elliott, and Richard J. Walters (Feb. 2022). "Interseismic Strain Accumulation Across the Main Recent Fault, SW Iran, From Sentinel-1 InSAR Observations". en. In: *Journal of Geophysical Research: Solid Earth* 127.2. ISSN: 2169-9313, 2169-9356. DOI: 10.1029/2021JB022674. URL: https://onlinelibrary.wiley.com/doi/10.1029/2021JB022674 (visited on 06/01/2023).

Wilding, John D., Weiqiang Zhu, Zachary E. Ross, and Jennifer M. Jackson (Feb. 2023). "The magmatic web beneath Hawai'i". en. In: *Science* 379.6631, pp. 462–468. ISSN: 0036-8075, 1095-9203. DOI: 10.1126/science.ade5755. URL: https://www.science.org/doi/10.1126/science.ade5755 (visited on 05/10/2023).

Wolf Volcano Special Report No. 1 - 2022 (Jan. 2022). Special 01. Campus "Ing. José Rubén Orellana", Facultad de Ingeniería Civil 6to. Piso. Av. Ladrón de Guevara E11-253: Instituto Geofísico Escuela Politécnica Nacional. URL: https://www.igepn.edu.ec/servicios/noticias/1908-informe-volcanico-especial-wolf-2022-001.

Wolf Volcano Special Report No. 2 - 2022 (Jan. 2022). Special 02. Campus "Ing. José Rubén Orellana", Facultad de Ingeniería Civil 6to. Piso. Av. Ladrón de Guevara E11-253: Instituto Geofísico Escuela Politécnica Nacional. URL: https://igepn.edu.ec/servicios/noticias/1931-informe-especial-volcan-wolf-no-2022-002.

Wolf Volcano Special Report No. 3 - 2022 (May 2022). Special 03. Campus "Ing. José Rubén Orellana", Facultad de Ingeniería Civil 6to. Piso. Av. Ladrón de Guevara E11-253: Instituto Geofísico Escuela Politécnica Nacional. URL: https://igepn.edu.ec/servicios/noticias/1931-informe-especial-volcan-wolf-no-2022-003.

Xu, Jiandong, Guoming Liu, Jianping Wu, Yuehong Ming, Qingliang Wang, Duxin Cui, Zhiguan Shangguan, Bo Pan, Xudong Lin, and Junqing Liu (Aug. 2012). "Recent unrest of Changbaishan volcano, northeast China: A precursor of a future eruption?: UNREST OF CHANGBAISHAN VOLCANO IN CHINA". en. In: *Geophysical Research Letters* 39.16, n/a–n/a. ISSN: 00948276. DOI: 10.1029/2012GL052600. URL: http://doi.wiley.com/10.1029/2012GL052600 (visited on 05/26/2020).

Xu, Wenbin, Sigurjón Jónsson, Joël Ruch, and Yosuke Aoki (Sept. 2016). "The 2015 Wolf volcano (Galápagos) eruption studied using Sentinel-1 and ALOS-2 data: The 2015 Wolf Eruption in the Galápagos". en. In: *Geophysical Research Letters* 43.18, pp. 9573–9580. ISSN: 00948276. DOI: 10.1002/2016GL069820. URL: http://doi.wiley.com/10.1002/2016GL069820 (visited on 12/12/2022).

Xu, Xiaohua, David T. Sandwell, and Bridget Smith-Konter (July 2020). "Coseismic Displacements and Surface Fractures from Sentinel-1 InSAR: 2019 Ridgecrest Earthquakes". en. In: *Seismological Research Letters* 91.4, pp. 1979–1985. ISSN: 0895-0695, 1938-2057. DOI: 10.1785/0220190275. URL: https://pubs.geoscienceworld.org/

ssa/srl/article/91/4/1979/580045/Coseismic-Displacements-and-Surface-Fractures-from (visited on 06/01/2023).

Yu, Chen, Zhenhong Li, and Nigel T. Penna (Jan. 2018a). "Interferometric synthetic aperture radar atmospheric correction using a GPS-based iterative tropospheric decomposition model". en. In: *Remote Sensing of Environment* 204, pp. 109–121. ISSN: 00344257. DOI: 10.1016/j.rse.2017.10.038. URL: http://linkinghub.elsevier.com/retrieve/pii/S0034425717305011 (visited on 12/02/2017).

Yu, Chen, Zhenhong Li, Nigel T. Penna, and Paola Crippa (Oct. 2018b). "Generic Atmospheric Correction Model for Interferometric Synthetic Aperture Radar Observations". en. In: *Journal of Geophysical Research: Solid Earth* 123.10, pp. 9202–9222. ISSN: 2169-9313, 2169-9356. DOI: 10.1029/2017JB015305. URL: https://onlinelibrary.wiley.com/doi/10.1029/2017JB015305 (visited on 05/20/2021).

Yun, S., P. Segall, and H. Zebker (Feb. 2006). "Constraints on magma chamber geometry at Sierra Negra Volcano, Galápagos Islands, based on InSAR observations". en. In: *Journal of Volcanology and Geothermal Research* 150.1-3, pp. 232–243. ISSN: 03770273. DOI: 10.1016/j.jvolgeores.2005.07.009. URL: https://linkinghub.elsevier.com/retrieve/pii/S0377027305002611 (visited on 03/18/2022).

Zeeuw-van Dalfsen, Elske de, Rikke Pedersen, Andrew Hooper, and Freysteinn Sigmundsson (Feb. 2012). "Subsidence of Askja caldera 2000–2009: Modelling of deformation processes at an extensional plate boundary, constrained by time series InSAR analysis". en. In: *Journal of Volcanology and Geothermal Research* 213-214, pp. 72–82. ISSN: 03770273. DOI: 10.1016/j.jvolgeores.2011.11.004. URL: http://linkinghub.elsevier.com/retrieve/pii/S0377027311003003 (visited on 08/07/2018).

Appendix A

Supporting information for Chapter 2

Contents of this file

1. Figures A1 to A5
2. Tables A1 to A25

Introduction Appendix A contains supporting information for Chapter 2. This includes supporting figures that are referenced in the text, as well as tables of data that are referred to in figures, and tables of various modelling parameters.

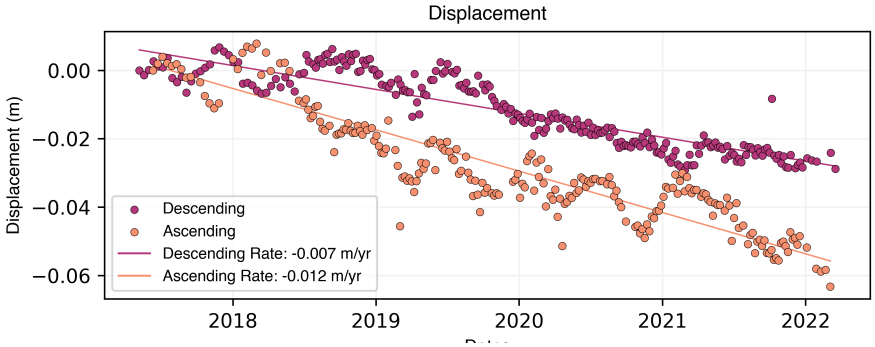

Fig. A1: Time series of post-intrusion subsidence subsidence on the eastern flank of Cerro Azul following the 2017 uplift. The time series are for a point at -0.913 ^{o} N, -91.374^{o} E, relative to a reference area between -90.967 ^{o} E, -90.964 ^{o} E, and -0.957 ^{o} N – -0.950 ^{o} N

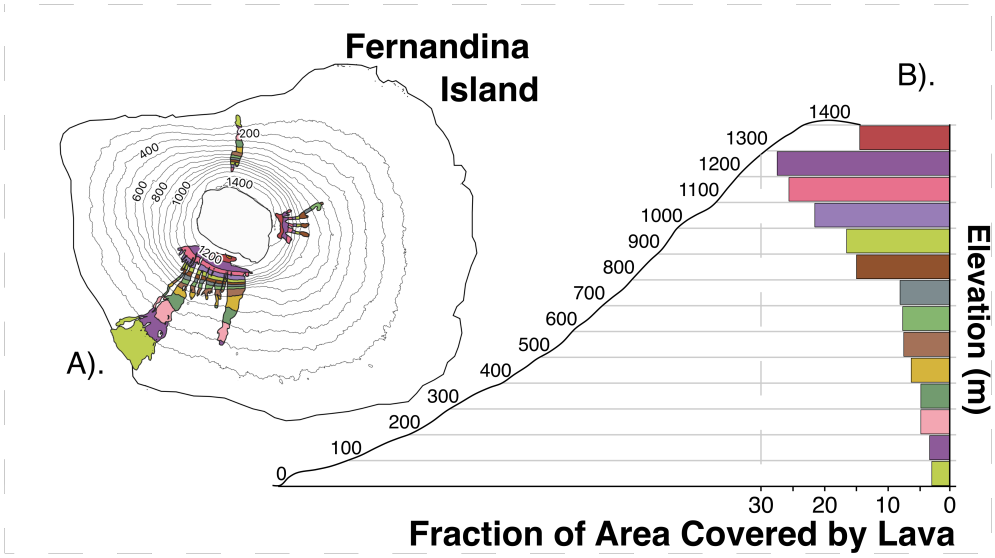

Fig. A2: Extent of lava coverage at Fernandina, with each eruption since 1995. A). Total extent of lava coverage, with each colour representing 100 m of elevation change. B). Fraction of area, in 100 m elevation intervals, covered with lava. The histogram is presented with a topographic profile.

Table A1: Estimated resurfacing times with elevation at Fernandina.

Elevation (m)	Lava Extent (km^2)	Fraction Covered	Resurfacing Time (Yr)
0–100	8	3	833
100–200	3	3.3	758
200–300	3	4.6	543
300–400	2.3	4.7	532
400–500	2.2	6.3	397
500–600	1.9	7.4	338
600–700	1.4	7.6	329
700–800	1.2	7.9	316
800–900	1.6	14.8	169
900–1000	1.4	16.4	152
1000–1100	1.9	21.4	117
1100–1200	2.4	25.4	98
1200–1300	3.1	27.4	91
1300–1400	1.5	14.4	174

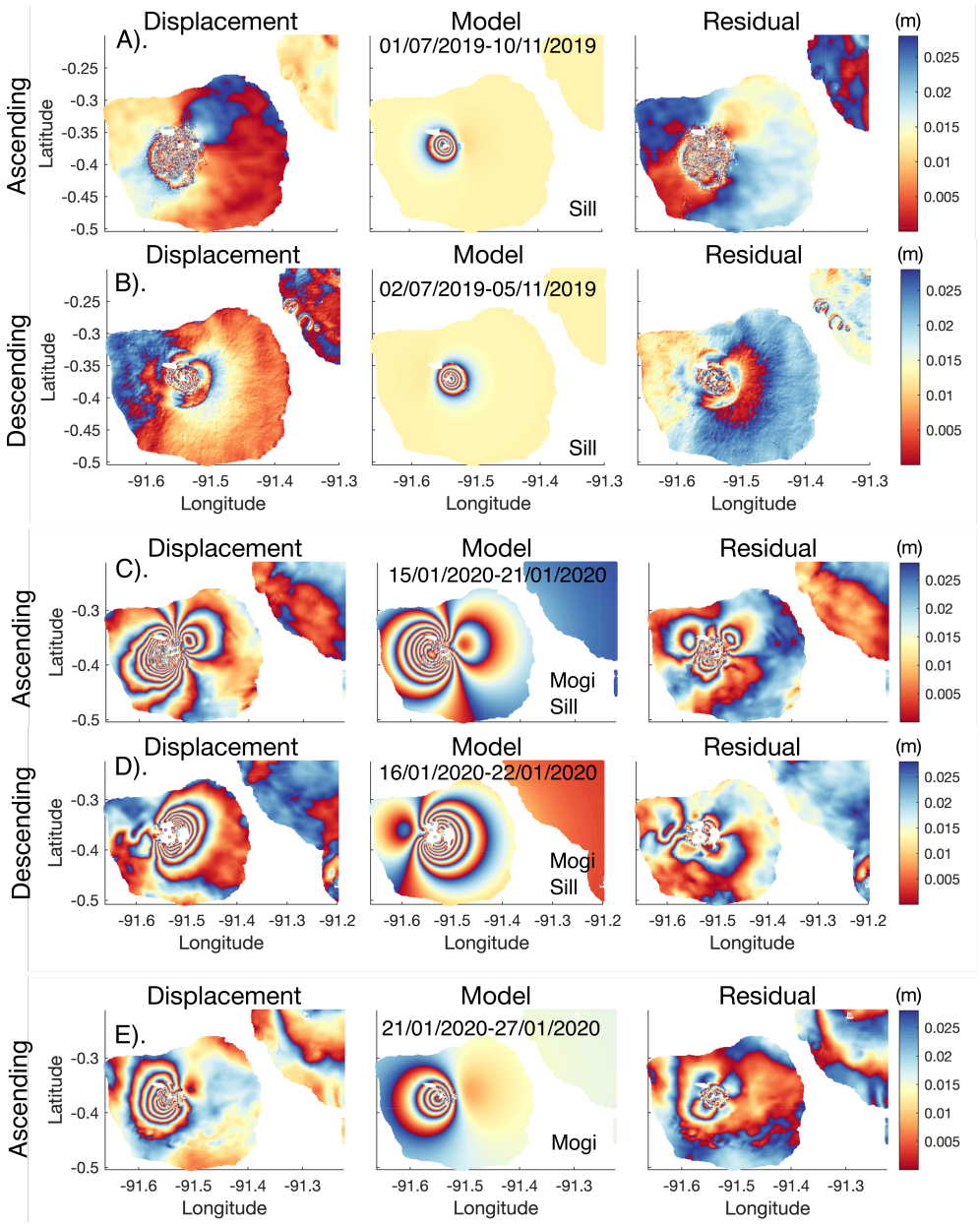

Fig. A3: Results of geodetic source modelling for the 2020 eruption of Fernandina. Full results in Tables A14– A19. A). Data, model, residual for cumulative displacement at Fernandina from 1/07/2019–10/11/2019, in the ascending track direction. B). Data, model, residual for cumulative displacement at Fernandina from 2/07/2019–05/11/2019, in the descending track direction. C). Data, model, residual for cumulative displacement at Fernandina from 15/01/2020–21/01/2020, in the ascending track direction. D). Data, model, residual for cumulative displacement at Fernandina from 16/01/2020–22/01/2020, in the descending track direction. E). Data, model, residual for cumulative displacement at Fernandina from 21/01/2020–27/01/2020, in the ascending track direction.

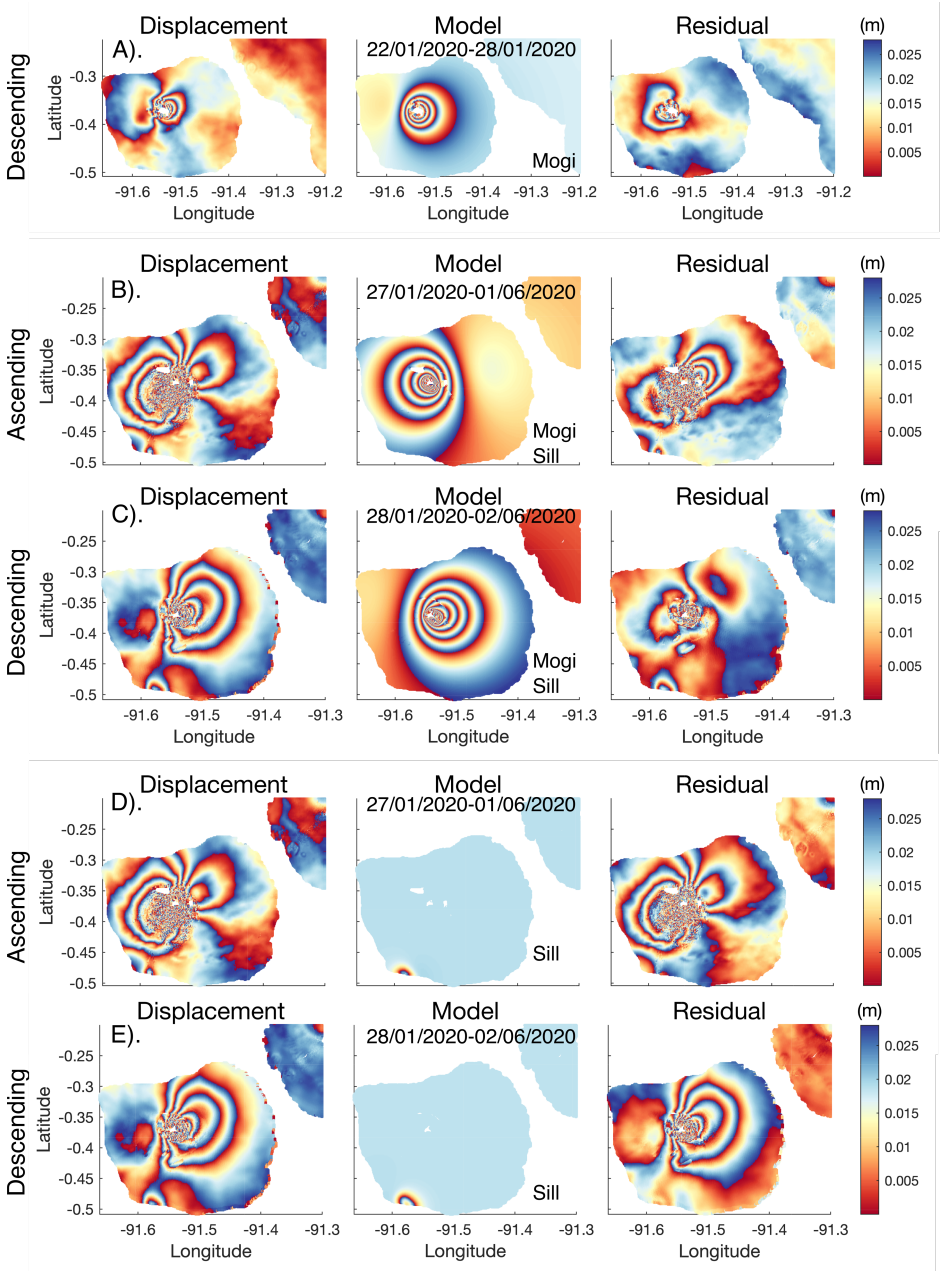

Fig. A4: Results of geodetic source modelling for the 2020 eruption of Fernandina. Full results in Tables A14– A19. A). Data, model, residual for cumulative displacement at Fernandina from 22/07/2020–28/01/2020, in the descending track direction. B). Data, model, residual for cumulative displacement at Fernandina from 27/01/2020–01/06/2020, in the ascending track direction. C). Data, model, residual for cumulative displacement at Fernandina from 28/01/2020–02/06/2020, in the descending track direction. D). Data, model, residual for cumulative displacement at Fernandina from 27/01/2020–01/06/2020, in the ascending track direction. E). Data, model, residual for cumulative displacement at Fernandina from 28/01/2020–02/06/2020, in the descending track direction.

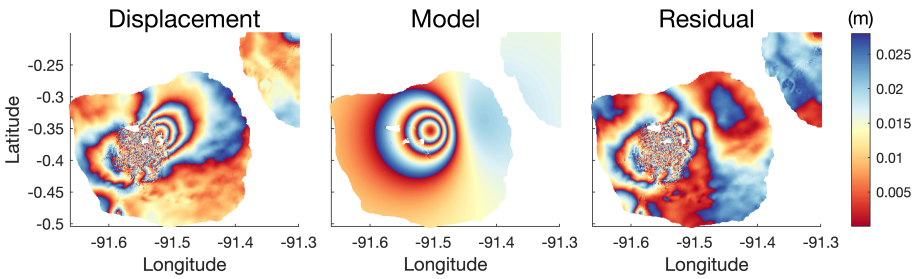

Fig. A5: Data, modelling, and residual for geodetic source modelling of the residual post-eruption of Fernandina, in the ascending track direction. The input data is the residual presented in Figure A4D, spanning 27/01/2020–01/06/2020.

Table A2: Lava volume estimates for recent Galápagos Eruptions. Volumes that could not be found in literature are estimated using the areas presented in Figure 2.2, and previous measurements of lava thickness. [1]Rowland et al. (2003) estimate average thicknesses of 4.5 m for the 1998 eruption of Cerro Azul, [2]average thickness for the 2017 and 2005 circumferential eruptions at Fernandina was 2 m (Vasconez et al., 2018).

Volcano	Year	Fissure Type	Volume (m^3)	Volume Reference	Area Reference
Wolf[a]	2015	Circumferential	$8.7x10^6$	Bernard et al. (2019)	Xu et al. (2016)
Wolf[b]	2022	Radial	$2.3x10^7$	S. Aguaiza (pers. comm.)	*Wolf Volcano Special Report No. 3 - 2022* (2022)
Fernandina[c]	1995	Radial	$5.5x10^7$	Vasconez et al. (2018)	Rowland et al. (2003)
Fernandina[d]	2005	Circumferential	$1.8x10^7$	Vasconez et al. (2018)	Bagnardi et al. (2013)
Fernandina[e]	2009	Radial	$5.7x10^7$	Vasconez et al. (2018)	Bagnardi et al. (2013)
Fernandina[f]	2017	Circumferential	$13 \pm 6.5x10^6$	Vasconez et al. (2018)	*Special Volcanic Report - Fernandina - 2020 - No. 3* (2020)
Fernandina[g]	2018	Radial	$7.92 \pm 4x10^6$	Vasconez et al. (2018)	*Special Volcanic Report - Fernandina - 2020 - No. 3* (2020)
Fernandina[h]	2020	Circumferential	$6x10^6$	Estimated here[2]	*Special Volcanic Report - Fernandina - 2020 - No. 3* (2020)
Cerro Azul[i]	1998	Radial	$5.4x10^7$	Rowland et al. (2003)	Rowland et al. (2003)
Cerro Azul[j]	2008	Radial	$4.7x10^7$	Estimated here[1]	Galetto et al. (2020)
Sierra Negra[k]	2005	Rim	$1.5x10^8$	Vasconez et al. (2018)	Geist et al. (2008)
Sierra Negra[l]	2018	Rim and Distal	$1.9 \pm 0.94x10^8$	Vasconez et al. (2018)	Vasconez et al. (2018)

Table A3: Details of previous sources models of displacement at Alcedo volcano. Complex deformation patterns generally requires either extreme or multiple sources. Lines separate periods when there is multiple sources. Where S is a spherical source, CDM is a Compound Dislocation Model, and RD is a Rectangular Dislocation. Horizontal lines distinguish events.

Reference	Depth	Geometry	Duration	ΔV (m^3)	Location	Instrument
Hooper et al. (2007)	2.2 km	Pipe	1997–2001	-1.3×10^6	Caldera	ERS-1/2
Bagnardi (2014)	3.0 km	S + Fault	2007–2009	Radius: 0.2 km	Caldera	ALOS-1
Galetto et al. (2019)	2.1 km	CDM	2007–2010	8.7×10^6	S. Caldera	Envisat, ALOS-1
Galetto et al. (2019)	1 km	Fault	2007–2010	-	S. Caldera	Envisat, ALOS-1
Galetto et al. (2019)	2.1 km	RD	2007–2010	7×10^6	S. Caldera	Envisat, ALOS-1
Galetto et al. (2019)	1 km	Fault	2007–2010	-	S. Caldera	Envisat, ALOS-1
Galetto et al. (2019)	2.3 km	CDM	01/10–06/10	-3.9×10^6	S. Caldera	Envisat, ALOS-1
Galetto et al. (2019)	2.1 km	CDM	01/10–06/10	2.8×10^6	W. Caldera	Envisat, ALOS-1
Galetto et al. (2019)	2.7 km	RD	01/10–06/10	-2.3×10^6	S. Caldera	Envisat, ALOS-1
Galetto et al. (2019)	3.1 km	RD	01/10–06/10	2.3×10^6	W. Caldera	Envisat, ALOS-1
Galetto et al. (2019)	3.4 km	RD	07/10–03/11	4.1×10^6	S. Caldera	Envisat, ALOS-1

Table A4: Details of previous sources models of displacement at Cerro Azul volcano. Multiple sources are inferred during almost all of the unrest periods .Lines separate periods when there is multiple sources. Data from Guo et al. (2019) all span the co-unrest period, and are inverted from individual interferograms.

Reference	Depth	Geometry	Duration	ΔV (m^3)	Location	Instrument
Amelung et al. (2000)	5 km	Mogi	1992–1997	N/A	Caldera	ERS-1/2
Baker (2012)	6.1 km	Mogi	1998	N/A	Caldera	ERS, Radarsat-1
Bagnardi (2014)	6.08 km	Mogi	1998	Radius: 0.2 km	Caldera	
Baker (2012)	6.2 km	Mogi	2008	N/A	Caldera	Envisat, ALOS-1
Baker (2012)	3.2 km	Dislocation	2008	4.6×10^7	SE. Flank	Envisat, ALOS-1
Baker (2012)	5.7 km	Mogi	2008	N/A	Caldera	Envisat, ALOS-1
Baker (2012)	2.1 km	Dislocation	2008	7.2×10^7	SE. Flank	Envisat, ALOS-1
Baker (2012)	6.4 km	Mogi	2008	N/A	Caldera	Envisat, ALOS-1
Baker (2012)	1.3 km	Dislocation	2008	3.1×10^7	SE. Flank	Envisat, ALOS-1
Galetto et al. (2020)	4.9 km	Mogi	10/07–04/08	11×10^6	Caldera	ALOS-1
Galetto et al. (2020)	3.3 km	RD Dike	04/08–09/08	N/A	SE. Flank	ALOS-1[a]
Galetto et al. (2020)	3.5 km	RD Dike	04/08–09/08	69.2×10^6	SE. Flank	ALOS-1[a]
Galetto et al. (2020)	5.2 km	RD Sill	04/08–09/08	-27.2×10^6	Caldera	ALOS-1[a]
Galetto et al. (2020)	5.2 km	RD Sill	04/08–09/08	-10.4×10^6	Caldera	ALOS-1[a]

[a] Model 1: 2 dikes 2 sills

Table A5: Details of previous sources models of displacement at Cerro Azul volcano continued. Multiple sources are inferred during almost all of the unrest periods .Lines separate periods when there is multiple sources. Data from Guo et al. (2019) all span the co-unrest period, and are inverted from individual interferograms.

Reference	Depth	Geometry	Duration	ΔV (m^3)	Location	Instrument
Galetto et al. (2020)	3.3 km	RD Dike	04/08–05/08	9.9×10^6	SE. Flank	Envisat
Galetto et al. (2020)	5.2 km	RD Sill	04/08–05/08	-11.5×10^6	Caldera	Envisat
Galetto et al. (2020)	3 km	RD Dike	05/08–07/08	56.7×10^6	SE. Flank	Envisat
Galetto et al. (2020)	5.2 km	RD Sill	05/08–07/08	-25.4×10^6	Caldera	Envisat
Galetto et al. (2020)	3.3 km	RD Dike	04/08–09/08	N/A	SE. Flank	ALOS-1[b]
Galetto et al. (2020)	3.5 km	RD Dike	04/08–09/08	68.1×10^6	SE. Flank	ALOS-1[b]
Galetto et al. (2020)	5.2 km	RD Sill	04/08–09/08	-31.1×10^6	Caldera	ALOS-1[b]
Galetto et al. (2020)	3.8 km	RD Dike	04/08–09/08	23.9×10^6	SE. Flank	ALOS-1[b]
Guo et al. (2019)	3.2 km	Mogi	07/03–19/03	-3.34×10^6	Caldera	Sentinel-1
Guo et al. (2019)	4.8 km	Sill	07/03–19/03	6.4×10^6	SE. Flank	Sentinel-1
Guo et al. (2019)	5.95 km	Mogi	08/03–20/03	-3.58×10^7	Caldera	Sentinel-1
Guo et al. (2019)	5.77 km	Sill	08/03–20/03	3.14×10^7	SE. Flank	Sentinel-1
Guo et al. (2019)	5.97 km	Mogi	19/03–31/03	-4.37×10^7	Caldera	Sentinel-1
Guo et al. (2019)	5.4 km	Sill	19/03–31/03	5.7×10^7	SE. Flank	Sentinel-1
Guo et al. (2019)	4.45 km	Mogi	20/03–01/04	-1.92×10^7	Caldera	Sentinel-1
Guo et al. (2019)	6.62 km	Sill	20/03–01/04	3.85×10^7	SE. Flank	Sentinel-1
Bagnardi (2017)	6 km	Mogi	2017	N/A	Caldera	Sentinel-1
Bagnardi (2017)	5 km	Sill	2017	$2 - 4 \times 10^7$	SE. Flank	Sentinel-1

[a] Model 1: 2 dikes 2 sills

[b] Model 2: 3 dikes 1 sill

Table A6: Details of previous sources models of displacement at Darwin volcano. There are a handful of models here as Darwin has been the subject of only three studies where model geometries were retrieved.

Reference	Depth	Geometry	Duration	ΔV (m^3)	Location	Instrument
Amelung et al. (2000)	3 km	Mogi	1992–1998	N/A	Caldera	ERS-1/2
Amelung et al. (2000)[a]	2.7 km	Mogi	1992–1998	5.8×10^6	Caldera	ERS-1/2
Manconi et al. (2007)	3.25 km[b]	Mogi	1992–1998	4.93×10^6	Caldera	ERS-1/2
Manconi et al. (2007)	4.25 km[c]	Mogi	1992–1998	7.74×10^6	Caldera	ERS-1/2
Bagnardi (2014)	3.1 km	Mogi	1992–2000	10×10^6	Caldera	ERS-1/2

[a] in Manconi et al. (2007).
[b] Upper Bounds
[c] Lower Bounds

Table A7: Table of known deformation sources at Fernandina. Includes shallow, deeper, and radial sources for both eruptive and non-eruptive periods.

Reference	Depth	Geometry	Duration	ΔV (m^3)	Location	Instrument
Amelung et al. (2000)	3 km	Mogi	1998–1999	N/A	Caldera	ERS-1/2
Jónsson et al. (1999)	0 km	Mogi	1995	7.5×10^6	SW. Flank	ERS-1/2
Bagnardi and Amelung (2012)	1.1 km	RD	01/07–07/07	1.1×10^6	Caldera	Envisat
Bagnardi and Amelung (2012)	4.9 km	Spheroid	09/07–04/08	N/A	Caldera	Envisat
Bagnardi and Amelung (2012)	4.5 km	Sill	08/07–09/07	19×10^6	SE. Flank	Envisat
Chadwick et al. (2011)	0.93 km	Sill	01/03–04/05	0.75×10^6	Caldera[a]	GPS/Envisat
Chadwick et al. (2011)	6.07 km	Mogi	01/03–04/05	5.07×10^6	Caldera[a]	GPS/Envisat
Chadwick et al. (2011)	1.18 km	Sill	08/05–11/06	1.36×10^6	Caldera[a]	GPS/Envisat
Chadwick et al. (2011)	3.92 km	Mogi	08/05–11/06	2.93×10^6	Caldera[a]	GPS/Envisat
Chadwick et al. (2011)	1.55 km	Mogi	01/03–04/05	1.6×10^6	Caldera[b]	GPS/Envisat
Chadwick et al. (2011)	10.5 km	Mogi	01/03–04/05	4.84×10^6	Caldera[b]	GPS/Envisat
Chadwick et al. (2011)	1.52 km	Mogi	08/05–11/06	2.5×10^6	Caldera[b]	GPS/Envisat
Chadwick et al. (2011)	10.1 km	Mogi	08/05–11/06	1.1×10^6	Caldera[b]	GPS/Envisat
Chadwick et al. (2011)	0	Dike	04/05/–09/05	8.9×10^6	Flank[c]	GPS/Envisat
Chadwick et al. (2011)	1.06	Sill	04/05/–09/05	-0.61×10^6	Caldera[c]	GPS/Envisat
Chadwick et al. (2011)	5	Mogi	04/05/–09/05	-3.02×10^6	Caldera[c]	GPS/Envisat

[a] Model 1; [c] Model 3
[b] Model 2

Table A8: Table of known deformation sources at Fernandina continued. Includes shallow, deeper, and radial sources for both eruptive and non-eruptive periods.

Reference	Depth	Geometry	Duration	ΔV (m^3)	Location	Instrument
Chadwick et al. (2011)	0 km	Dike	04/05/–09/05	1.7×10^6	Flank[d]	GPS/Envisat
Chadwick et al. (2011)	0.67 km	Dike	04/05/–09/05	6.45×10^6	Flank[d]	GPS/Envisat
Chadwick et al. (2011)	1.06 km	Sill	04/05/–09/05	0.92×10^6	Caldera[d]	GPS/Envisat
Chadwick et al. (2011)	5 km	Mogi	04/05/–09/05	-6.2×10^6	Caldera[d]	GPS/Envisat
Chadwick et al. (2011)	0 km	Dike	04/05/–09/05	2.58×10^6	Flank[e]	GPS/Envisat
Chadwick et al. (2011)	0.79 km	Dike	04/05/–09/05	5.3×10^6	Flank[e]	GPS/Envisat
Chadwick et al. (2011)	0 km	Dike	04/05/–09/05	1.89×10^6	Flank[e]	GPS/Envisat
Chadwick et al. (2011)	1.06 km	Sill	04/05/–09/05	0.83×10^6	Caldera[e]	GPS/Envisat
Chadwick et al. (2011)	5 km	Mogi	04/05/–09/05	-6.4×10^6	Caldera[e]	GPS/Envisat
Pepe et al. (2017)	2.1 km	Pipe	2012–2013	6.5×10^7	Caldera	COSMO-SkyMed
Bagnardi et al. (2013)	0.8 km	Sill	2009	7.29×10^6	Caldera	ERS-1/2, Envisat, JERS-1
Bagnardi et al. (2013)	4.93 km	Penny	2009	N/A	Caldera	ERS-1/2, Envisat, JERS-1
Bagnardi et al. (2013)	1.08 km	Sill	2009	-4.8×10^6	SW. Flank	ERS-1/2, Envisat, JERS-1
Bagnardi et al. (2013)	0.65 km	Dike	2009	6.92×10^6	SW. Flank	ERS-1/2, Envisat, JERS-1
Bagnardi et al. (2013)	0 km	Dike	2009	2.81×10^6	SW. Flank	ERS-1/2, Envisat, JERS-1
Bagnardi et al. (2013)	0.64 km	Sill	1995	3.47×10^6	Caldera	ERS-1/2, Envisat, JERS-1
Bagnardi et al. (2013)	0 km	Dike	1995	6.09×10^6	SW. Flank	ERS-1/2, Envisat, JERS-1

[d] Model 4

Table A9: Details of previous sources models of displacement at Sierra Negra volcano

Reference	Depth	Geometry	Duration	ΔV (m^3)	Location	Instrument
Amelung et al. (2000)	2.2 km	Sill	1992–1997	N/A	Caldera	ERS-1/2
Amelung et al. (2000)	1.9 km	Sill	1998–1999	N/A	Caldera	ERS-1/2
Amelung et al. (2000)	2.3–2.9 km	Sill	1997–1998	N/A	Caldera	ERS-1/2
Amelung et al. (2000)	0 km	Fault	1997–1998	N/A	Caldera	ERS-1/2
Jónsson et al. (2005)	2 km	Sill	1992–1999	$2–6\times10^8$	Caldera	ERS-1/2
Chadwick et al. (2006)	2.2 km	Sill	02/04–02/05	$1.7\times10^8\ ^*yr^{-1}$	Caldera	Envisat, cGPS
Chadwick et al. (2006)	0 km	Fault	04/2005	N/A	Caldera	Envisat, cGPS
Geist et al. (2006a)	2.3 km	Mogi	2000-2002	2.6×10^8	Caldera	GPS, Gravimeter
Geist et al. (2006a)	2.1 km	Sill	2000-2002	4.1×10^8	Caldera	GPS, Gravimeter
Yun et al. (2006)	1.9 km	Sill	1998–1999	6.7×10^8	Caldera	ERS
Jónsson (2009)	2.2 km	Sill	02/04–01/05	N/A	Caldera	Envisat, cGPS
Jónsson (2009)	0	Fault	04/2005	N/A	Caldera	Envisat, cGPS
Bagnardi (2014)	2.27 km	Sill	1992–2010	N/A	Caldera	-
Gaddes et al. (2019)	2 km	Sill	12/14–07/18		Caldera	Sentinel-1

Table A10: Details of previous sources models of displacement at Wolf volcano

Reference	Depth	Geometry	Duration	ΔV (m^3)	Location	Instrument
Amelung et al. (2000)	2 km	Mogi	1992–1997	N/A	Caldera	ERS-1/2
Bagnardi (2014)	1.43 km	RD	1992–2010	5×10^6	Caldera	
Xu et al. (2016)	5.2 km	Sill	05/2015	-1.54×10^7	Caldera	Sentinel-1, ALOS-2
Xu et al. (2016)	5 km	Sill	06/2015	-1.5×10^7	Caldera	Sentinel-1, ALOS-2
Xu et al. (2016)	5 km	Sill	05/15–07/15	-2.15×10^7	Caldera	Sentinel-1, ALOS-2
Xu et al. (2016)	1.3 km	Sill	05/2015	-1.7×10^6	Caldera	Sentinel-1, ALOS-2
Xu et al. (2016)	1.2 km	Sill	06/2015	-0.9×10^6	Caldera	Sentinel-1, ALOS-2
Xu et al. (2016)	1.3 km	Sill	05/15–07/15	-2.8×10^6	Caldera	Sentinel-1, ALOS-2
Xu et al. (2016)	0 km	Dike	05/2015	0.5×10^6	Rim	Sentinel-1, ALOS-2
Xu et al. (2016)	0 km	Dike	05/15–06/15	0×10^6	Rim	Sentinel-1, ALOS-2
Xu et al. (2016)	0 km	Dike	06/2015	N/A	Rim	Sentinel-1, ALOS-2
Xu et al. (2016)	0 km	Dike	05/15–07/15	1×10^6	Rim	Sentinel-1, ALOS-2
Xu et al. (2016)	N/A km	Dike	05/2015	N/A	Caldera	Sentinel-1, ALOS-2
Xu et al. (2016)	N/A km	Dike	05/15–06/15	N/A	Caldera	Sentinel-1, ALOS-2
Xu et al. (2016)	0 km	Dike	06/2015	0.3×10^6	Caldera	Sentinel-1, ALOS-2
Xu et al. (2016)	0 km	Dike	05/15–07/15	0.4×10^6	Caldera	Sentinel-1, ALOS-2
De Novellis et al. (2017)	1.5 km	Sill	2004–2010	1×10^6	Caldera	Sentinel-1
De Novellis et al. (2017)	1.4 km	Spheroid	2004-2010	N/A	Caldera	Sentinel-1
De Novellis et al. (2017)	1.5 km	Sill	05/2015	-1.8×10^6	Caldera	Sentinel-1
De Novellis et al. (2017)	0.1 km	Dike	05/2015	6×10^6	Rim	Sentinel-1
De Novellis et al. (2017)	1.5 km	Sill	06/15–07/15	-1.75×10^6	Caldera	Sentinel-1

Table A11: Alcedo best-fit parameters (from 06/01/2017–30/09/2021)

Model Parameter	Optimal	Mean	Median	2.5%	97.5%
Sill Length	3328.7	3097.69	3232.96	1466.51	3770.22
Sill Width	4794.14	4658.87	4676.6	4010.34	5185.77
Sill Depth	1934.25	2219.55	2152.05	1665.99	3137.51
Sill Strike	207.15	209.051	208.784	198.99	220.82
Sill X	-13220.4	-13172.2	-13186.2	-13455.3	-12808.8
Sill Y	-4321.31	-4272.33	-4278.05	-4648.59	-3864.57
Sill Opening	-0.125	-0.173	-0.141	-0.423	-0.10
InSAR Const.	0.018	0.0184	0.018	0.0137	0.023
InSAR Const.	-0.031	-0.030	-0.030	-0.0342	-0.02

Table A12: Cerro Azul best-fit parameters (from 05/07/2017–04/10/2022)

Model Parameter	Optimal	Mean	Median	2.5%	97.5%
Sill Length	9540.71	9536.53	9536.79	9348.25	9720.94
Sill Width	124.82	254.65	264.20	129.52	335.94
Sill Depth	6308.62	6303.04	6302.51	6228.65	6379.66
Sill Strike	229.38	229.416	229.42	228.39	230.42
Sill X	-4510.74	-4549	-4550.18	-4603.09	-4490.1
Sill Y	-18012.9	-17970.8	-17969.4	-18034.2	-17915.7
Sill Opening	24.012	12.481	11.26	8.93	22.99
InSAR Const.	1.44e-05	0.0001	0.0001	-0.001	0.001
InSAR Const.	-0.017	-0.017	-0.017	-0.018	-0.016

Table A13: Darwin best-fit parameters (from 23/10/2019–14/06/2021)

Model Parameter	Optimal	Mean	Median	2.5%	97.5%
Sill Length	143.676	350.223	313.766	126.645	742.109
Sill Width	2273.56	2213.53	2231.92	1676.91	2680.65
Sill Depth	3342.57	3350.31	3348.04	3218.95	3490.9
Sill Strike	243.848	243.709	243.875	232.734	254.468
Sill X	3027.43	3034.46	3035.42	2821.63	3248.02
Sill Y	12796.5	12761.1	12766	12494.9	13013.4
Sill Opening	4.91355	2.52284	2.37883	0.931934	5.62199
InSAR Const.	0.018	0.0181	0.018	0.017	0.019
InSAR Const.	-0.002	-0.002	-0.002	-0.003	-0.002

Table A14: Fernandina pre-eruptive (01/07/2019–10/11/2019) best-fit parameters

Model Parameter	Optimal	Mean	Median	2.5%	97.5%
Sill Length	1626.04	1624.03	1625.69	1444.53	1765.66
Sill Width	57.1699	100.965	73.4386	50.0182	244.593
Sill Depth	2177.02	2173.44	2173.03	2124.87	2223.74
Sill Strike	132.06	132.588	132.59	128.215	136.987
Sill X	-15029	-15040.7	-15034.8	-15091.9	-15010.2
Sill Y	9083.18	9067.53	9073.74	9012.79	9100.41
Sill Opening	17.82	12.96	14.11	4.22	19.87
InSAR Const.	0.041	0.0411	0.041	0.04	0.042

Table A15: Fernandina pre-eruptive (04/12/2019–09/01/2020) best-fit parameters ([a] Depth lower limit at 5 km)

Model Parameter	Optimal	Mean	Median	2.5%	97.5%
Sill Length	2109.36	2519.53	2401.91	1060.91	4495.25
Sill Width	10276.7	12367.5	11446.5	7098.01	19602.7
Sill Depth[a]	4987.03	4671.62	4763.54	3866.45	4991.32
Sill Strike	338.921	340.281	340.245	331.726	349.013
Sill X	-17151	-17409	-17415	-18039.1	-16752.2
Sill Y	-860.848	-1035.96	-1025.91	-1591.59	-510.755
Sill Opening	0.29	0.27	0.248	0.117	0.551
InSAR Const.	-0.017	-0.015	-0.015	-0.018	-0.012

Table A16: Fernandina post-eruptive (15/01/2020–21/01/2020) best-fit parameters

Model Parameter	Optimal	Mean	Median	2.5%	97.5%
Mogi X	-15127.2	-15163.6	-15166.1	-15193.3	-15116.5
Mogi Y	9021.05	8964.86	8960.82	8888.83	9046.04
Mogi Depth	2262.41	2257.11	2257.62	2229.99	2282.04
Mogi DV	2.89e+07	2.81e+07	2.81e+07	2.71e+07	2.91e+07
Sill Length	1650.08	1819.46	1806.72	1662.05	2021.46
Sill Width	1347.74	1623.39	1611.38	1352.9	1900.27
Sill Depth	2575.88	2501.54	2499.66	2415.54	2581.48
Sill Strike	84.4448	77.1589	76.4371	69.6594	90.5214
Sill X	-15074	-14993.5	-14987.7	-15140.1	-14896
Sill Y	8431.95	8263.41	8268.12	8087.62	8437.12
Sill Opening	-8.595	-6.291	-6.292	-8.51	-4.474
InSAR Const.	-0.055	-0.055	-0.055	-0.057	-0.053
InSAR Const.	-0.013	-0.013	-0.013	-0.0142	-0.012

Table A17: Fernandina post-eruptive (21/01/2020–27/01/2020) best-fit parameters

Model Parameter	Optimal	Mean	Median	2.5%	97.5%
Mogi X	-14972	-14973.3	-14973.	-15006.4	-14939.5
Mogi Y	8847.18	8842.16	8842.33	8801.1	8882.16
Mogi Depth	3154.19	3162.11	3162.18	3096.74	3230.07
Mogi DV	6.52e+06	6.55e+06	6.55e+06	6.27e+06	6.86e+06
InSAR Const.	0.017	0.0164	0.0164	0.0152	0.018
InSAR Const.	-0.053	-0.053	-0.053	-0.054	-0.052

Table A18: Fernandina post-eruptive (27/01/2020–01/06/2020) best-fit parameters

Model Parameter	Optimal	Mean	Median	2.5%	97.5%
Mogi X	-14306.2	-14276.6	-14298.6	-14340.4	-14095.9
Mogi Y	9444.53	9481.28	9462.11	9411.1	9659.21
Mogi Depth	5438.96	5641.75	5463.43	5268.77	6953.38
Mogi DV	-1.81e+07	-1.9e+07	-1.82e+07	-2.55e+07	-1.72e+07
Sill Length	1392.68	1268.42	1376.84	415.581	1426.38
Sill Width	2364.29	2318.97	2358.77	2006.99	2393.16
Sill Depth	742.623	815.227	752.192	705.918	1269.05
Sill Strike	213.054	213.913	213.38	211.708	219.16
Sill X	-15797.4	-15758.3	-15788.7	-15815.4	-15526.3
Sill Y	9450.06	9442.33	9445.59	9390.97	9472.76
Sill Opening	-0.33	-0.487	-0.343	-1.78	-0.32
InSAR Const.	0.035	0.036	0.035	0.034	0.041
InSAR Const.	0.009	0.01	0.009	0.008	0.015

Table A19: Fernandina post-eruptive (27/01/2020–01/06/2020) best-fit parameters for SW coast

Model Parameter	Optimal	Mean	Median	2.5%	97.5%
Sill Length	3480.18	3677.59	3654.58	3157.48	4287.55
Sill Width	1309.01	900.469	946.658	86.0892	1624.66
Sill Depth	1472.73	1573.15	1574.79	1359.85	1784.3
Sill Strike	316.608	318.525	318.44	310.984	326.592
Sill X	-18465.4	-18563.5	-18552.7	-18883.7	-18308.8
Sill Y	-4022.42	-4262.93	-4251.47	-4741.99	-3834.26
Sill Opening	-0.09	-0.26	-0.131	-1.5	-0.07
InSAR Const.	0.019	0.019	0.019	0.018	0.0195
InSAR Const.	0.001	0.001	0.001	0.001	0.002

Table A20: Fernandina post-eruptive (27/01/2020–01/06/2020) best-fit parameters for residual ascending data

Model Parameter	Optimal	Mean	Median	2.5%	97.5%
Mogi X	-9698.96	-9694.63	-9695.07	-9839.84	-9547.25
Mogi Y	11206.2	11203.4	11202.5	11103.6	11305.8
Mogi Depth	4393.45	4399.39	4399.33	4244.31	4555.39
Mogi DV	-9.36e+06	-9.38e+06	-9.38e+06	-9.96e+06	-8.82e+06
InSAR Const.	0.014182	0.0141917	0.0141931	0.0133282	0.0150666

Table A21: Wolf sill (14/11/2015–24/12/2021) best-fit parameters

Model Parameter	Optimal	Mean	Median	2.5%	97.5%
Sill Length	170.457	240.661	225.946	160.353	389.486
Sill Width	4171.77	4163.99	4164.42	4096.86	4230.22
Sill Depth	2608.71	2602.87	2602.9	2578.05	2627.14
Sill Strike	164.115	164.111	164.112	163.286	164.951
Sill X	14995.2	14997.8	14997.8	14971.9	15024
Sill Y	-8518.5	-8516.62	-8516.56	-8544.58	-8488.18
Sill Opening	8.79095	6.59241	6.61958	3.84514	9.34561
InSAR Const.	0.0273449	0.0273784	0.0273785	0.0268931	0.027858

Table A22: Wolf dike (14/11/2015–24/12/2021) best-fit parameters

Model Parameter	Optimal	Mean	Median	2.5%	97.5%
Dike Length	1454.27	1441.36	1444.97	1312.79	1544.54
Dike Width	7748.71	7735.3	7735.44	7553.47	7913.9
Dike Depth	1482.75	1483.07	1482.59	1456.92	1510.75
Dike Dip	-34.3384	-34.3373	-34.3424	-35.0192	-33.6374
Dike Strike	162.236	162.141	162.138	161.481	162.831
Dike X	14764.2	14768.8	14769	14741.8	14794.3
Dike Y	-8556.14	-8558.99	-8559.24	-8585.96	-8532.27
Dike Opening	0.947789	0.957385	0.952969	0.883719	1.06198
InSAR Const.	0.0157998	0.0159474	0.0159457	0.0153844	0.0165414

Table A23: Wolf sill–sill (14/11/2015–24/12/2021) best-fit parameters

Model Parameter	Optimal	Mean	Median	2.5%	97.5%
Sill Length	3508.4	3498.9	3498.83	3449.24	3546.94
Sill Width	2189.81	2193.31	2192.21	2144.36	2246.23
Sill Depth	1545.32	1544.16	1544.27	1509.51	1579.67
Sill Strike	284.425	284.812	284.825	283.149	286.36
Sill X	16630.6	16631.8	16631.5	16608.4	16655.4
Sill Y	-7091.35	-7093.66	-7094.34	-7129.28	-7055.5
Sill Opening	0.428466	0.428237	0.42808	0.412842	0.444602
Sill Length	250.568	477.078	446.19	203.871	1133.9
Sill Width	4432.56	4448.66	4449.94	3923.8	4941.9
Sill Depth	5295.31	5272.95	5271.06	5093.87	5468.74
Sill Strike	158.272	158.079	157.98	153.782	162.795
Sill X	17889.1	17878.1	17874.5	17618.8	18153.5
Sill Y	-7303.52	-7314.57	-7317.48	-7501.93	-7119.37
Sill Opening	8.3342	5.53913	4.56539	1.78435	9.79795
InSAR Const.	0.0146571	0.0146072	0.0146114	0.0138319	0.0153353

Table A24: Parameters used in lava subsidence modelling.

Variable	Symbol	Value	Units	Reference
Ambient Temp.	T_a	20	$°C$	
Convective Heat Transfer Coeff.	h_c	75	$Wm^{-2}K^{-1}$	Patrick (2004)
Density	ρ	2500	kgm^{-3}	Annen (2017)
Emissivity	ϵ	0.95		Patrick (2004)
Ground Temp.	T_G^0	25	$°C$	
Initial Lava Temp.	T_L^0	1200	$°C$	
Poissons Ratio	ν	0.25		Chaussard (2016)
Specific Heat	c_p	1000	$Jkg^{-1}K^{-1}$	Annen (2017)
Stefan-Boltzmann Constant	σ	5.67×10^{-8}	$Wm^{-2}K^{-4}$	Patrick (2004)
Thermal Conductivity	k	2.5	$Wm^{-1}K^{-1}$	Annen (2017)
Thermoelastic Expansion Coeff.	η	3.4×10^{-5}	K^{-1}	Chaussard (2016)

Table A25: Parameters used in MELTS modelling. Parameters from Aiuppa et al. (2022) and Davis et al. (2021). Values for CO_2, and S have been excluded for compliance with MELTS.

Pressure (Bars)	fO_2 Path	Δ fO_2	SiO2	TiO2	Al2O3	FeO
250	NNO	-1.5	48	2.7	15.4	10
	MgO	CaO	Na2O	K2O	MnO	H2O
	8.2	11.7	2.3	0.3	0.1	1

Appendix B

Supporting information for Chapter 3

Contents of this file

1. Figures B1 to B21
2. Tables B1 to B4

Introduction Appendix B contains supporting information for Chapter 3. This includes supporting figures that are referenced in the text, as well as tables of data listing the acquisition dates of Sentinel-1 data.

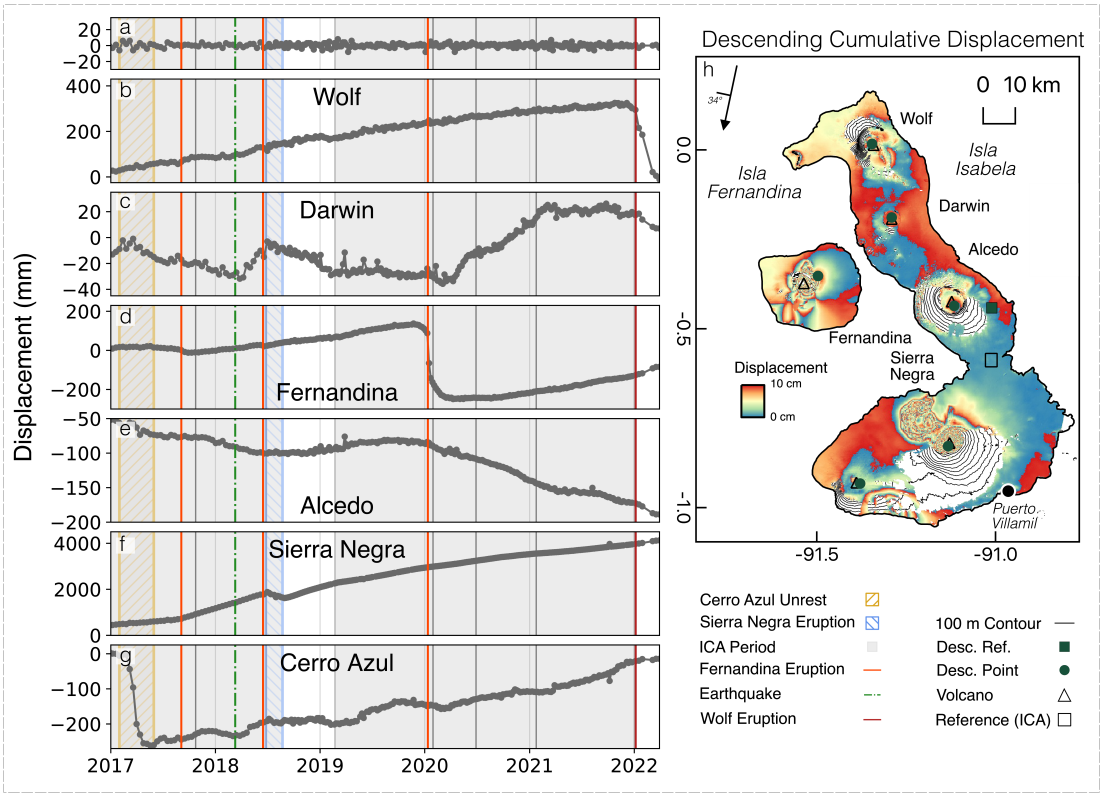

Fig. B1: Descending Sentinel-1 data for the Western Galápagos. **a**, Time series of displacement of the reference pixel, showing its variation with time. **b**–**g**, Time series of displacement at each of the major volcanoes of the Western Galápagos, from 07/01/2017–30/03/2022. Annotated are known periods of significant unrest, including unrest at Cerro Azul, and eruptions at each of Fernandina, Sierra Negra, and Wolf. The grey areas denote the periods used for Independent Component Analysis, as presented in this study. **h**, Wrapped cumulative displacement map of the Western Galápagos, across the entire time series. Each fringe corresponds to 10 cm of range change in the satellite line-of-sight. The arrow shows the satellite heading, as well as the average incidence angle. The annotated points refer to pixels used during correlation analysis, while the reference area is used during Independent Component Analysis (Figure 3.2).

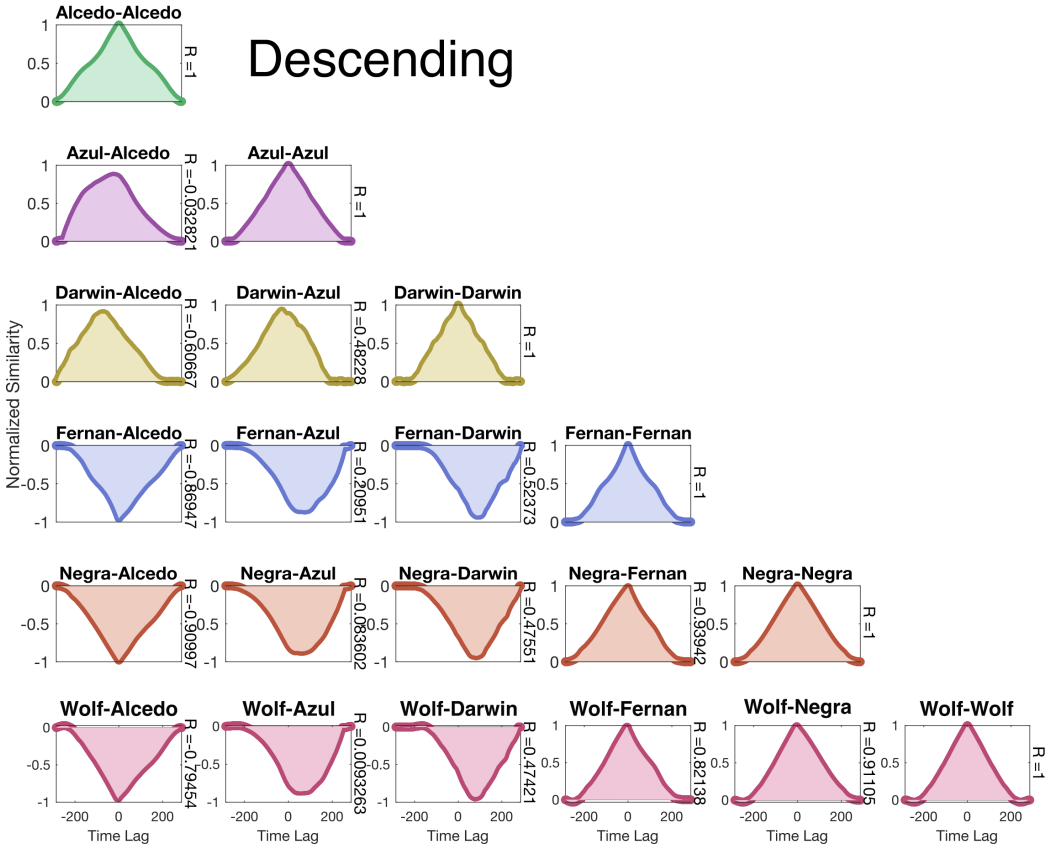

Fig. B2: Results of cross-correlation analysis for the entire time series of each volcanic pair, in Descending. Similarity between time series is presented on the y-axis, while time lag is presented on the X. The time lag refers to satellite acquisitions between time series points being compared (e.g. a lag of five means there was five satellite acquisitions between points). When cross-correlation analysis is performed on a time-series and a duplicate of itself, the resulting plots will be have a symmetrical triangular shape, as similarity is maximised at a time lag of zero, and then decays in both positive and negative time lag directions (e.g. Darwin-Darwin). The symmetrical triangular shapes when each volcano is plotted against itself represents this maximised similarity at zero time lag. Asymmetrical triangular shapes (not centred at time lag of zero) occur when the compared time series are most similar when temporally offset (e.g. Darwin–Wolf). The correlation coefficient for each pair of time series is annotated on the right y-axis.

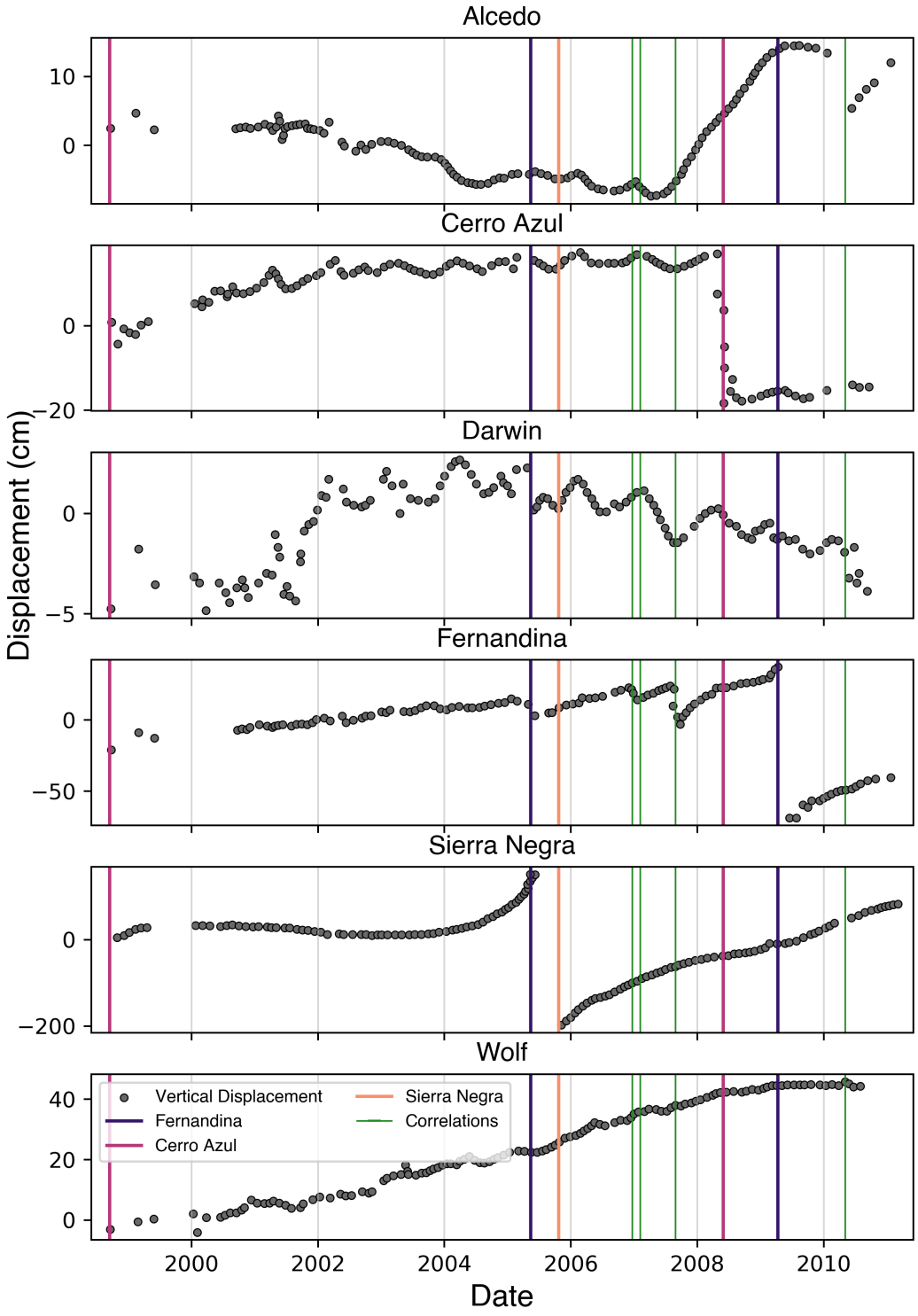

Fig. B3: Time series of displacement at each volcano in the Western Galápagos from 1998–2011, modified from (Baker, 2012). In each case, dots represent vertical displacement, in centimetres, while the vertical lines represent various eruptions. The erupted volcano is denoted by colour, while the episodes of correlated displacements observed by (Baker, 2012) are marked by vertical green lines. These data are a compilation from multiple satellite missions (ERS-1/2, Envisat, Radarsat, AlOS-1.)

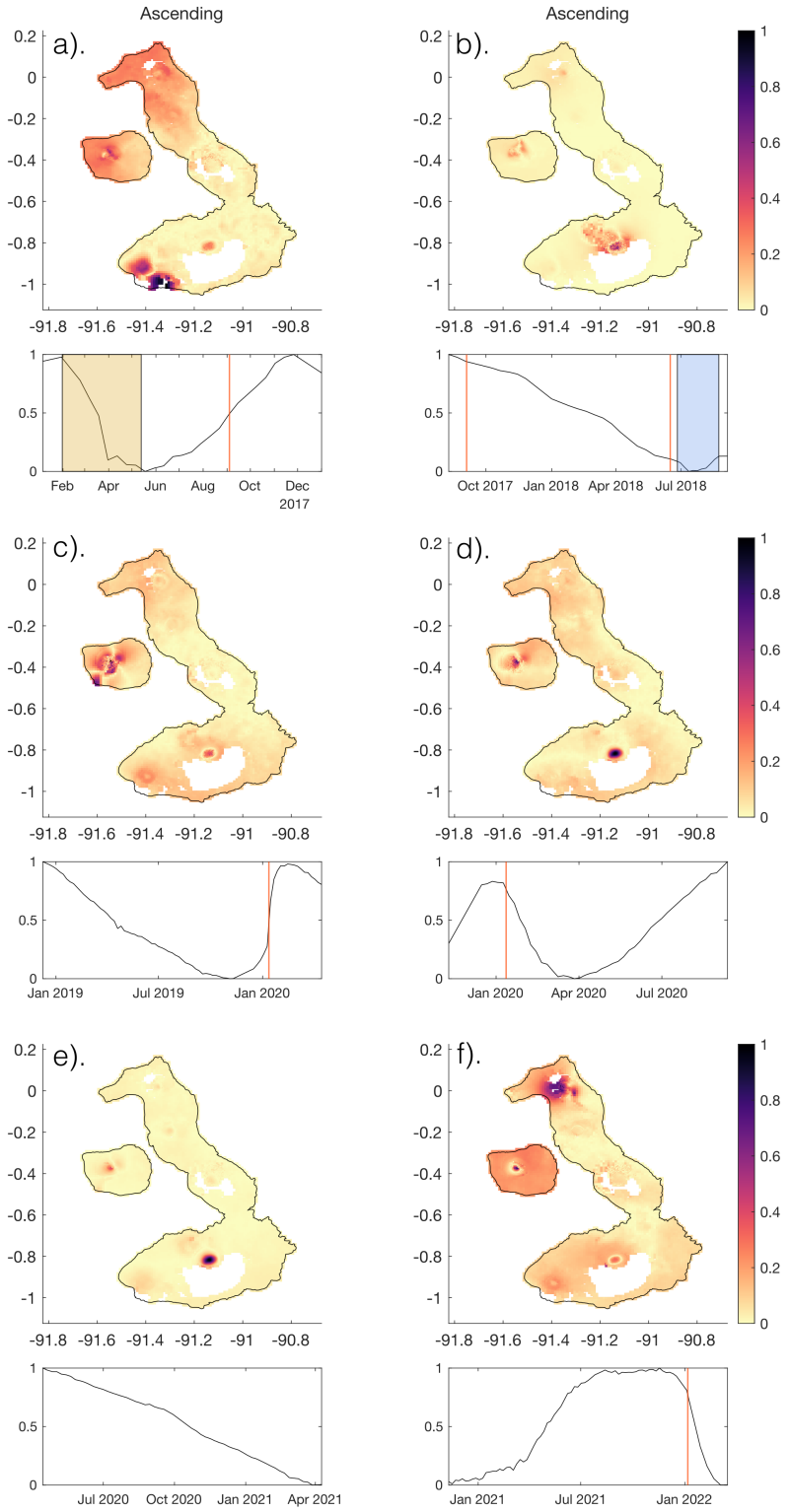

Fig. B4: Spatially reconstructed unmixing values for each independent component, in Ascending Data; the periods over which we perform ICA is informed by Figure 3.3. In each map, colors represent the relative strength of the retrieved independent component, providing a spatial representation of temporal data, while the lower panel shows the normalised independent component. There is some temporal overlap between each independent component, to account for overlapping windows in Figure 3.3. **a**, 10/15/2016–01/02/2018: 2017 unrest at Cerro Azul, and eruption of Fernandina. **b**, 08/11/2017–09/11/2018: eruptions at Fernandina in 2017 and 2018, and Sierra Negra in 2018. **c**, 12/10/2018–04/15/2020: 2020 eruption at Fernandina. **d**, 11/17/2019 09/12/2020: 2020 eruption of Fernandina. **e**, 04/15/2020–04/10/2021: no major volcanic unrest. **f**, 11/11/2020–03/18/2022: 2022 eruption of Wolf.

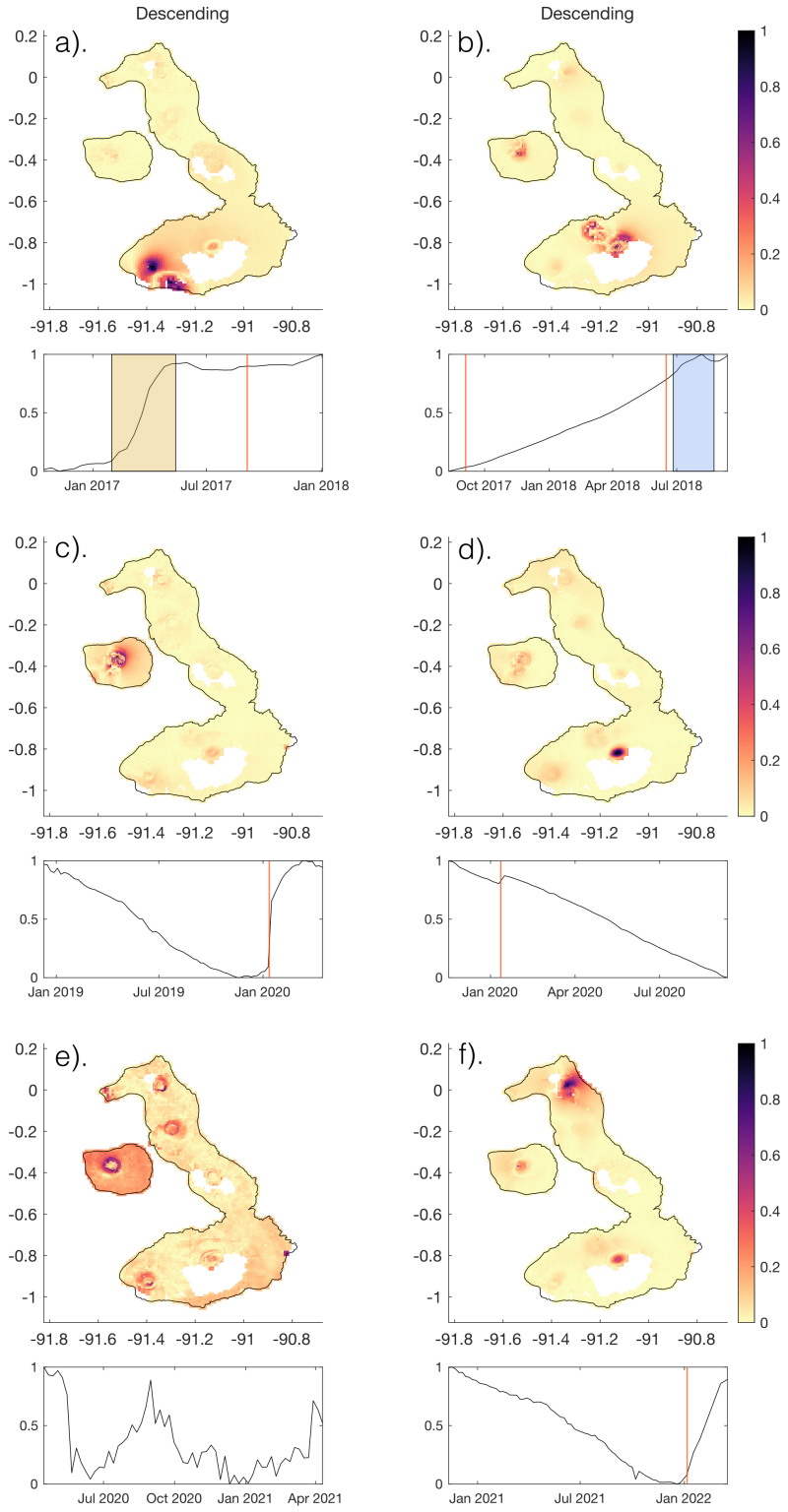

Fig. B5: Spatially reconstructed unmixing values for each independent component, in Descending Data; the periods over which we perform ICA is informed by Figure 3.3. In each map, colors represent the relative strength of the retrieved independent component, providing a spatial representation of temporal data, while the lower panel shows the normalised independent component. There is some temporal overlap between each independent component, to account for overlapping windows in Figure 3.3. **a**, 10/15/2016–01/02/2018: 2017 unrest at Cerro Azul, and eruption of Fernandina. **b**, 08/11/2017–09/11/2018: eruptions at Fernandina in 2017 and 2018, and Sierra Negra in 2018. **c**, 12/10/2018–04/15/2020: 2020 eruption at Fernandina. **d**, 11/17/2019 09/12/2020: 2020 eruption of Fernandina. **e**, 04/15/2020–04/10/2021: no major volcanic unrest. **f**, 11/11/2020–03/18/2022: 2022 eruption of Wolf.

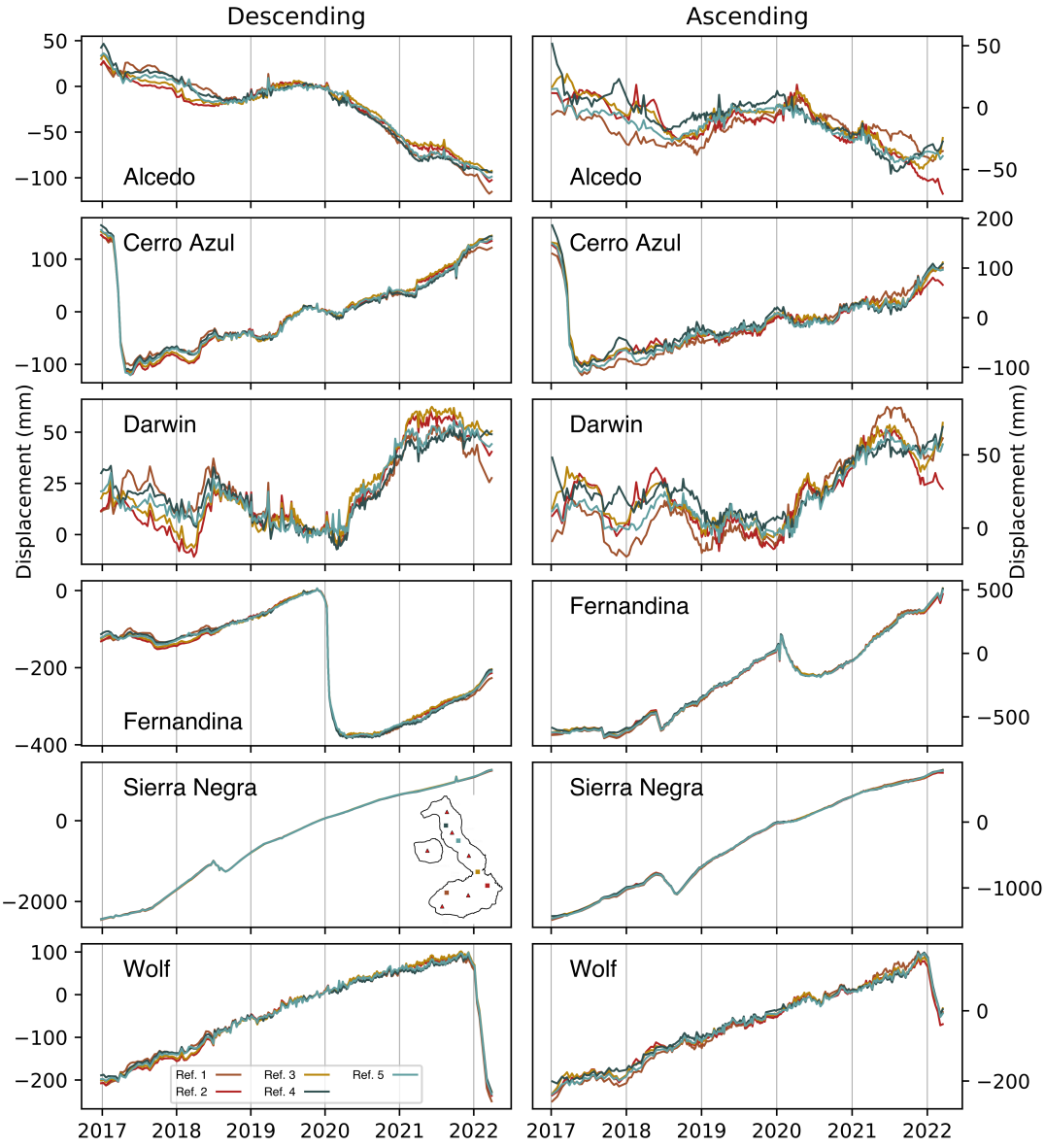

Fig. B6: Influence of choice of reference pixel, at each volcano. In each case, the plotted pixel is held constant. Descending and Ascending time series are presented in each column, while a different volcano is plotted in each row. Line colours correspond to the plotted reference pixel, the location of which is presented in the inset map.

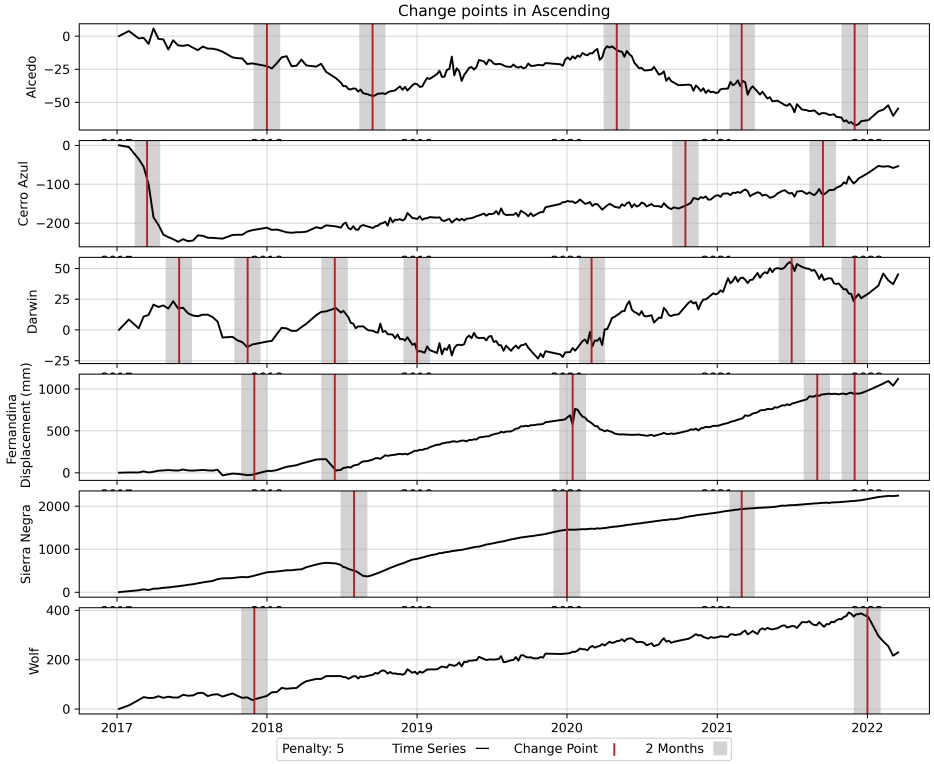

Fig. B7: Change points at each Western Galápagos volcano in the ascending track direction, from 2017–2022, as identified on the basis of changes in rate or direction. Change points are annotated in red, while the grey boxes illustrate a one month period either side of the change point.

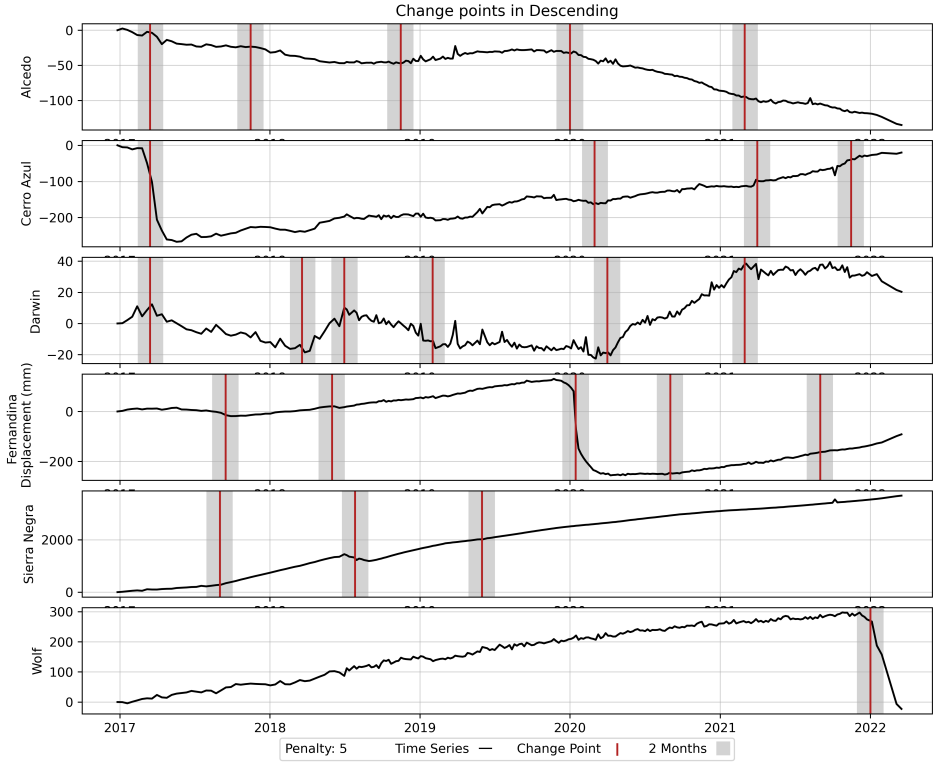

Fig. B8: Change points at each Western Galápagos volcano in the descending track direction, from 2017–2022, as identified on the basis of changes in rate or direction. Change points are annotated in red, while the grey boxes illustrate a one month period either side of the change point.

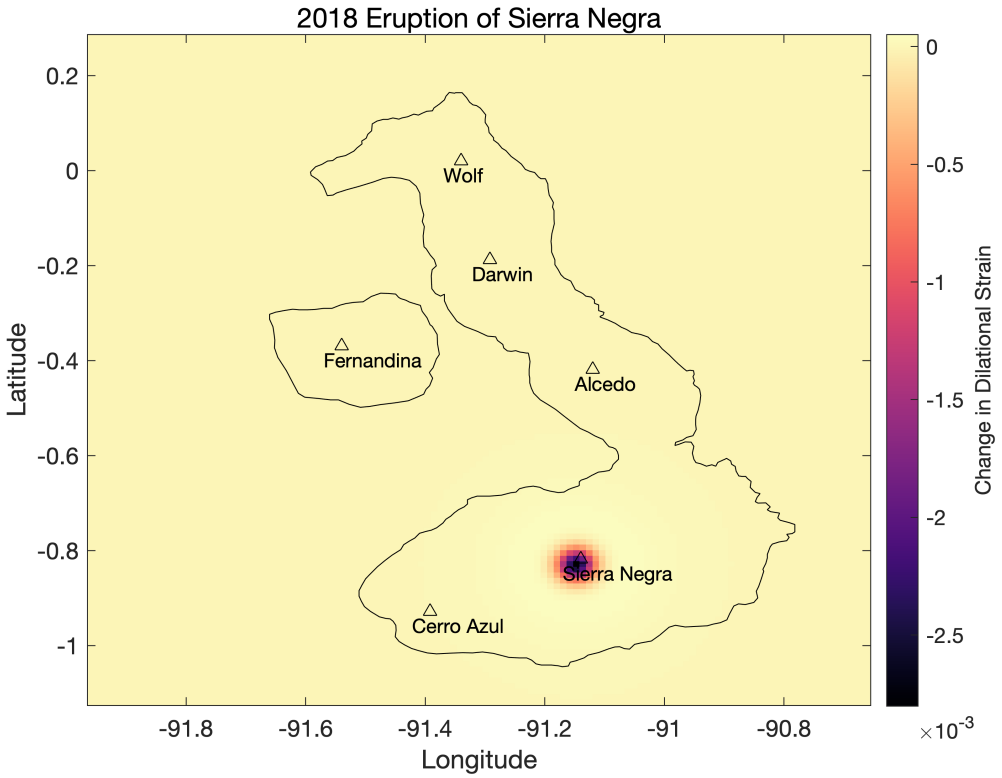

Fig. B9: Dilational strain associated with the 2018 eruption of Sierra Negra, modelled using Coulomb 3.1 (Lin and Stein, 2004). The eruption is approximated as a point source with a volume decrease of $-2x10^8\ m^3$ (Vasconez et al., 2018)

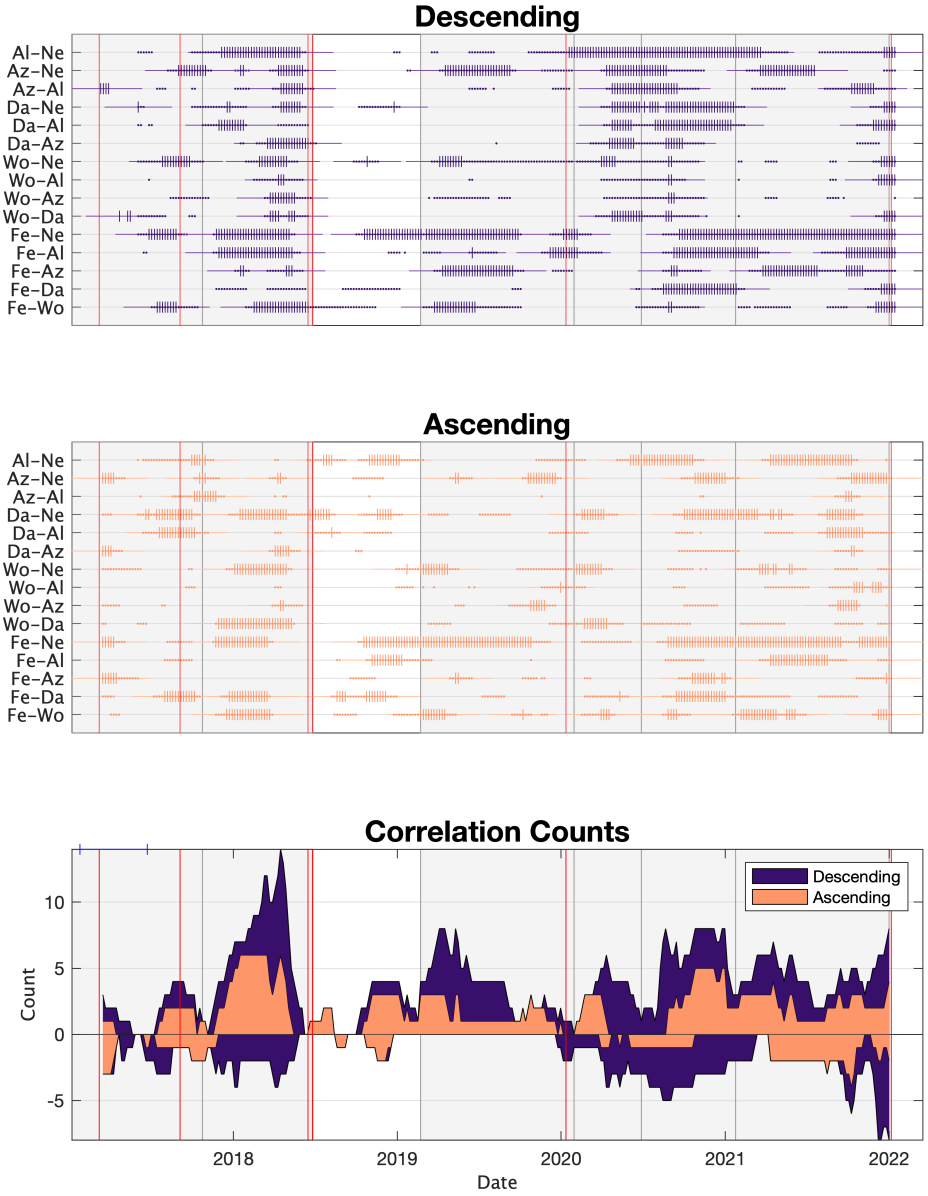

Fig. B10: Periods of heightened correlation between Western Galápagos volcanoes, determined using windowed correlation analysis, using a window size of 150 days. Red lines illustrate a significant unrest event (e.g. eruption). **a**–**b**, Pairwise correlation coefficients for Western Galápagos volcanoes. The location of the pixel used to create each time series is illustrated in Figure 3.1. Vertical lines and dots at each volcanic pair denote a respective correlation coefficients of $>|\ 0.9\ |$ and $>|\ 0.75\ |$ across the corresponding window, with each point plotted at the centre of the window. Horizontal lines illustrate the temporal extent of each window. **c**, Stacked area plot of correlation coefficients of $>|\ 0.9\ |$ to illustrate periods of heightened correlation. These identified periods are separated by grey boxes.

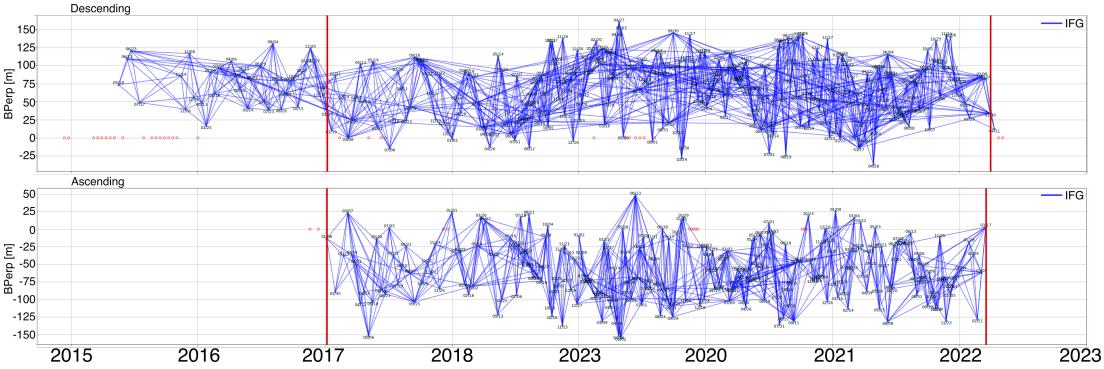

Fig. B11: Perpendicular baselines for either track direction.

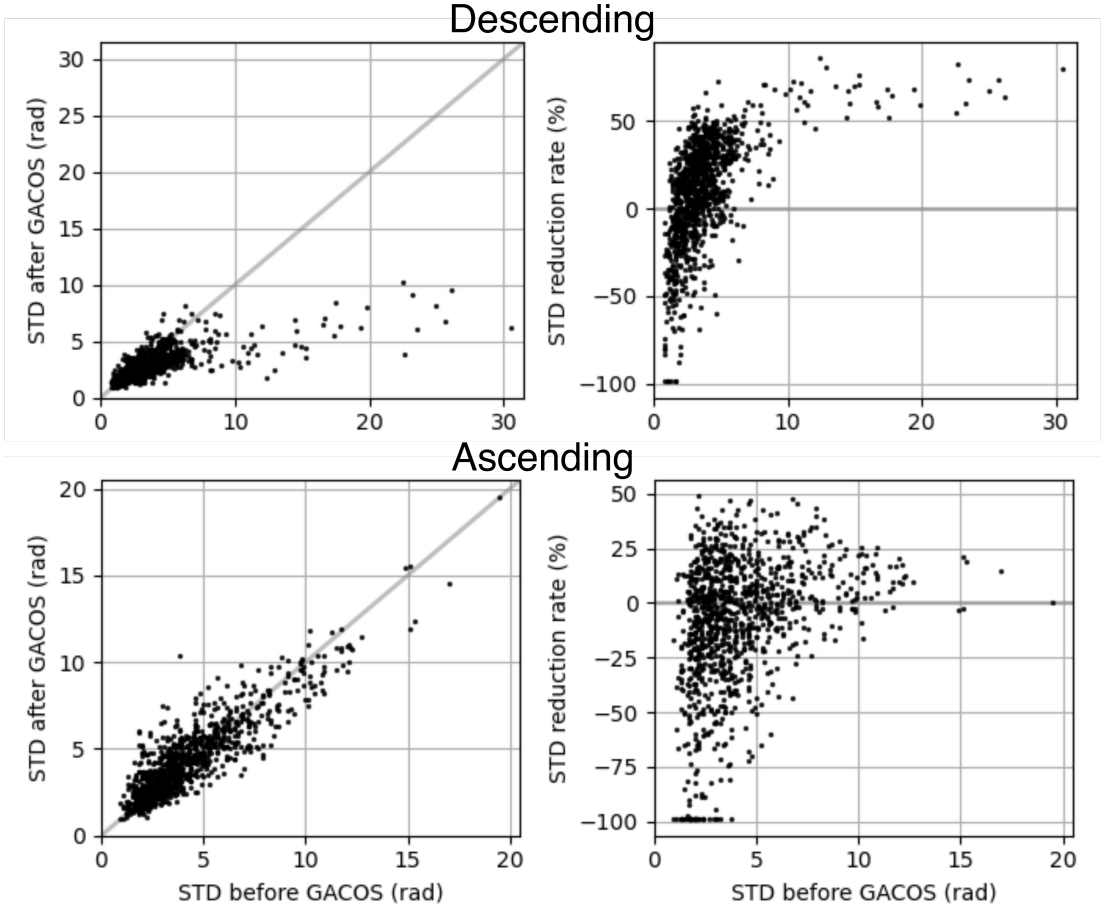

Fig. B12: Effect of GACOS correction on each data set. The left columns plot the mean standard deviation before correction against that after correction, while the right columns plot the percentage change in standard deviation due to the correction.

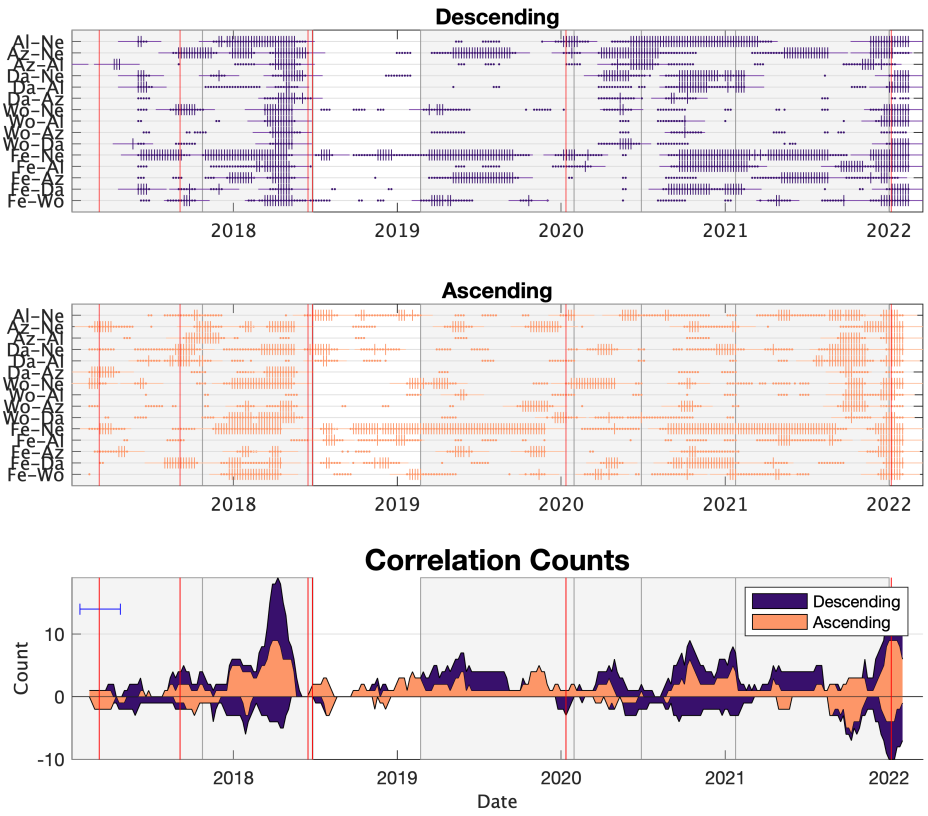

Fig. B13: Periods of heightened correlation between Western Galápagos volcanoes, determined using windowed correlation analysis. Here, with a window size of 15 acquisitions (approximately 3 months, the extent of which is shown by the horizontal black line), to show the affect of alternating the window size.

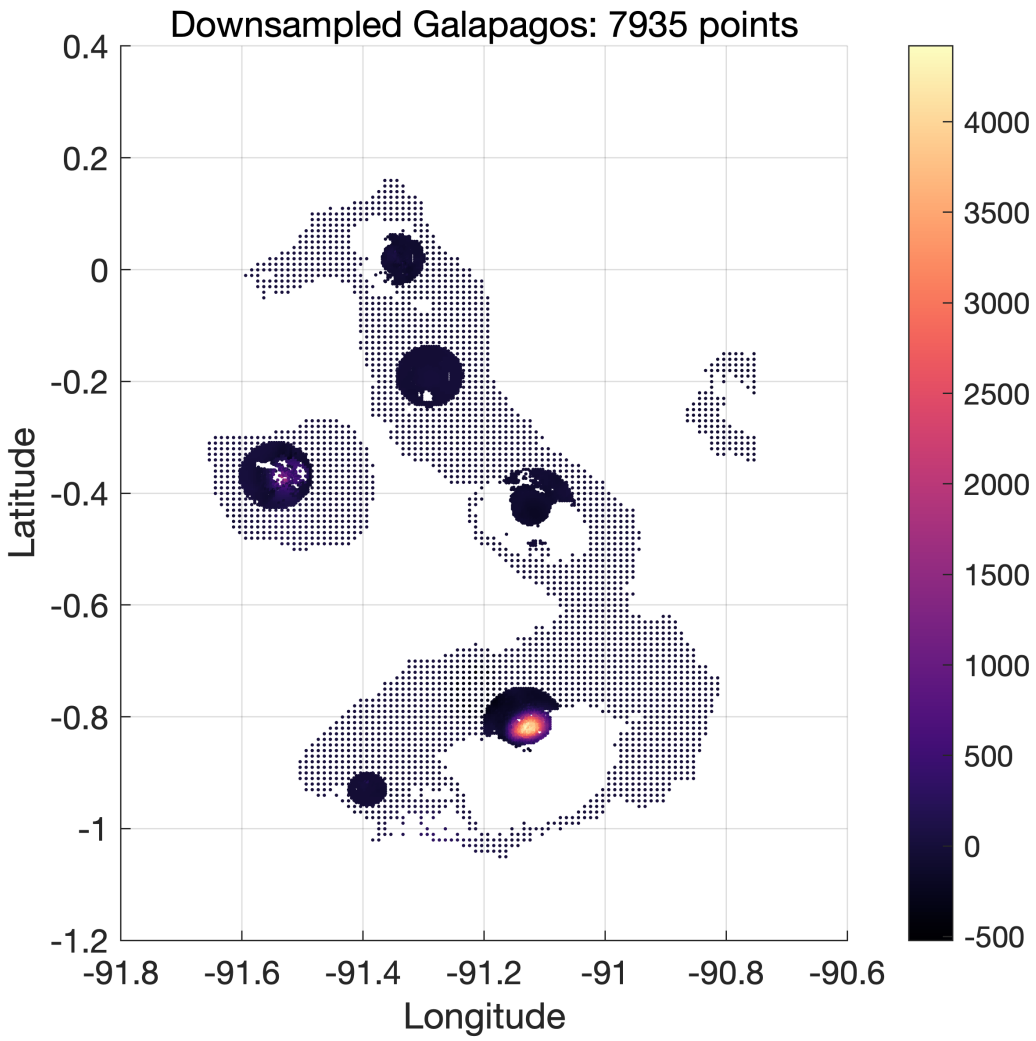

Fig. B14: The downsampled descending dataset used for Independent Component Analysis. Each point corresponds to the location of one time series of displacement

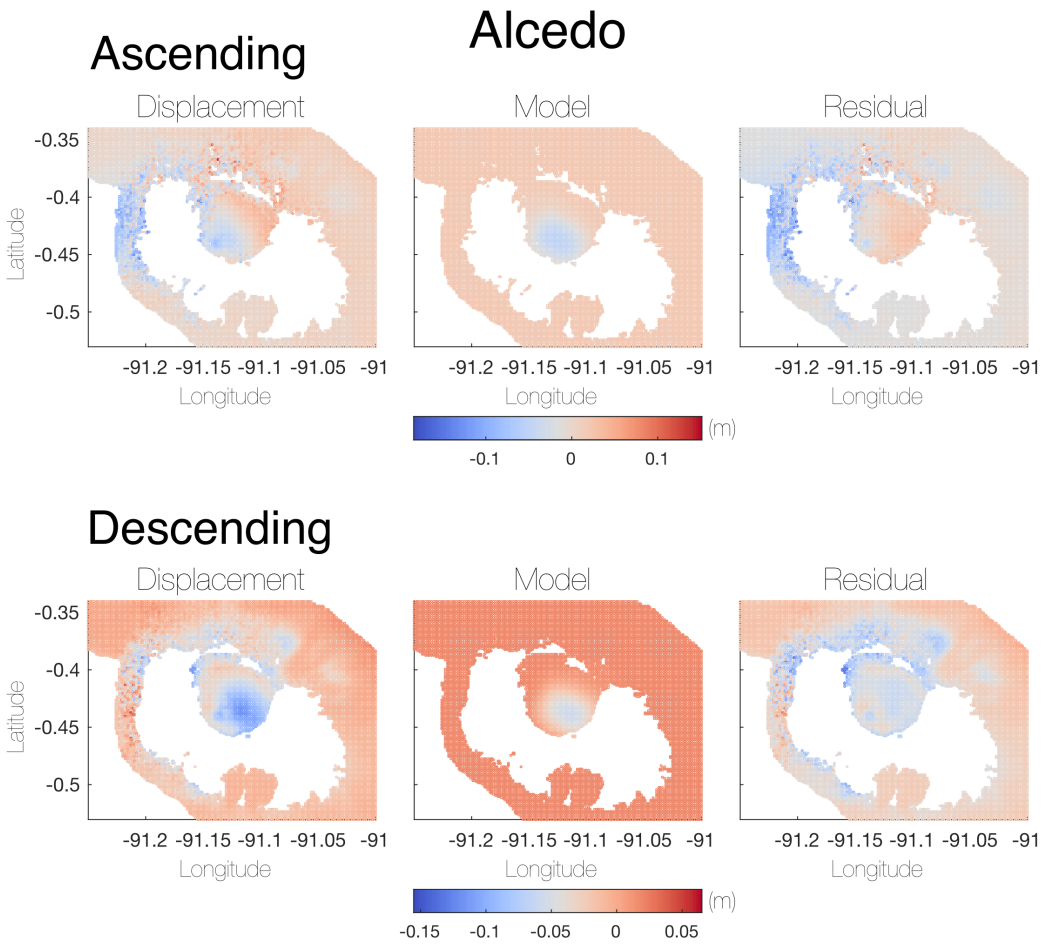

PARAM.	OPTIMAL	2.5%	97.50%
Length (m)	3328.7	1466.51	3770.22
Width (m)	4794.14	4010.34	5185.77
Depth (m)	1934.25	1665.99	3137.51
Strike (m)	207.155	198.998	220.828
X (m)	-13220.4	-13455.3	-12808.8
Y (m)	-4321.31	-4648.59	-3864.57
Opening (m)	-0.125198	-0.423341	-0.105476
InSAR Const.	0.0182488	0.0137716	0.0231403
InSAR Const.	-0.0315067	-0.0342392	-0.0274933

Fig. B15: Data, model, and residual for the best fitting sill source at Alcedo, from 26/12/2016–01/10/2021. The optimal source parameters, as well as the 2.5% and 97.5% bounds are presented in the underlying table.

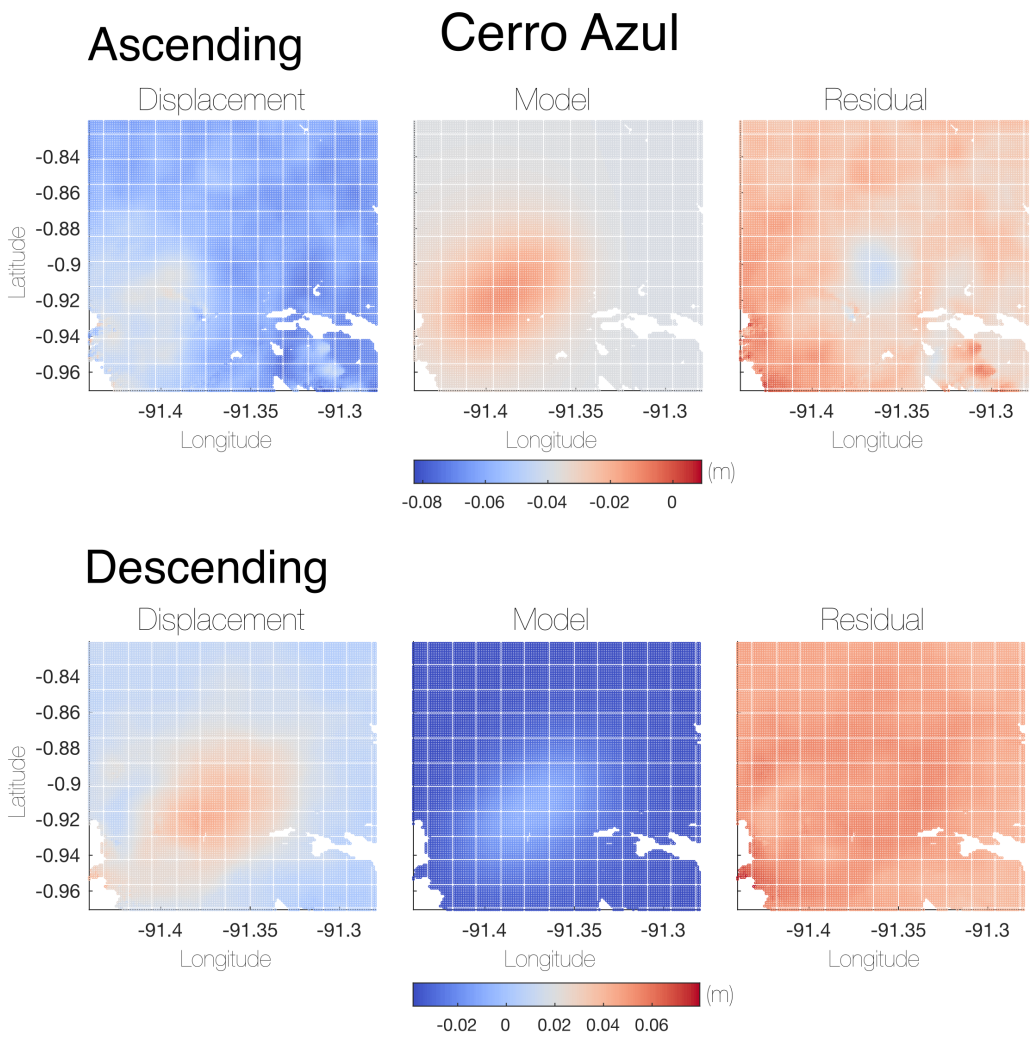

PARAM.	OPTIMAL	2.5%	97.50%
Length (m)	271.185	150.162	313.129
Width (m)	7678.99	7541.83	7771.15
Depth (m)	4522.96	4303.95	4518.23
Strike (m)	145.552	145.081	146.86
X (m)	2944.73	2858.59	2987.62
Y (m)	-4627.32	-4672.01	-4557.39
Opening (m)	1.04704	0.880844	1.71992
InSAR Const.	-0.0382424	-0.0379602	-0.0316358
InSAR Const.	0.0115861	0.0116052	0.012296

Fig. B16: Data, model, and residual for the best fitting sill source at Cerro Azul, from 02/02/2020–03/01/2021. The optimal source parameters, as well as the 2.5% and 97.5% bounds are presented in the underlying table.

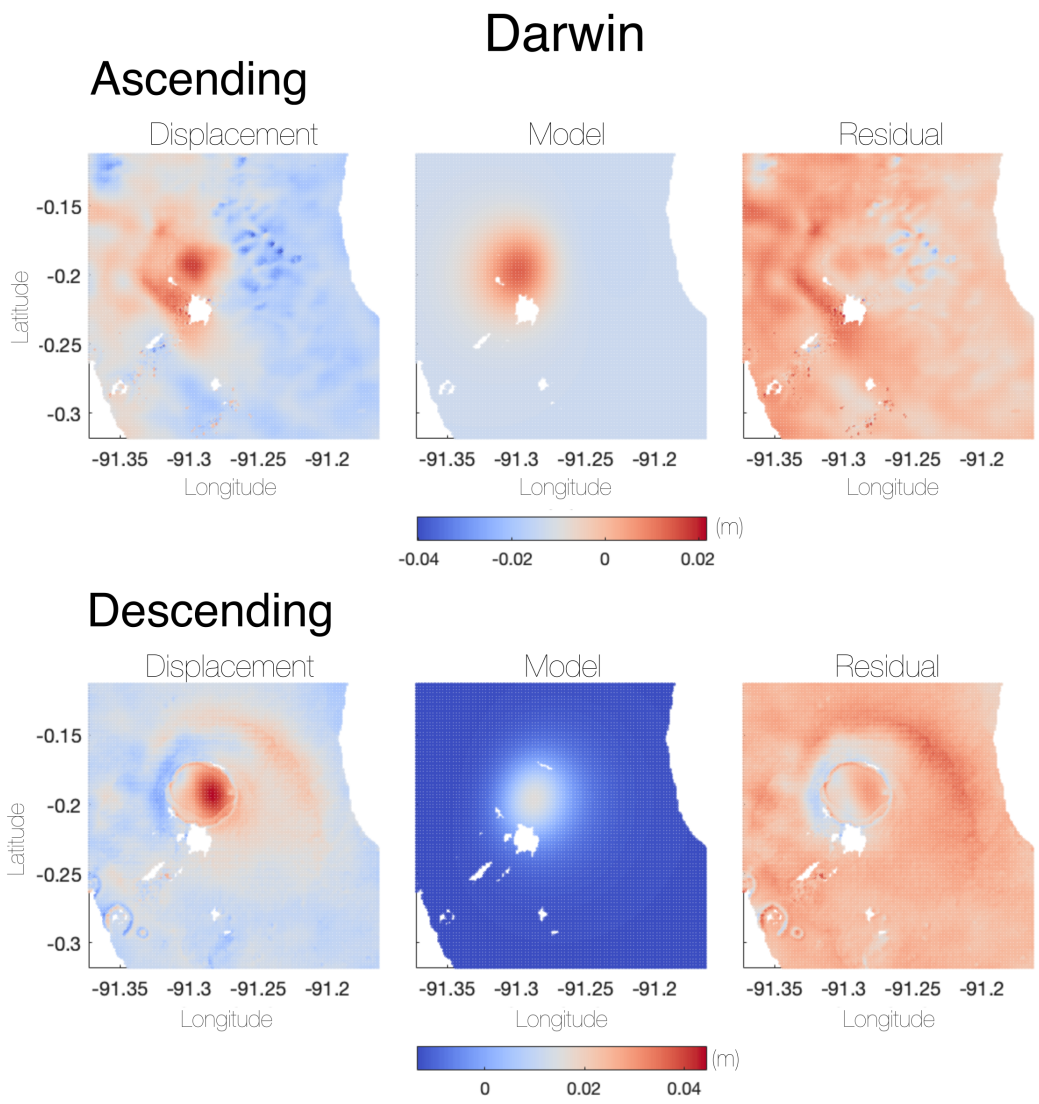

PARAM.	OPTIMAL	2.5%	97.50%
Length (m)	188.77	124.452	1051.43
Width (m)	3643.94	1259.22	4492.73
Depth (m)	4264.53	4015.04	4733.31
Strike (m)	105.663	90.3973	284.478
X (m)	2627.74	2282.73	3442.42
Y (m)	9519.86	9003.75	12161.7
Opening (m)	2.13353	0.46785	4.00451
InSAR Const.	-0.0134238	-0.014303	-0.0127242
InSAR Const.	0.0096809	0.00864868	0.01064

Fig. B17: Data, model, and residual for the best fitting sill source at Darwin, from 01/07/2020–28/03/2021. The optimal source parameters, as well as the 2.5% and 97.5% bounds are presented in the underlying table.

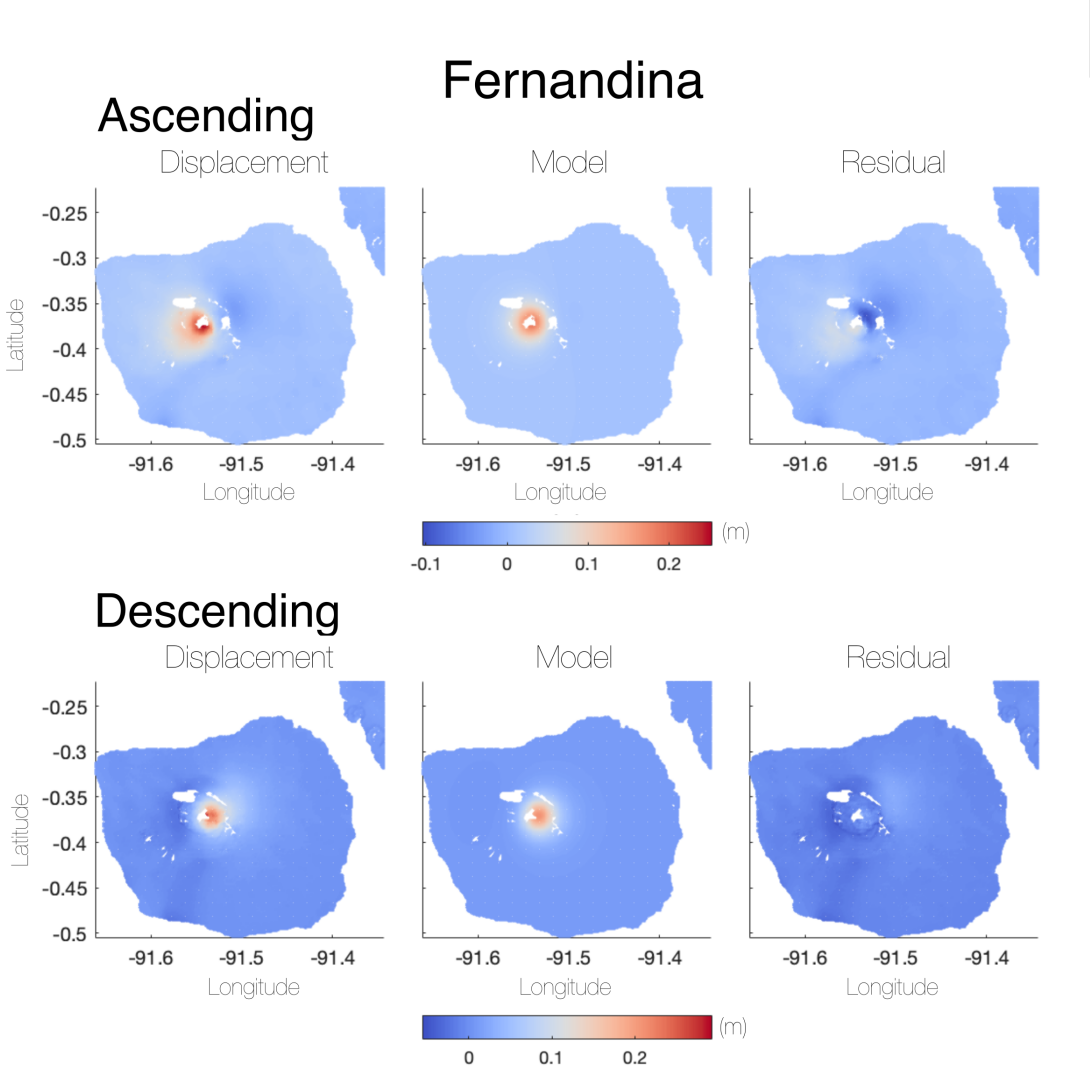

PARAM.	OPTIMAL	2.5%	97.50%
Length (m)	896.577	707.449	1260.96
Width (m)	108.212	111.66	271.713
Depth (m)	3106.91	3076.91	3140.76
Strike (m)	51.4147	44.9203	57.6794
X (m)	12757.5	12754.9	12822.6
Y (m)	-339.407	-404.027	-335.622
Opening (m)	49.16	14.139	49.6947
InSAR Const.	0.00971126	0.00922391	0.0104413
InSAR Const.	0.00482871	0.00456167	0.00502437

Fig. B18: Data, model, and residual for the best fitting sill source at Fernandina, from 01/07/2020–28/03/2021. The optimal source parameters, as well as the 2.5% and 97.5% bounds are presented in the underlying table.

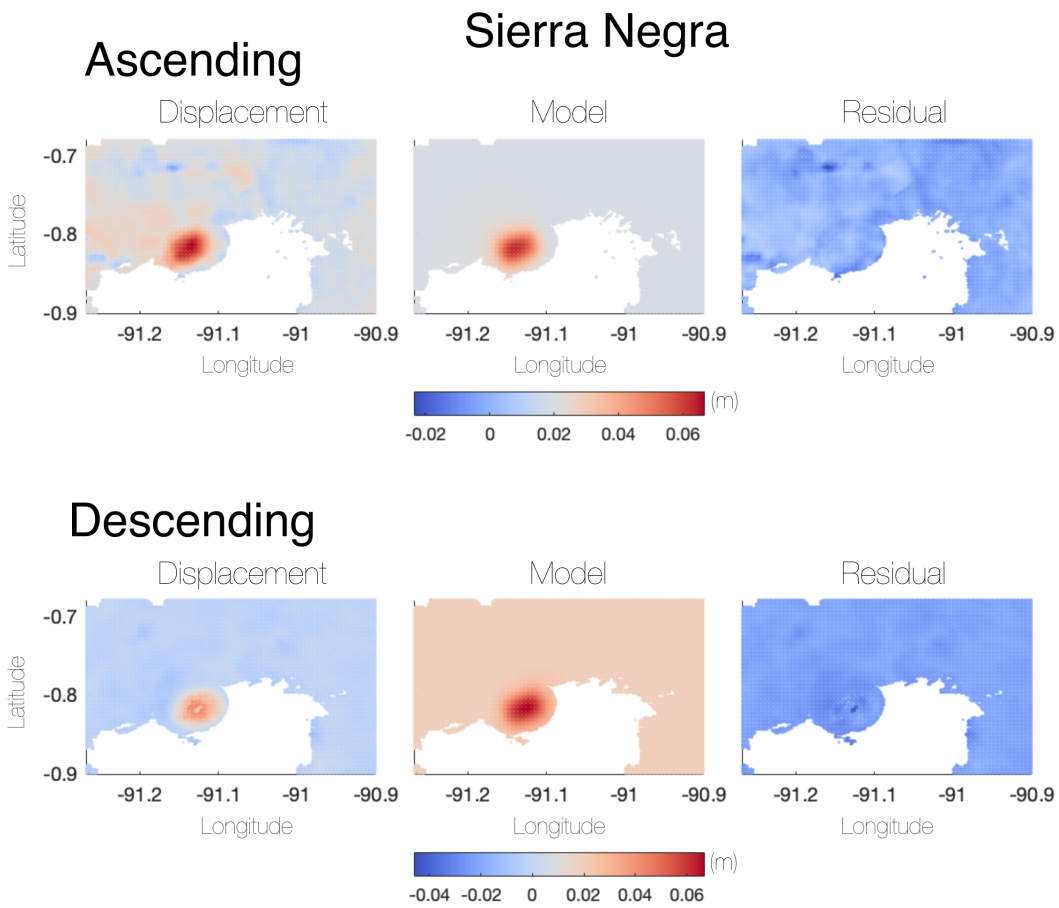

PARAM.	OPTIMAL	2.5%	97.50%
Length (m)	128.048	104.925	923.512
Width (m)	4553.33	4123.59	4930.47
Depth (m)	1957.84	1796.54	2082.25
Strike (m)	218.158	214.464	221.842
X (m)	13783	13417.1	14179.7
Y (m)	-6381.72	-6582.94	-6222.33
Opening (m)	1.05408	0.14301	1.3071
InSAR Const.	-0.0086843	-0.0093517	-0.0077237
InSAR Const.	0.00391561	0.00308953	0.00466889

Fig. B19: Data, model, and residual for the best fitting sill source at Sierra Negra, from 29/12/2020–03/02/2021. The optimal source parameters, as well as the 2.5% and 97.5% bounds are presented in the underlying table.

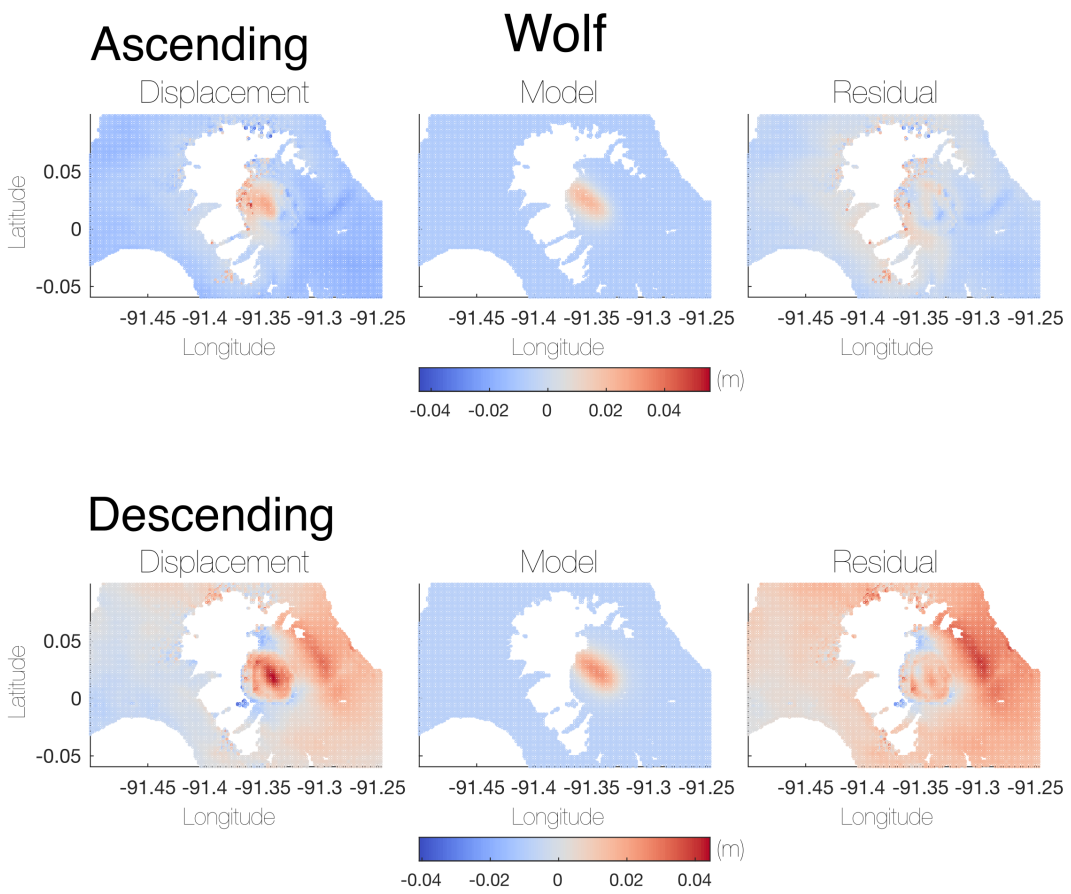

PARAM.	OPTIMAL	2.5%	97.50%
Length (m)	128.048	104.925	923.512
Width (m)	4553.33	4123.59	4930.47
Depth (m)	1957.84	1796.54	2082.25
Strike (m)	218.158	214.464	221.842
X (m)	13783	13417.1	14179.7
Y (m)	-6381.72	-6582.94	-6222.33
Opening (m)	1.05408	0.14301	1.3071
InSAR Const.	-0.0086843	-0.0093517	-0.0077237
InSAR Const.	0.00391561	0.00308953	0.00466889

Fig. B20: Data, model, and residual for the best fitting sill source at Wolf, from 01/06/2020–27/05/2021. The optimal source parameters, as well as the 2.5% and 97.5% bounds are presented in the underlying table.

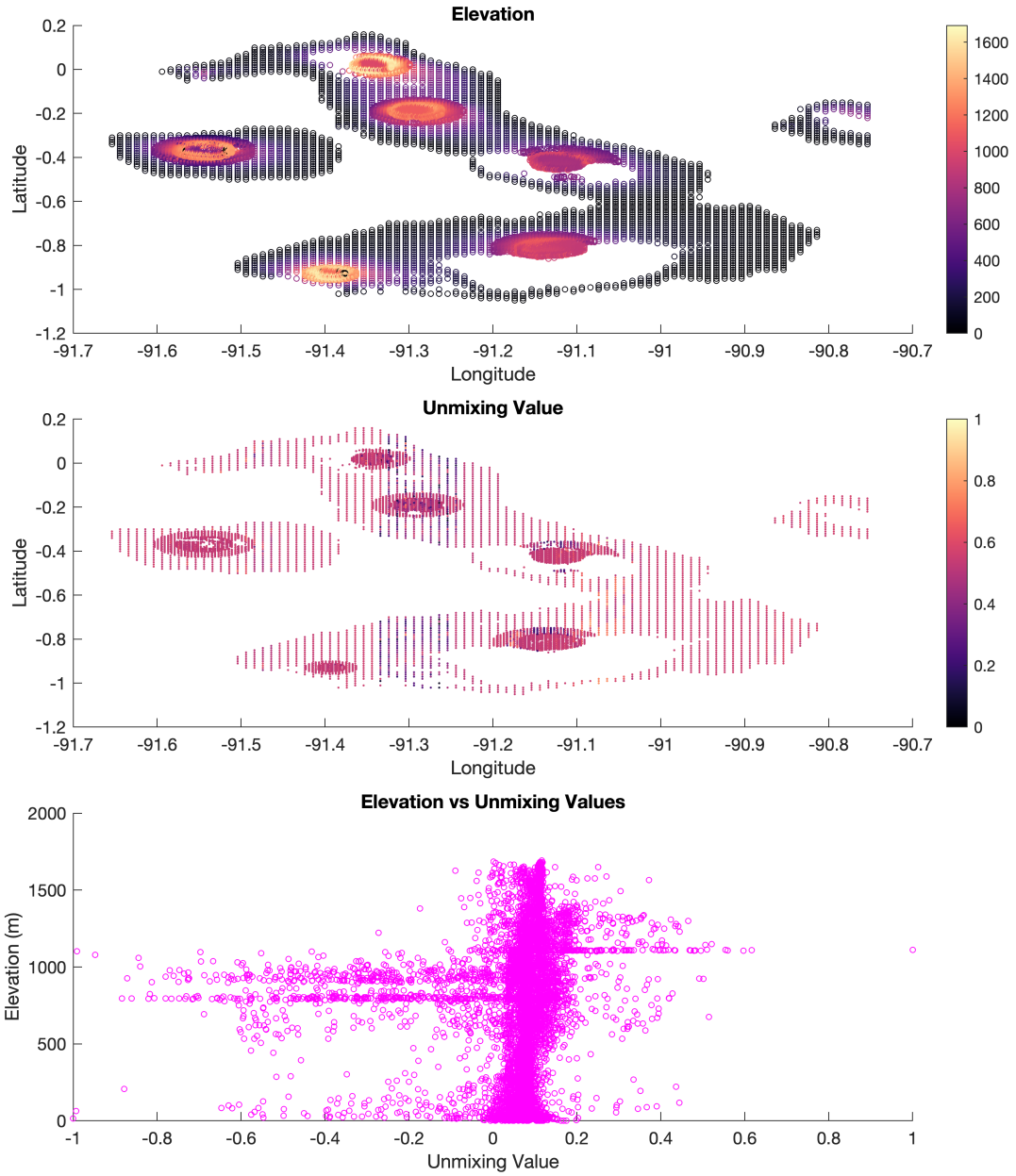

Fig. B21: Topography vs unmixing values. The panels show downsampled elevation, downsampled unmixing values, and both of these plotted against one another.

11/08/2017	05/09/2018	21/04/2019	29/12/2019	07/08/2020	17/03/2021	25/10/2021
23/08/2017	11/09/2018	27/04/2019	04/01/2020	13/08/2020	23/03/2021	31/10/2021
04/09/2017	17/09/2018	03/05/2019	10/01/2020	19/08/2020	29/03/2021	06/11/2021
16/09/2017	23/09/2018	09/05/2019	16/01/2020	25/08/2020	04/04/2021	12/11/2021
28/09/2017	29/09/2018	21/05/2019	22/01/2020	31/08/2020	10/04/2021	18/11/2021
10/10/2017	05/10/2018	27/05/2019	28/01/2020	06/09/2020	16/04/2021	24/11/2021
22/10/2017	11/10/2018	02/06/2019	03/02/2020	12/09/2020	22/04/2021	06/12/2021
03/11/2017	17/10/2018	14/06/2019	09/02/2020	18/09/2020	28/04/2021	12/12/2021
15/11/2017	23/10/2018	20/06/2019	15/02/2020	24/09/2020	04/05/2021	18/12/2021
27/11/2017	29/10/2018	26/06/2019	21/02/2020	30/09/2020	10/05/2021	24/12/2021
09/12/2017	04/11/2018	02/07/2019	27/02/2020	06/10/2020	16/05/2021	05/01/2022
21/12/2017	10/11/2018	14/07/2019	04/03/2020	12/10/2020	22/05/2021	17/01/2022
02/01/2018	16/11/2018	20/07/2019	10/03/2020	18/10/2020	28/05/2021	29/01/2022
14/01/2018	22/11/2018	26/07/2019	16/03/2020	24/10/2020	03/06/2021	06/03/2022
26/01/2018	28/11/2018	01/08/2019	22/03/2020	30/10/2020	09/06/2021	18/03/2022
07/02/2018	04/12/2018	07/08/2019	28/03/2020	05/11/2020	15/06/2021	30/03/2022
19/02/2018	10/12/2018	13/08/2019	03/04/2020	11/11/2020	21/06/2021	
03/03/2018	16/12/2018	19/08/2019	09/04/2020	17/11/2020	27/06/2021	
15/03/2018	22/12/2018	25/08/2019	15/04/2020	23/11/2020	03/07/2021	

Table B1: Dates used in the Descending data set (256 in total). These data are taken from both Sentinel-1A and Sentinel-1B, using orbit number 128, covering the islands of both Fernandina and Isabela

07/01/2017	27/03/2018	28/12/2018	31/08/2019	21/04/2020	29/11/2020	09/07/2021
19/01/2017	08/04/2018	03/01/2019	06/09/2019	27/04/2020	05/12/2020	15/07/2021
31/01/2017	20/04/2018	09/01/2019	12/09/2019	03/05/2020	11/12/2020	21/07/2021
12/02/2017	02/05/2018	15/01/2019	18/09/2019	09/05/2020	17/12/2020	27/07/2021
24/02/2017	14/05/2018	21/01/2019	30/09/2019	15/05/2020	23/12/2020	02/08/2021
08/03/2017	26/05/2018	27/01/2019	06/10/2019	21/05/2020	29/12/2020	08/08/2021
20/03/2017	07/06/2018	02/02/2019	12/10/2019	27/05/2020	04/01/2021	14/08/2021
01/04/2017	19/06/2018	08/02/2019	18/10/2019	02/06/2020	10/01/2021	20/08/2021
13/04/2017	01/07/2018	20/02/2019	24/10/2019	08/06/2020	16/01/2021	26/08/2021
25/04/2017	07/07/2018	26/02/2019	30/10/2019	14/06/2020	22/01/2021	01/09/2021
07/05/2017	13/07/2018	04/03/2019	05/11/2019	20/06/2020	28/01/2021	07/09/2021
19/05/2017	25/07/2018	10/03/2019	17/11/2019	26/06/2020	03/02/2021	13/09/2021
31/05/2017	31/07/2018	16/03/2019	23/11/2019	02/07/2020	09/02/2021	19/09/2021
12/06/2017	06/08/2018	22/03/2019	29/11/2019	08/07/2020	15/02/2021	25/09/2021
24/06/2017	12/08/2018	28/03/2019	05/12/2019	14/07/2020	21/02/2021	01/10/2021
06/07/2017	18/08/2018	03/04/2019	11/12/2019	20/07/2020	27/02/2021	07/10/2021
18/07/2017	24/08/2018	09/04/2019	17/12/2019	26/07/2020	05/03/2021	13/10/2021
30/07/2017	30/08/2018	15/04/2019	23/12/2019	01/08/2020	11/03/2021	19/10/2021
11/08/2017	05/09/2018	21/04/2019	29/12/2019	07/08/2020	17/03/2021	25/10/2021

Table B2: Dates used in the Descending data set continued(256 in total). These data are taken from both Sentinel-1A and Sentinel-1B, using orbit number 128, covering the islands of both Fernandina and Isabela

06/01/2017	01/05/2018	14/01/2019	30/08/2019	26/04/2020	22/12/2020	13/08/2021
30/01/2017	13/05/2018	20/01/2019	05/09/2019	02/05/2020	28/12/2020	19/08/2021
23/02/2017	25/05/2018	26/01/2019	11/09/2019	08/05/2020	03/01/2021	25/08/2021
07/03/2017	18/06/2018	01/02/2019	17/09/2019	14/05/2020	09/01/2021	31/08/2021
19/03/2017	30/06/2018	19/02/2019	23/09/2019	20/05/2020	15/01/2021	06/09/2021
31/03/2017	06/07/2018	25/02/2019	29/09/2019	26/05/2020	27/01/2021	12/09/2021
12/04/2017	12/07/2018	03/03/2019	05/10/2019	01/06/2020	02/02/2021	18/09/2021
24/04/2017	18/07/2018	09/03/2019	11/10/2019	07/06/2020	08/02/2021	24/09/2021
06/05/2017	24/07/2018	15/03/2019	23/10/2019	13/06/2020	14/02/2021	30/09/2021
18/05/2017	30/07/2018	21/03/2019	29/10/2019	19/06/2020	20/02/2021	06/10/2021
30/05/2017	05/08/2018	27/03/2019	04/11/2019	25/06/2020	26/02/2021	12/10/2021
11/06/2017	11/08/2018	02/04/2019	10/11/2019	01/07/2020	04/03/2021	18/10/2021
23/06/2017	17/08/2018	08/04/2019	16/12/2019	07/07/2020	10/03/2021	24/10/2021
05/07/2017	23/08/2018	14/04/2019	22/12/2019	13/07/2020	16/03/2021	30/10/2021
17/07/2017	04/09/2018	20/04/2019	28/12/2019	25/07/2020	22/03/2021	05/11/2021
29/07/2017	16/09/2018	26/04/2019	03/01/2020	31/07/2020	28/03/2021	11/11/2021

Table B3: Dates used in the Ascending data set (204 in total). These data are taken from both Sentinel-1A and Sentinel-1B, using orbit number 106, covering the islands of both Fernandina and Isabela

10/08/2017	22/09/2018	02/05/2019	09/01/2020	12/08/2020	09/04/2021	17/11/2021
22/08/2017	28/09/2018	08/05/2019	15/01/2020	18/08/2020	15/04/2021	23/11/2021
03/09/2017	04/10/2018	14/05/2019	21/01/2020	24/08/2020	21/04/2021	29/11/2021
15/09/2017	10/10/2018	20/05/2019	27/01/2020	30/08/2020	27/04/2021	05/12/2021
09/10/2017	16/10/2018	26/05/2019	02/02/2020	05/09/2020	03/05/2021	11/12/2021
21/10/2017	22/10/2018	01/06/2019	08/02/2020	11/09/2020	09/05/2021	17/12/2021
02/11/2017	28/10/2018	13/06/2019	14/02/2020	17/09/2020	15/05/2021	04/01/2022
14/11/2017	03/11/2018	19/06/2019	20/02/2020	29/09/2020	21/05/2021	28/01/2022
26/11/2017	09/11/2018	25/06/2019	26/02/2020	23/10/2020	27/05/2021	09/02/2022
01/01/2018	15/11/2018	01/07/2019	03/03/2020	29/10/2020	08/06/2021	21/02/2022
13/01/2018	21/11/2018	07/07/2019	09/03/2020	04/11/2020	14/06/2021	05/03/2022
25/01/2018	27/11/2018	13/07/2019	15/03/2020	10/11/2020	20/06/2021	17/03/2022
06/02/2018	03/12/2018	19/07/2019	21/03/2020	16/11/2020	26/06/2021	
18/02/2018	09/12/2018	25/07/2019	27/03/2020	22/11/2020	02/07/2021	
02/03/2018	21/12/2018	31/07/2019	02/04/2020	28/11/2020	08/07/2021	
14/03/2018	27/12/2018	06/08/2019	08/04/2020	04/12/2020	14/07/2021	
26/03/2018	02/01/2019	18/08/2019	14/04/2020	10/12/2020	26/07/2021	
07/04/2018	08/01/2019	24/08/2019	20/04/2020	16/12/2020	07/08/2021	

Table B4: Dates used in the Ascending data set continued (204 in total). These data are taken from both Sentinel-1A and Sentinel-1B, using orbit number 106, covering the islands of both Fernandina and Isabela

Appendix C

Supporting information for Chapter 4

Contents of this file

1. Figures C1 to C9
2. Tables C1 to C8
3. Detailed discussion around results of Asama, Paka, Silali and TVZ.

Introduction Appendix C contains supporting information for Chapter 4. This includes supporting figures that are referenced in the text, as well as tables of various modelling parameters.

Asama

Asama is an andesitic volcano, located on the Japanese Island of Honshu. It is located 140 km northwest of Tokyo, and is the most active volcano on Honshu, having erupted 6 times in the 21st century alone, most recently in 2019 (Figure C6) (at the time of writing) (Venzke, 2023). Given its activity and proximity to a major population centre, Asama is well monitored, with levelling data as far back as 1902 (Murase et al., 2007). These data show that, between periods of inflation, Asama steadily subsided for a >20 yr period, from 1943–1967. Wang et al. (2019) use ALOS-2 and Sentinel-1 data to study Asama from 2014–2018, identifying two distinct zones of subsidence, one on the northeastern flank attributed to hydrothermal depressurisation, with maximum rates of -14 mm yr^{-1}, and one on the southeastern flank attributed to flank instability, with maximum rates of -12 mm yr^{-1}. Though magmatic crystallisation has not been previously suggested as a cause of subsidence here, we include Asama as a candidate volcano as the long term, low-rate deformation is consistent with that expected at a

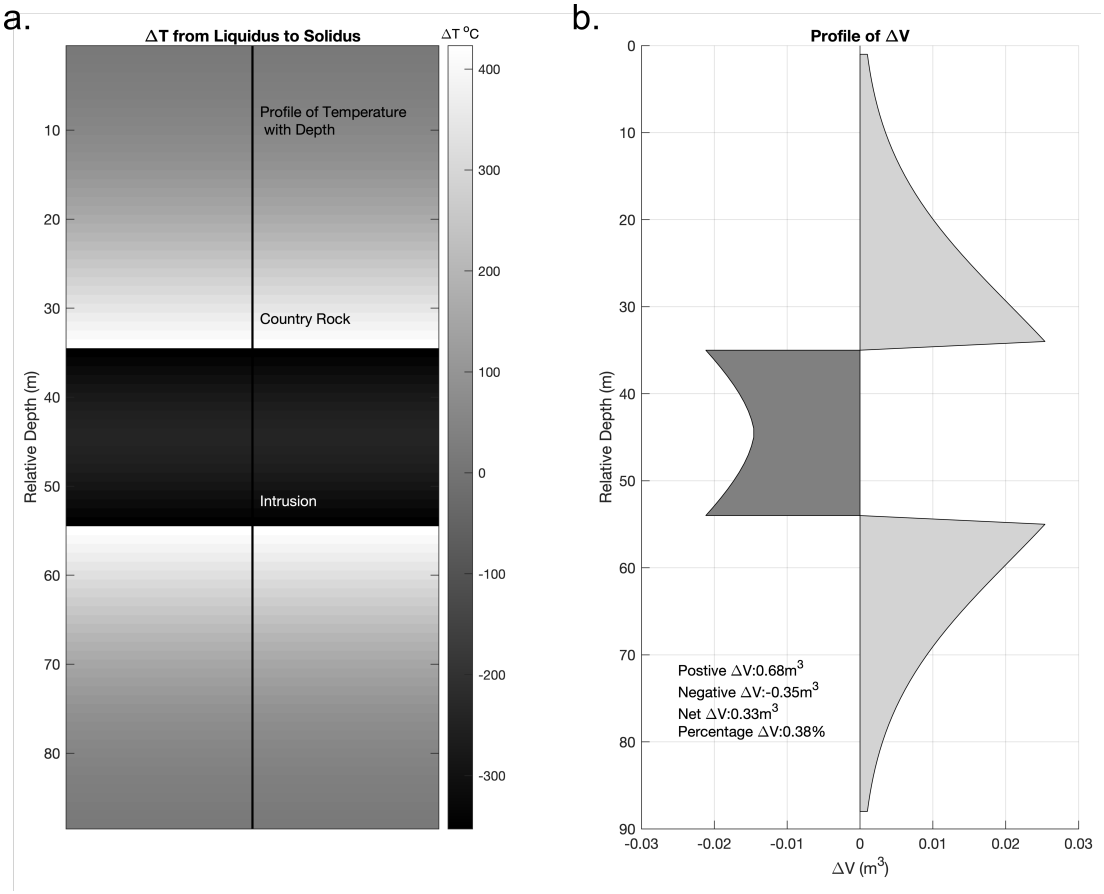

Fig. C1: Thermal expansion versus thermal contraction in the area around a theoretical 20 m thick sill. This is intruded at liquidus temperature into country rock at 400°C, and cooled until the solidus is reached. A. Temperature change in the sill and surrounding rock from the time of intrusion to the point when the sill is fully crystalline. B. Profile of volume change in the sill, and in the area around the sill. Areas of expansion due to temperature increase are shown in light grey, and areas of contraction due to temperature decrease are shown in dark grey.

crystallising magma. Using Sentinel-1 data, we construct time series of subsidence, relative to urban and forested areas, from 2015–2021 (Figure C6). Here, there is cumulative subsidence of >10 cm for a point on the NE flank of the volcano, at at 36.41 N, 138.54 E. However, this subsidence is non-linear, possibly due to hydrothermal activity (Wang et al., 2019), or magma intrusion associated with the 2019 eruption (Figure C6).

At Asama, current subsidence profiles require an intrusion, emplaced at 4 km depth (Table C6), of 50 m thickness, emplaced at either $0.05^{o}C\ M^{-1}$ (RSS: 1.47) or of 5000 m width (RSS: 0.74). Like Alcedo, the 50 m thick by 5000 m wide sill is a better fit. We model this for a magma intruded in 2003, the end of a 13 year eruptive quiescence at Asama (between 1990–2003). However, it has erupted 5 times since its 2003 eruption, suggesting that crystallisation has likely been augmented by fresh magma supply.

Next, we consider the effect of crystallisation at mature volcanoes, where there is

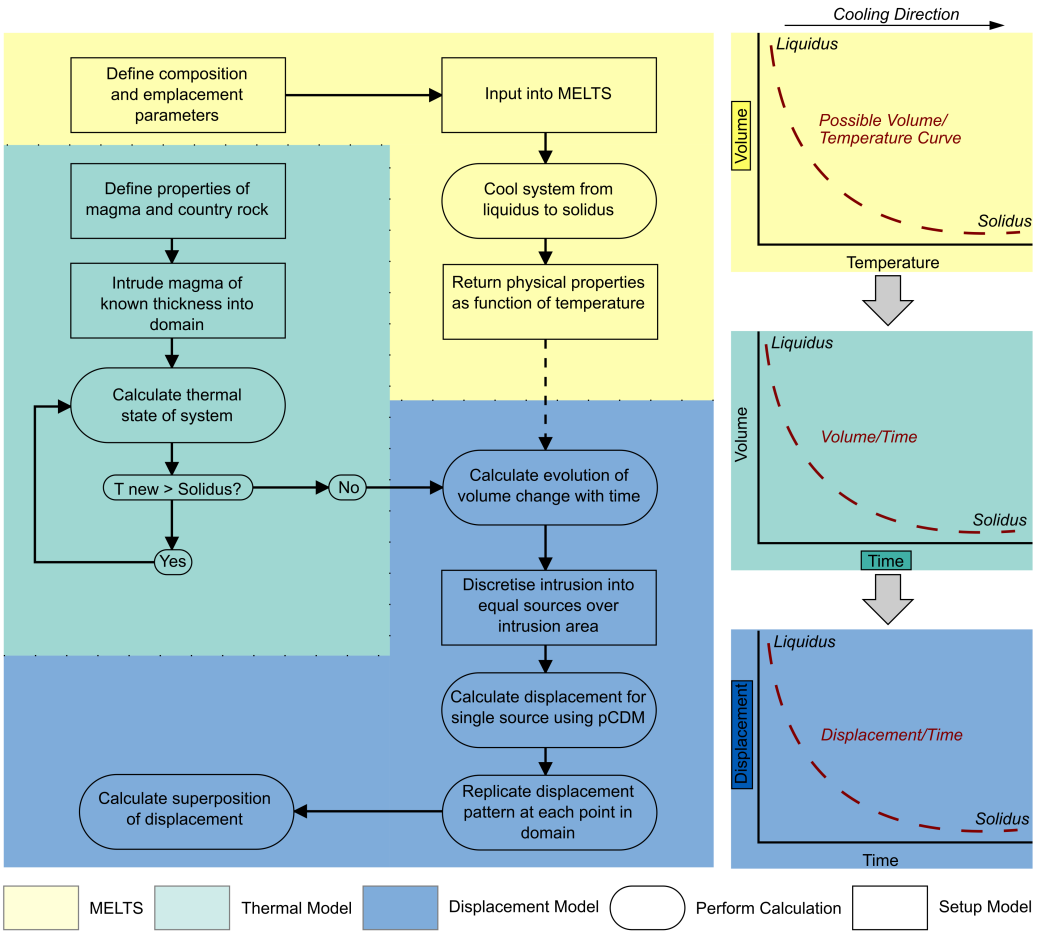

Fig. C2: Flowchart of modelling approach. Colours define stage of modelling process, progressing from petrological modelling with MELTS, to a finite difference thermal model, and a displacement model. Schematics show the changing variable with each stage of the model. The changed variable is highlighted on the corresponding axis.

no evidence of recent eruptive activity. We study Paka, Silali, and the Taupo Volcanic Zone, where the most recent eruptions at each occurred 7550 BCE, 5050 BCE, and 260 CE, respectively (Venzke, 2023). In each case, geothermal activity, and long-term subsidence is the primary observable volcanic activity.

Paka

Paka is a trachytic/basaltic shield volcano located in the Kenyan rift (Venzke, 2023). It is inactive, last erupting 7550 BCE, though has active surface hydrothermal activity (Venzke, 2023). Paka underwent an uplift episode (>21 cm) between 2006–2007, from a source at 2.8 km deep (Biggs et al., 2009). Albino et al. (2022) observe linear subsidence at Paka between 2015–2020, at rates of -0.7 mm yr^{-1}, and suggest that it may be due to hydrothermal or magmatic activity, or residual tropospheric signals. We construct time series at Paka from 2015–2021, and also see linear subsidence (< 6 cm

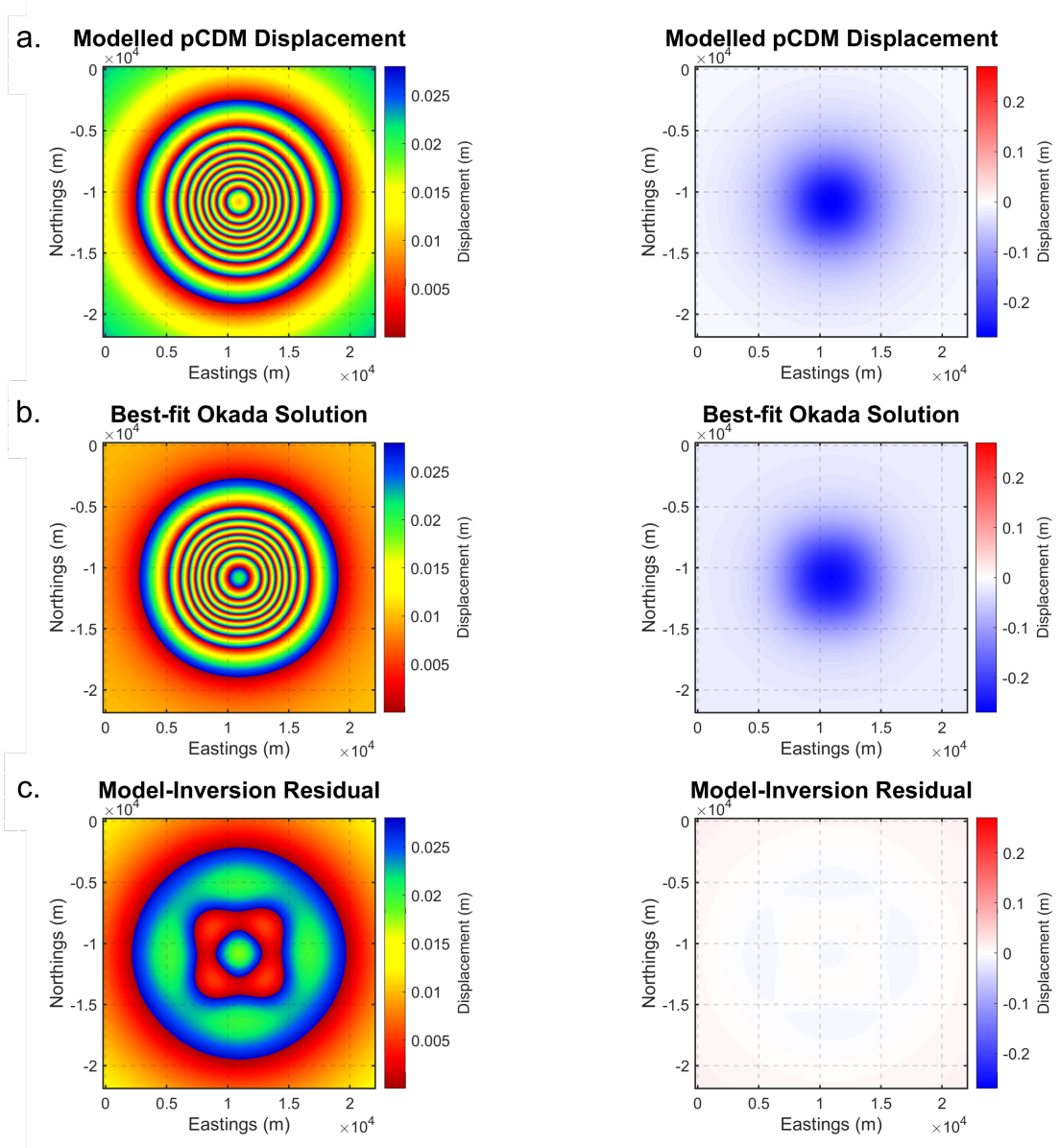

Fig. C3: Comparison between the pCDM approach, and a rectangular dislocation.

cumulative) at the volcano (Figure C7), relative to two areas on opposite sides of the Kenyan Rift. There were no urban areas to test these reference areas against, though as noted by Albino et al. (2022), the aridity of the East African Rift suggests that phase bias contributions are probably minor, as consistent soil moisture content should not introduce phase inconsistencies (Maghsoudi et al., 2022). We consider Paka as a candidate for crystallisation modelling as given the subsidence observation there, and evidence of magma intrusion during 2007 unrest.

Biggs et al. (2016) observe multiple phases of uplift at Paka from 2006–2010. We find a best fit due to crystallisation when magma is emplaced in 2008, halfway through

this observation period. This magma intruded in 2008, at 2.8 km depth (Table C4), has a best fit of 40 m thickness, emplaced at either $0.03^oC\ M^{-1}$ (RSS: 2.97) or of 5000 m width (RSS: 0.19). However, the non-linear shape of the modelled curve suggests that crystallisation from this intrusion can be ruled out as primary cause of long-term subsidence. Paka has an established hydrothermal system, and the northwestern flank is a prospective site for geothermal development (Mibei et al., 2022). As such it probable that subsidence here is altered by volatile and hydrothermal behaviour (Sections 4.5.2, and 4.5.3), or by large scale thermo-elastic contraction (Section 4.5.1).

Silali

Like Paka, Silali is a trachytic/basaltic shield volcano located in the Kenyan rift (Venzke, 2023). It too is extrusively inactive, last erupting 5050 BCE, though Biggs et al. (2016) observed subsidence at rates of 1–2 cm yr^{-1} between 2006–2010. Albino et al. (2022) again observed linear subsidence at Silali between 2015–2020, at rates of -0.7 mm yr^{-1}, and propose similar mechanisms as Paka. We construct time series at Silali from 2015–2021, relative to two reference areas on opposite sides of the Kenyan Rift, and also see sustained linear subsidence of $<$ 6 cm (Figure C8). We consider crystallisation here as other causes of long-term subsidence (such as lava flow contraction) are unlikely given that Silali has not erupted in over 7000 years (Venzke, 2023).

At Silali, maximum subsidence rates are calculated with a sill at 3.9 km depth (Table C7), of 50 m thickness, emplaced at either $0.03^oC\ M^{-1}$ (RSS: 0.21) or with 4000 m width (RSS: 0.22). Both of these models can well account for long-term subsidence following the sill emplacement, from 2006 (the first observation of subsidence at Silali (Biggs et al., 2016), such that the we model maximum crystallisation rates). However, like Paka, it is possible that Silali has been subsiding for an extended period, though the historic lack of volcano monitoring in the Kenyan Rift prevents a better estimate of magma intrusion date than that from Biggs et al. (2016).

Taupo Volcanic Zone

The Taupo Volcanic Zone (TVZ) is a 300 km long region on the north island of New Zealand, extending from Lake Taupo in the south, northwards towards the bay of plenty (Hamling et al., 2015). Hamling et al. (2015) use GPS and InSAR data to observe subsidence rates of up to 20 mm yr^{-1} here, and attribute it to the contraction of a sill at 6 km depth, due to magma crystallisation. We observe linear subsidence of $<$20 cm, for a point in the Central TVZ, relative to areas of cropland and Rotarua, for a point at -38.45 N, 176.18 E. Clearly, there are areas of greater subsidence at the southern sector of the TVZ, though this coincides with the Wairakei Geothermal plant (Figure C9), suggesting a combination of magmatic and geothermal sources.

Here, subsidence is modelled with a sill at 6 km (Table C8) (Hamling et al., 2015), of 200 m thickness, emplaced at either $0.03^oC\ M^{-1}$ (RSS: 2.33) or with 6000 m width (RSS: 0.6), though the intrusion of 200 m by 6000 m is a much better fit. This intrusion was emplaced in 2003 (the first observation of subsidence at the TVZ (Hamling et al., 2015)). Similar to the examples in the Kenyan rift, though 2003 marks the first observation of long-term InSAR subsidence, it is probable that the source magma has been emplaced for a much longer period. The Wairakei Power Station has been active since the 1950s, suggesting that magmatic heat source there has been established before our 2003 estimate.

Table C1: References used in Figure 4.2

Volcano	Reference	Volcano	Reference
Akutan	Lu and Dzurisin (2014)	Krafla	Sturkell et al. (2006)
Alcedo	Hooper et al. (2007)	Kupreaof	Parker et al. (2014)
Amukta	Lu and Dzurisin (2014)	Lassen	Parker et al. (2016)
Aniakchak	Lu and Dzurisin (2014)	Makushin	Lu and Dzurisin (2014)
Asama	Murase et al. (2007) and Wang et al. (2019)	Medicine Lake	Parker et al. (2014)
Askja	Zeeuw-van Dalfsen et al. (2012)	Mono Lake	Tizzani et al. (2007)
Bezymianny	Grapenthin et al. (2013)	Mt. Baker	Crider et al. (2011)
Cerro Blanco	Henderson and Pritchard (2013)	Nabro	Hamlyn et al. (2018)
Changbaishan	Xu et al. (2012)	Seguam	Lu and Dzurisin (2014)
Emmons Lake	Lu and Dzurisin (2014)	Silali	Albino et al. (2022)
Fisher	Lu and Dzurisin (2014)	Taupo Volcanic Zone	Hamling et al. (2015)
Haledebi	Biggs et al. (2011)	Tendurek Dagi	Bathke et al. (2013)
Kilauea	Patrick et al. (2019)	Timanfaya	Purcell et al. (2022)
Kiska	Lu and Dzurisin (2014)		

Table C2: Parameters used for Alcedo

Variable	Value	Units	Reference
Time Series			
FrameID[a]	128D_09016_110500		
Coherence Thresh.	0.2		
Loop Closure Thresh.	3	*Rads.*	
Point Latitude	-0.430	°	
Point Longitude	-91.115	°	
GACOS avg. $\Delta\sigma^b$	10	%	
MELTS[c]			
SiO_2	48	$wt\%$	Aiuppa et al. (2022)
TiO_2	2.7	$wt\%$	Aiuppa et al. (2022)
Al_2O_3	15.4	$wt\%$	Aiuppa et al. (2022)
FeO	10	$wt\%$	Aiuppa et al. (2022)
MgO	8.2	$wt\%$	Aiuppa et al. (2022)
CaO	11.7	$wt\%$	Aiuppa et al. (2022)
Na_2O	2.3	$wt\%$	Aiuppa et al. (2022)
K_2O	0.3	$wt\%$	Aiuppa et al. (2022)
MnO	0.1	$wt\%$	Aiuppa et al. (2022)
FO_2 *Path*	-1.5NNO		Aiuppa et al. (2022)
Pressure	750	$Bars$	Bagnardi (2014)[d]
Modelling			
Depth	3000	m	Bagnardi (2014)
Width	3000	m	Galetto et al. (2019)
Start Date	2007		Galetto et al. (2019)
Geo. Grad.	0.025	$^oC\ m^{-1}$	

[a] From LiCSAR system; [a] σ: Standard Deviation
[c] Samples from Aiuppa et al. (2022) H_2O excluded
[d] Litho. pressure: 250 $Bars\ Km^{-1}$

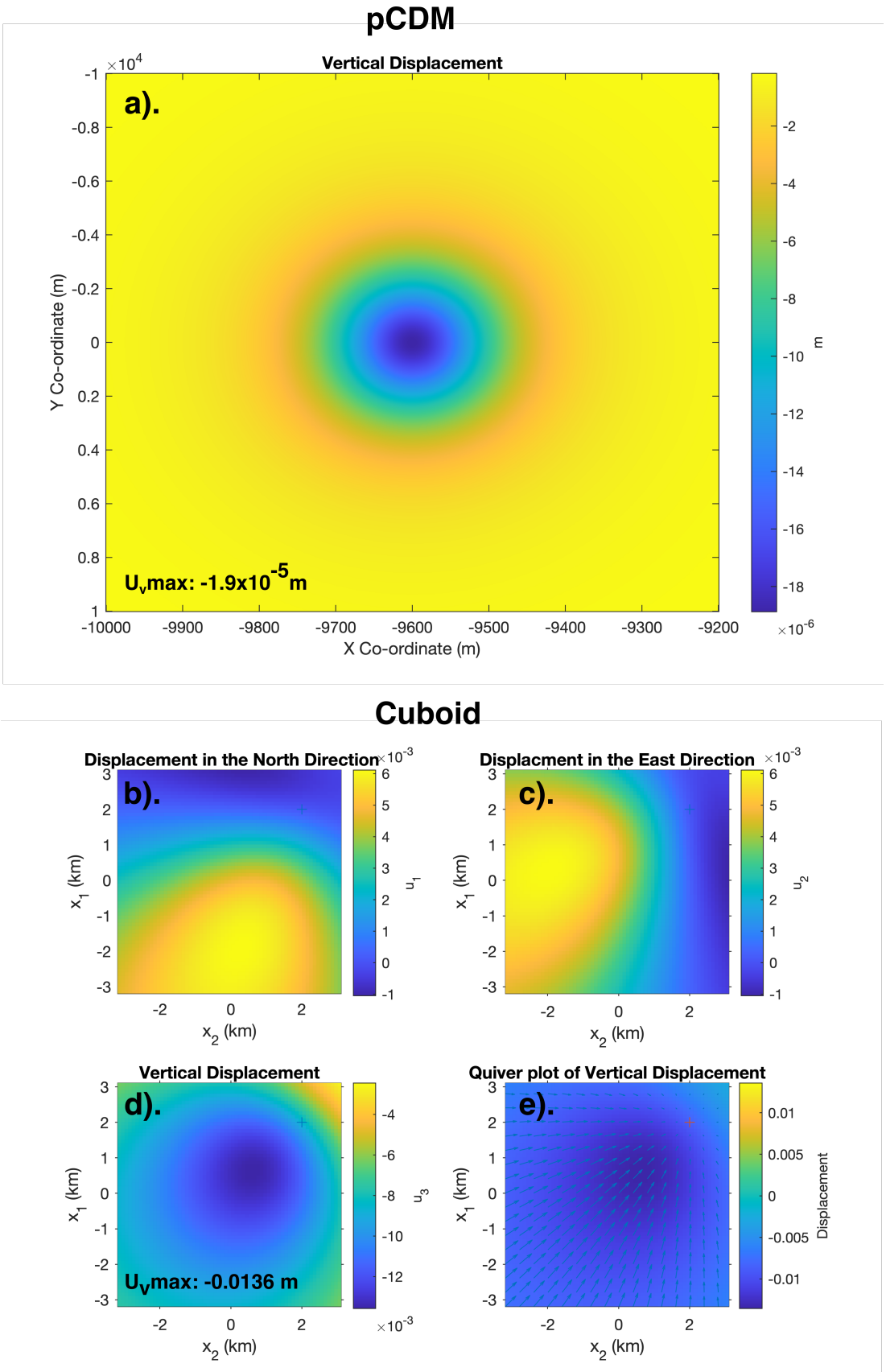

Fig. C4: Comparison between the pCDM approach and a cuboid source. In both, the source is at 3 km depth. For the cuboid source, the length and thickness are 25 m, with strain values of -0.1 on each axis. In the pCDM, the volume loss is approximately 1500 m^3 (equivalent to initial thickness of 25 m by length of 25 m by width of 25 m, contracting by 10%). a). Vertical displacement from a pCDM source. b). Displacement in the north direction from a cuboid source. c). Displacement in the east direction from a cuboid source. d). Vertical displacement from a cuboid source. e). Quiver plot of vertical displacement from a cuboid source.

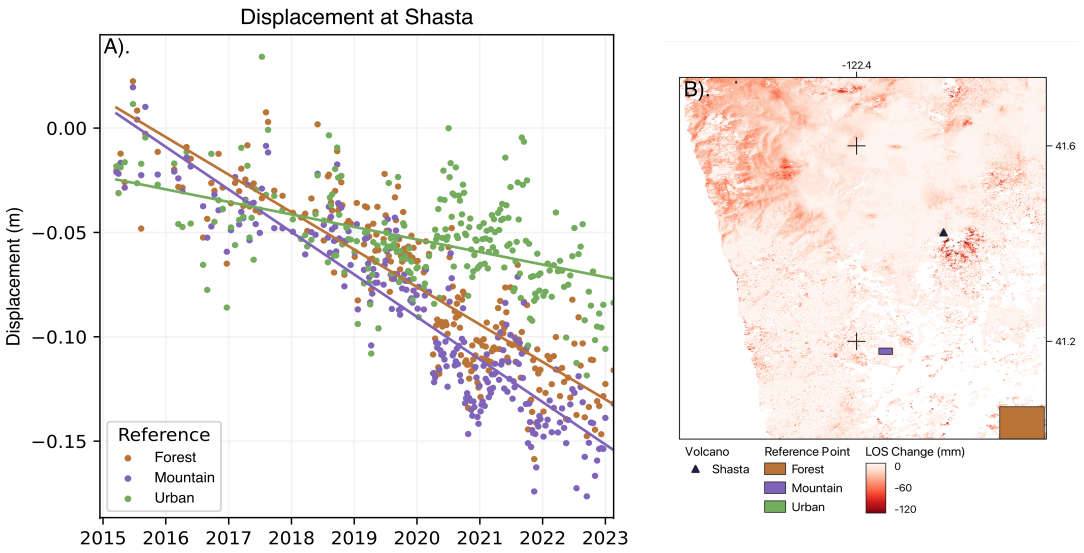

Fig. C5: Impact of alternating reference location at Mt. Shasta. The coloured points indicate a different reference location, while the lines are the least-squares fit of each time series. The cumulative displacement map shows the location of each reference, and the plotted point.

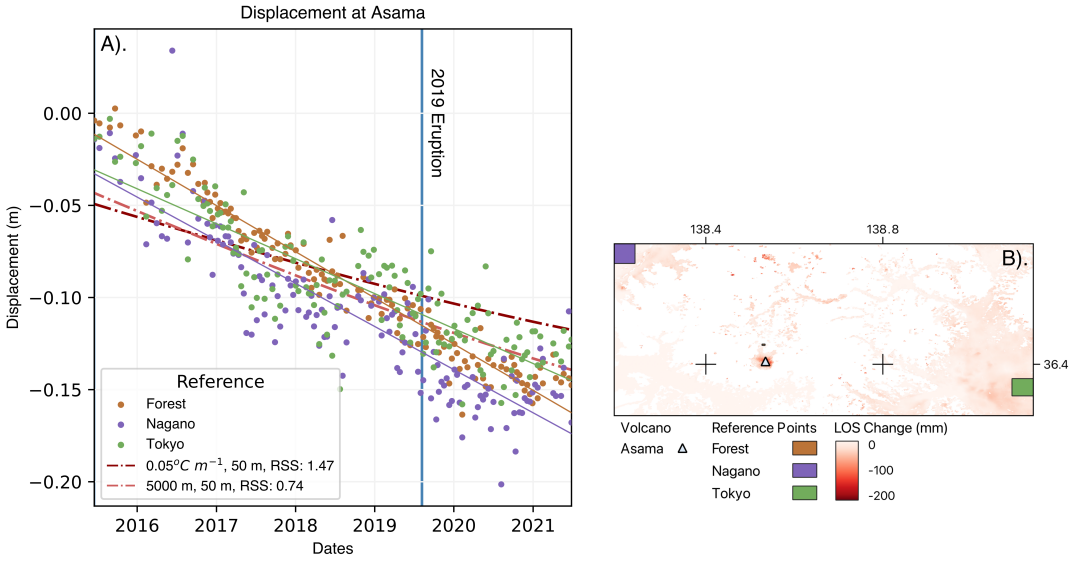

Fig. C6: Influence of crystallisation at Asama. A). Time series at Asama spanning from 17/06/2015–27/06/2021, with the blue line indicating the date of the 2019 eruption at Asama. The coloured scatter points represent deformation at Asama relative to various reference areas, as annotated on the legend, while the coloured lines show linear regressions for each set of scatter points. Time, and displacement in metres are given on the x- and y-axes, respectively, while the hatched red lines show estimated model predictions. B). Map showing cumulative displacement the location of the plotted point and reference areas, while the crosses indicate the grid of latitude and longitude.

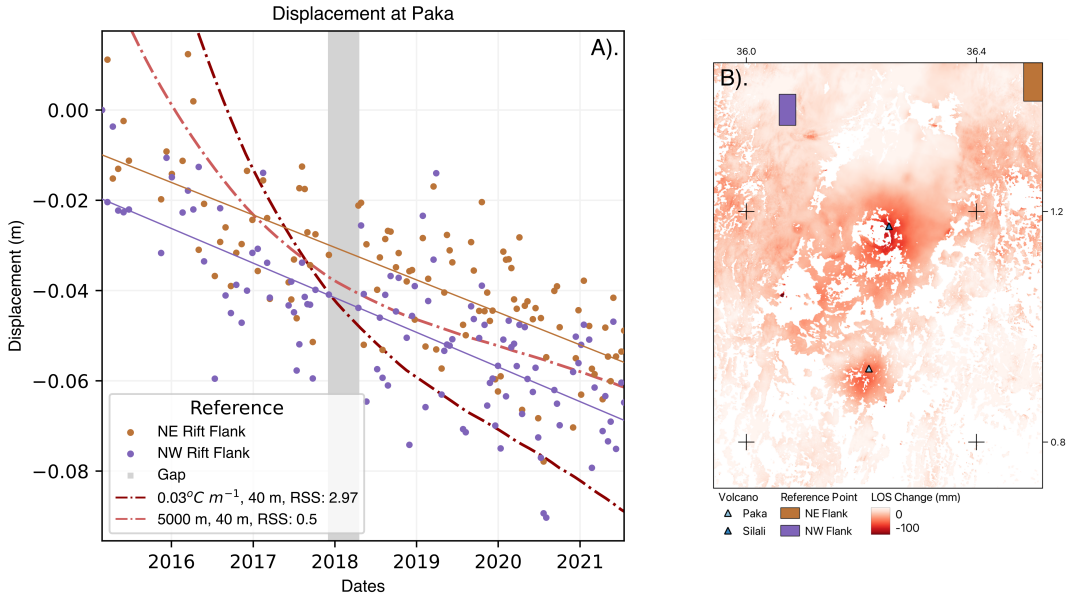

Fig. C7: Deformation due to crystallisation at Paka. A). Time Series of subsidence at Paka from 25/05/2015–17/07/2021. The plotted colours, and associated linear regressions, indicate deformation relative to two areas on opposing sides of the Kenyan Rift. The vertical grey bar indicates a data gap, while the hatched red lines show predicted subsidence due to crystallisation. B). Map of cumulative displacement showing the location of the plotted point (blue triangle) and reference areas (crosses indicate the grid of latitude and longitude).

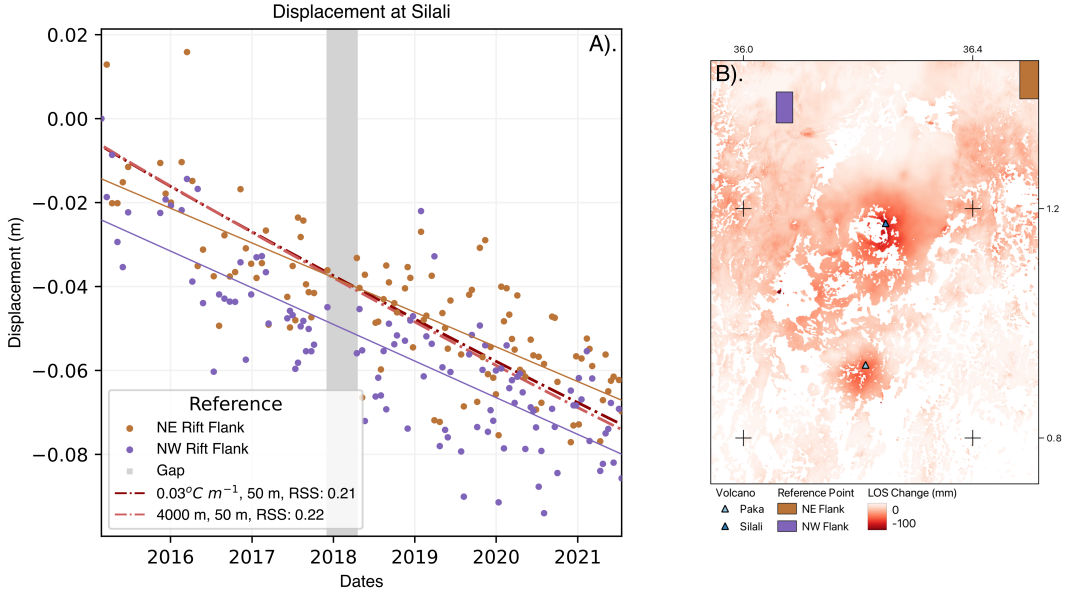

Fig. C8: Deformation due to crystallisation at Silali. A). Time series at Silal i from 25/05/2015–17/07/2021. The plotted colours, and associated linear regressions, indicate deformation relative to two areas on opposing sides of the Kenyan Rift, while the vertical grey bar denotes a data gap. The hatched red lines show predicted subsidence due to crystallisation. B). Map of cumulative displacement showing the location of the plotted point (blue triangle) and reference areas (crosses indicate the grid of latitude and longitude).

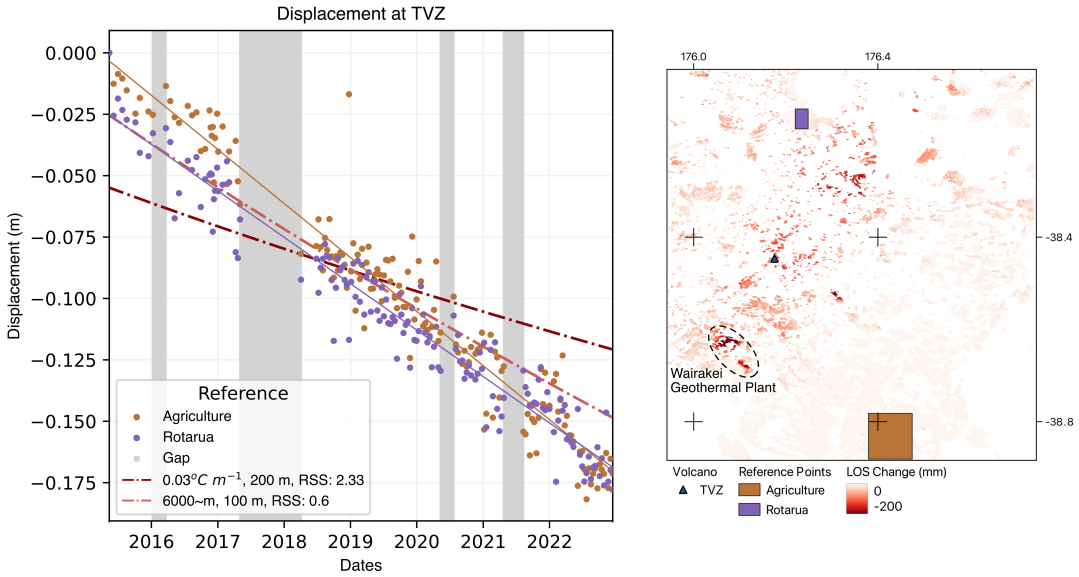

Fig. C9: Effect of crystallisation at the Taupo Volcanic Zone. A). Time series of subsidence for a point in the Taupo Volcanic Zone, from 14/05/2015–15/12/2022. The plotted colours represent deformation relative to two separate reference areas: cropland to the south of the TVZ, and the urban centre of Rotarua. The vertical grey bars show data gaps in the time series, while the hatched red lines show model predictions. Time, and displacement in metres are given on the x- and y-axes, respectively. B). Map of cumulative displacement showing the location of the plotted point (blue triangle) and reference areas, while the location of the Wairakei Geothermal Plant is indicated. Crosses indicate the grid of latitude and longitude.

Table C3: Parameters used for Asama

Variable	Value	Units	Reference
Time Series			
FrameID[a]	039A_05372_151515		
Coherence Thresh.	0.15		
Loop Closure Thresh.	6	*Rads.*	
Point Latitude	36.41	°	
Point Longitude	138.538	°	
GACOS avg. $\Delta\sigma^b$	29	%	
MELTS			
SiO_2	60.24	$wt\%$	Tsuya (1933)
TiO_2	0.7	$wt\%$	Tsuya (1933)
Al_2O_3	16.43	$wt\%$	Tsuya (1933)
Fe_2O_3	1.54	$wt\%$	Tsuya (1933)
FeO	2.26	$wt\%$	Tsuya (1933)
MgO	3.92	$wt\%$	Tsuya (1933)
CaO	7.07	$wt\%$	Tsuya (1933)
Na_2O	3	$wt\%$	Tsuya (1933)
K_2O	1.16	$wt\%$	Tsuya (1933)
MnO	0.11	$wt\%$	Tsuya (1933)
P_2O_5	0.13	$wt\%$	Tsuya (1933)
Pressure	1000	$Bars$	Wang et al. (2019)[c]
Modelling			
Depth	4000	m	Wang et al. (2019)
Width	4000	m	
Start Date	2003		Venzke (2023)
Geo. Grad.	0.025	$^oC\ m^{-1}$	

[a] From LiCSAR system; [b] Standard Deviation
[c] Litho. pressure: 250 $Bars\ Km^{-1}$

Table C4: Parameters used for Paka

Variable	Value	Units	Reference
Time Series			
FrameID[a]	152D_08915_131313		
Coherence Thresh.	0.2		
Loop Closure Thresh.	3	*Rads.*	
Point Latitude	0.927	°	
Point Longitude	36.213	°	
GACOS avg. $\Delta\sigma^b$	9	%	
MELTS			
SiO_2	48.8	$wt\%$	Mibei et al. (2021)
TiO_2	1.6	$wt\%$	Mibei et al. (2021)
Al_2O_3	16.8	$wt\%$	Mibei et al. (2021)
FeO	9.9	$wt\%$	Mibei et al. (2021)
MgO	6.8	$wt\%$	Mibei et al. (2021)
CaO	11.6	$wt\%$	Mibei et al. (2021)
Na_2O	3.0	$wt\%$	Mibei et al. (2021)
K_2O	0.8	$wt\%$	Mibei et al. (2021)
MnO	0.2	$wt\%$	Mibei et al. (2021)
P_2O_5	0.2	$wt\%$	Mibei et al. (2021)
FO_2 *Path*	FMQ		
Pressure	700	*Bars*	Biggs et al. (2009)[c]
Modelling			
Depth	2800	m	Biggs et al. (2009)
Width	11000	m	Biggs et al. (2009)
Start Date	1999		
Geo. Grad.	0.025	$^oC\ m^{-1}$	

[a] From LiCSAR system; [b] Standard Deviation
[c] Litho. pressure: 250 $Bars\ Km^{-1}$

Table C5: Parameters used for Shasta

Variable	Value	Units	Reference
Time Series			
FrameID[a]	137A_04835_131313		
Coherence Thresh.	0.15		
Loop Closure Thresh.	6	*Rads.*	
Point Latitude	41.416	°	
Point Longitude	-122.235	°	
GACOS avg. $\Delta\sigma^b$	23	%	

[a] As used in the LiCSAR system; [b] Standard Deviation

Table C6: Parameters used for Sierra Negra

Variable	Value	Units	Reference
Time Series			
FrameID[a]	128D_09016_110500		
Coherence Thresh.	0.2		
Loop Closure Thresh.	3	*Rads.*	
Point Latitude	-0.758	°	
Point Longitude	-91.239	°	
GACOS avg. $\Delta\sigma^b$	10	%	
MELTS[c]			
SiO_2	48	$wt\%$	Aiuppa et al. (2022)
TiO_2	2.7	$wt\%$	Aiuppa et al. (2022)
Al_2O_3	15.4	$wt\%$	Aiuppa et al. (2022)
FeO	10	$wt\%$	Aiuppa et al. (2022)
MgO	8.2	$wt\%$	Aiuppa et al. (2022)
CaO	11.7	$wt\%$	Aiuppa et al. (2022)
Na_2O	2.3	$wt\%$	Aiuppa et al. (2022)
K_2O	0.3	$wt\%$	Aiuppa et al. (2022)
MnO	0.1	$wt\%$	Aiuppa et al. (2022)
FO_2 *Path*	-1.5NNO		Aiuppa et al. (2022)
Pressure	250	$Bars$	Davis et al. (2021)[d]
Modelling			
Depth	1000	m	Davis et al. (2021)
Width	4000	m	
Start Date	2018		Venzke (2023)
Geo. Grad.	0.025	$^oC\ m^{-1}$	

[a] From LiCSAR system; [a] σ: Standard Deviation
[c] Samples from Aiuppa et al. (2022) H_2O excluded
[d] Litho. pressure: 250 $Bars\ Km^{-1}$

Table C7: Parameters used for Silali

Variable	Value	Units	Reference
Time Series			
FrameID[a]	152D_08915_131313		
Coherence Thresh.	0.2		
Loop Closure Thresh.	3	*Rads.*	
Point Latitude	1.174	°	
Point Longitude	36.248	°	
GACOS avg. $\Delta\sigma$[b]	9	%	
MELTS			
SiO_2	64.93	$wt\%$	Macdonald et al. (1995)
TiO_2	0.85	$wt\%$	Macdonald et al. (1995)
Al_2O_3	14.52	$wt\%$	Macdonald et al. (1995)
FeO	4.74	$wt\%$	Macdonald et al. (1995)
MgO	0.73	$wt\%$	Macdonald et al. (1995)
CaO	1.77	$wt\%$	Macdonald et al. (1995)
Na_2O	5.27	$wt\%$	Macdonald et al. (1995)
K_2O	5.07	$wt\%$	Macdonald et al. (1995)
MnO	0.22	$wt\%$	Macdonald et al. (1995)
P_2O_5	0.17	$wt\%$	Macdonald et al. (1995)
FO_2 *Path*	FMQ		
Pressure	975	*Bars*	Robertson (2015)[c]
Modelling			
Depth	3900	m	Robertson (2015)
Width	4000	m	
Start Date	2006		
Geo. Grad.	0.025	$^oC\ m^{-1}$	

[a] From LiCSAR system; [b] Standard Deviation
[c] Litho. pressure: 250 $Bars\ Km^{-1}$

Table C8: Parameters used for Taupo

Variable	Value	Units	Reference
Time Series			
FrameID[a]	073D_12785_121717		
Coherence Thresh.	0.15		
Loop Closure Thresh.	3	*Rads.*	
Point Latitude	-38.625	°	
Point Longitude	176.075	°	
GACOS avg. $\Delta\sigma^b$	14	%	
MELTS			
SiO_2	74.99	$wt\%$	Blake et al. (1992)
TiO_2	0.24	$wt\%$	Blake et al. (1992)
Al_2O_3	13.36	$wt\%$	Blake et al. (1992)
Fe_2O_3	2.37	$wt\%$	Blake et al. (1992)
MgO	0.29	$wt\%$	Blake et al. (1992)
CaO	1.51	$wt\%$	Blake et al. (1992)
Na_2O	4.23	$wt\%$	Blake et al. (1992)
K_2O	2.87	$wt\%$	Blake et al. (1992)
MnO	0.08	$wt\%$	Blake et al. (1992)
P_2O_5	0.06	$wt\%$	Blake et al. (1992)
FO_2 *Path*	FMQ		
Pressure	1500	$Bars$	Hamling et al. (2015)[c]
Modelling			
Depth	6000	m	Hamling et al. (2015)
Width	4000	m	
Start Date	2003		
Geo. Grad.	0.025	$^oC\ m^{-1}$	

[a] From LiCSAR system; [b] Standard Deviation
[c] Litho. pressure: 250 $Bars\ Km^{-1}$